A MULTI-PHASE STRUCTURAL CONSTITUTIVE MODEL FOR INSIGHTS INTO SOFT TISSUE REMODELING MECHANISMS

by

Silvia Wognum

B.Sc. in Biomedical Engineering, Eindhoven University of Technology, 2002

M.Sc. in Biomedical Engineering, Eindhoven University of Technology, 2004

Submitted to the Graduate Faculty of
The Swanson School of Engineering in partial fulfillment
of the requirements for the degree of
Doctor of Philosophy

University of Pittsburgh
2010

UNIVERSITY OF PITTSBURGH
SWANSON SCHOOL OF ENGINEERING

This dissertation was presented

by

Silvia Wognum

It was defended on
July 9, 2010
and approved by
Steven D. Abramowitch, PhD, Assistant Professor, Department of Bioengineering
Changfeng Tai, PhD, Assistant Professor, Department of Urology
Richard E. Debski, PhD, Associate Professor, Department of Bioengineering
Anne M. Robertson, PhD, Associate Professor, Department of Mechanical Engineering and Materials Science
Dissertation Director: Michael S. Sacks, PhD, John A. Swanson Endowed Chair in Bioengineering, Departments of Bioengineering, CEE and MEMS

A MULTI-PHASE STRUCTURAL CONSTITUTIVE MODEL FOR INSIGHTS INTO SOFT TISSUE REMODELING MECHANISMS

Silvia Wognum, PhD

University of Pittsburgh, 2010

All tissues in the human body continuously grow, remodel, and adapt to changes in their physiological environment, in order to maintain homeostasis or to retain it in case of pathologies. The growth and remodeling (G&R) process results in changes in structure and composition. To elucidate how observed changes in tissue components are related to altered tissue level mechanical behavior, structural constitutive models are required with physiologically relevant model parameters. Specifically what is required is a finite deformation constitutive model describing the tissue mechanical behavior, in combination with the appropriate kinematics for the multiple tissue components, and experimental data of a relevant tissue application. An excellent example is the urinary bladder wall (UBW), which undergoes profound remodeling in response to different pathologies, such as spinal cord injury (SCI). The overall objective of this dissertation was to develop a morphologically-driven, multi-phase constitutive model that would allow for separate investigation of the contribution of individual tissue components to the tissue-level remodeling process.

As a first step, a constitutive model was developed of UBW extracellular matrix (ECM). Removing the smooth muscle cells from UBW tissue via decellularization allowed for the separate mechanical and structural investigation of UBW ECM. It was shown that the presence of *de novo* produced elastin in the UBW ECM post-SCI induced, indirectly, a distinct mechanical behavior with higher compliance, allowing for a higher overall extensibility of the post-SCI UBW and increased bladder storage capacity. The ECM constitutive model was extended and modified to be able to apply it to a multi-component tissue with individual model components existing in different reference states. Parameters were determined from biaxial mechanical data of decellularized and intact UBW tissue using a step-wise fitting approach implemented in MATLAB. As an initial step towards a theoretical G&R framework, a parametric analysis was performed to investigate if observed mechanical changes in post-SCI UBW were due to changes in morphology or intrinsic constituent properties. The developed

model has the potential to explain underlying remodeling mechanisms of individual constituents in muscular tissues in several pathologies (*e.g*. UBW post-SCI), and predict remodeling events in a tissue engineering setting of muscular tissues.

TABLE OF CONTENTS

PREFACE ..... **XVIII**

NOMENCLATURE ..... **XXI**

1.0 INTRODUCTION **1**

1.1 SCOPE **1**

1.2 CONSTITUTIVE MODELS OF SOFT TISSUES **3**

1.2.1 Introduction **3**

1.2.2 Stress and strain – measurement and definitions **3**

1.2.3 Thermodynamic considerations **5**

1.2.4 Phenomenological hyperelastic constitutive models **9**

1.2.5 Structural constitutive models **13**

1.3 GROWTH AND REMODELING **14**

1.3.1 Growth models **14**

1.3.2 Mixture theories **15**

1.4 OBJECTIVES AND OUTLINE **17**

2.0 DEVELOPMENT O F S TRUCTURAL CO NSTITUTIVE M ODELS FO R MULTI-PHASE SOFT TISSUES **20**

2.1 ORIGINAL CONSTITUTIVE MODEL FORMULATION **21**

2.1.1 Assumptions **21**

2.1.2 Tissue level framework **22**

2.1.3 ECM component – phenomenological fiber ensemble model **23**

2.1.4 ECM component – fiber ensemble model with recruitment 24

2.1.5 Fiber recruitment function 26

2.2 MODIFIED CONSTITUTIVE MODEL FORMULATION TO ACCOUNT FOR WORKLESS CHANGE IN REFERENTIAL CONFIGURATION 27

2.2.1 Rational and assumptions 27

2.2.2 Model modifications 28

2.3 CORRECTED FIBER STRESS-STRAIN RELATION 33

2.3.1 Rationale 33

2.3.2 Fiber model modifications 35

2.4 CONSTITUTIVE MODEL FOR MUSCLE COMPONENT 41

2.5 SUMMARY 42

3.0 MODEL IMPLEMENTATION, MODEL VALIDATION, AND METHODS OF PARAMETER ESTIMATION 44

3.1 MODEL IMPLEMENTATION AND VALIDATION 45

3.1.1 MATLAB numerical integration functions 45

3.1.2 Validation of fiber model 45

3.1.3 Validation of fiber model at the ensemble level 49

3.1.4 Discrete fiber simulations 51

3.1.5 Synthetic data 55

3.2 PARAMETER ESTIMATION 59

3.2.1 Background 59

3.2.2 MATLAB parameter estimation functions 61

3.2.3 Parameter estimation components for ensemble model 62

3.2.4 Parameter estimation methods for structural model 64

3.2.5 Additional GUI details 65

3.2.6 Validation of implementation of fitting process 66
3.3 SUMMARY 67
4.0 APPLICATION TO URINARY BLADDER TISSUE 68
4.1 BACKGROUND ON THE URINARY BLADDER 68
4.1.1 Bladder anatomy and structure 68
4.1.2 Bladder function 70
4.2 THE URINARY BLADDER WALL AND SPINALCORD INJURY 72
4.2.1 Clinical spinal cord injury 72
4.2.2 Experimental SCI in a rat model 75
4.3 THE URINARY BLADDER AS A REMODELING SYSTEM 79
5.0 EXPERIMENTAL METHODS TO COMPLETE THE EXPERIMENTAL DATABASE 80
5.1 URINARY BLADDER WALL ECM SPECIMEN PREPARATION 81
5.1.1 Tissue preparation 81
5.1.2 Decellularization 82
5.2 BIAXIAL MECHANICAL TESTING OF DECELLULARIZED SPECIMENS 83
5.2.1 Kinematics of a biaxial test and stress and strain calculations 83
5.2.2 Biaxial mechanical testing procedure 85
5.3 TISSUE STRUCTURE AND COMPOSITION 87
5.3.1 Structure of bladder ECM 87
5.3.2 Collagen orientation 88
5.3.3 Volume fractions 88
5.4 REANALYSIS OF AVAILABLE DATA TO MAKE USABLE FOR MODEL 89
5.4.1 Methods of spinalization 89

5.4.2 Intact bladder biaxial mechanical data – normal and post-SCI 89
5.4.3 SM orientation and area fraction data at different post-SCI time points 90
5.4.4 Biochemical composition data 92
5.4.5 Mechanical data of post-SCI UBW ECM 92
6.0 ON THE MECHANICAL ROLE OF DE NOVO SYNTHESIZED ELASTIN IN THE URINARY BLADDER WALL 94
6.1 INTRODUCTION 94
6.2 METHODS 97
6.2.1 Experimental methods 97
6.2.2 Constitutive model 97
6.2.3 Normal UBW ECM fiber ensemble model fitting 99
6.2.4 Determination of normal UBW ECM mechanical behavior 100
6.2.5 Normal and post-injury stress-stretch data analyses 101
6.2.6 Determination of normal and post-injury UBW ECM mechanical behavior 101
6.3 RESULTS 102
6.3.1 General observations 102
6.3.2 Structure of normal and post-injury UBW ECM 103
6.3.3 Biaxial mechanical testing results of normal UBW ECM 106
6.3.4 Mechanical effect of elastin on UBW ECM 107
6.3.5 Fiber ensemble model fitting 108
6.3.6 Determination of UBW ECM mechanical behavior 112
6.4 DISCUSSION 116
6.4.1 Summary 116
6.4.2 Normal UBW ECM mechanical behavior 118

6.4.3 Reference states 118
6.4.4 Decellularization 119
6.4.5 ECM structure and composition 119
6.4.6 Collagen-elastin interaction 120
6.4.7 Collagen fiber super-coiling 120
6.4.8 Model extensions 121
6.4.9 Conclusion 122
7.0 A STRUCTURAL CONSTITUTIVE MODEL FOR A MUSCLE–CONNECTIVE TISSUE COMPOSITE 123
7.1 INTRODUCTION 123
7.2 CONSTITUTIVE MODEL 126
7.3 METHODS 130
7.3.1 Summary of experimental methods 130
7.3.2 Parameter estimation methods for ensemble model 130
7.3.3 Parameter estimation methods for structural model 131
7.3.4 ECM strain energy in Ω_1 and transforming ECM strain energy in Ω_1 to Ω_0 132
7.3.5 Average ECM parameters 135
7.3.6 Intact tissue strain energy 136
7.3.7 Smooth muscle strain energy and constitutive model 137
7.4 RESULTS 137
7.4.1 Volume fractions general specimen observations 137
7.4.2 ECM model fitting results 140
7.4.3 Average ECM parameters and strain energy 143
7.4.4 Intact UBW and smooth muscle strain energy 147
7.5 DISCUSSION 153

7.5.1 Summary 153
7.5.2 Reference state, preconditioning and permanent set 153
7.5.3 Parameter estimation 155
7.5.4 Application to multiple experimental data sets of UBW 157
7.5.5 Smooth muscle 159
7.5.6 Conclusion 161
8.0 TOWARDS A MODEL TO SIMULATE SOFT TISSUE REMODELING AND ELUCIDATE MECHANICSMS 162
8.1 INTRODUCTION 162
8.2 LITERATURE REVIEW OF AVAILABLE G&R MODELS 163
8.3 URINARY BLADDER WALL REMODELING 167
8.3.1 Constituent data 167
8.3.2 Intact tissue strain energy at the 10-day post-SCI time point 172
8.3.3 Parametric investigation 174
8.3.4 Predicting altered UBW mechanical behavior at 10 days post-SCI 175
8.4 CONCLUSION 182
9.0 SUMMARY AND CONCLUSIONS 184
9.1 SUMMARY OF MAIN FINDINGS 185
9.1.1 On the mechanical role of de novo synthesized elastin in the urinary bladder wall 185
9.1.2 A structural constitutive model for a muscle–connective tissue composite 185
9.1.3 Towards a model for soft tissue remodeling 187
9.2 FUTURE STUDIES 188
9.2.1 Simulating time-course UBW remodeling 188
9.2.2 Modeling UBW in physiological state 189

9.2.3 Simulating remodeling in a tissue engineering setting of (smooth) muscle-rich tissues 191

9.2.4 Simulating right ventricle remodeling in response to pulmonary hypertension 192

APPENDIX A 194

APPENDIX B 196

APPENDIX C 199

APPENDIX D 207

BIBLIOGRAPHY 218

LIST OF TABLES

Table 3.1. Overview of settings discrete fiber simulations. 52

Table 5.1. Overview of mechanical data 84

Table 6.1. Mean and SEM values of specimen observations (n = 7) 102

Table 6.2. Average model parameters. 109

Table 7.1. UBW ECM specimen information. 139

Table 7.2. ECM model parameters defined in Ω_0. 142

Table 7.3. Comparison of the lower bound stretch values from the model fit with calculated cut-off values. 142

Table 8.1. Comparison of model parameters of UBW at 10 days post-SCI to normal 178

LIST OF FIGURES

Figure 1.1. Schematic representation of the multiplicative decomposition of the deformation gradient. 15

Figure 2.1. Schematic of the representative volume element. 21

Figure 2.2. The process of fiber recruitment explained by building up from a single fiber. 25

Figure 2.3. A collagen fiber can be assumed to be linear in terms of force – displacement and hence in terms of P-λ. 34

Figure 2.4. Schematic representation of the linear-elastic fiber relation. 36

Figure 2.5. Representation of a fiber ensemble by a set of springs with variable slack lengths. 37

Figure 2.6. Schematic overview of the interrelations of the components of the multi-phase structural constitutive model. The numbers refer to the equations, as summarized below. 42

Figure 3.1. Stress-strain behavior of a single straight fiber, with a linear material model in terms of in S-E (η =100). 46

Figure 3.2. Stress-strain behavior of a fiber with slack, with a linear material model in terms of in S-E (η =100). 47

Figure 3.3. Stress-strain behavior of a single fiber exhibiting a linear material model in terms of P-λ (η =100). 47

Figure 3.4. Stress-strain behavior of a fiber with slack exhibiting a linear material model in terms of P-λ (η =100). 48

Figure 3.5. Maximum slope of the fiber stress-strain curve for different slack stretches. 49

Figure 3.6. Ensemble behavior for different recruitment functions for both fiber models. 50

Figure 3.7. Comparison of model stress calculations with results of discrete fiber simulation 7 (Table 3.1). 54

Figure 3.8. Validation of the model implementation without recruitment. 56

Figure 3.9. Validation of the model implementation with beta recruitment for different loading regimes. 58

Figure 3.10. Angular dependence of the ensemble permanent set stretch and its effect on the recruitment function. 59

Figure 3.11. Contour plots of the objective function as function of different values of K and σ_R. 66

Figure 4.1. Schematic of the human urinary bladder. 69

Figure 4.2. Schematic of a rat urinary bladder. 69

Figure 4.3. Histological assessment of intact and decellularized rat bladders. 72

Figure 4.4. Time course of spinal cord injury, in a clinical setting and in the experimental rat model of SCI. 74

Figure 4.5. Morphology of normal and (10-day) SCI rat bladders. 74

Figure 4.6. Time course changes in SM fiber orientation and biaxial mechanical behavior post-SCI. 76

Figure 4.7. Microarray analysis (Affymetrix Gene Chip®) of detrusor RNA from normal and SCI rats. 77

Figure 4.8. Time course changes in compliance post-SCI by two different measures. 78

Figure 4.9. Area fractions of muscle and collagen in normal, 10-day (redrawn from [109]) and 10-week SCI rat bladders, fixed at 50% volume capacity. 78

Figure 5.1. The process of specimen preparation from an intact rat urinary bladder to a mounted testing specimen. 82

Figure 5.2. Schematic of all possible different reference states (Ω) encountered during biaxial mechanical testing. 85

Figure 5.3. Biaxial mechanical experimental setup. 86

Figure 6.1. Cross-sections of intact bladder specimens, stained with Picro-Sirius red stain. 104

Figure 6.2. Structure of normal bladder ECM. 105

Figure 6.3. Structure of post-SCI bladder ECM. 105

Figure 6.4. Stress-stretch results of biaxial mechanical testing of normal decellularized bladder specimens (mean ± SEM, n = 7), with respect to two different reference states. 106

Figure 6.5. Comparing equibiaxial stress data of normal and post-injury decellularized UBW, referenced to Ω_4. 107

Figure 6.6. Representative error space plot of the fiber ensemble model with bimodal recruitment. 109

Figure 6.7. Representative plot of determining the maximum tangent modulus. 110

Figure 6.8. Model fitting results of one representative normal bladder ECM specimen (referenced to Ω_3). 111

Figure 6.9. Average recruitment function of 6 samples. 111

Figure 6.10. Collagen fiber orientation distribution in UBW ECM. 113

Figure 6.11. Average tissue-level model prediction. 114

Figure 6.12. Prediction of behavior of normal and post-injury decellularized bladder tissue. 115

Figure 6.13. Schematic showing the effects of SCI on organ level storage function and UBW compliance. 117

Figure 7.1. Schematic overview of the interrelations of the components of the multi-phase structural constitutive model. The numbers refer to the equations. 127

Figure 7.2. Schematic of a bar subjected to uniaxial tension. 133

Figure 7.3. Volume fractions of tissue constituents as determined through lyophilization of UBW specimens. 138

Figure 7.4. Schematic of UBW volume fractions from two different sources and the integration of information. 140

Figure 7.5. Representative results of bladder ECM fitting. 141

Figure 7.6. Average fiber recruitment and distribution. 144

Figure 7.7. Strain range and average ECM strain energy. 144

Figure 7.8. Fitting of average ECM strain energy data to obtain average ECM parameters. 146

Figure 7.9. Fit of work data of intact UBW in Ω_0 to Fung model and comparison to stress-strain data. 147

Figure 7.10. Strain energy surface and contour plots for intact UBW and its two components ECM and SM. 149

Figure 7.11. Smooth muscle orientation data and fit. 150

Figure 7.12. Fit result of the smooth muscle strain energy for a model with a bimodal continuous distribution. 151

Figure 7.13. Fit result of the smooth muscle strain energy for the model with discrete orthogonal SM bundles. 152

Figure 8.1. Collagen and smooth muscle area fraction data from histomorphometry. 168

Figure 8.2. Mass fraction changes of soluble collagen and elastin in UBW tissue as a result of SCI. 169

Figure 8.3. Bladder weight at different time-points post-SCI. 170

Figure 8.4. Collagen, elastin, and SM mass changes as a function of time post-SCI. 170

Figure 8.5. Smooth muscle orientation for normal UBW and at two time points post-SCI. 171

Figure 8.6. Fit of work data of intact UBW at 10 days post-SCI in Ω_1 to Fung model. 172

Figure 8.7. Comparison of intact tissue strain energy of normal and 10-day post-SCI data sets in Ω_0. 173

Figure 8.8. Strain energy of 10-day post-SCI UBW. 177

Figure 8.9. Collagen and SM fiber distribution post-SCI. 178

Figure 8.10. Normal and post-SCI Comparison for collagen component. 179

Figure 8.11. Normal and post-SCI Comparison for smooth muscle component. 180

Figure 8.12. Comparison of cross sections through the strain energy surfaces for individual tissue components. 181

Figure 8.13. Comparison of cross sections through the strain energy surfaces for A) ECM and B) SM. 182

PREFACE

This dissertation is the result of almost five years of research in the laboratory of Dr. Michael Sacks in the Department of Bioengineering at the University of Pittsburgh. My research and the resulting dissertation would not have been possible without the support of several people who I would like to thank here. Firstly, I would like to thank my advisor, Dr. Michael Sacks, for giving me the opportunity to work in his lab. We first met at the European Society of Biomechanics conference in The Netherlands, in June 2004, where we were introduced to each other by my Master's thesis advisor Dr. Jacques Huyghe. I am grateful to Dr. Sacks for the fruitful discussions about "The Model" that gave me great insights into, and increased my interest in, continuum mechanics in general and constitutive modeling in particular. Secondly, I would like to thank the members of my dissertation committee for their guidance and contribution to this work.

My research stemmed from intensive collaboration with Dr. Michael Chancellor and Dr. Naoki Yoshimura in the Department of Urology. I would like to thank the previous and current members of their group for their inspiring lab meetings and for providing rat bladder tissue. Specifically, I would like to thank Masataka (Masa) Yano for training me to perform rat surgery in order to remove the urinary bladder and Vickie Erickson for helping me with all my general urology research needs. I would also like to thank Dr. DeGroat from the Department of Pharmacology for allowing me to present in his group's lab meetings and for his inspiring discussions and feedback that helped me frame my theoretical research within the relevant clinical problem.

I got a head start in the lab and on the bladder project from Kevin (Khash) Toosi, whose Master's thesis research I followed up on. He taught me everything he knew related to the urinary bladder and the relevant experimental and data analysis techniques, and introduced me to all people in the urology field that were invaluable in my dissertation research. I would have loved to have him as a mentor for a longer period than just that first week. His experimental data,

as well as that of Claire Gloeckner and Jiro Nagatomi, were crucial to my research. I would like to thank all three of them for collecting and organizing the data and always being available for answering my questions and digging deep in their memory and data files. I especially want to express my gratitude to Claire for her exceptional organization of data and lab notebooks, which allowed me to retrieve every piece of data that I needed as far back as 2001. I would also like to extend my thanks to all the people who proofread and edited my manuscript and dissertation chapters. In no particular order: Linda van Roosmalen, Rebecca (Long) Heise, Kevin Toosi, David Schmidt, Bahar Fata, Erinn Joyce, Donna Haworth, and Paul Enders. Lastly, I would like to thank my undergraduate assistants Jessica Wagner and Yuzhou Xin. I enjoyed the mentoring experience very much, and Yuzhou's programming assistance was invaluable.

I would like to thank several people at the Department of Bioengineering: Dr. Harvey Borovetz, Lynette Spataro, Joan Williamson and Glenn Peterson. I would further like to thank the subsequent administrative assistants of our lab for all their assistance: Anna Goldman, Lynn Ekis, Beth Markocic, and Karen Connor. The past and present (student and postdoc) members of the lab have made my research experience very pleasant. I would like to especially mention a couple of people. I started in the lab at the same time as Diana Gaitan and Chad Eckert and our lunch conversations were one of the highlights of the day in the first years. My friendship with Diana will stay forever and I would have truly wished to graduate together. I would also like to thank Erinn Joyce for being there for me when I needed emotional support and Bahar Fata for her companionship in the “computational center.” Furthermore, I would like to mention the “smooth muscle or bladder group”, Rebecca Heise and Aron Parekh, and thank them for the collaborative research environment.

I am very thankful to my parents and sister for always being there for me. My parents have always encouraged me in my drive to accomplish the highest possible in education and have supported me all the way, first in Eindhoven and next all the way in the USA. I have had a great time in Pittsburgh and this would not have been possible without my friends, both in the US and in The Netherlands. In addition to those people already listed above, I would especially like to mention the following people, in no particular order: Marianne, Willemijn, Mirjam, Tamara, Kristie, Wilma, Marieke, Aschwin, Lisa, Sam, Laurie, Jess, Candace, Lauren, Aafke, WJ, Kate, Masha, Ilya, Federico, Fatos, Priya, Brandon, John, Antonio, Joost, Melanie, and Eefje.

And last but surely not least, I would like to thank my husband Paul for his constant support and love. He initially suggested pursuing a PhD abroad, and without his persistence we would never have ended up in Pittsburgh. Our relationship has grown stronger during our time here and I'm very grateful to Paul for everything he is and has meant to me. On a practical note, I am also very grateful for allowing me to use his "big machine" at CMU. These four cores saved me a lot of time in performing my research.

Finally, I would like to list two statements that summarize the process of my PhD research quite well:

"It all depends on your frame of reference."

"Archeology is an important component of Bioengineering."

NOMENCLATURE

Acronyms

Acronym	Description
ECM	Extracellular matrix
SCI	Spinal cord injury
SALS	Small angle light scattering
PK	Piola Kirchhoff
UBW	Urinary bladder wall
SM	Smooth muscle
MTM	Maximum tangent modulus; estimate for K
det	Determinant

Sub- and superscripts

Symbol	Description
an(iso)	(an)isotropic
t	true
f	fiber
ens	ensemble
s	slack
lb	lower bound
ub	upper bound
col	collagen
SMb, SMbC, SMbL	Smooth muscle bundle, circumferential SM bundle, longitudinal SMb
R	Referring to a variable of the fiber distribution function R
SMC, SML	Circumferential smooth muscle, longitudinal smooth muscle

Symbols

Symbol	Description
ρ	Density
I	Identity tensor
F, **F**	Deformation gradient (tensor)
E, **E**	Green strain (tensor)
C, **C**	Right Cauchy-Green strain (tensor)
B, **B**	Left Cauchy-Green strain (tensor)
U, **U**	Right stretch tensor. **U** = **F** without rotation.
λ	Stretch
J	Jacobian, volume ratio, $J = \det\mathbf{F}$
S, **S**	Second Piola Kirchhoff Stress (tensor)
P, **P**	First Piola Kirchhoff Stress or Lagrangian stress (tensor)
t, **t**	Cauchy stress (tensor)
N, n	Vector describing the fiber direction in Ω_0, in Ω_1
Ψ	Strain energy density function
I	Strain invariant
ϕ	Volume/mass fraction
R	Fiber distribution function, represented by a beta function
D	Fiber recruitment function, represented by a beta function
B	Beta function
y	Scaled strain/stretch variable in beta function. $y = [0, 1]$
x	Variable of integration, over slack stretch/strain range
Ω	Reference state/configuration
θ	Fiber angle in absolute initial configuration Ω_0
β, θ'	Fiber angle in reference configuration Ω_1
η	Collagen fiber modulus
K	Effective collagen fiber modulus; $K = \eta\phi_f$
d_1	Constant of exponential fiber ensemble model
d_2	Exponent of exponential fiber ensemble model

a	Exponent of exponential recruitment function
b	Constant of linear portion of exponential recruitment function
μ	Mean of beta recruitment function (normalized; in terms of y)
σ	Standard deviation of beta recruitment function (normalized; in terms of y)
γ	Scaling factor in double beta recruitment function
s	Shape parameter of beta distribution
σ_R	Standard deviation of fiber distribution R, represented by a beta function (in rad)
μ_R	Mean of fiber distribution R (in rad)
f	Force
δ	Displacement
l	Length
A	Area
V	Volume

1.0 INTRODUCTION

1.1 SCOPE

All tissues in the human body continuously grow, remodel, and adapt to changes in their physiological environment, resulting in changes in structure and composition. In addition to adaptation within normal physiological ranges, pathologies and their subsequent adaptations account for a large part of observable tissue-level changes. Remodeling has been defined as a change in structure resulting in altered material properties that is achieved by reorganizing existing constituents or by synthesizing new constituents of different organization [65, 150]. The main load-bearing constituents of many native tissues are (smooth) muscle, collagen and elastin, and growth and remodeling (G&R) involves production and degradation of all these tissue components, as well as reorientation of the fibrous components, resulting in changes in wall thickness, tissue mass, and tissue structure.

G&R in soft tissues has been studied most extensively in the vasculature [4, 8, 45, 62, 66]. Sustained changes in flow or pressure (e.g. hypertension), induce altered turnover of cells, collagen, and possibly elastin, and these changes may alter the mechanical and structural properties of the tissue as well as its geometry and biological function. In the vascular field, it has been recognized that "there is a pressing need to predict growth and remodeling of arteries in response to altered mechanical environments and to elucidate the underlying mechanisms" [62], and because of the abundance of available literature on G&R in vasculature, it may serve as a basis for studying G&R in other tissues. However, the driving mechanisms and the underlying processes for G&R are tissue-dependent, and hence a universal mechano-growth law likely does not exist [150]. On the other hand, general trends among tissues with similar compositions should be apparent.

To elucidate how observed changes in tissue components are related to altered net mechanical behavior at the tissue level, structural constitutive models are required with physiologically relevant model parameters. To develop a complete model of G&R in muscular soft tissues that undergo large deformations, the following main components are needed:

- A finite deformation constitutive model describing the elastic tissue mechanical behavior, in combination with the appropriate kinematics for the multiple tissue components.
- Kinetic equations describing the time-dependent G&R.
- Experimental data of a relevant tissue application.

An excellent example application is the urinary bladder wall (UBW), which has as main load-bearing components collagen and smooth muscle (SM), undergoes large deformations, and exhibits highly nonlinear and anisotropic mechanical behavior. Moreover, it undergoes profound remodeling in response to different pathologies, such as spinal cord injury (SCI) [34, 47, 50, 102, 106-109, 137, 152, 172, 174]. The urinary bladder wall tissue appears to remodel to compensate for the change in mechanical environment that exists as a result of the specific pathology, and attempts to restore normal organ-level function, *i.e.*, storage and voiding, through an unknown cell-to-tissue signaling mechanisms. This is in contrast to what is believed in the vascular field where blood vessels remodel to restore homeostatic wall stress. However, complete functional recovery of the bladder is never achieved because of lack of return of neural control.

This dissertation provides a general modeling framework for elucidation of underlying mechanisms of tissue-specific remodeling processes, specifically applied to remodeling in the UBW as a result of SCI. The next sections will first introduce all relevant concepts and terminology of constitutive models and growth and remodeling, as well as the available literature on current studies in theoretical growth and remodeling.

1.2 CONSTITUTIVE MODELS OF SOFT TISSUES

1.2.1 Introduction

The theoretical description of the mechanical behavior of a material is captured in a constitutive model, and the functional form of this equation can only be determined by experiments. The stress-strain results of mechanical testing provide constitutive models with model parameters. Soft tissues can be characterized by a complex geometry, composite nature, and highly non-linear, finite deformation, often anisotropic mechanical behavior, which complicates determining constitutive relations for soft tissues. The most general type of constitutive models used for soft tissues are so-called phenomenological models. Y.C. Fung is considered the pioneer of constitutive models for soft tissues and many researchers have used variations of the so-called "Fung-type" models for many different soft tissue applications [38, 56, 83, 85, 148]. Fung models are widely used because they are capable of capturing the highly non-linear mechanical behavior over a wide strain range. However, whereas Fung models and phenomenological models in general capture the general stress-strain behavior, they lack the ability to capture the underlying mechanisms contributing to tissue behavior, and the model parameters are not based on physiological phenomena. Structural models, on the other hand, are based on microstructural tissue features that are experimentally measurable and have the ability to relate tissue level mechanical response to individual fibrillar constituent properties.

1.2.2 Stress and strain – measurement and definitions

The mechanical behavior and material parameters of tissues are determined through mechanical testing. Uniaxial testing is the most basic form of mechanical testing and subjects tissue strips to loading in one direction only and leaves one edge stress-free, which is never the case *in vivo*. Furthermore, uniaxial loading experiments cannot provide the full relationship between all stress and strain components in a constitutive relation [39]. Whole organ testing is more physiological, but the complex stress and strain boundary conditions on most organs, due to external loading by the surrounding organs or an irregular geometry, prevent accurate investigation of isolated tissue response. For planar membrane tissues, planar biaxial testing over a wide strain range with

physiological loading levels is the most desirable testing method. It has been shown that biaxial testing can be successfully used to investigate mechanical behavior of various planar soft tissues, e.g., skin, diaphragm, epicardium, myocardium, heart valve tissue, and urinary bladder wall [10, 39, 47, 85, 91, 147, 173]. Biaxial tests assume a membrane approximation, and hence, the stress in the direction normal to the plane of testing is zero. This allows for a two-dimensional specialization within the framework of a three-dimensional theory[58]. When biaxial testing is performed with the testing specimen's material axes aligned with the testing apparatus, and no shear deformations are applied, shear stresses are zero.

Most soft tissues behave in a viscoelastic manner, with characteristics of stress-relaxation when held at a constant strain, creep when held at a constant stress, and hysteresis when subjected to cyclic loading and unloading. The loading-unloading behavior can be simplified to a pseudo-elastic behavior when the tissue is preconditioned and the stress-strain relation is repeatable. The loading branch and the unloading branch are each represented by its own unique constitutive equation. Pseudo-elasticity is a convenient description of the stress-strain relationship in cyclic loading specifically. Soft tissues are also often assumed to be incompressible, i.e., constant volume under loading.

The two important measures in a material's mechanical behavior are stress, defined in its simplest form as force divided by the area it is acting on, and stretch or strain, measures of a change in length upon loading. An important aspect of defining a tissue's stress-strain behavior is the definition of zero stress state or reference state. In this state no loading is applied and the material is assumed to be completely stress-free. In the case of finite deformations, several different definitions of stress and strain are used. Let the vector $\mathbf{X}$ represent the position of a point P in the reference configuration, and $\mathbf{x}$ the position of that same material point in a deformed configuration. Then, the deformation gradient tensor $\mathbf{F}$ describes the transformation of the line segment d$\mathbf{X}$ to d$\mathbf{x}$ as $\mathbf{F} = \partial\mathbf{x}/\partial\mathbf{X}$. A change in an infinitesimal volume element (dV) from the reference to the deformed configuration is defined as $J = dV/dV_0 = \det\mathbf{F}$, which is equivalent to $J = \rho/\rho_0 = \det\mathbf{F}$ due to conservation of mass. In here, ρ is the tissue density in the current configuraiton and det$\mathbf{F}$ is the determinant of $\mathbf{F}$.

Because $\mathbf{F}$ contains rigid body motions, alternative measure of strains are defined that purely represent deformations giving rise to strain energy. The Right Cauchy-Green tensor $\mathbf{C}$, the

Left Cauchy-Green tensor **B**, and the Green-Lagrange or Green's strain tensor **E** are defined in Eq.(1.1), where **I** is the identity tensor.

$$\begin{aligned} \mathbf{C} &= \mathbf{F}^T\mathbf{F} \\ \mathbf{B} &= \mathbf{F}\mathbf{F}^T \\ \mathbf{E} &= \frac{1}{2}\left(\mathbf{C}-\mathbf{I}\right) \end{aligned} \tag{1.1}$$

The Cauchy stress tensor **t** is derived from the traction vectors acting on a body's surfaces and is defined in the deformed configuration; in a uniaxial sense it is defined as force divided by deformed area. The Lagrangian or 1st Piola Kirchhoff stress tensor **P** is defined in the referential configuration and in a uniaxial sense is defined as force dived by initial area. The 1st Piola Kirchhoff stress tensor is related to the Cauchy stress tensor as $\mathbf{P} = J\mathbf{F}^{-1}\mathbf{t}$. The 2nd Piola Kirchhoff stress tensor **S**, which has no direct physical meaning and represents a very useful stress measure in computational mechanics because it is a symmetric tensor, is in turn related to **t** as follows: $\mathbf{S} = J\mathbf{F}^{-1}\mathbf{t}\mathbf{F}^{-T}$. Eq. (1.2) gives an overview of all relations, including those between **P** and **S**.

$$\begin{aligned} \mathbf{P} &= J\mathbf{F}^{-1}\mathbf{t} = J\mathbf{t}\mathbf{F}^{-T} \\ \mathbf{S} &= J\mathbf{F}^{-1}\mathbf{t}\mathbf{F}^{-T} \\ \mathbf{P} &= \mathbf{F}\mathbf{S} = \mathbf{S}\mathbf{F}^T \\ \mathbf{S} &= \mathbf{F}^{-1}\mathbf{P} = \mathbf{P}\mathbf{F}^{-T} \end{aligned} \tag{1.2}$$

All three stress measures will be used throughout this dissertation, without restating the relations.

1.2.3 Thermodynamic considerations

Thermodynamic considerations place important restrictions on the functional form of constitutive equations [151]. These are based on the first and second laws of thermodynamics for a thermomechanical continuum, in which thermal and mechanical effects dominate the material's behavior, and where electrical, chemical and other effects are ignored. The following text is largely based on "Nonlinear theory of elasticity. Applications in biomechanics", Chapter 5 by Taber [151], and concepts were verified by consulting "Nonlinear solid mechanics. A continuum approach for engineering" by Holzapfel [53], and "The non-linear field theories of mechanics" by Truesdell and Noll [153]. Extended derivations can be found in these works; the following

section provides a summary of the relevant concepts. The first law of thermodynamics deals with conservation of energy. For an arbitrary material region of a thermomechanical continuum, the principle of conservation of energy can be written in the form

$$\dot{K} + \dot{U} = \dot{P} + \dot{Q}\,, \tag{1.3}$$

where K is the kinetic energy, U the internal energy (consists of thermal energy and strain energy), P the mechanical power input (the rate of work done on a body by applied loads) and Q the rate of heat input. The left side represents rate of change in internal energy, the right side the rate of change in energy that is added externally. For an arbitrary volume element that deforms from dV into dv, Eq.(1.3), written in the local form, and in terms of the Cauchy stress tensor $\mathbf{t}$, or the first Piola Kirchhoff stress tensor $\mathbf{P}$, respectively, results in:

$$\begin{aligned} \rho\dot{u} - \mathbf{t} : \mathbf{D} - \rho r + \bar{\nabla} \cdot \mathbf{q} = 0 \\ \rho_0 \dot{u} - \mathbf{P} : \dot{\mathbf{F}}^T - \rho_0 r + \nabla \cdot \mathbf{q}_0 = 0 \end{aligned}\,. \tag{1.4}$$

In this, the following definitions hold. ρ_0 is the mass density in the reference configuration; ρ is the mass density in the deformed state; u the internal energy per unit mass; $\mathbf{D}$ the rate-of-deformation tensor; $\mathbf{F}$ the deformation gradient tensor; r the rate of heat production per unit mass due to internal sources; $\mathbf{q}$ and $\mathbf{q}_0$ the outward-directed heat flux vectors per unit deformed and undeformed surface area, respectively; ∇ is the gradient operator, and $\bar{\nabla}$ is the gradient operator with respect to the deformed state. The resulting form of the first law of thermodynamics (Eq. (1.4)) states that the rate of increase in internal energy of a volume element ($\rho\dot{u}$ or $\rho_0\dot{u}$) is equal to the sum of the rate of work done by the stresses on the element, i.e. the stress power ($\mathbf{t} : \mathbf{D}$ or $\mathbf{P} : \dot{\mathbf{F}}^T$), the rate of internal heat production (ρr or $\rho_0 r$), and the rate of heat flow into the element ($-\bar{\nabla} \cdot \mathbf{q}$ or $-\bar{\nabla} \cdot \mathbf{q}_0$).

The first law of thermodynamics basically states that work can be converted into heat and *vice versa*, so that the total energy remains constant, but it does not consider dissipated energy. The second law of thermodynamics restricts the direction of energy conversion processes and is based on the concept of entropy (Σ). For a solid body, the second law of thermodynamics states that the time-rate of change of the total entropy in a body is greater than or equal to the sum of the influx of entropy through the surface of the body and the entropy generated by internal heat sources. The Lagrangian local forms of this relation, which is also called the Clausius-Duhem inequality, is given by

$$\dot{\Sigma} - \frac{r}{T} + \frac{1}{\rho_0} \nabla \cdot \left(\frac{\mathbf{q}_0}{T} \right) \geq 0 \,. \tag{1.5}$$

The possible forms for constitutive equations are restricted by thermodynamic considerations based on Eqs. (1.4) and (1.5). The relevant constitutive principles for a thermomechanical material include *coordinate invariance*, *determinism*, *local action*, *equipresence*, *material objectivity*, *physical admissibility*, and *material symmetry*. The first six are described below; the principle of *material symmetry* is used when specific forms of constitutive equations for elastic materials are derived, taking into account symmetries in the material.

The principle of *coordinate invariance* states that constitutive equations must be independent of the coordinate system that is used to describe the motion of a body, and hence should be developed in tensor form. The principle of *determinism* states that the stress distribution in a body at a given time is depended on the history of deformation and temperature. For an elastic material however, no energy is dissipated and temperature effects are neglected, so the stress at time *t* depends only on the instantaneous deformation. The principle of *local action* indicates that the motion and temperature at a point in a thermoelastic body can be determined from the values and the spatial derivatives of the dependent constitutive variables at a nearby point. For simple materials, this suggests, together with the principle of determinism, that the constitutive equations for a thermoelastic material can be written in the form

$$\begin{aligned} \mathbf{t} &= \mathbf{t}\left(\mathbf{R}, \mathbf{F}, T, \nabla T\right) \\ \mathbf{q} &= \mathbf{q}\left(\mathbf{R}, \mathbf{F}, T, \nabla T\right) \\ u &= u\left(\mathbf{R}, \mathbf{F}, T, \nabla T\right) \\ \Sigma &= \Sigma\left(\mathbf{R}, \mathbf{F}, T, \nabla T\right) \end{aligned} \,, \tag{1.6}$$

where **R** defines the spatial dependency. The principle of *equipresence* states that an independent variable that appears in one constitutive equation for a material, must be present in all constitutive equations for that material. This is useful if other effects are to be included.

The principle of *material objectivity* or *material frame indifference* states that constitutive equations must be invariant under rigid motions of the spatial reference frame. In other words, the events occurring at a point in a body must be independent of the motion of the observer. The deformation gradient tensor **F** is per definition an objective quantity, since it describes changes relative to a given reference configuration. Under a change of reference frame, a general second

order tensor **T** transforms through the rotation tensor **Q** as $\mathbf{T}^* = \mathbf{Q}\cdot\mathbf{T}\cdot\mathbf{Q}^T$. Since deformation and temperature are objective, the constitutive relations for a thermoelastic material (Eq. (1.6)) are frame indifferent. Using the conversion definitions of stress measures (Eq. (1.2)), this eventually states

$$\begin{aligned}\mathbf{S} &= g(\mathbf{U}) \\ &= f(\mathbf{C}), \\ &= h(\mathbf{E})\end{aligned} \tag{1.7}$$

where *g*, *f* and *h* are called response functions, and **U** is the right stretch tensor which is obtained through polar decomposition of **F** ($\mathbf{F} = \mathbf{Q}\cdot\mathbf{U}$). For small rotations, this also holds for the other stress tensors **t** and **P**.

The principle of *physical admissibility* states that constitutive equations must be consistent with any of the basic laws of continuum mechanics, including the first and second laws of thermodynamics (Eqs. (1.4) and (1.5)). Stating these equations in terms of the 2nd Piola Kirchhoff stress **S** and eliminating *r* between these two equations yields

$$\rho_0\left(T\dot{\Sigma} - \dot{u}\right) + \mathbf{S}:\dot{\mathbf{E}} = 0. \tag{1.8}$$

Eq. (1.8) can now be combined with the general constitutive equations in Eq. (1.6) and the case is considered for which temperature is considered to be the independent variable. It is convenient to introduce the Helmholtz free energy function per unit undeformed volume as

$$\psi = u - T\Sigma, \tag{1.9}$$

as a replacement for the internal energy *u*. Then, Eq. (1.6) is replaced by

$$\psi = \psi\left(\mathbf{R}, \mathbf{E}, T, \nabla T\right), \tag{1.10}$$

and Eq. (1.8) is transformed to

$$-\rho_0\left(\dot{\psi} + \Sigma\dot{T}\right) + \mathbf{S}:\dot{\mathbf{E}} = 0. \tag{1.11}$$

Combining Eqs. (1.10) and (1.11), and using the chain rule yields

$$\left(\mathbf{S} - \rho_0\frac{\partial\psi}{\partial\mathbf{E}}\right):\dot{\mathbf{E}} - \rho_0\left(\Sigma + \frac{\partial\psi}{\partial T}\right)\dot{T} - \rho_0\frac{\partial\psi}{\partial\nabla T}\cdot\nabla\dot{T} = 0. \tag{1.12}$$

For independent strain and temperature distributions, each of the three terms equals zero. And since **E** and T (and hence $\dot{\mathbf{E}}$ and $\dot{T}$) can be chosen arbitrarily, the expressions in parentheses must be zero. This results in the relations:

$$\mathbf{S} = \rho_0 \frac{\partial \psi}{\partial \mathbf{E}}$$
$$\Sigma = -\frac{\partial \psi}{\partial T} \quad . \tag{1.13}$$
$$\frac{\partial \psi}{\partial \nabla T} = 0$$

If the deformation is isothermal ($\dot{T} = 0$) which is usually considered to be the case for biological tissues, then $\psi = \psi(\mathbf{R}, \mathbf{E})$ and the material behaves elastically. In this case, a strain energy density function Ψ is defined as

$$\Psi(\mathbf{R}, \mathbf{E}) = \rho_0 \psi(\mathbf{R}, \mathbf{E}), \tag{1.14}$$

per unit undeformed volume. Since the density ρ_0 of the undeformed body is independent of deformation, Eq. (1.13) gives the constitutive equation

$$\mathbf{S} = \frac{\partial \Psi}{\partial \mathbf{E}}, \tag{1.15}$$

where the 2nd Piola Kirchhoff stress tensor is derived from the scalar strain energy density function Ψ.

1.2.4 Phenomenological hyperelastic constitutive models

A material with a constitutive relation of the form described by Eq. (1.15) is called a hyperelastic material. In other words, the mechanical properties of a hyperelastic material are characterized completely by a scalar strain energy density function. During an isothermal deformation, the strain energy is associated with the free energy per unit undeformed (reference) volume, and the strain energy is zero in the reference state. Materials which keep the volume constant throughout a deformation are characterized by the incompressibility constraint

$$J = \det \mathbf{F} = 1 \tag{1.16}$$

For incompressible materials with $J = 1$, Eq. (1.15) is expressed as

$$\mathbf{S} = 2\frac{\partial \Psi}{\partial \mathbf{C}} - p\mathbf{C}^{-1} = \frac{\partial \Psi}{\partial \mathbf{E}} - p\mathbf{C}^{-1}, \tag{1.17}$$

where p is a Lagrange multiplier that is determined from the equations of motion and boundary conditions (kinematic constraints) and is usually associated with the hydrostatic pressure in a

tissue. Taber [151] notes that this terminology often has been a source of confusion in the biomechanics literature. In fact, p generally does not have a direct physical interpretation, but is just a Lagrange multiplier that is needed to enforce the incompressibility constraint (Eq. (1.16)) [151]. Note that in the measures for stress as defined in Eq. (1.2), $J = 1$ for incompressible materials.

A strain energy function exists for a perfectly elastic material; hyperelasticity is a subclass of (non-linear) elasticity, where the stress state of a material is independent of its loading history. The actual work done by the stress field on a hyperelastic material during a certain time interval depends only on the initial and final configurations, i.e., it is path independent [53]. Under the assumption of pseudoelasticity, the strain energy function should technically be referred to as a pseudo-strain energy function. In the rest of this dissertation, the general term strain energy is used. Under the condition of plane stress (with $S_{13} = S_{23} = S_{33} = 0$) for planar biaxial deformation, the strain energy is dependent on the strain components E_{11}, E_{22}, E_{12}, E_{33}. Because of the incompressibility constraint (Eq. (1.16)), the 33-component can be calculated from the other components and only three of the four components are independent [58]. A reduced strain energy function can be defined as

$$\hat{\Psi}\left(E_{11}, E_{22}, E_{12}\right) = \Psi\left(E_{11}, E_{22}, E_{12}, E_{33}\right). \tag{1.18}$$

and the stress components are derived from this as

$$\begin{aligned} S_{11} &= \frac{\partial \hat{\Psi}}{\partial E_{11}} \\ S_{22} &= \frac{\partial \hat{\Psi}}{\partial E_{22}} \\ S_{12} &= \frac{\partial \hat{\Psi}}{\partial E_{12}} - C_{12} C_{33}^2 \frac{\partial \Psi}{\partial E_{33}} \end{aligned} \quad . \tag{1.19}$$

When shear components are assumed to be negligible, this reduces to

$$\begin{aligned} S_{11} &= \frac{\partial \hat{\Psi}}{\partial E_{11}} \\ S_{22} &= \frac{\partial \hat{\Psi}}{\partial E_{22}} \end{aligned} \quad . \tag{1.20}$$

Note that Holzapfel reemphasizes that "there is a significant difference between a planar specialization of a three-dimensional strain energy function and an *a priori* two-dimensional strain energy function" [58].

The most common type of constitutive models used for soft tissues are phenomenological models, which are usually of a polynomial or exponential form. A very well-known example of a phenomenological constitutive model, originally introduced by Fung [39] but used and extended by many researchers afterwards, is of the form

$$\Psi = c \cdot \exp\left[f\left(a_i, \mathbf{E}\right)\right], \tag{1.21}$$

where the function f generally consists of polynomial terms of the components of $\mathbf{E}$ of varying order (with constants a_i), depending on the specific set of mechanical data. The most general form of Eq. (1.21) is given by (in indicial notation with the summation convention) [40]:

$$\Psi = \frac{1}{2}\alpha_{ijkl}E_{ij}E_{kl} + \left(\beta_0 + \beta_{mnpq}E_{mn}E_{pq}\right)\exp\left(\gamma_{ij}E_{ij} + \kappa_{ijkl}E_{ij}E_{kl} + \ldots\right). \tag{1.22}$$

Another form of phenomenological constitutive equation is expressed in terms of a set of independent strain invariants of $\mathbf{C}$ or $\mathbf{B}$ [144]. The first three (principal) invariants are defined as

$$\begin{aligned} I_1 &= tr\,\mathbf{C} = tr\,\mathbf{B} = \lambda_1^2 + \lambda_2^2 + \lambda_1^2 \\ I_2 &= \frac{1}{2}\left[\left(tr\mathbf{B}\right)^2 - tr\mathbf{B}^2\right] = \lambda_1^2\lambda_2^2 + \lambda_1^2\lambda_3^2 + \lambda_2^2\lambda_3^2 \\ I_3 &= \det\mathbf{C} = \det\mathbf{B} = J^2 = \lambda_1^2\lambda_2^2\lambda_1^2 \end{aligned}. \tag{1.23}$$

These invariants are used to define the strain energy for isotropic materials, i.e.

$$\Psi = \Psi\left(\mathbf{C}\right) = \Psi\left(\lambda_1, \lambda_2, \lambda_3\right), \tag{1.24}$$

which results in the three principal stresses (Cauchy, 1st Piola Kirchhoff, and 2nd Piola Kirchhoff, respectively) in an incompressible material (a=1,2,3) to be defined as (see also [53])

$$\begin{aligned} t_a &= J^{-1}\lambda_a \frac{\partial\Psi}{\partial\lambda_a} \\ P_a &= \frac{\partial\Psi}{\partial\lambda_a} \\ S_a &= \frac{1}{\lambda_a}\frac{\partial\Psi}{\partial\lambda_a} \end{aligned}. \tag{1.25}$$

For incompressible materials (Eq. (1.16)) $I_3 = 1$, and the two principle invariants I_1 and I_2 are the only independent deformation variables [53].

Many different forms of strain energy functions for isotropic soft deformable materials in terms of the principal stretches have been proposed in the literature. On the other hand, many materials, and in fact, most biological tissues, are characterized as anisotropic and cannot be described by isotropic constitutive equations. A material is considered anisotropic when its material properties are direction dependent. These materials can be viewed as being composed of an isotropic matrix material (ground substance) and one or more families of fibers responsible for the anisotropy, with the derivation of the constitutive relation based on the principle of *material symmetry*. This approach, initially proposed by Spencer [143, 144] and leveraged by Holzapfel [55], can be viewed as a "hybrid" approach, between pure phenomenological and fully structural. The simplest representation of this is transverse isotropy, with one family of fibers. The fiber direction in the reference configuration is defined by a unit vector **a**(**X**), and its structural tensor is defined as $\mathbf{a}\otimes\mathbf{a}$. The so-called pseudo-invariants of **C** and **a**, related to the fibers, are now introduced as

$$\begin{aligned} I_4 &= \mathbf{a}^T\mathbf{C}\mathbf{a} = \lambda_A^2 \\ I_5 &= \mathbf{a}^T\mathbf{C}^2\mathbf{a} \end{aligned}, \tag{1.26}$$

where λ_A is the stretch in fiber family *A*. For a transversely isotropic material, the strain energy is written in terms of the five invariants as $\Psi = \Psi\left(I_1, I_2, I_3, I_4, I_5\right)$. When a material consists of two families of fibers, where the second fiber family is defined by the unit vector **b**, additional strain invariants are defined associated with this additional fiber family and the interaction between the two families. The invariants I_6-I_8 are defined as

$$\begin{aligned} I_6 &= \mathbf{b}^T\mathbf{C}\mathbf{b} = \lambda_B^2 \\ I_7 &= \mathbf{b}^T\mathbf{C}^2\mathbf{b} \\ I_8 &= \mathbf{a}^T\mathbf{C}\mathbf{b} \end{aligned}. \tag{1.27}$$

In soft tissues, the strain energy function is often divided into an isotropic and an anisotropic part representing the isotropic matrix and the fibers, respectively, resulting in

$$\Psi = \Psi_{iso}\left(I_1, I_2\right) + \Psi_{aniso}\left(I_4, I_5, \ldots\right), \tag{1.28}$$

when assuming incompressibility ($I_3 = 1$). This is often simplified to [55]

$$\Psi = \Psi_{iso}\left(I_1\right) + \Psi_{aniso}\left(I_4, I_6\right). \tag{1.29}$$

Different specific functional forms of Ψ_{iso} and Ψ_{aniso} have been proposed in the literature, where for Ψ_{iso} often a neo-Hookean formulation is used

$$\Psi_{iso} = \frac{c}{2}\left(I_1 - 3\right), \tag{1.30}$$

and for Ψ_{aniso} many different phenomenological expressions similar to Eq. (1.22) have been proposed (*e.g.* [54-56, 67, 69, 110, 176]). An interesting generalization of the invariant based method has been presented by Ehret and Itskov [70]. They present a constitutive model for fiber-reinforced materials consisting of an arbitrary number of fibers, where each fiber is represented by its individual structural tensor and a weight factor.

1.2.5 Structural constitutive models

Whereas phenomenological and strain-invariant based models have provided many useful insights into soft tissue mechanical behavior, they do not capture the underlying mechanisms of tissue behavior. Structural constitutive models, on the other hand, attempt to integrate information on tissue composition and structure to avoid ambiguities in material characterization, and to allow for separate investigation of the contribution of each individual tissue component to the tissue behavior. Note that in several studies, derivations from the invariant based approach are considered structural [56, 57]. However, although the inclusion of fiber families can be considered structural, the fiber response is characterized by a phenomenological relation. This is in contrast to how the term structural is defined in this dissertation.

The generally accepted structural approach is based on the assumption that the overall tissue mechanical behavior results from the collective contribution of the individual fibrous and cellular components, with experimentally measurable model parameters describing individual components. Structurally-guided material models are not limited to the study of soft biological tissues. The textile industry has utilized this approach in many different forms for woven and non-woven fabrics (e.g., [36, 73, 105]). For planar collagenous tissues, the structurally-based theoretical framework was initially developed by Lanir [59, 82, 84, 86]. He based his studies on earlier work on uniaxial elastic models based on the undulated structure of collagen fibers in tendons, skin, aortic tissue and general connective tissues and on two biaxial models that considered the rotation of fibers during deformation (see references in [84]). In this modeling technique, the tissue level response is related to the collective contribution of individual fiber ensembles, and the fibrillar connective tissue is treated by homogenizing the fiber ensemble

response. Individual fibers are assumed to bear load only when stretched beyond a specific slack strain, and fibers are recruited upon loading. Sacks [129] later extended this approach by demonstrating that the complete planar biaxial mechanical response of the tissue could be simulated by combining the fiber ensemble stress-strain response, derived from a single equibiaxial test, with an experimentally determined fiber angular distribution.

A similar structural approach combining a fiber recruitment function with the invariant based approach considering one family of fibers has been applied to the vascular wall [178, 180]. These are the most sophisticated applications of structural models currently available in the literature. Note, that no one study has succeeded yet to fully combine a fiber recruitment function and a fiber distribution function and apply it to a full set of mechanical data. This will be done in the current dissertation, and the complete constitutive modeling approach will be described and extended in Chapter 2.0.

1.3 GROWTH AND REMODELING

1.3.1 Growth models

Growth and remodeling is involved in many pathological as well as normal physiological processes, such as tissue maintenance and aging; adaptations to altered loads, *e.g.* in exercise; wound healing in responses to injury or clinical treatment; and progression of disease [6]. Theoretical models of G&R will allow for elucidation of the underlying mechanisms of specific remodeling processes.

A generally accepted model for growth describes volumetric mass growth, as initially developed for uniform growth under mechanical load by Hsu [61], developed for bone by Cowin and coworkers (*e.g.* [21]), and extended and formalized within the framework of finite elasticity by Skalak (*e.g.* [138]). Combining these theories, Rodriguez *et al*. [123] formulated a continuum theory that accounts for the coupling between stress and finite growth, where they introduced and employed the multiplicative decomposition of the total deformation gradient into its elastic and growth parts (Figure 1.1). In all the above theories, growth is prescribed *a priori* via kinematics based on assumed constitutive relations for the evolution of stress-free

configurations. A thorough and extended derivation of a general constitutive theory of stress-modulated growth of pseudo-elastic soft living tissues, utilizing this decomposition, is given by Lubarda and Hoger [96]. Menzel added fiber reorientation to this theory of multiplicative growth in a 3D Finite Element implementation [101]. Davol *et al*. recently implemented the theory for a multi-constituent cartilage tissue in a 3D Finite Element formulation [31]. These general theories of growth were computationally very convenient and have been proven very useful; however, they only model consequences of G&R, and not the fundamental process by which G&R occurs, i.e. the continual production and removal of constituents.

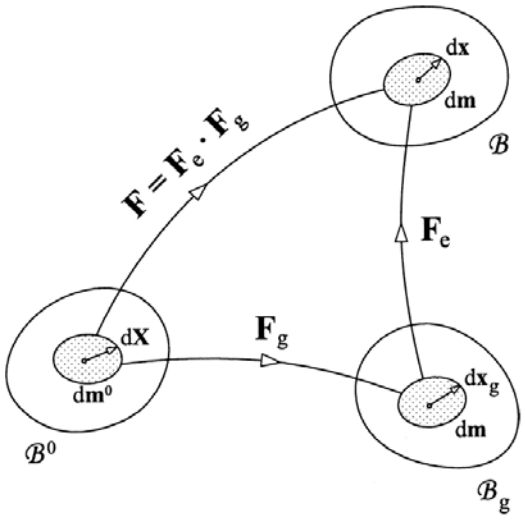

Figure 1.1. Schematic representation of the multiplicative decomposition of the deformation gradient. The deformation gradient is composed into its elastic and growth parts The mass of an infinitesimal volume element in the initial configuration B_0 is dm^0. T he corresponding mass in the configuration B_g and B is dm. Reprinted with permission from [95]. Copyright @ ASME, 2004.

1.3.2 Mixture theories

Mixture theory, which combines continuum theories for the motion and deformation of solids and fluids, with general principles of chemistry, might be better suited for modeling G&R. This was pointed out in a recent comprehensive study by Ateshian on using theories of mixtures for biological systems [5]. In a somewhat narrower context, Garikipati *et al*. provided a mixture

theory which coupled mass transport with mechanics for the application of growth, where the solid constituents originate from tissue precursors that are dissolved in the fluid constituent, allowing application of conservation of mass [43]. In a companion paper they also covered remodeling, which they defined as a motion of material points in material space [44].

Humphrey and coworkers have developed what could perhaps be called the most extensive modeling framework for tissue remodeling utilizing the so-called constrained mixture approach, where the tissue is assumed to be a mixture of multiple (solid) constituents, which are constrained to deform together [65]. This theory has mainly been applied in studies on the vascular wall. The theory of mixtures is used to account for the separate contributions of each constituent, and homogenization is done through a rule-of-mixtures model for the stress response. Formal ideas of mixture theory for mass balance are melded with the less stringent concept of rule-of-mixtures for linear momentum balance.

The theory has been refined over the years, and eventually it was suggested to consider two classes of constituents: those that are soluble and structurally not significant (*e.g.* cytokines and chemokines), and those that are insoluble but structurally significant (*e.g.* collagen, muscle) [6]. Stress-dependent kinetic models of the turnover of cells and ECM have been incorporated [66], as well as equations for fiber reorientation [7]. Each constituent is produced and degraded, which can be represented in the model by evolution equations (or kinetic relations) for the mass or mass density production [66]. Constituent turnover involves complex chemical reactions, but first order kinetics can often provide reasonable descriptions [46]. The specific form of the kinetic relations will be dictated by experimental data, as pointed out by Rao *et al*. [118]. With these types of expressions, a new equilibrium state is reached when the stress is equal again to the homeostatic value, and the production rate is zero. Different forms of the survival function have been proposed in the literature, depending on the physiological remodeling process; see examples in [7, 8, 65, 68, 118]. The constrained mixture approach has been applied successfully by Humphrey and coworkers to various questions and open problems in vascular mechanics.

As stated in a recent review by Humphrey [64], the rule-of-mixtures relation allows one to retain many of the advances in non-linear biomechanics by simply writing the net strain energy function in terms of the energies stored in individual constituents as they are produced. The fact that changing rates of production (protein synthesis and cell proliferation) and associated half-lives are accounted for, enables basic mechanisms of G&R to be modeled

mathematically rather than merely modeling the kinematic consequences of such turnover. Changes in geometry are computed naturally in the constrained mixture model of G&R simply by satisfying linear momentum balance at each G&R time point. Note, that current functional forms are in a state of infancy, and appropriate constitutive relations need to be derived based on experimental data. This holds especially for the rates of mass density production and survival functions, but also for the strain energy functions. Each of these constitutive equations will need to be derived uniquely for each new application. Variations of the mixture approach, sometimes in combination with other approaches, have been implemented by other groups and have been used in different applications [52, 78, 79, 116, 154-156, 170].

1.4 OBJECTIVES AND OUTLINE

G&R is an evolving and important research area and there is a need for theoretical models to describe G&R processes for different tissues in order to elucidate underlying mechanisms. To develop such a model, a constitutive model is needed that captures the underlying multi-component tissue structure, combined with kinetic equations describing the G&R processes in the individual tissue components. One highly remodeling muscular tissue system is the vasculature, where most literature on theoretical G&R is available. G&R theories developed for the vasculature provide a good basis for a general structurally based constitutive model of a remodeling multi-component soft tissue, and will hence lay the basis for our future model. However, what will need to be kept in mind is that these theories all assume that the tissue is remodeling to restore homeostatic stress values, in contrast to restoring normal physiological organ function in a pathological situation.

A similarly highly remodeling muscular tissue is the urinary bladder wall, as evidenced by our extensive experimental database of remodeling in the UBW as a result of SCI. This database will provide us with the opportunity to apply our model to a specific tissue system to elucidate key remodeling mechanisms. The experimental data suggests that distinct mechanical stimuli, such as prolonged periods of high strain or stress, or frequent short-term intermittent loading, induce different remodeling events to compensate for the change in mechanical environment in an attempt to restore normal organ-level function. Because of the lack of

restoration of other important physiological factors, the remodeling results in a pathological process. This is in contrast to the general assumption that tissues remodel in response to changes in local stress conditions to restore homeostatic stress values.

While our model will be applied to the specific application of the urinary bladder wall, it is developed in a fully generalized manner, using a step-wise approach. In its general form, it can be used for any multi-phase (muscular) soft tissue as well as in remodeling predictions in a tissue engineering setting. The novelty of our approach lays firstly in the sophistication of the multi-component constitutive model. Each model component is derived separately through the use of decellularized tissue specimens. As the first step, the collagen constituent was modeled based on its unique coiled and crimped structure, using the fiber ensemble as the basic unit. In the next step, this model was combined with an expression for the inactivated muscle component. The unique feature of this approach was that both constituents were expressed to a common, intact tissue reference state, while the collagen mechanical behavior was determined in decellularized tissues. To enable this approach, our currently existing structural constitutive model for collagenous tissues was re-derived based on a physically realistic fiber model and to include permanent set effects to account for processes such as decellularization and preconditioning. The model was utilized in terms of strain energy which allowed determination of an average mechanical response of both tissue components. The resulting morphologically based multi-component model laid the important and necessary basis for future G&R studies. As an initial step towards this goal, parametric studies were performed in order to explain changes in UBW mechanical behavior at 10 days after initiation of SCI. The hypothesis that was investigated is that changes in UBW mechanical properties as a result of SCI can be explained by morphological changes alone, without intrinsic changes in constituent properties.

This dissertation is based on three main objectives. The first objective was to formulate a constitutive model of extracellular matrix (ECM) to elucidate basic remodeling mechanisms in this specific tissue component, specifically, the mechanical role of *de novo* synthesized elastin on urinary bladder ECM. The second objective was to develop a morphologically driven constitutive model of a multi-phase tissue, applied to the urinary bladder wall. A common experimentally-attainable stress-free reference state for all tissue components laid at the basis of this model. To achieve this objective, the existing structural model was re-derived to include two necessary modifications; a physically realistic fiber model, and a formulation to account for

multiple tissue components existing in different reference states. As an essential part of this, a robust parameter estimation procedure was developed. The third and last objective was to obtain insights into UBW remodeling as a result of SCI. More specifically, to elucidate if mechanical changes in UBW tissue after spinal cord injury can be explained by morphological changes, *e.g.*, constituent mass fractions and fiber orientation, without intrinsic changes in constituent properties. Mechanical and structural data of UBW tissue from a rat model of SCI was re-analyzed and the developed multi-phase constitutive model was used to investigate changes in model parameters in order to explain the mechanical behavior of UBW after SCI at the 10-day time point. It is anticipated that this will lay the basis for a generalized modeling framework of remodeling in multi-phase muscular soft tissues.

The objectives are addressed in this dissertation in the following order. Chapters 2.0 - 5.0 provide the relevant background and specific methods for the actual studies, which in turn are described in Chapters 6.0 - 8.0. First, the constitutive modeling approach is introduced and important and novel modifications to the model are described in Chapter 2.0. This is followed by a chapter on validation and numerical implementation of the model, as well as methods for parameter estimation (Chapter 3.0). In Chapter 4.0 an extensive review of the urinary bladder wall and the available experimental data on remodeling as a result of SCI is provided. Chapter 5.0 describes the methods used to provide a complete experimental database needed for the model. This includes analyses on the available experimental data presented in the previous chapter. Chapter 6.0 describes the study that addresses the first objective, where the mechanical role of *de novo* synthesized elastin in the urinary bladder wall is investigated. In Chapter 7.0 the complete morphologically based constitutive model of a multi-component tissue is summarized and model parameters are determined from experimental data of the urinary bladder wall. This model is used in Chapter 8.0 to investigate the mechanical behavior of the urinary bladder wall after spinal cord injury at the 10-day time point. In Chapter 9.0 the main findings are summarized, and as part of future directions, an initial remodeling framework is proposed, which has the potential to simulate urinary bladder wall remodeling at different time points after spinal cord injury. The conclusion of this dissertation will show that the developed morphologically based multi-phase constitutive model will serve as a basis to elucidate remodeling mechanisms in various applications, such as specific tissue pathologies and tissue engineering settings.

2.0 DEVELOPMENT OF STRUCTURAL CONSTITUTIVE MODELS FOR MULTI-PHASE SOFT TISSUES

The structural approach as introduced in section 1.2.5, where each model parameter has physiological significance, allows for separate investigation of the contribution of each individual tissue component to the tissue's mechanical behavior, and eventually will provide the ability to elucidate changes as a result of pathological processes. The structural constitutive model described in this chapter builds upon the theoretical work formally introduced by Lanir [59, 82, 84, 86], in which the tissue-level response is related to the collective contribution of individual fiber ensembles. The term fiber ensemble refers to a collection of fibers sharing a common orientation. This modeling technique treats the fibrillar ECM component by homogenizing the fiber ensemble response. This modeling approach for planar collagenous tissues is integrated into a multi-component structural constitutive model by combining it with a description for a second component. To facilitate this, the current structural constitutive model is re-derived based on a new, correct fiber stress-strain relation and the inclusion of a so-called permanent set deformation in order to take into account multiple reference states of separate model components. This chapter describes the development of this structural model, starting from the basis in section 2.1, and extending it in subsequent sections. Parts of this chapter (specifically sections 3 and 2.1.5) are based on S. Wognum, D.E. Schmidt, M.S. Sacks, *On the mechanical role of de novo synthesized elastin in the urinary bladder wall*, J Biomech Eng, 2009, 131(10): 101018 [175], Copyright @ ASME.

2.1 ORIGINAL CONSTITUTIVE MODEL FORMULATION

2.1.1 Assumptions

It is assumed that a representative volume element (RVE) can be identified that is large enough to represent the processes associated with the microstructure of the material in some average sense, yet small compared to the characteristic length scale of the microstructure (Figure 2.1). The RVE is treated as a three-dimensional continuum, and within the RVE, the following assumptions are made (see also [129]):

1. The tissue can be idealized as a network of fibers of varying types and structures, all embedded within a compliant ground matrix. The two fiber families considered in the current study are collagen and muscle.
2. Fiber-fiber interactions are ignored, so that the net tissue response is the sum of the individual fibers responses.

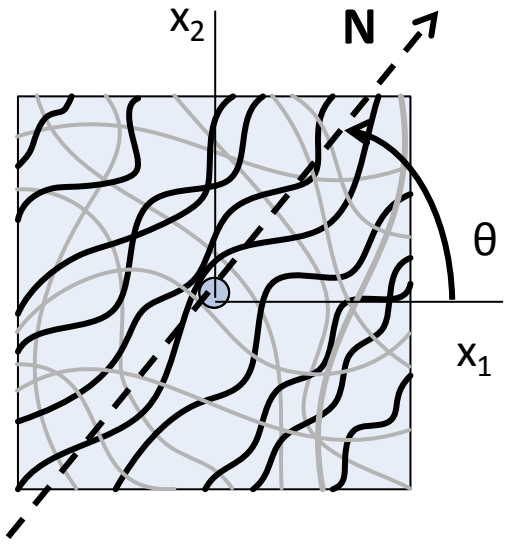

Figure 2.1. Schematic of the representative volume element.
Fiber ensembles are an idealized group of fibers of varying undulation, aligned along the same angle θ, represented by the unit vector **N**.

3. Hydrostatic forces generated by the matrix are considered negligible compared to the fiber forces, and are handled by assuming these components collectively induce an incompressible behavior at tissue level.
4. Contributions from non-load bearing constituents are combined with the ground matrix.
5. Collagen fibers are intrinsically undulated (also called crimped) and gradually straighten with increased stretch. The load required to straighten the collagen fiber is considered negligible compared to the load transmitted by the stretched fiber. Once a fiber has been stretched to a straightened state, it will transmit load and will be considered linear elastic. Note, that the exact meaning of this last point is addressed in section 2.3.

In the following, the RVE is simplified, and treated as a two-dimensional planar continuum.

2.1.2 Tissue level framework

The tissue level strain energy density Ψ of the RVE is assumed to result from the contribution of smooth muscle (*SM*) and extracellular matrix (*ECM*), weighted by their respective volume fractions ϕ and is defined as

$$\Psi\left(\mathbf{E}\right)=\sum_{i}\phi_{i}\Psi\left(\mathbf{E}\right)=\phi_{ECM}\Psi_{ECM}\left(\mathbf{E}\right)+\phi_{SM}\Psi_{SM}\left(\mathbf{E}\right). \tag{2.1}$$

If the tissue is considered to consist mostly of water (tissue density = ~1 g/ml), and if individual constituent densities are assumed to be equal, volume fractions can be approximated by mass fractions. Assuming a pseudoelastic, hyperelastic material response, the tissue-level 2nd Piola Kirchhoff stress **S** is derived from the strain energy as (see also Chapter 1.0 Eq. (1.17))

$$\mathbf{S}(\mathbf{E})=\frac{\partial\Psi\left(\mathbf{E}\right)}{\partial\mathbf{E}}-p\mathbf{C}^{-1}=\phi_{ECM}\frac{\partial\Psi_{ECM}\left(\mathbf{E}\right)}{\partial\mathbf{E}}+\phi_{SM}\frac{\partial\Psi_{SM}\left(\mathbf{E}\right)}{\partial\mathbf{E}}-p\mathbf{C}^{-1}, \tag{2.2}$$

where the Lagrange multiplier p accounts for the incompressible nature associated with non-fibrillar tissue components. p was eliminated as a result of the configuration of planar biaxial testing (see also section 1.2.4, Eqs. (1.18)-(1.20)).

A structurally based modeling approach for planar collagenous tissues is employed for the ECM strain energy function, where the contribution of individual fiber ensembles acting at independent orientations is summed over all orientations, using a statistical fiber orientation distribution function. Thus, it assumes the form

$$\Psi_{ecm}\left(\mathbf{E}\right)=\int_{\theta}R(\theta)\ \Psi_{col}^{ens}(\theta,\mathbf{E})\,d\theta=\int_{\theta}R\left(\theta\right)\ \Psi_{col}^{ens}\left(E^{ens}\left(\theta\right)\right)d\theta\,, \tag{2.3}$$

where *col* stands for collagen, R(θ) is the fiber angular density function, Ψ_{col}^{ens} is the strain energy associated with an individual collagen fiber ensemble (*ens*), and $E^{ens}=\mathbf{N}^{T}\mathbf{E}\mathbf{N}$ is the uniaxial Green-Lagrange strain acting in the ensemble direction, defined by a unit vector parallel to the fiber axis in the reference configuration $\mathbf{N}(\theta)$. The effective ensemble response has been modeled with a phenomenological expression [9, 129] as well as with a formulation accounting for the recruitment process [129]. Both approaches are described next.

2.1.3 ECM component – phenomenological fiber ensemble model

Exponential models have been successfully used to describe the nonlinear effective fiber ensemble stress-strain relation. In our group, a two-parameter exponential model has been defined which was applied to the aortic valve [9, 129]:

$$S^{ens}\left(E^{ens}\right)=d_{1}\left[\exp\left(d_{2}E^{ens}\right)-1\right]. \tag{2.4}$$

Using this exponential fiber model form for the fiber ensemble response, this model can be considered hybrid, in the sense that the fiber orientation distribution is defined in a structural manner and can be determined experimentally, whereas the fiber ensemble model itself is phenomenological.

A modified version of this model considers the fact that collagen fibers are being recruited up to an upper bound ensemble strain E_{ub} where all fibers are straight. The effective fiber ensemble response follows de exponential response of Eq. (2.4) up to this upper bound strain, and when the upper bound strain is reached, the fiber ensemble is assumed to behave in a linear elastic manner with a modulus equal to the tangent modulus at E_{ub}, under the assumption that straight collagen fibers behave linear elastic. This results in the following fiber ensemble model:

$$S^{ens}\left(E^{ens}\right)=\begin{cases} d_{1}\left[\exp\left(d_{2}E^{ens}\right)-1\right] & \textit{for}\quad 0<E^{ens}<E_{ub} \\ \left.\dfrac{\partial S^{ens}}{\partial E^{ens}}\right|_{E^{ens}=E_{ub}}\left[E^{ens}-E_{ub}\right]+d_{1}\left[\exp\left(d_{2}E_{ub}\right)-1\right] & \textit{for}\quad E^{ens}>E_{ub} \end{cases}. \tag{2.5}$$

2.1.4 ECM component – fiber ensemble model with recruitment

The structural formulation for collagen fibers assumes that the fibers are crimped and transmit load only if stretched beyond the point where all the crimp has disappeared, i.e. the slack stretch or strain. Once in straightened condition, fibers are assumed to follow a linear elastic material model. In the case of straight fibers without slack this implies $S_f = \eta E_t$ or $\Psi_f = \frac{\eta}{2} E_t^2$, where η is the fiber modulus and E_t is the true fiber strain. In case of undulated fibers, E_t is related to the ensemble or fiber strain by $E_t = \frac{E^{ens} - E_s}{1 + 2E_s}$, where E_s is the fiber slack strain. This process is schematically depicted in Figure 2.2. In terms of E_t, the fiber stress-strain relation for an undulated fiber is

$$S_f = \frac{\partial \Psi_f}{\partial E_f} = \frac{\partial \Psi_f}{\partial E_t}\frac{\partial E_t}{\partial E_f} = \eta \frac{E_f - E_s}{1 + 2E_s}\frac{1}{1 + 2E_s} = \eta \frac{E_f - E_s}{\left(1 + 2E_s\right)^2}. \tag{2.6}$$

The ensuing fiber ensemble strain energy and stress-strain relation are then described as the sum of individual fiber strain energies of the ensemble (Figure 2.1), weighted by the distribution of slack strains D, as

$$\begin{aligned} \Psi_{col}^{ens}\left(E^{ens}\right) &= \int_0^{E^{ens}} D(x)\Psi_f(x)\,dx = \frac{\eta}{2}\phi_f \int_0^{E^{ens}} D(x)\left[\frac{E^{ens} - x}{1 + 2x}\right]^2 dx \\ S_{col}^{ens}(E^{ens}) &= \int_0^{E^{ens}} D(x) S_f(x)\,dx = \eta\phi_f \int_0^{E^{ens}} D(x)\frac{E^{ens} - x}{\left[1 + 2x\right]^2} dx \end{aligned}. \tag{2.7}$$

In this η is the collagen fiber modulus, ϕ_f the collagen fiber fraction, and $D(x)$ a recruitment function. For convenience, ϕ_f is often absorbed in the effective fiber modulus K:

$$K = \phi_f \eta. \tag{2.8}$$

$D(x)$ describes the fraction of fibers realizing a fully straightened state at a given strain magnitude, which is effectively the distribution of slack strains $D(E_s)$. D is defined over $E_s \in [E_{lb}, E_{ub}]$, where E_{ub} is the upper bound strain defining an ensemble strain state where all fibers are straight, and E_{lb} the ensemble strain where recruitment begins (E_{lb} can be assumed to equal zero in many cases).

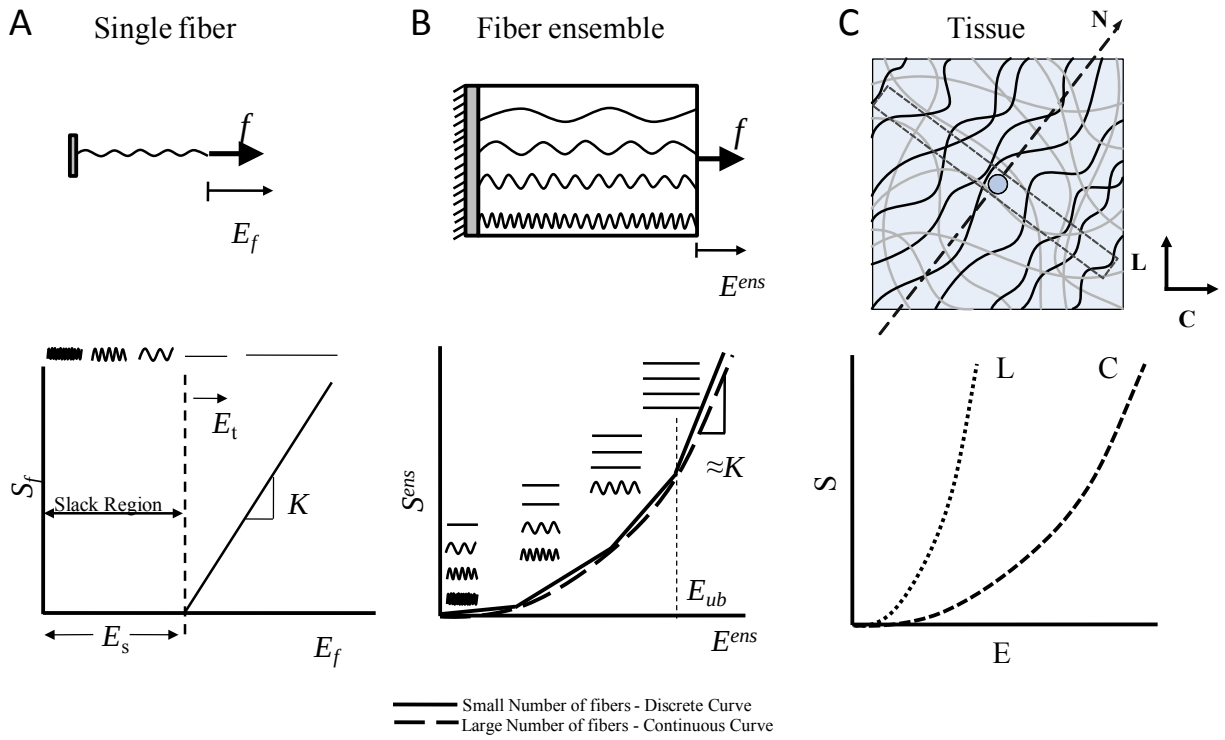

Figure 2.2. The process of fiber recruitment explained by building up from a single fiber. A)Uniaxial loading of a crimped fiber, with the corresponding stress-strain (S_f-E) curve. K is the fiber modulus. B) Uniaxial loading of an ensemble of fibers with the corresponding S^{ens}-E^{ens} curve indicating how recruitment of individual fibers results in a nonlinear stress-strain curve. C) Scaling it up to the tissue-level with anisotropic biaxial mechanical behavior resulting from specific distribution of fiber ensembles (see also Figure 1.1).

Under equibiaxial strain conditions, E_{11} equals E_{22}, and zero shear is assumed ($E_{12} = 0$). Because of the symmetry of $R(\theta)$ and the fact that $D(x)$ does not depend on θ, the fiber ensemble stress-strain relationship could be obtained directly from the experimental data using $S^{ens} = S_{11} + S_{22}$, and $E^{ens}=E_{11}=E_{22}$ [86, 129]. Hence, the parameters of the fiber ensemble model (Eq. (2.7)) could be experimentally determined directly from an equibiaxial stretch protocol.

Combining Eqs. (2.2), (2.3) and (2.7) leads to a complete formulation for stress in the ECM component

$$\mathbf{S}(\mathbf{E}) = \eta\phi_f \int_{-\frac{\pi}{2}}^{\frac{\pi}{2}} R(\theta) \left\{ \int_0^{E^{ens}(\theta)} D(x) \frac{E^{ens}(\theta) - x}{\left[1+2x\right]^2} dx \right\} \mathbf{N} \otimes \mathbf{N}\, d\theta \,. \tag{2.9}$$

The fiber distribution function $R(\theta)$ is represented by a beta distribution function with mean μ_R and standard deviation σ_R.

2.1.5 Fiber recruitment function

Forms and functions describing fiber recruitment, a process in which fibers in an individual ensemble engage into load transmission as they become fully straightened, has been presented in the literature [129]. The recruitment function $D(E_s)$ can be represented by different functions. The simplest relation is of exponential form:

$$D\left(E_s\right)=\frac{\left[\exp\left(a\frac{E_s}{E_{ub}}\right)-1+b\frac{E_s}{E_{ub}}\right]}{E_{ub}\left[\frac{b}{2}+\frac{\left(\exp\left(a\right)-1\right)}{a}-1\right]}, \tag{2.10}$$

where the denominator is introduced to ensure $\int_0^{E_{ub}} D(x)dx=1$. This function is implemented in the parameter estimation user interface (Chapter 3.0 , but it is not actually used in the present study.

As an initial step, the recruitment function $D(E_s)$ is represented by means of a unimodal modified beta distribution with mean μ and standard deviation σ [100]. The beta distribution $B(y)$ is defined on the interval $y \in [0, 1]$, which is modified to be defined on the interval $[0, E_{ub}]$, with $y = E_s/E_{ub}$, so that

$$D\left(E_s,\mu,\sigma\right)=\begin{cases}\dfrac{B(y,s_1,s_2)}{E_{ub}} & 0\le E_s\le E_{ub}\\ 0 & \text{otherwise}\end{cases}, \tag{2.11}$$

where s_1 and s_2 are shape parameters computed from μ and σ using

$$s_1=\frac{\mu^2-\mu^3-\mu\sigma^2}{\sigma^2},\quad s_2=s_1\frac{1-\mu}{\mu}. \tag{2.12}$$

The beta function is restricted to a unimodal shape with a lower bound of zero and to prevent the upper bound going to infinity, by enforcing $s_1,s_2 > 1$. Note, that for an unbound function $\mu,\sigma\in[0,1]$.

This model is extended by adopting a structurally guided form for the fiber ensemble strain energy. To take into account both levels of fiber uncoiling present in the bladder collagen fiber network, $D(E_s)$ is modified to the following bimodal distribution (with j = 1,2, and γ a scaling factor):

$$D(E_s, \mu_j, \sigma_j, \gamma) = \gamma D_1 + (1-\gamma) D_2 . \tag{2.13}$$

The parameters are bound in a similar manner, *i.e.* the shape parameters are larger than 1, and to enforce two distinguishable peaks, $\mu_1 < \mu_2$.

To estimate the fiber effective modulus (K, Eq. (2.8)), we note that if the tissue would consist of all straight fibers, the maximum tangent modulus (MTM) would equal K. At strain values $E^{ens} > E_{ub}$, all fibers are recruited, and MTM is determined using

$$MTM = \left. \frac{\partial S^{ens}(E^{ens})}{\partial E^{ens}} \right|_{E^{ens} \geq E_{ub}} = K \int_0^{E_{ub}} \frac{D(x)}{(1+2x)^2} dx . \tag{2.14}$$

The greater the degree of slacked fibers that exists in the tissue (either a longer slack length per fiber, or more slacked fibers), the lower the MTM is as compared to K. Hence, MTM provides a lower bound value for K, because the integral on the right hand side of Eq. (2.14) is lower than 1 because of the presence of fiber slack. Note this problem is solved by the model modifications introduced in the next section (section 2.2).

2.2 MODIFIED CONSTITUTIVE MODEL FORMULATION TO ACCOUNT FOR WORKLESS CHANGE IN REFERENTIAL CONFIGURATION

2.2.1 Rational and assumptions

Extensions to the above model formulation are derived to allow handling of changes in tissue reference state geometry due to mechanisms such as decellularization and preconditioning. These model modifications are necessary because quantitative tissue structural information such as fiber orientation is available in a different state (typically a non-preconditioned, unloaded state) than the state that the mechanical test is performed in. Moreover, in the case of multi-component tissues, physical and structural properties of individual components are not all available in the same referential configuration. Procedures such as decellularization and preconditioning induce permanent set-like deformations. During mechanical testing the tissue reverts to the post-preconditioned state when unloaded, and the strain energy density function should be defined in

this state. This essentially results in a reference configuration wherein the tissue's strain energy function is defined, that is different from the initial state.

The ECM model parameters are determined from decellularized tissue, with respect to a reference configuration in decellularized state. In the current novel approach, all model parameters are described in the intact configuration, whereas the mechanical data were obtained in the post-preconditioned decellularized configuration. The relevant states are defined as follows: Ω_0 is the initial configuration state (the intact state in this specific case) and is stress-free, Ω_1 is the reference configuration (the post-preconditioned decellularized state in this specific case) and is thus considered stress-free as well, Ω_t is the configuration at time *t* where loading has been applied. The key assumptions are:

1. Changes are due to alterations in the initial configuration only, which implies that volume/mass fractions remain unchanged, and the internal mechanical energy remains zero. All changes in internal component configurations are not associated with any change in internal energy (*e.g.* fiber orientation, degree of undulation, thickness, length).
2. Tissue dimensions and internal architecture change under the affine assumption. Thus, the configuration of all constituent fibers in the altered reference state (after all changes in initial specimen geometry have taken place) can be predicted.
3. The configurational change is homogeneous, and can be thus described by a deformation gradient tensor with constant components. The deformation gradient tensor associated with this change ($\Omega_0 \rightarrow \Omega_1$) is named ${}^{1}_{0}\mathbf{F}$. As $\mathbf{F}$ is a two-point tensor, the general notation that is used is ${}^{\beta}_{\alpha}\mathbf{F}$, where a bold capital represents a tensor quantity, and α and β represent the first and second state used, respectively.
4. To be consistent with the undulated linear fiber model, all fibers remain undulated in the new reference state.

These assumptions result in a series of model modifications.

2.2.2 Model modifications

I. The deformation gradient tensors associated with $\Omega_0 \rightarrow \Omega_1$ and $\Omega_1 \rightarrow \Omega_t$, are defined as ${}^{1}_{0}\mathbf{F}$ and ${}^{t}_{1}\mathbf{F}$, respectively. Following Eqs. (1.1), the associated strain relations are defined by

$$
\begin{aligned}
{}^{t}_{0}\mathbf{F} &= {}^{t}_{1}\mathbf{F}\,{}^{1}_{0}\mathbf{F} \\
{}^{t}_{0}\mathbf{C} &= {}^{t}_{0}\mathbf{F}^{T}\,{}^{t}_{0}\mathbf{F} \\
{}^{t}_{0}\mathbf{E} &= \frac{1}{2}({}^{t}_{0}\mathbf{C}-\mathbf{I})
\end{aligned}
\quad . \tag{2.15}
$$

Based on ${}^{1}_{0}\mathbf{F}$, the ensemble Green's strain associated with this deformation is defined as

$$
{}^{1}_{0}E^{ens} = \mathbf{N}^{T}\,{}^{1}_{0}\mathbf{E}\,\mathbf{N}, \tag{2.16}
$$

and the ensemble Green strain in Ω_0 is related to the ensemble Green strain in Ω_1 through

$$
{}^{t}_{0}E^{ens} = {}^{t}_{1}E^{ens} + {}^{1}_{0}E^{ens} + 2\,{}^{t}_{1}E^{ens}\,{}^{1}_{0}E^{ens}. \tag{2.17}
$$

II. The following collagen fiber architecture strain requirements are specified, based on the existence of a lower and upper bound ensemble strain, ${}_{0}E_{lb}$ and ${}_{0}E_{ub}$ respectively, in between which recruitment takes place.

a. All fibers remain slack for ${}^{t}_{0}E^{ens} = \left[0, {}_{0}E_{lb}\right]$.

b. All recruitment occurs for ${}^{t}_{0}E^{ens} = \left[{}_{0}E_{lb}, {}_{0}E_{ub}\right]$.

c. All recruitment ceases for ${}^{t}_{0}E^{\varepsilon} = \left[{}_{0}E_{ub}, {}_{0}E^{ens}_{\max}\right]$, where ${}_{0}E^{ens}_{\max}$ is the largest possible ensemble strain prior to any yielding or failure.

d. ${}_{0}E_{lb}, {}_{0}E_{ub}, {}_{0}E^{ens}_{\max} \in \Omega_0$

III. θ is defined as the fiber orientation in Ω_0 , β_1 as the orientation of the same fiber in Ω_1, and β_t as the orientation of the same fiber or ensemble at time *t*. θ' defines the integration variable in Ω_1. Note here that all angles are referred to the coordinate system of Ω_0 and θ' is defined on the half space [-π/2, π/2]. Using these definitions, and with a known ${}^{1}_{0}\mathbf{F}$, the fiber distribution $R_1(\theta')$ in Ω_1 is defined in terms of $R(\theta)$. First, θ is defined in terms of θ' using the following relations

$$
\begin{aligned}
\lambda_f^{-1} &= \sqrt{\mathbf{n}^{T}\,{}^{1}_{0}\mathbf{F}^{-T}\,{}^{1}_{0}\mathbf{F}^{-1}\mathbf{n}} \\
\mathbf{N}(\theta) &= \lambda_f\,{}^{1}_{0}\mathbf{F}^{-1}\mathbf{n} = \frac{{}^{1}_{0}\mathbf{F}^{-1}\mathbf{n}}{\sqrt{\mathbf{n}^{T}\,{}^{1}_{0}\mathbf{F}^{-T}\,{}^{1}_{0}\mathbf{F}^{-1}\mathbf{n}}}, \\
\theta &= \tan^{-1}\left(\frac{N_2}{N_1}\right)
\end{aligned}
\tag{2.18}
$$

where $\mathbf{n}$=[cos(θ'); sin(θ')] is the fiber orientation vector in Ω_1, and N_i (i = 1,2) are the components of $\mathbf{N}$. Using these relations, and following Dafalias [24], $R_1(\theta')$ is obtained from a known $R_0(\theta)$ in Ω_0 through

$$R_1\left(\theta'\right) = R_0\left[\theta\left(\theta', {}^1_0\mathbf{F}\right)\right] \frac{\mathbf{N}^T\left[\theta\left(\theta', {}^1_0\mathbf{F}\right)\right] {}^1_0\mathbf{F}^T \, {}^1_0\mathbf{F} \;\mathbf{N}\left[\theta\left(\theta', {}^1_0\mathbf{F}\right)\right]}{{}^1_0J}, \tag{2.19}$$

where ${}^1_0J = \left|{}^1_0\mathbf{F}\right|$. This expression is derived based on the assumption that the total number of fibers after deformation is the same as in the reference configuration, which yields the relation $\frac{R_1}{R_0} = \frac{d\theta}{d\theta'}$. Furthermore, using the definition of the projection of a cone defined in terms of stereo angles and area vectors, together with Nanson's formula that describes the relation between the area vector in the current and reference configurations, and transforming it into 2D, this results in $\frac{R_1}{R_0} = \frac{d\theta}{d\theta'} = \frac{\lambda_f^2}{J}$. λ_f is the stretch in the fiber defined as $\lambda_f^2 = \mathbf{N}^T\mathbf{F}^T\mathbf{F}\;\mathbf{N}$ (see also Eq. (2.18)). $R_0(\theta)$ is represented by a beta distribution function with parameters μ_R and σ_R.

IV. Since all deformations due to applied loading occur in Ω_1, and following Eq. (2.3), Ψ is defined in Ω_1 as

$$\Psi_{ECM}\left({}^t_1\mathbf{E}\right) = \int_{\theta'} R'\left(\theta'\right)\, \Psi^{ens}_{col}\left({}^t_1E^{ens}\left(\theta'\right)\right) d\theta', \tag{2.20}$$

where ${}^t_1\mathbf{E}$ is the Green's strain associated with $\Omega_1 \rightarrow \Omega_t$. Using Eq. (2.2), while assuming incompressibility and specializing for planar biaxial deformations (*i.e.* using a membrane approximation) this results in the constitutive equation for the ECM component

$${}^t_1\mathbf{S}_{ECM}\left({}^t_1\mathbf{E}\right) = \int_{-\pi/2}^{\pi/2} R'\left(\theta'\right) \frac{\partial \Psi^{ens}}{\partial {}^t_1E^{ens}} \frac{\partial {}^t_1E^{ens}}{\partial {}^t_1\mathbf{E}} d\theta' = \int_{-\pi/2}^{\pi/2} R'\left(\theta'\right)\, S^{ens}_{col}\left({}^t_1E^{ens}\left(\theta'\right)\right) \mathbf{n}\otimes\mathbf{n} d\theta'. \tag{2.21}$$

V. At the ensemble level, the slack strains, and hence the recruitment function D, are defined in Ω_1, but D needs to utilize parameters referred to Ω_0. The recruitment function $D_1\left({}^t_1E_s\right)$ in Ω_1 is derived from the recruitment function $D\left({}^t_0E_s\right)$ in Ω_0 as follows. $D\left({}^t_0E_s\right)$ is first defined using a beta distribution function $B(y)$, with a mean μ and standard deviation σ defined in terms of ${}^t_0E^{ens}$, mapped to the interval $\left[{}_0E_{lb}, {}_0E_{lb}\right]$, with $\left[{}_0E_{lb}, {}_0E_{lb}\right] \in \Omega_0$, using

$$D\left({}_0^t E_s, \mu, \sigma\right) = \begin{cases} \dfrac{B(y, s_1, s_2)}{{}_0E_{lb} - {}_0E_{ub}} & {}_0E_{lb} \le {}_0E_s \le {}_0E_{ub} \\ 0 & \text{otherwise} \end{cases}, \tag{2.22}$$

where s_1 and s_2 are shape parameters computed from μ and σ using Eq. (2.12), and with $y\left({}_0E_s\right) = \dfrac{{}_0E_s - {}_0E_{lb}}{{}_0E_{ub} - {}_0E_{lb}}$. μ and σ are mapped on $y \in [0, 1]$, as required by the beta distribution, but can also be expressed in terms of strain using $\mu = \dfrac{\mu_y - {}_0E_{lb}}{{}_0E_{ub} - {}_0E_{lb}}$ and $\sigma = \dfrac{\sigma_y}{\left({}_0E_{ub} - {}_0E_{lb}\right)^2}$.

To utilize this in stress-strain calculations in Ω_1, the following definition is used, following Eqs. (2.15) - (2.17):

$${}_0^1E^{ens} = \mathbf{N}\left[\theta\left(\theta', {}_0^1\mathbf{F}\right)\right]^{\mathrm{T}} {}_0^1\mathbf{E}\,\mathbf{N}\left[\theta\left(\theta', {}_0^1\mathbf{F}\right)\right], \tag{2.23}$$

This can also be obtained using Eq. (2.18), as follows:

$$\begin{aligned} {}_0^1\lambda^{ens} &= \sqrt{\mathbf{N}^{\mathrm{T}}\,{}_0^1\mathbf{F}^T\,{}_0^1\mathbf{F}\,\mathbf{N}} = \frac{1}{\sqrt{\mathbf{n}^T\,{}_0^1\mathbf{F}^{-T}\,{}_0^1\mathbf{F}^{-1}\mathbf{n}}} = \lambda_f \\ {}_0^1E^{ens} &= \tfrac{1}{2}\left({}_0^1\lambda_{ens}{}^2 - 1\right) \end{aligned} \tag{2.24}$$

This is used to define the expressions for lower and upper bound strain in Ω_1:

$${}_1E_{lb} = \frac{E_{lb} - {}_0^1E_{ens}\left(\theta\left(\theta', {}_0^1\mathbf{F}\right)\right)}{1 + 2\,{}_0^1E_{ens}\left(\theta\left(\theta', {}_0^1\mathbf{F}\right)\right)}, \quad {}_1E_{ub} = \frac{E_{ub} - {}_0^1E_{ens}\left(\theta\left(\theta', {}_0^1\mathbf{F}\right)\right)}{1 + 2\,{}_0^1E_{ens}\left(\theta\left(\theta', {}_0^1\mathbf{F}\right)\right)}, \tag{2.25}$$

and this gives for y:

$$y\left({}_1E_s\right) = \frac{{}_1E_s\left(\theta'\right) - {}_1E_{lb}\left(\theta\left(\theta', {}_0^1\mathbf{F}\right)\right)}{{}_1E_{ub}\left(\theta\left(\theta', {}_0^1\mathbf{F}\right)\right) - {}_1E_{lb}\left(\theta\left(\theta', {}_0^1\mathbf{F}\right)\right)}. \tag{2.26}$$

To satisfy the normalization requirement in Ω_1, D is now defined as

$$D_1\left({}_1E_s, \theta', \mu, \sigma\right) = \begin{cases} \dfrac{B\left(y, s_1, s_2\right)}{{}_1E_{ub}\left(\theta\left(\theta', {}_0^1\mathbf{F}\right)\right) - {}_1E_{lb}\left(\theta\left(\theta', {}_0^1\mathbf{F}\right)\right)} & {}_1E_{lb} \le {}_1^tE_s \le {}_1E_{ub} \\ 0 & \textit{otherwise} \end{cases}. \tag{2.27}$$

With $D_1(x)$ given by Eq. (2.27), the fiber ensemble stress-strain relation is described as

$$ {}_1^tS^{ens}\left({}_1^tE^{ens}(\theta')\right)=\eta\phi_f\int_0^{{}_1^tE^{ens}(\theta')}D_1(x,\theta')\frac{{}_1^tE^{ens}(\theta')-x}{\left[1+2x\right]^2}dx\,. \tag{2.28} $$

Note also that η is defined in Ω_0, and hence η in Eq. (2.28) is the actual fiber modulus, *i.e.*, it has the same value as if the fiber ensemble stress-strain relation is defined in Ω_0. This can be proven by considering a uniaxial bar in Ω_0 with cross-sectional area A_0 and length l_0 subjected to a force f, and the same bar in Ω_1, now with a cross-sectional area A_1 and length l_1 after a uniaxial permanent set equal to ${}_0^1\lambda = l_1/l_0$. The incompressibility assumption requires that ${}_0^1\lambda = l_1/l_0 = A_0/A_1$. The Lagrangian stress in Ω_0 can be expressed in terms of the Lagrangian stress P in Ω_1 as

$$ {}_0^tP=\frac{f}{A_0}=\frac{f}{A_1}\cdot\frac{A_1}{A_0}=\frac{1}{{}_0^1\lambda}\,{}_1^tP\,. \tag{2.29} $$

and since for this simple case P = Sλ the 2nd Piola Kirchhoff stress is given as

$$ {}_0^tS=\frac{1}{{}_0^1\lambda^2}\,{}_1^tS \tag{2.30} $$

Next, using the fiber model given by Eq. (2.6), using ${}_0^t\lambda = {}_0^1\lambda\,{}_1^t\lambda$, and naming the fiber modulus in Ω_0 η, and the fiber modulus in Ω_1 η^*:

$$ \begin{aligned} {}_0^tS&=\frac{\eta}{2}\frac{{}_0^t\lambda^2-{}_0\lambda_s^{\,2}}{{}_0\lambda_s^{\,2}\cdot{}_0\lambda_s^{\,2}}\\ \frac{1}{{}_0^1\lambda^2}\,{}_1^tS&=\frac{\eta^*}{2\,{}_0^1\lambda^2}\cdot\frac{{}_1^t\lambda^2-{}_1\lambda_s^{\,2}}{{}_1\lambda_s^{\,2}\cdot{}_1\lambda_s^{\,2}}=\frac{\eta^*}{2\,{}_0^1\lambda^2}\cdot\frac{\frac{{}_0^t\lambda^2}{{}_0^1\lambda^2}-\frac{{}_0\lambda_s^{\,2}}{{}_0^1\lambda^2}}{\frac{{}_0\lambda_s^{\,2}}{{}_0^1\lambda^2}\cdot\frac{{}_0\lambda_s^{\,2}}{{}_0^1\lambda^2}}\,.\\ &=\frac{{}_0^1\lambda^2}{2\,{}_0^1\lambda^2}\cdot\frac{{}_0^t\lambda^2-{}_0\lambda_s^{\,2}}{{}_0\lambda_s^{\,2}\cdot{}_0\lambda_s^{\,2}}=\frac{\eta^*}{2}\frac{{}_0^t\lambda^2-{}_0\lambda_s^{\,2}}{{}_0\lambda_s^{\,2}\cdot{}_0\lambda_s^{\,2}} \end{aligned} \tag{2.31} $$

Thus, this proves that $\eta = \eta^*$, and the fiber modulus in Ω_0 is indeed the same modulus as in the modified model defined in Ω_1.

Combining Eqs. (2.21) and (2.28), with $K = \phi_f\eta$, and expressing it in component form results in

$$\left(S_{ECM}\right)_{11}=\frac{\partial\Psi}{\partial\,{}_1^tE_{11}}=K\int_{-\pi/2}^{\pi/2}R_1(\theta')\left\{\int_0^{{}_1^tE^{ens}(\theta')}D(x,\theta')\frac{{}_1^tE^{ens}(\theta')-x}{\left[1+2x\right]^2}dx\right\}\cos^2(\theta')d\theta'$$

$$\left(S_{ECM}\right)_{22}=\frac{\partial\Psi}{\partial\,{}_1^tE_{22}}=K\int_{-\pi/2}^{\pi/2}R_1(\theta')\left\{\int_0^{{}_1^tE^{ens}(\theta')}D(x,\theta')\frac{{}_1^tE^{ens}(\theta')-x}{\left[1+2x\right]^2}dx\right\}\sin^2(\theta')d\theta' \quad . \quad (2.32)$$

$$\left(S_{ECM}\right)_{12}=\frac{\partial\Psi}{\partial\,{}_1^tE_{12}}=K\int_{-\pi/2}^{\pi/2}R_1(\theta')\left\{\int_0^{{}_1^tE^{ens}(\theta')}D(x,\theta')\frac{{}_1^tE^{ens}(\theta')-x}{\left[1+2x\right]^2}dx\right\}\cos(\theta')\sin(\theta')d\theta'$$

Following section 2.1.5, $B(y)$ in Eqs. (2.22) and (2.27) is modified to a bimodal distribution, where $B(y) = \gamma B_1(y) + (1-\gamma)B_2(y)$ (with j = 1,2, and γ a scaling factor). A total of 10 model parameters is now defined: K, μ_R, σ_R, μ_1, σ_1, γ, μ_2, σ_2, ${}_0E_{lb}$, ${}_0E_{ub}$, all referred to Ω_0. Furthermore, under equibiaxial strain conditions, E_{11} equals E_{22}, and when zero shear is assumed (E_{12}=0), the original fiber ensemble stress-strain relationship could be obtained directly from the experimental data in Ω_1 using $S^{ens} = S_{11} + S_{22}$, and ${}_1E^{ens}={}_1E_{11}={}_1E_{22}$ [86, 129]. Note that this does not provide values for ${}_0E_{lb}$ and ${}_0E_{ub}$, but rather only provides an estimate of the shape of $D(x)$, with values for ${}_1E_{lb}$ and ${}_1E_{ub}$, where in turn estimates of ${}_0E_{lb}$ and ${}_0E_{ub}$ can be derived from. It also does not provide a value for K in Ω_0, because the permanent set induces an extra scaling effect on top of the effect of the slack stretch, as was explained with Eq. (2.14).

2.3 CORRECTED FIBER STRESS-STRAIN RELATION

2.3.1 Rationale

Most structural models rely on non-specific statements of linearity of the stress-strain relation. However, the exact choice of stress and strain measures will greatly influence what this actually means. Our original fiber model as described in section 2.1.4 assumes that the 2nd Piola Kirchhoff stress in the fiber is linearly related to the fiber Green's strain. However, observations from X-ray diffraction experiments on heart valve and tendon have shown that collagen fibers in reality exhibit a linear force-displacement relation [90, 132, 133]. Lagrangian tension vs. collagen D-spacing showed a linear relation in the mitral valve (Figure 2.3 A) [90].

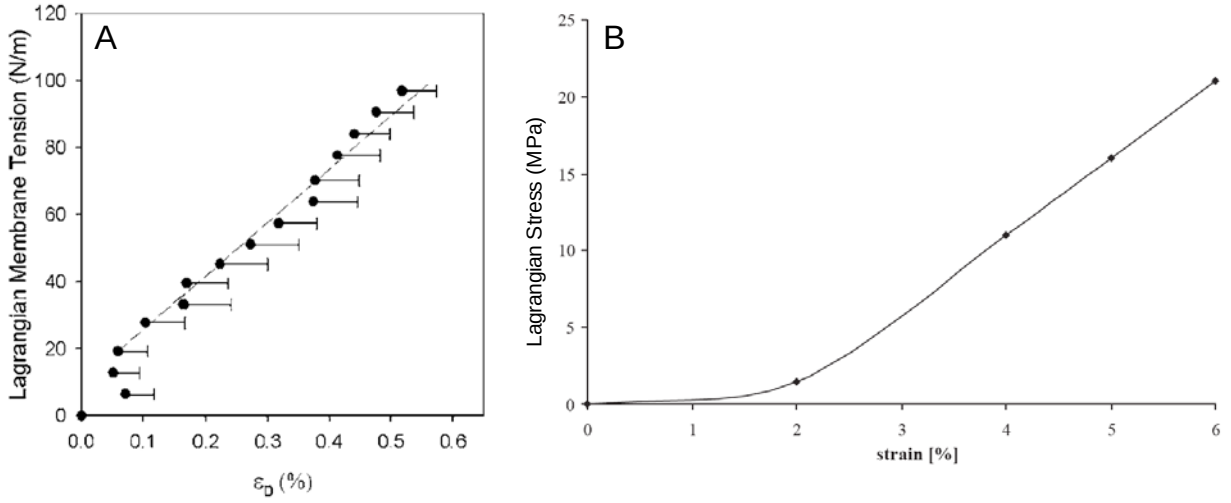

Figure 2.3. A collagen fiber can be assumed to be linear in terms of force – displacement and hence in terms of P-λ. A) Relationship between collagen fibrillar D-period strain (ε_D) and applied equibiaxial tissue tension. Reprinted with permission from [90]. Copyright @ ASME, 2007. B) Stress–strain curve of the collagen fibrils–GAG system in a molecular dynamics simulation. Lagrangian stress was calculated by assuming that the force calculated through the nonlinear equation system acts on a square section whose edge is given by the sum of the diameter and the interfibrillar distance. Reprinted from [120]. Copyright (2003), with permission from Elsevier Science Ltd.

The same type of linear relation was assumed in molecular dynamics simulations of collagen fibrils and collagen molecules [120, 164]. In these studies, the collagen fibril-GAG complex exhibited a linear stress-strain relation in terms of Lagrangian stress and engineering strain (Figure 2.3 B) [120], and collagen molecules showed a 2nd order relation in terms of potential energy vs. molecule length, which implies a linear stress-strain relation with a constant modulus [164].

When a fiber is linear in terms of force-displacement or P-λ, it cannot be linear in S-E, since Green's strain has a nonlinear character as a result of its nonlinear relation to stretch (Eq. (1.1)) and hence displacement. In this section, a new fiber stress-strain relation is derived based on the assumption that a collagen fiber behaves linearly in terms of force-displacement. In addition, a macroscopic reference length is used instead of the individual fiber reference length as was the case in the original formulation. Defining this new fiber stress-strain relation will increase the physical realism of the model and will make it more intuitive since stretch is a linear measure, whereas Green's strain is nonlinear. In addition, as will be shown in Chapter 3.0, the original model exhibits covariance between the fiber effective stiffness parameter K and the

parameters defining the recruitment function D. The new fiber stress-strain relation decouples K and D, as will be proven in the next section (2.3.2) and illustrated in Chapter 3.0.

2.3.2 Fiber model modifications

Consider a fiber of length l_0 with cross section A_0 subjected to a force f (Figure 2.4 A). The force induces a displacement $\delta = l - l_0$ in the fiber, and the relation between force and displacement is given by $f = \mu^* \cdot \delta$, where μ^* is the stiffness of the bar. Normalizing the force by initial area and displacement by original length gives the traditional linear stress-stretch relationship $P(\lambda)$

$$\begin{aligned} f &= \frac{A_0 E}{l_0} \cdot \delta \\ \frac{f}{A_0} &= E \cdot \frac{\delta}{l_0} \\ P &= E \cdot [\lambda - 1] \end{aligned} \quad , \tag{2.33}$$

where P is the 1st Piola Kirchhoff stress under the large deformation assumption, λ is the stretch in the fiber, and E is the elastic modulus. Next, consider a fiber with slack length l_s (Figure 2.4 B).

Upon application of a force f, the fiber uncrimps and starts bearing load after a displacement δ_s. The increasing force is linearly related to the "true" displacement δ_t as given by $f = \mu \cdot \delta_t$, where μ is the stiffness, and $\delta_t = \delta - \delta_s$. Following the rationale of Eq.(2.33), this gives the following stress-stretch relationship:

$$\begin{aligned} f &= \frac{A_0 \eta}{l_0} \cdot \delta_t \\ \frac{f}{A_0} &= \eta \cdot \frac{\delta - \delta_s}{l_0} \\ P &= \eta \cdot [\lambda - \lambda_s] \end{aligned} \quad . \tag{2.34}$$

In here, the definition $\lambda_s = \delta_s / l_0$ is used. Note, that in the case of an ensemble of crimped fibers with different slack lengths l_s, l_0 is the only commonly known length for all fibers. l_0 can be seen as a macroscopic normalization length.

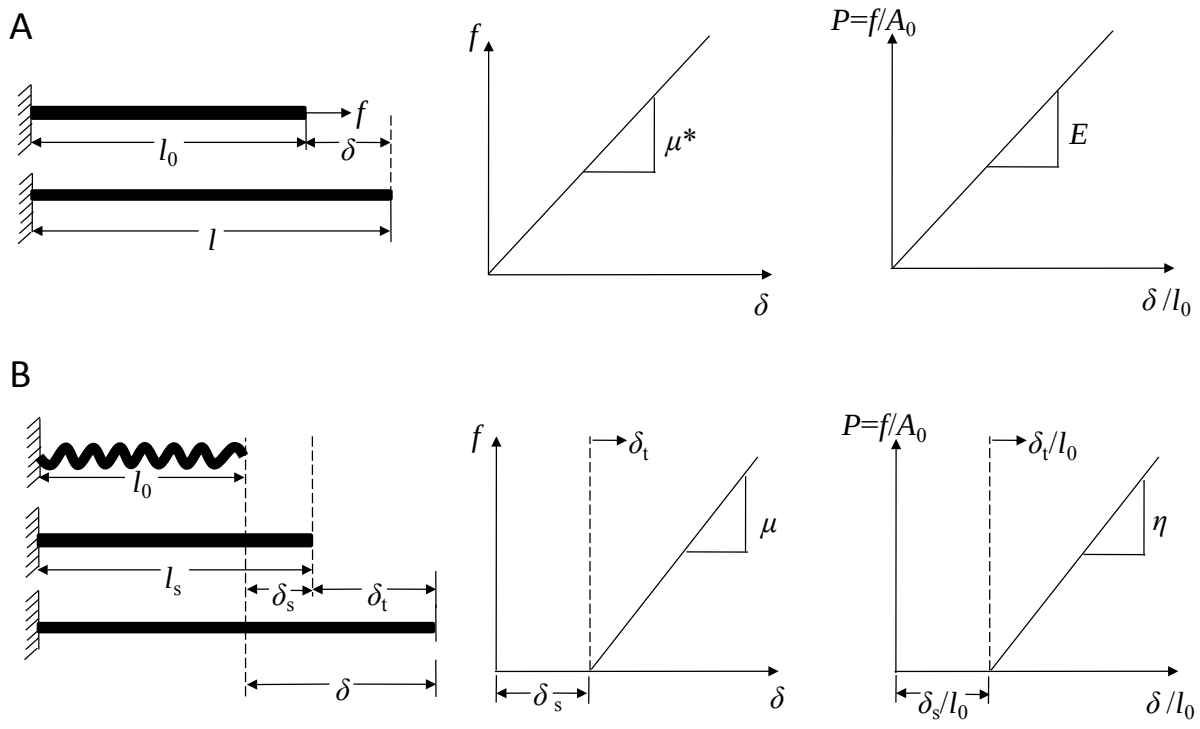

Figure 2.4. Schematic representation of the linear-elastic fiber relation.
A) Loading of a straight fiber (cross-section A, length l) with the corresponding force (f)-displacement (δ) and stress (P)-stretch curves. μ^* and E are the fiber stiffness and modulus, respectively. B) Loading of a crimped fiber, with the corresponding force (f)-displacement (δ) and stress (P)-stretch curves. μ and η are the fiber stiffness and modulus, respectively.

This concept is visualized Figure 2.5 by a set of springs with equal stiffness (μ) but with different slack lengths (δ_s). The front of the virtual box is displaced to the right and when it hits a spring, the spring starts contributing to the total force, where the total force is the sum of the individual forces: $f = \sum_i f_i$. When the stress in each spring is calculated by Eq. (2.34), and all stresses are summed up to determine the total stress in the ensemble, it can be shown that the only appropriate reference length is the macroscopic reference length l_0 (with A_0 equals the total cross-sectional area of all springs):

$$\begin{aligned} f &= \mu\left[\delta - \left(\sum_i \delta_{si}\right)\right] \\ \frac{f}{A_0} &= \frac{\eta}{l_0}\left[\delta - \left(\sum_i \delta_{si}\right)\right]. \\ P &= \eta\left[\lambda - \left(\sum_i \delta_{si}\right)\right] \end{aligned} \tag{2.35}$$

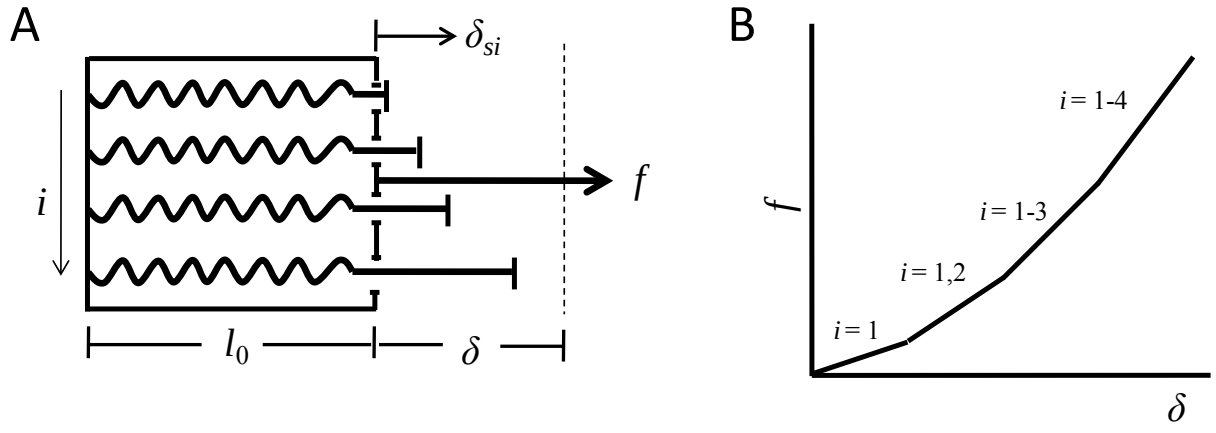

Figure 2.5. Representation of a fiber ensemble by a set of springs with variable slack lengths.
A) A displacement (δ) is applied to a set of four springs with equal stiffness and each spring is loaded at a different moment. Force is produced by the individual springs as soon as they hit the front of the load applicator. B) Force-displacement diagram for the four springs in panel A. At each next level, an extra spring contributes to the total force.

In terms of 2nd Piola Kirchhoff stress, Eq. (2.34) becomes

$$S = \frac{P}{\lambda} = \frac{\eta}{\lambda}\left[\lambda - \lambda_s\right] = \eta \cdot \left[1 - \frac{\lambda_s}{\lambda}\right], \tag{2.36}$$

and converting stretch to Green's strain (following Eq. (1.1), $E = \tfrac{1}{2}\left(\lambda^2 - 1\right)$ or $\lambda = \sqrt{1+2E}$) results in

$$S = \eta \cdot \left[1 - \frac{\sqrt{1+2E_s}}{\sqrt{1+2E}}\right], \tag{2.37}$$

with E_s the slack strain. Eq. (2.37) replaces the linear relation $S=\eta E_t$ described in section 2.1.4. This fiber stress-strain relation can in this form be implemented in the modified model outlined in section 2.2, yielding a complete formulation in terms of Green's strain. Following Eq. (2.28), the ensemble model then is defined as:

$${}_1^t S^{ens}\left({}_1^t E^{ens}\right) = \eta\phi_f \int_0^{{}_1^t E^{ens}} D_1\left(x\right)\left[1 - \frac{\sqrt{1+2x}}{\sqrt{1+2\,{}_1^t E^{ens}}}\right] dx\,. \tag{2.38}$$

As a final step, the model is completely expressed in terms of ensemble stretch, *i.e.*, Eq. (2.36) is combined with a recruitment function defined in terms of slack stretch, instead of slack Green's strain. The recruitment function, originally given by Eqs. (2.25)-(2.27) is now defined as:

$$D_1\left({}_1\lambda_s, \theta', \mu, \sigma\right) = \begin{cases} \dfrac{B\left(y, s_1, s_2\right)}{{}_1\lambda_{ub}\left(\theta\left(\theta', {}_0^1F\right)\right) - {}_1\lambda_{lb}\left(\theta\left(\theta', {}_0^1F\right)\right)} & {}_1\lambda_{lb} \le {}_1^t\lambda_s \le {}_1\lambda_{ub} \\ 0 & \textit{otherwise} \end{cases}, \tag{2.39}$$

with

$${}_1\lambda_{lb} = \frac{{}_0\lambda_{lb}}{{}_0^1\lambda_{ens}\left(\theta\left(\theta', {}_0^1F\right)\right)}, \quad {}_1\lambda_{ub} = \frac{{}_0\lambda_{ub}}{{}_0^1\lambda_{ens}\left(\theta\left(\theta', {}_0^1F\right)\right)}, \tag{2.40}$$

and

$$y\left({}_1\lambda_s\right) = \frac{{}_1\lambda_s\left(\theta'\right) - {}_1\lambda_{lb}\left(\theta\left(\theta', {}_0^1F\right)\right)}{{}_1\lambda_{ub}\left(\theta\left(\theta', {}_0^1F\right)\right) - {}_1\lambda_{lb}\left(\theta\left(\theta', {}_0^1F\right)\right)}, \tag{2.41}$$

and where the slack stretch ${}_1\lambda_s$ runs from 1 to ${}_1^t\lambda_{ens}^{\max}$. The mean and standard deviation are defined in terms of the normalized parameter *y*, but can also be expressed in terms of stretch using $\mu = \dfrac{\mu_y - {}_0\lambda_{lb}}{{}_0\lambda_{ub} - {}_0\lambda_{lb}}$ and $\sigma = \dfrac{\sigma_y}{\left({}_0\lambda_{ub} - {}_0\lambda_{lb}\right)^2}$.

The ensemble relation as defined in Eq. (2.38) in terms of *S*-*E*, cannot be directly formulated in terms of P-λ , following a similar rationale as was described in Eqs. (2.29) and (2.31). In terms of *P*-λ this rationale results in the following statements

$$\begin{aligned} {}_0^tP &= \eta\left({}_0^t\lambda - {}_0\lambda_s\right) \\ \frac{1}{{}_0^1\lambda}\,{}_1^tP &= \frac{\eta^*}{{}_0^1\lambda}\left({}_1^t\lambda - {}_1\lambda_s\right) = \frac{\eta^*}{{}_0^1\lambda}\left(\frac{{}_0^t\lambda}{{}_0^1\lambda} - \frac{{}_0\lambda_s}{{}_0^1\lambda}\right). \\ &= \frac{\eta^*}{{}_0^1\lambda^2}\left({}_0^t\lambda - {}_0\lambda_s\right) \end{aligned} \tag{2.42}$$

Thus, $\eta = \dfrac{\eta^*}{\left({}_0^1\lambda\right)^2}$, and in the ensemble relation this is accounted for as follows

$${}_1^tP^{ens}\left({}_1^t\lambda^{ens}\right) = \eta\phi_f\,{}_0^1\lambda^2\int_1^{{}_1^t\lambda^{ens}} D_1(x)\left({}_1^t\lambda^{ens} - x\right)dx\,, \tag{2.43}$$

or in terms of 2nd Piola Kirchhoff stress

$${}_1^tS^{ens}\left({}_1^t\lambda^{ens}\right) = \eta\phi_f\,{}_0^1\lambda^2\int_1^{{}_1^t\lambda^{ens}} D_1(x)\left(1 - \frac{x}{{}_1^t\lambda^{ens}}\right)dx\,. \tag{2.44}$$

In Eq. (2.43), *D* and η are completely uncoupled, and when no permanent set deformation is present (${}_0^1\lambda = 1$), η can be directly determined from an equibiaxial strain experiment (see also section 2.1.5 and Eq. (2.14)) using the relation

$$TM = \frac{\partial P^{ens}(\lambda^{ens})}{\partial\lambda^{ens}} = \eta\phi_f\int_1^{{}_1^t\lambda_{ub}} D(x)dx\,. \tag{2.45}$$

When $\lambda^{ens} \geq \lambda_{ub}$, the integral equals 1 and $\eta = \mathrm{MTM}/\phi_f$.

The tissue level model, including the modifications for the permanent set and the modifications for the fiber model is now given by

$$\left(S_{ECM}\right)_{11}=\eta\phi_f\int_{-\pi/2}^{\pi/2}R_1\left(\theta'\right){}_0^1\lambda\left(\theta'\right)^2\left\{\int_1^{{}_1^t\lambda^{ens}(\theta')}D\left(x,\theta'\right)\left(1-\frac{x}{{}_1^t\lambda^{ens}\left(\theta'\right)}\right)dx\right\}\cos^2\left(\theta'\right)d\theta'$$

$$\left(S_{ECM}\right)_{22}=\eta\phi_f\int_{-\pi/2}^{\pi/2}R_1\left(\theta'\right){}_0^1\lambda\left(\theta'\right)^2\left\{\int_1^{{}_1^t\lambda^{ens}(\theta')}D\left(x,\theta'\right)\left(1-\frac{x}{{}_1^t\lambda^{ens}\left(\theta'\right)}\right)dx\right\}\sin^2\left(\theta'\right)d\theta' \qquad (2.46)$$

$$\left(S_{ECM}\right)_{12}=\eta\phi_f\int_{-\pi/2}^{\pi/2}R_1\left(\theta'\right){}_0^1\lambda\left(\theta'\right)^2\left\{\int_1^{{}_1^t\lambda^{ens}(\theta')}D\left(x,\theta'\right)\left(1-\frac{x}{{}_1^t\lambda^{ens}\left(\theta'\right)}\right)dx\right\}\cos\left(\theta'\right)\sin\left(\theta'\right)d\theta'$$

The tissue level strain energy is derived by returning to the fiber stress-strain relation in terms of P-λ (Eq. (2.34)). For analogy, we assume that the fibers are isotropic and we are only interested in the stress along the fiber length. The 1st PK stress in the fiber direction is derived from the strain energy in terms of the principal stretches (Chapter 1.0, Eq. (1.25)) [53]:

$$P_f=\frac{\partial\Psi}{\partial\lambda_f}. \qquad (2.47)$$

We postulate the following fiber strain energy relation:

$$\Psi_f=\frac{\eta}{2}\left[\lambda_f-\lambda_s\right]^2. \qquad (2.48)$$

The ECM strain energy is now given by:

$$\begin{aligned}{}_1\Psi_{ECM}&=\int_{-\pi/2}^{\pi/2}R\left(\theta'\right){}_0^1\lambda\left(\theta'\right)^2\Psi_{col}^{ens}\left({}_1^t\lambda^{ens}\left(\theta'\right)\right)d\theta'\\&=\frac{K}{2}\int_{-\pi/2}^{\pi/2}R\left(\theta'\right){}_0^1\lambda\left(\theta'\right)^2\left\{\int_1^{{}_1^t\lambda^{ens}(\theta')}D\left(x,\theta'\right)\left[{}_1^t\lambda^{ens}\left(\theta'\right)-x\right]^2dx\right\}d\theta'\end{aligned}. \qquad (2.49)$$

To check that Eq. (2.49) is indeed correct, the 2nd Piola Kirchhoff stress is derived from the strain energy, this time formulated in terms of the Right Cauchy Green tensor **C**, as:

$${}_1^t\mathbf{S}_{ECM}=2\frac{\partial\Psi_{ECM}}{\partial\mathbf{C}}=\int_{-\pi/2}^{\pi/2}R\left(\theta'\right){}_0^1\lambda\left(\theta'\right)^2\frac{\partial\Psi_{col}^{ens}}{\partial\,{}_1^t\lambda^{ens}}\frac{\partial\,{}_1^t\lambda^{ens}}{\partial\mathbf{C}}d\theta' \qquad (2.50)$$

with

$$\frac{\partial\Psi_{col}^{ens}}{\partial\,{}_1^t\lambda^{ens}}=K\left[{}_1^t\lambda^{ens}\left(\theta'\right)-{}_1\lambda_s\right], \qquad (2.51)$$

and

$$\frac{\partial\,{}_1^t\lambda^{ens}}{\partial\mathbf{C}}=\frac{\mathbf{n}\otimes\mathbf{n}}{2\sqrt{\mathbf{n}^T\,{}_1^t\mathbf{C}\mathbf{n}}}=\frac{\mathbf{n}\otimes\mathbf{n}}{2\,{}_1^t\lambda^{ens}}, \qquad (2.52)$$

which is equal to Eq. (2.46).

2.4 CONSTITUTIVE MODEL FOR MUSCLE COMPONENT

For the smooth muscle component, two *a priori* forms of the strain energy density function are defined. The first option assumes a similar form as for collagen, based on fiber families that run at a specific angle, using a continuous bimodal distribution function R_{sm}

$$ {}^{t}_{0}\mathbf{S}_{SM}\left(\mathbf{E}\right)=\int_{-\pi/2}^{\pi/2}R_{SM}\left(\theta\right)s_{SMb}\left(E_{SMb}\left(\theta\right)\right)\mathbf{N}\otimes\mathbf{N}d\theta\,, \tag{2.53} $$

where $E_{SMb}=\mathbf{N}^{T}\,{}^{t}_{0}\mathbf{E}\mathbf{N}$ is the stretch in the smooth muscle fiber bundle (b = bundle). Depending on the SM structure, different forms of the distribution function can be assumed. Based on the available experimental data on SM orientation of UBW, a bimodal distribution is proposed, where the individual distributions R_{SMC} and R_{SML} are each described by a beta distribution and are weighted by a factor γ_{SMC}, similar to the collagen recruitment function (Eq. (2.13)):

$$ R_{SM}\left(\theta\right)=\gamma_{SMC}\cdot R_{SMC}\left(\theta\right)+\left[1-\gamma_{SMC}\right]\cdot R_{SML}\left(\theta\right). \tag{2.54} $$

The second option assumes two discrete orthogonal families of fiber bundles. The model form is derived from the theory for fiber reinforced composites, based on strain invariants (Eqs . (1.29), (1.26) (1.27)). The smooth muscle component is assumed to consist of two families of fibers that do not interact, and hence the strain energy can be described by

$$ \Psi_{SM}=\Psi_{aniso}\left(I_4,I_6\right)=\Psi\left(\lambda_A^2,\lambda_B^2\right)=\Psi_A\left(\lambda_A^2\right)+\Psi_B\left(\lambda_B^2\right), \tag{2.55} $$

where A and B refer to the two fiber families, and λ_A and λ_B are the stretch in fiber family A and B, respectively, defined as (*cf*. Eq. (2.16)):

$$ \begin{aligned} \lambda_A^2&=\mathbf{a}^T\mathbf{C}\mathbf{a}\\ \lambda_B^2&=\mathbf{b}^T\mathbf{C}\mathbf{b} \end{aligned} \tag{2.56} $$

Next, it is assumed that the two fiber families are oriented at $\theta = 0^0$ (C) and 90^0 (L) weighted by a fraction γ_{SMC}, and Greens's strain is used instead of stretch (Eq. (2.15); $E=\tfrac{1}{2}\left(\lambda^2-1\right)$). This gives for the discrete SM stress-strain relation:

$$ {}^{t}_{0}\mathbf{S}_{SM}\left({}^{t}_{0}\mathbf{E}\right)=\sum_{\theta=0,1/2\pi}s_{SMb}\left(E_{SMb}\right)=\gamma_{SMC}\cdot s_{SMC}\left(E_{SMbC}\right)+\left(1-\gamma_{SMC}\right)\cdot s_{SML}\left(E_{SMbL}\right) \tag{2.57} $$

Under biaxial loading and assuming no shear it holds that $E_{SMbC} = E_{11}$, and $E_{SMbL} = E_{22}$. For both model options, the exact constitutive equation a phenomenological exponential constitutive equation is assumed for an ensemble of SM fibers following Eq. (2.4):

$$s_{SMb}\left(E_{SMb}\right) = d_1 \cdot \left[\exp\left(d_2 \cdot E_{SMb}\right) - 1\right] \tag{2.58}$$

These two options, *i.e.*, the model with a continuous distribution or with a discrete distribution, are explored and compared in Chapter 7.0 (*cf.* [12]).

2.5 SUMMARY

An overview of the relevant equations and their interrelations is given in Figure 2.6 and Appendix A. The tissue level constitutive equation is built up from a combination of an ECM and an SM constitutive equation. The ECM constitutive equation is described in terms of a fiber distribution function and a constitutive equation for a fiber ensemble, and the fiber ensemble is described by a fiber recruitment function in combination with a fiber constitutive model. All equations are defined in Ω_1, but model parameters are defined in Ω_0. The smooth muscle constitutive equation is defined in terms of a continuous distribution function or a discrete number of fiber families. All relevant equations are also repeated below.

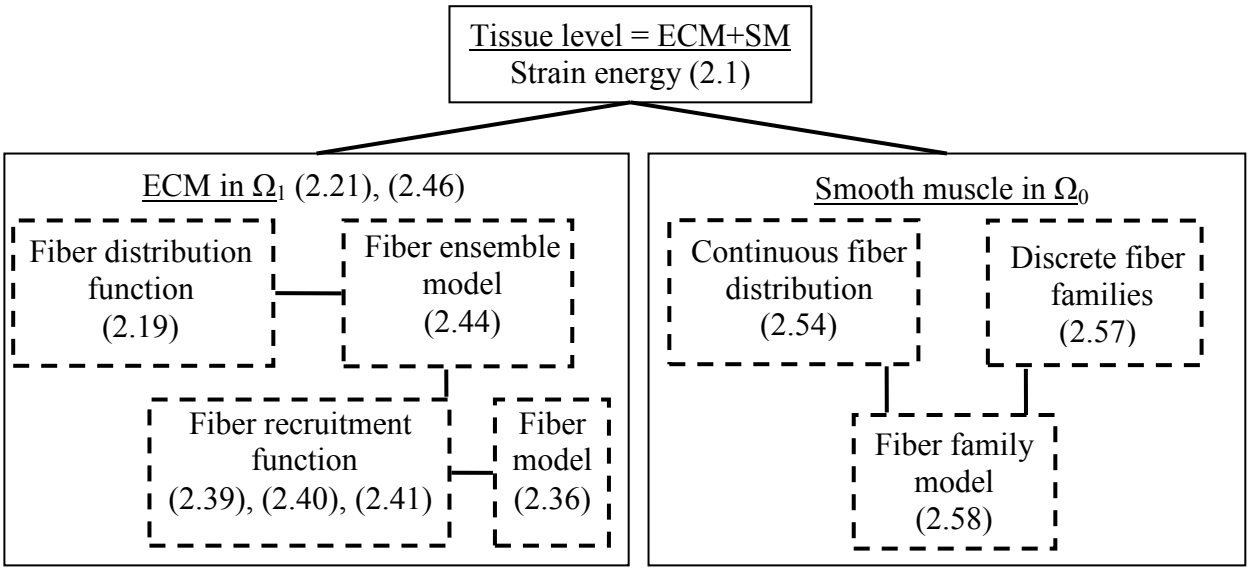

Figure 2.6. Schematic overview of the interrelations of the components of the multi-phase structural constitutive model. The numbers refer to the equations, as summarized below.

$$\Psi(\mathbf{E}) = \sum_i \phi_i \Psi(\mathbf{E}) = \phi_{ECM} \Psi_{ECM}(\mathbf{E}) + \phi_{SM} \Psi_{SM}(\mathbf{E}). \tag{2.1}$$

$$\mathbf{S}(\mathbf{E}) = \frac{\partial \Psi(\mathbf{E})}{\partial \mathbf{E}} = \phi_{ECM} \mathbf{S}_{ECM}(\mathbf{E}) + \phi_{SM} \mathbf{S}_{SM}(\mathbf{E}), \tag{2.2}$$

$${}_1^t\mathbf{S}_{ECM}\left({}_1^t\mathbf{E}\right) = \int_{-\pi/2}^{\pi/2} R'(\theta')\, S_{col}^{ens}\left({}_1^tE^{ens}(\theta')\right)\mathbf{n}\otimes\mathbf{n}d\theta' \tag{2.21}$$

$$R_1(\theta') = R_0\left[\theta\left(\theta', {}_0^1\mathbf{F}\right)\right]\frac{\mathbf{N}^T\left[\theta\left(\theta', {}_0^1\mathbf{F}\right)\right]{}_0^1\mathbf{F}^T\,{}_0^1\mathbf{F}\;\mathbf{N}\left[\theta\left(\theta', {}_0^1\mathbf{F}\right)\right]}{{}_0^1J} \tag{2.19}$$

$${}_1^tS^{ens}\left({}_1^t\lambda^{ens}\right) = \eta\phi_f\,{}_0^1\lambda^2\int_1^{{}_1^t\lambda^{ens}} D_1(x)\left(1-\frac{x}{{}_1^t\lambda^{ens}}\right)dx \tag{2.44}$$

$$D_1\left({}_1\lambda_s, \theta', \mu, \sigma\right) = \begin{cases} \dfrac{B(y, s_1, s_2)}{{}_1\lambda_{\text{ub}}\left(\theta\left(\theta', {}_0^1\mathbf{F}\right)\right) - {}_1\lambda_{\text{lb}}\left(\theta\left(\theta', {}_0^1\mathbf{F}\right)\right)} & {}_1\lambda_{lb} \le {}_1^t\lambda_s \le {}_1\lambda_{ub} \\ 0 & \text{otherwise} \end{cases} \tag{2.39}$$

$${}_1\lambda_{\text{lb}} = \frac{{}_0\lambda_{\text{lb}}}{{}_0^1\lambda_{\text{ens}}\left(\theta\left(\theta', {}_0^1\mathbf{F}\right)\right)}, \quad {}_1\lambda_{\text{ub}} = \frac{{}_0\lambda_{\text{ub}}}{{}_0^1\lambda_{\text{ens}}\left(\theta\left(\theta', {}_0^1\mathbf{F}\right)\right)} \tag{2.40}$$

$$y\left({}_1\lambda_{\text{s}}\right) = \frac{{}_1\lambda_{\text{s}}(\theta') - {}_1\lambda_{\text{lb}}\left(\theta\left(\theta', {}_0^1\mathbf{F}\right)\right)}{{}_1\lambda_{\text{ub}}\left(\theta\left(\theta', {}_0^1\mathbf{F}\right)\right) - {}_1\lambda_{\text{lb}}\left(\theta\left(\theta', {}_0^1\mathbf{F}\right)\right)} \tag{2.41}$$

$$S = \frac{P}{\lambda} = \frac{\eta}{\lambda}\left[\lambda - \lambda_s\right] = \eta\cdot\left[1-\frac{\lambda_s}{\lambda}\right] \tag{2.36}$$

$${}_0^t\mathbf{S}_{SM}(\mathbf{E}) = \int_{-\pi/2}^{\pi/2} R_{SM}(\theta)\, s_{SMb}\left(E_{SMb}(\theta)\right)\mathbf{N}\otimes\mathbf{N}d\theta \tag{2.53}$$

$$R_{SM}(\theta) = \gamma_{SMC}\cdot R_{SMC}(\theta) + \left[1-\gamma_{SMC}\right]\cdot R_{SML}(\theta) \tag{2.54}$$

$${}_0^t\mathbf{S}_{SM}\left({}_0^t\mathbf{E}\right) = \gamma_{SM}\cdot s_{SMbC}\left(E_{SMbC}\right) + \left(1-\gamma_{SM}\right)\cdot s_{SML}\left(E_{SMbL}\right) \tag{2.57}$$

$$s_{SMb}\left(E_{SMb}\right) = d_1\cdot\left[\exp\left(d_2\cdot E_{SMb}\right)-1\right] \tag{2.58}$$

3.0 MODEL IMPLEMENTATION, MODEL VALIDATION, AND METHODS OF PARAMETER ESTIMATION

The model equations of Chapter 2.0 were implemented in MATLAB (MathWorks Inc.; v.7.6.0 R2008a for the first study and v.7.8.0 R2009a for the later studies) through a series of function files, which are called from script files or from a graphical user interface (GUI), in order to calculate model stress values and perform parameter estimation. Each separate component of the model is implemented in an individual function file. The function files are called to calculate model values when parameters are known and are called by the fitting routines to determine parameter values. In addition, function files are utilized for data manipulation such as extracting individual protocol data. All components are set up in a modular fashion. The ensemble model and the structural model, which includes the ensemble model, are each implemented through a separate series of function files.

This chapter describes the implementation of the structural model (section 3.1) and the implementation of the parameter estimation procedures (section 3.2) in MATLAB. Built-in algorithms are used for numerical integration and parameter estimation. Section 3.1 first provides background information on the specific MATLAB solvers and algorithms for numerical integration, followed by validation of the model modifications and the model implementation, using synthetic data. Section 3.2 provides background information on parameter estimation and on the specific MATLAB solvers and algorithms for parameter estimation, followed by the description of the actual fitting methods. The fitting procedure is implemented in two GUIs in order to provide full control over the data, fitting settings, and fitting output, including data inspection, choices of model type and algorithms, setting parameter bound values, calculating model values, etc. Two separate GUIs are developed; one for fitting the fiber ensemble model to equibiaxial strain data and one for fitting the complete structural model to multi-protocol biaxial mechanical data. This chapter is concluded with a summary (section 3.3).

3.1 MODEL IMPLEMENTATION AND VALIDATION

3.1.1 MATLAB numerical integration functions

The integrals in both the ensemble model and the tissue-level structural model were calculated using numerical integration techniques, also referred to as numerical quadrature. In general, if a function is smooth and well-behaved and the limits of integration are bounded, there are many methods of approximating the integral with arbitrary precision. In numerical integration, the integrand is evaluated at a finite set of integration points, and a weighted sum of these values is used to approximate the integral. The specific integration points and weights depend on the specific algorithm used, and in adaptive algorithms, these are adapted along the curve. The two MATLAB algorithms used in the current dissertation were "*quadl*" and "*quad*", which were both adaptive quadrature algorithms. Quadl uses recursive adaptive Lobatto quadrature and is an efficient algorithm for smooth integrands, at high accuracies. Quad uses adaptive Simpson quadrature and is most efficient for low accuracies with non-smooth integrands. Quadl was initially used for the first study. However, the possible non-smooth behavior of the beta function made quad the preferred method of integration. Detailed information for each function can be found in MATLAB's documentation.

3.1.2 Validation of fiber model

The usefulness of the fiber model modification, where the fiber is assumed linear in terms of 1st Piola Kirchhoff stress – stretch (P-λ) instead of in terms of 2nd Piola Kirchhoff stress – Green's strain (S-E), was demonstrated with some simple calculations. In the rest of this chapter, the former fiber model will be referred to as "S-E linear fiber model", and the latter as "P-λ linear fiber model". A single fiber, with a modulus η = 100, was stretched to a maximum stretch λ = 1.25. The stress-strain behavior (both S-E and P-λ) of the fiber, as well as the slope of the stress-strain curves, were investigated with and without the presence of slack in the fiber (see for the description of slack, section 2.1), for both fiber models.

A fiber that is linear in S-E, without slack, exhibited a nonlinear behavior in terms of P-λ, and the slope of the S-E curve equaled the fiber modulus at all strain values (Figure 3.1). When

slack was introduced in the fiber (slack stretch $\lambda_s = 1.15$), the slope of the *S*-*E* curve did not equal the fiber modulus (Figure 3.2). A fiber that is linear in *P*-λ exhibited moderate nonlinear behavior in terms of *S*-*E*, and the slope of the *P*-λ curve equaled the fiber modulus at all strain values (Figure 3.3). These characteristics were preserved when slack was introduced in the fiber (Figure 3.4).

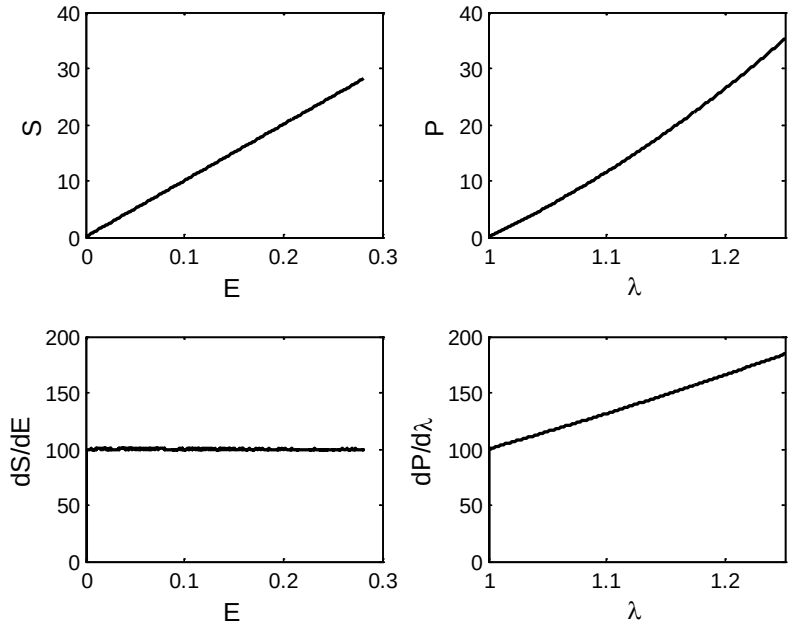

Figure 3.1. Stress-strain behavior of a single straight fiber, with a linear material model in terms of in *S*-*E* (η =100). A linear *S*-*E* relation with slope equal to 100 (left panels) results in a nonlinear *P*-λ relation (right panels).

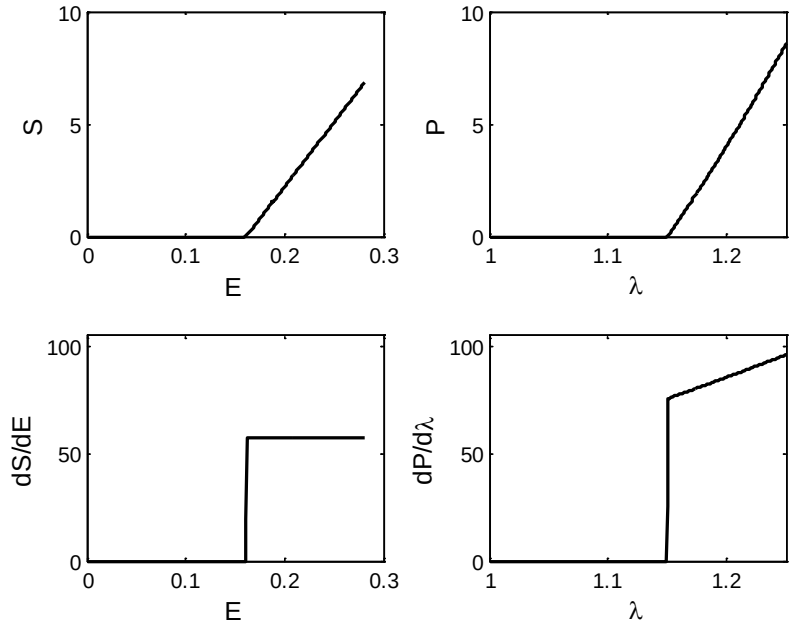

Figure 3.2. Stress-strain behavior of a fiber with slack, with a linear material model in terms of in *S*-*E* (η =100). A linear *S*-*E* relation after a slack stretch λ_s = 1.15, exhibits a slope *un*equal to 100 (left panels). Right panels depict the corresponding nonlinear *P*-λ relation and its slope.

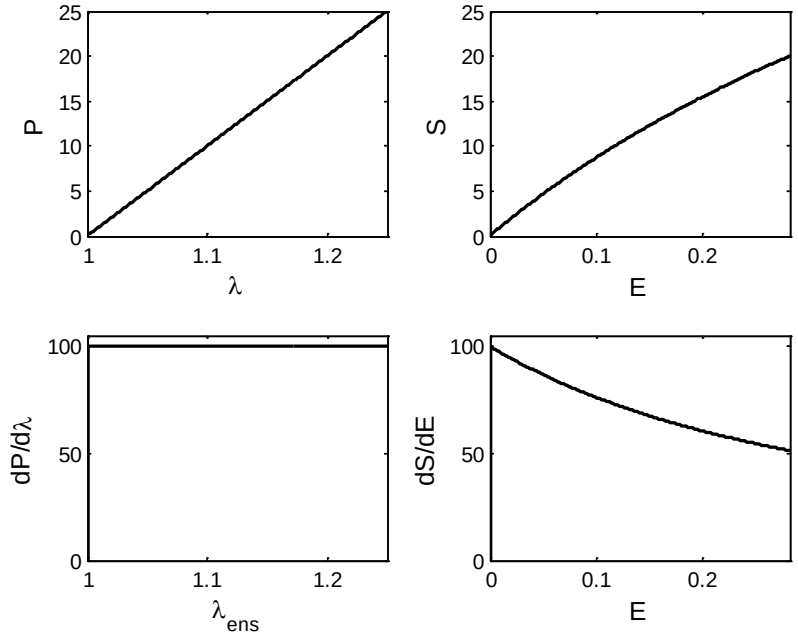

Figure 3.3. Stress-strain behavior of a single fiber exhibiting a linear material model in terms of *P*-λ (η =100). Left panels depict a linear *P*-λ relation with slope equal to 100, and right panels depict the corresponding *S*-*E* relation and its slope.

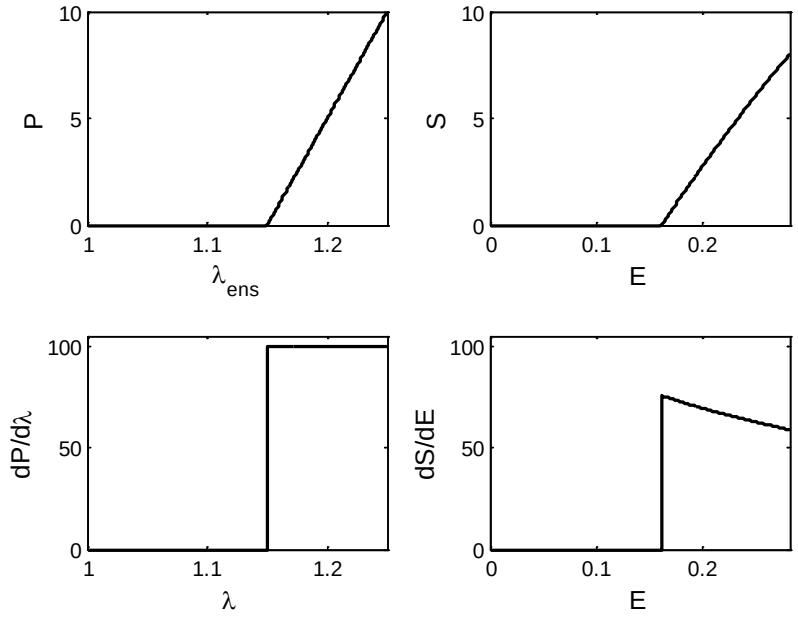

Figure 3.4. Stress-strain behavior of a fiber with slack exhibiting a linear material model in terms of P-λ (η =100). The slope of the P-λ curve after a slack stretch of 1.15 is equal to the fiber modulus.

3.1.3 Validation of fiber model at the ensemble level

At the level of the fiber ensemble, a distribution of slack stretches is assumed (through the distribution function $D(E_s)$ or $D(\lambda_s)$), and hence the above fiber level results should be extrapolated to the ensemble level. For the liner *S*-*E* fiber model, it is shown that the larger the slack strain, the more pronounced the scaling effect (Figure 3.5). This implies that each fiber in a fiber ensemble would have a different modulus η, and the maximum tangent modulus (MTM) of the fiber ensemble stress-strain curve (S^{ens}-E^{ens}) will not equal the effective fiber modulus. This scaling effect is due to the fact that each fiber is referenced to its own fiber reference length. This effect is illustrated at the ensemble level by analyzing the tangent modulus of S^{ens}-E^{ens} and P^{ens}-λ^{ens} curves (with $\phi_f \cdot \eta$=1000), for the two models respectively, for different recruitment functions (Figure 3.6). For the linear *P*-λ fiber model where the fibers are referenced to the same ensemble length, MTM equals the value of $\phi_f \cdot \eta$. Each fiber in the ensemble is characterized by the same modulus η, even with a distribution of slack lengths.

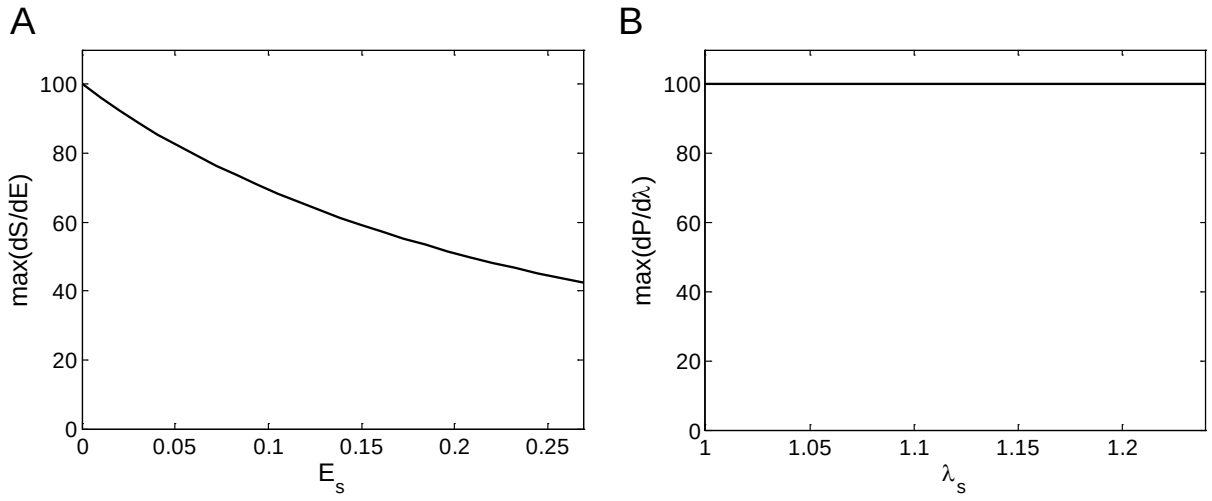

Figure 3.5. Maximum slope of the fiber stress-strain curve for different slack stretches.
A) Maximum slope of the *S*-*E* curve for different slack strains, with the linear *S*-*E* fiber model (η =100). Compare to Figure 3.2. B) Slope of the *P*-λ curve for different slack stretches, with the linear *P*-λ fiber model (η =100). The slope equals the fiber modulus (η =100). Compare to Figure 3.4.

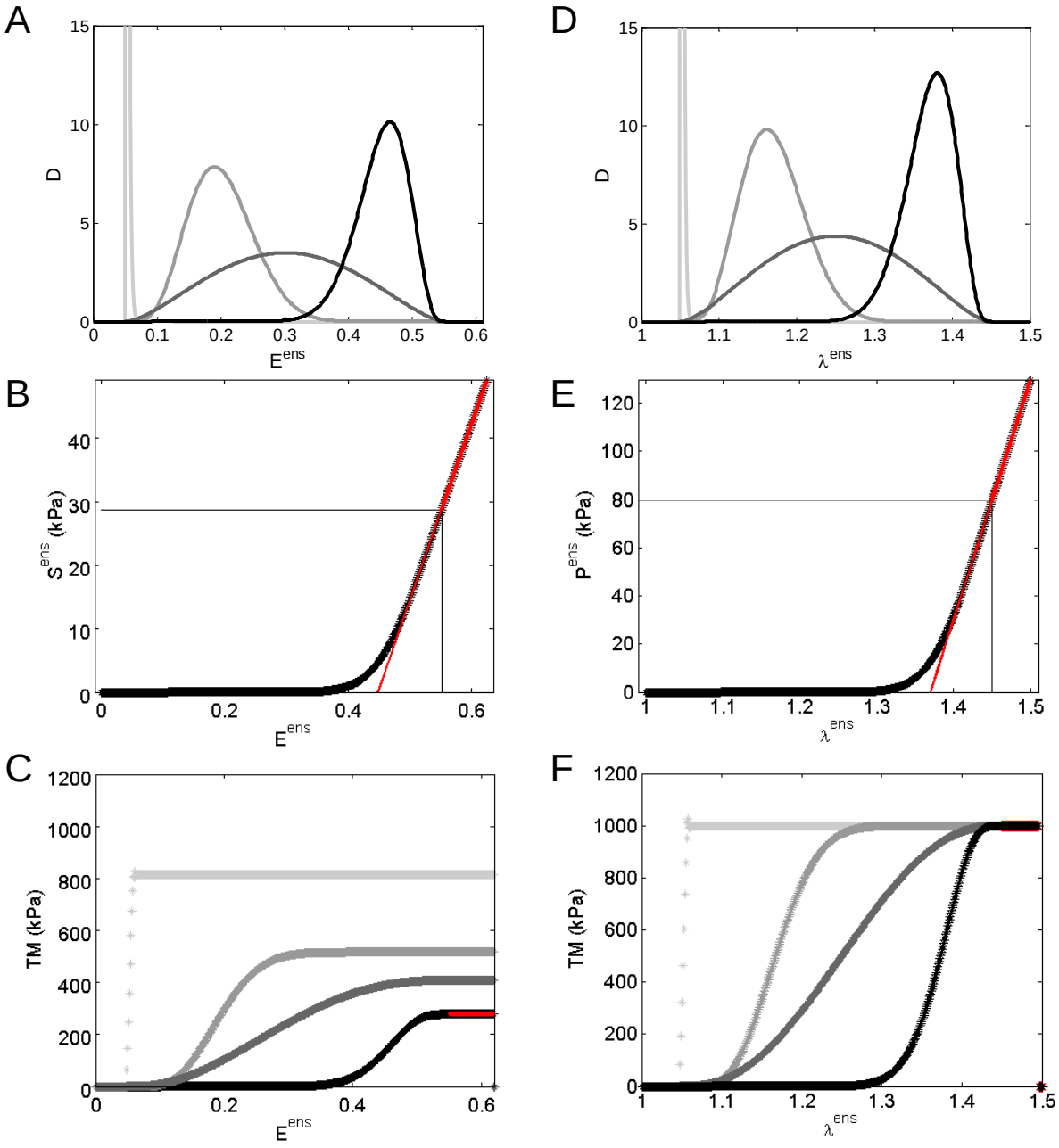

Figure 3.6. Ensemble behavior for different recruitment functions for both fiber models. Panel A-C represent the linear *S*-*E* fiber model; Panel D-F the linear *P*-λ fiber model. A-D) Recruitment functions with different values for the mean and standard deviation. B-E) The fiber ensemble response for one of the recruitment functions (black line). C-F) Tangent modulus (TM) calculations of the fiber ensemble response for each recruitment function. The linear *S*-*E* fiber model does not produce a MTM value of 1000, whereas the linear *P*-λ does.

3.1.4 Discrete fiber simulations

To test the implementation of both model modifications in MATLAB, *i.e.* the permanent set (section 2.2) and the *P*-λ linear fiber model (section 2.3), an objective data set was needed. This data was created by simulating the behavior of a set of discrete fibers under loading, which was implemented in the software package Mathcad (PTC, USA). First, a single set of circular fibers, 1 μm in diameter, imbedded in a tissue specimen of dimensions 10x10x1 mm, was simulated. The mechanical behavior of the individual fibers followed one of the two fiber models (*P*-λ linear fiber model and *S*-*E* linear fiber model), with a given slack stretch and/or a permanent set deformation. The tissue specimen was subjected to a defined uniaxial deformation. From this, the resulting forces in the individual fibers were calculated and summed up over the total number of fibers. This force was distributed over the specimen area, which gave the total stress (1st and 2nd Piola Kirchhoff stress) in the specimen composed of one fiber ensemble.

Next, a continuous fiber distribution was defined by a beta function with a given mean (μ_R) and standard deviation (σ_R), and a discrete set of fiber ensembles was created with a sufficient number of fiber ensembles and number of fibers per fiber ensemble, to match the continuous fiber distribution. The fiber ends were sorted and defined per specimen edge to distribute the fiber ensembles over angle θ. A total of 361 fiber ensembles was created, with 149,350 fibers per fiber ensemble. Subsequently, the tissue specimen that was defined by these fibers was subjected to a defined biaxial loading protocol, either in- or excluding a permanent set deformation. The forces in the fibers were translated into tissue-level stresses, and thus, the biaxial stress-strain behavior was simulated.

In these simulations, for simplicity, all fibers were assumed to be recruited at the same slack length, which is effectively the same as the single fiber description in section 3.1.2, and hence no fiber recruitment distribution function was included in the formulation. The simulations were created with increasing level of complexity, starting from a distributed set of fiber ensembles consisting of all straight fibers without slack and building up to fiber ensembles with slack and a permanent set effect subjected to shear loading. Table 3.1 gives an overview of the different tissue-level discrete fiber simulations (*i.e.*, with a distributed set of fiber ensembles). The standard deviation of the fiber distribution function ($R(\theta)$) equaled 15 deg (σ_R=15^o) and the fiber effective modulus equaled 1000 kPa (K=1000). The stress-strain output of these simulations

was used as data input for the fitting program to validate the implementation in MATLAB. The continuous model excluding a fiber recruitment function (compare to Eq. (2.32)) and with the *S-E* linear fiber model, is defined in terms of **S** as follows

$$\mathbf{S} = \eta \int_{-\pi/2}^{\pi/2} R_1(\theta') \frac{{}_1^t E^{ens}(\theta') - {}_1 E_s^{ens}(\theta')}{\left[1 + 2\,{}_1^t E_s^{ens}(\theta')\right]^2} \mathbf{n}(\theta') \otimes \mathbf{n}(\theta') d\theta', \tag{3.1}$$

and the model with the *P-λ* linear fiber model is defined in terms of **P** as

$$\mathbf{P} = \eta \int_{-\pi/2}^{\pi/2} R_1(\theta') \left[{}_1^t \lambda^{ens}(\theta') - {}_1 \lambda_s^{ens}(\theta') \right] \mathbf{n}(\theta') \otimes \mathbf{n}(\theta') d\theta'. \tag{3.2}$$

${}_1 E_s^{ens}(\theta')$ and ${}_1 \lambda_s^{ens}(\theta')$ are calculated from the given model parameters ${}_0 E_s^{ens}$ or ${}_0 \lambda_s^{ens}$, and ${}_0^1\mathbf{F}$, following Eqs. (2.23) and (2.24). When there is no permanent set (${}_0^1\mathbf{F} = \mathbf{I}$), it holds that θ'=θ and $\mathbf{n}(\theta') = \mathbf{N}(\theta)$, and all strain and stress terms referred to Ω_1 are equal to the same terms expressed in Ω_0. In the fitting process, the artificial data was scaled with a factor 1000 to decrease the calculation and fitting times.

Table 3.1. Overview of settings discrete fiber simulations.

sim.	fiber		F01					maxU1t			
no.	model	λs	descr.	11	12	21	22	descr.	11	12	22
1	S-E	0	none	1	0	0	1	equibiaxial	2	0	2
2		1.5	none	1	0	0	1	equibiaxial	2	0	2
3		1.5	equibiaxial	1	0	0	1	equibiaxial	2	0	2
4		1.5	unequal	1.2	0	0	1	equibiaxial	2	0	2
5		1.5	unequal	1.2	0	0	1	shear	2	0.1	2
6		1.5	shear	1.2	0.10	0.00	1	shear	2	0.1	2
7		1.5	shear	1.2	0.15	0.15	1	shear	2	0.15	2
8	P-λ	1	none	1	0	0	1	equibiaxial	2	0	2
9		1.5	none	1	0	0	1	equibiaxial	2	0	2
10		1.5	equibiaxial	1.1	0	0	1.1	equibiaxial	2	0	2
11		1.5	unequal	1.4	0	0	1.1	equibiaxial	2	0	2

Simulation 1 (Table 3.1) produced linear *S*-*E* curves, and the slope of the fiber ensemble stress-strain curve (S^{ens}-E^{ens}) equaled the value of *K*, as expected. A fiber relation that was linear in *S*-*E* produced a moderate nonlinearity in the *P*-λ curves as was also described above. Introducing a slack stretch in the fiber relation (simulation 2) produced a S^{ens}-E^{ens} relation with a slope that was lower than the value of *K*. This is an indication that in the complete model with a distribution of slack stretches, the MTM of the S^{ens}-E^{ens} curve can only be an indication of *K*, and MTM does not equal *K*. Adding a permanent set had the same effect on the S^{ens}-E^{ens} curve (simulations 3,4). An equibiaxial permanent set had no effect on $R(\theta)$-$R(\theta')$, as expected, and a permanent set with unequal components (simulations 5-7) resulted in a shift of $R(\theta')$ with respect to $R(\theta)$. The results of simulation 7 are depicted in Figure 3.7. The results of all simulations are depicted in Appendix C.

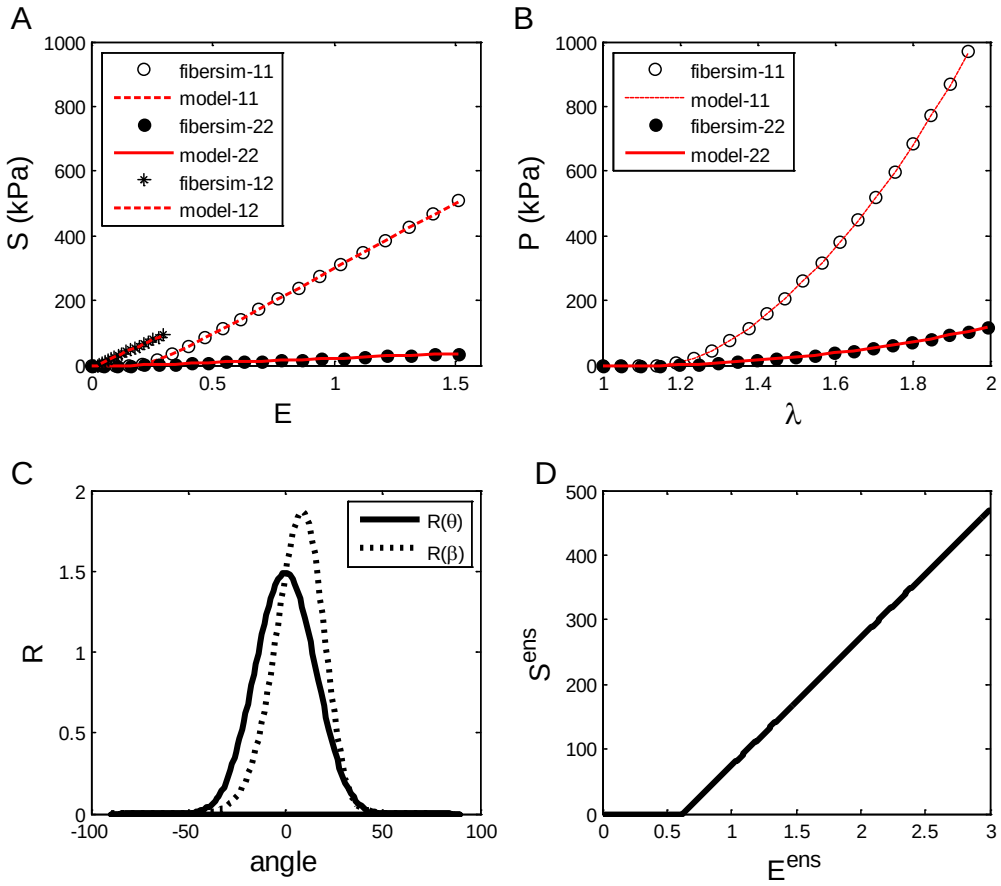

Figure 3.7. Comparison of model stress calculations with results of discrete fiber simulation 7 (Table 3.1). A) 2nd Piola Kirchhoff Stress vs. Green's strain for all three components. B) 1st Piola Kirchhoff Stress vs. stretch for the 11 and 22 components. C) Fiber distribution function in Ω_0 and Ω_1. D) Fiber ensemble stress vs. fiber ensemble strain. See also Figure C4.

Simulation 8, with a linear P-λ fiber model, produced linear P-λ curves, and the slope of the fiber ensemble stress-stretch curve (P^{ens}-λ^{ens}) equaled the value of K. This statement also held when slack was introduced in the fiber (simulation 9), in contrast to the linear S-E fiber model. However, when a permanent set was added (simulations 10 and 11), MTM did not equal K. In fact, the permanent set induced a defined scaling effect. For an equibiaxial permanent set, MTM and K ($K = \phi_f \eta$, Eq. (2.8)) are related as:

$$K = \frac{MTM}{{}^{1}_{0}\lambda_{ens}}. \tag{3.3}$$

When a permanent set is not equibiaxial, ${}^{1}_{0}\lambda_{ens}$ is a function of angle, and K can be derived from Eq. (3.3) if ${}^{1}_{0}\lambda_{ens}$ is replaced by the maximum value of ${}^{1}_{0}\lambda_{ens}(\theta)$. The results of simulation 11 are presented in Figure 3.8 A,B. For this specific simulation, the fiber stresses were also calculated with respect to Ω_0, using the model without permanent set.

3.1.5 Synthetic data

The implementation of the two model modifications was also tested with a set of synthetic data. A theoretical sample with dimensions 10x10x0.2mm in Ω_0 was subjected to a permanent set deformation ${}^{1}_{0}\mathbf{F}$ followed by a loading defined by an equibiaxial strain path (in Ω_1, no shear). The dimensions of the sample in Ω_0 were calculated from ${}^{1}_{0}\mathbf{F}$ and the dimensions in Ω_1. First Piola Kirchhoff stresses in Ω_1 were calculated for a defined equibiaxial strain path in Ω_1 (no shear) using the model equations. Forces were calculated from these stress values for corrected sample dimensions in Ω_1. These forces were used to calculate stresses in Ω_0, which were compared to stress values calculated using the model equations without permanent set. This validation was performed for both fiber models, but only the results of the P-λ fiber model are presented here, since this is the model of interest.

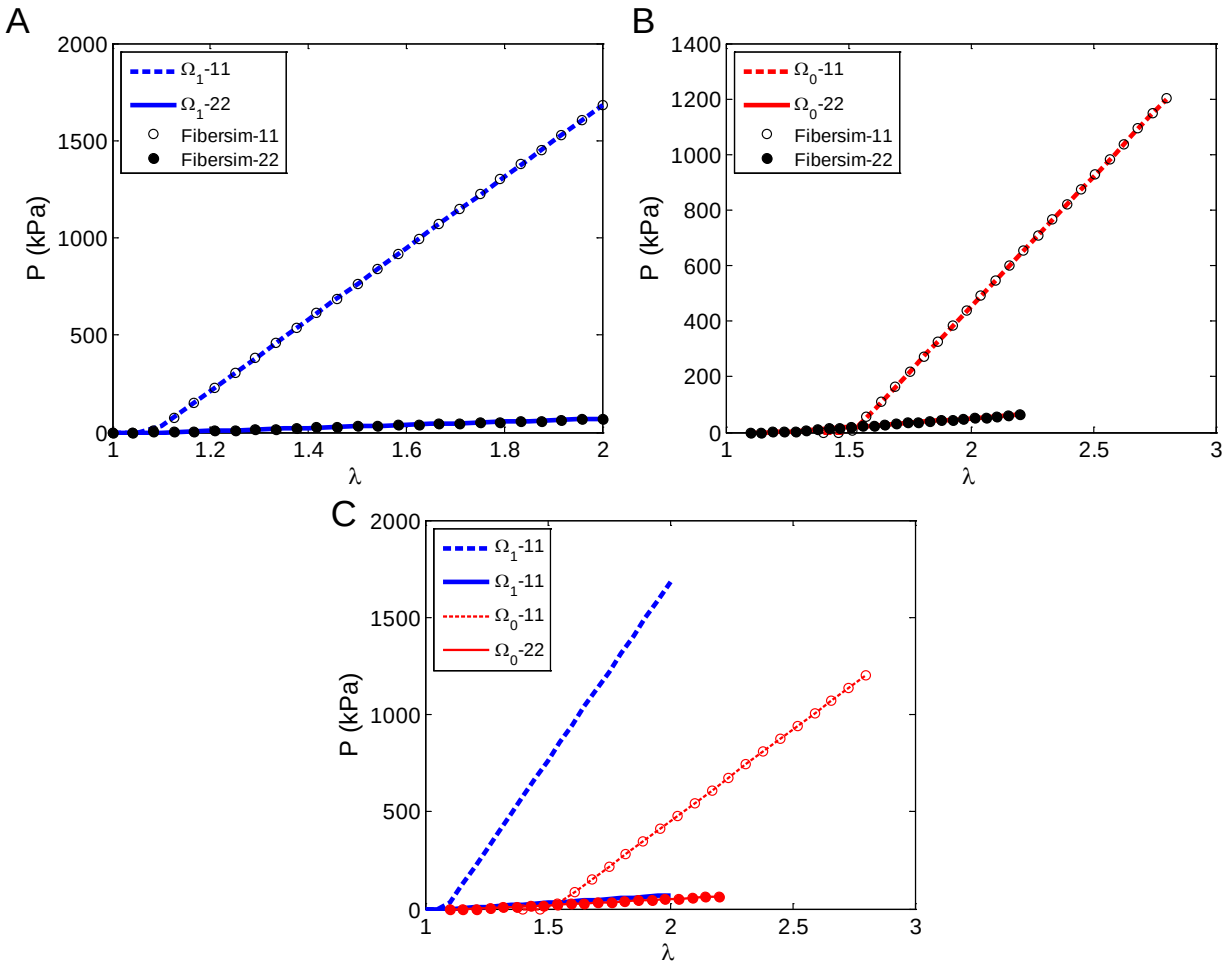

Figure 3.8. Validation of the model implementation without recruitment.
A) Comparison of the stress calculations in Ω_1 using the modified model, with the discrete fiber simulation output of simulation 11 (Table 3.1). B) Comparison of the stress calculations in Ω_0 using the modified model, with the discrete fiber simulation output of simulation 11. C) Comparison of model calculations in Ω_1 with model calculations in Ω_0. The blue and red lines are the same lines as in panel A and B, respectively. Red open and closed symbols represent the stresses in Ω_0 calculated from the forces, which were in turn calculated from the stresses in Ω_1. Red lines represent the stress calculations in Ω_0 using the model without permanent set.

First, the formulation of the model without recruitment as used for the synthetic fiber calculations was validated, using the settings of simulation 11 (Table 3.1). As mentioned in the previous section, the model stress calculations in Ω_1, as well as the model stress calculations in Ω_0, matched the stresses from the discrete fiber simulations (Figure 3.8 A,B). Stress values in Ω_0 calculated from the forces (red circles in Figure 3.8 C) were equal to the model stress values calculated by the unmodified model (red lines in Figure 3.8 C).

The same comparison was performed for the complete model formulation including recruitment (represented by a beta distribution function) for different settings. First, a virtual specimen was subjected to the same permanent set and equibiaxial loading with the following recruitment parameters: μ=0.75, σ=0.15, ${}_0\lambda_{\text{lb}}$=1.5, ${}_0\lambda_{\text{ub}}$=2 (Figure 3.9 A). Second, the same set of parameters was combined with a broader fiber distribution (σ_R=40^o) (Figure 3.9 B). Lastly, permanent set and loading conditions similar to the experimental data on UBW ECM were utilized, *i.e.*, ${}_0^1\mathbf{F} = \left[1.6\ 0; 0\ 2\right]$, maximum loading was ${}_1^t\mathbf{F} = \left[1.15\ 0; 0\ 1.15\right]$, ${}_0\lambda_{\text{lb}}$=1.8, ${}_0\lambda_{\text{ub}}$=2.1, σ_R=20^o, K=15,000 (Figure 3.9 C).

This set of parameters was used to explore the behavior of ${}_0^1\lambda^{ens} = \mathbf{N}(\theta)^T\ {}_0^1\mathbf{F}\mathbf{N}(\theta)$, as a function of angle θ (Figure 3.10 A). The model assumptions (section 2.2) stated that ${}_0\lambda_{lb} \geq {}_0^1\lambda^{ens}(\theta)$ for all values of θ. However, considering $R(\theta)$ with a preferred orientation around θ=0, the fibers are not evenly distributed over all angles, and the model requirement ${}_0\lambda_{lb} \geq {}_0^1\lambda^{ens}(\theta)$ can be relaxed. It could be shown that for σ_{R}=20^o, 95% of the fibers were oriented between a cutoff value θ_{cutoff} = +/-38 ($\int_{-\theta_{cutoff}}^{-\theta_{cutoff}} R(\theta)\,d\theta = 0.95$) (red dashed lines in Figure 3.10 A), and it can be stated that ${}_0\lambda_{lb} \geq {}_0^1\lambda^{ens}\left(\theta_{cutoff}\right)$ instead of the strict model requirement ${}_0\lambda_{lb} \geq \max\left({}_0^1\lambda^{ens}(\theta)\right)$. The chosen value of ${}_0\lambda_{\text{lb}}$=1.8 complied with that. Because of the angular dependency of ${}_0^1\lambda^{ens}$, ${}_1\lambda_{\text{lb}}$ and ${}_0\lambda_{\text{ub}}$ are also a function of angle, and hence, the recruitment function in Ω_1 is a function of angle (Figure 3.10 B). Figure 3.10 B shows D_1 for θ=0^o and θ=45^o.

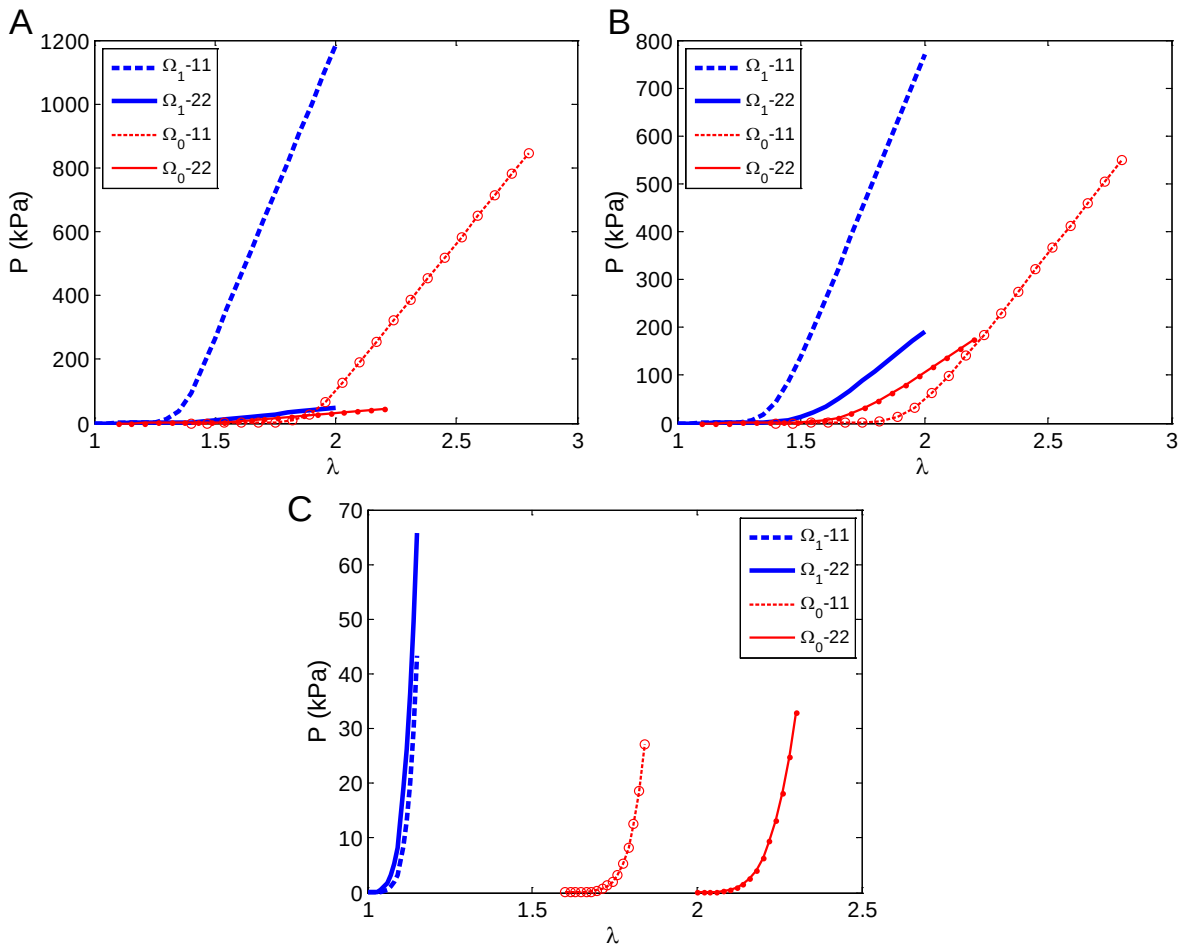

Figure 3.9. Validation of the model implementation with beta recruitment for different loading regimes. Comparison of model calculations in Ω_1 with model calculations in Ω_0. Red open and closed symbols represent the stresses in Ω_0 calculated from the forces, which were in turn calculated from the stresses in Ω_1. Red lines represent the stress calculations in Ω_0 using the model without permanent set. A) Permanent set values and equibiaxial loading regime of Figure 3.8. B) Same recruitment parameters and loading as A, with a broader fiber distribution of σ_R=40°. C) Permanent set and loading conditions similar to the experimental data on UBW ECM.

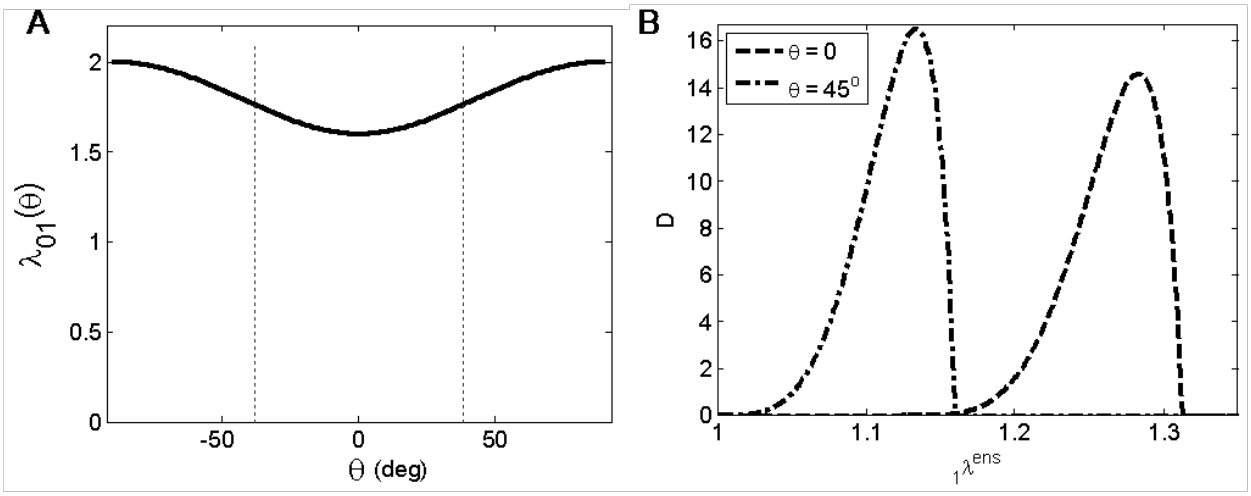

Figure 3.10. Angular dependence of the ensemble permanent set stretch and its effect on the recruitment function. A) The ensemble permanent set stretch ${}_0^1\lambda^{ens}$ is a function of angle θ. With $\sigma_R = 20^o$, 95% of the fibers is located between $\theta = -38$ and $\theta = 38^o$, indicated by the red dashed lines. ${}_0^1\lambda^{ens} = 1.75$ at this point. B) Recruitment function D in Ω_1 at two different values of θ.

3.2 PARAMETER ESTIMATION

3.2.1 Background

The process of parameter estimation, also referred to as model or data fitting or simply fitting, aims at determining parameter values for a model in order to recapitulate experimental data as closely as possible. An error function or objective function is minimized, which is usually defined as the sum-of-squared errors between the experimental data values and calculated model values. The lower the value of the objective function, the better the fit. Finding the minimum value of the objective function is an iterative procedure where, after defining a set of initial parameter values, the parameter values are altered in each iteration to minimize the objective function and to eventually reach the optimal set of parameters.

Different algorithms are available, many of which are referred to as gradient-based methods, where the parameter search is performed along the direction of steepest descent taking into account other information such as curvature, depending on the specific algorithm. Gradient-

based methods take advantage of the smooth behavior of the error surface. In general, it can be stated that the closer the initial parameter estimates are to the optimal parameter values, the faster the fitting process, and the more likely it is that the true optimal parameter values are found. When initial parameter estimates are not similar to the optimal parameter values, one risks locating a local minimum when using the gradient-based methods. Additionally, the possibility of finding a local minimum instead of a global minimum increases for highly complex functions and functions with many parameters where the error function does not behave smoothly. The first obvious solution to this problem is to more accurately define initial parameter estimates, but this is not always be feasible. The alternative is to use a different type of approach such as the genetic algorithm. The genetic algorithm uses the survival of the fittest concept taken from evolution theories. A group of parameters sets is maintained instead of just one working solution set, and based on how well each set fits the data, it is either used to produce better candidate solutions or discarded.

Many of these algorithms have been implemented in software packages such as MATLAB, and in more recent years and in more recent releases of MATLAB, more sophisticated algorithms have become available, and the implementations itself have become more sophisticated. In this chapter, three different constrained minimization algorithms, readily available in MATLAB, are described that were implemented for the specific biaxial mechanical stress-strain data used in this dissertation and eventually integrated in a MATLAB GUI. The next section (section 3.2.2) describes the three specific MATLAB algorithms that were implemented. Only one of these algorithms was used for the parameter estimation performed for this dissertation. The constrained minimization algorithm “fmincon” was chosen because it allowed for application of nonlinear constraints on the parameters, which was required to constrain the shape of the beta distribution functions (see below, section 3.2.2). Possible problems with local minima were avoided by carefully choosing initial parameter estimates derived from specific knowledge of the experimental data and inspecting two-dimensional error surfaces for specific sets of parameter values. This allowed for a carefully guided step-wise fitting process, which was contrary to “brute-force” fitting.

3.2.2 MATLAB parameter estimation functions

The complete structural constitutive model (Chapter 2.0) is highly nonlinear because of the recruitment and distribution functions. This highly nonlinear model required a nonlinear parameter optimization or curve fitting algorithm. The MATLAB function "*lsqcurvefit*" is especially designed for curve fitting purposes of nonlinear functions and is formulated such that it defines the least-squares problem internally, while the user only provides the function. By default, lsqcurvefit uses the (large scale) trust-region-reflective algorithm, which is a subspace trust-region method and is based on the interior-reflective Newton method. Trust-region methods are based on the basic idea to approximate the function f with a simpler function g, which reasonably reflects the behavior of function f in a neighborhood around the point x. This neighborhood is the trust region. This algorithm allows the user to define bounds on the parameters and hence perform constrained optimization. Lsqcurvefit also has to option to use the Levenberg-Marquardt method, but this method does not allow bounds on the parameters. Lsqcurvefit also does not allow nonlinear (in)equality constraints on the parameters, which are needed for the beta recruitment function. Note also, that the trust-region-reflective method does not allow equal upper and lower bounds.

Another MATLAB algorithm for constrained minimization that does allow nonlinear (in)equality constraints on the parameters is "*fmincon*". Fmincon is a gradient-based method that is designed to work on problems where the objective and constraint functions are both continuous and have continuous first derivatives. For curve-fitting purposes, fmincon requires the user to define the function to be optimized in terms of a least-squares formulation. Fmincon has the option to use three algorithms. These algorithms are the trust-region-reflective algorithm, the active-set algorithm, and the interior-point algorithm. The trust-region-reflective algorithm is the default algorithm, but this requires the user to explicitly define the gradient as part of the objective function and it does not allow inequality constraints. If the gradient is not provided and inequality constraints are defined in the problem, the (medium-scale) active-set algorithm is chosen. This algorithm uses the sequential quadratic programming method. At each major iteration, three steps are performed. First, an approximation is made of the Hessian of the Lagrangian function using a quasi-Newton updating method. This is then used to generate a quadratic programming sub-problem. The solution of this problem is used to form a search

direction for the Quasi-Newton line-search procedure. The genetic algorithm (GA) was also implemented in the GUI described below but was not used in the current study. Detailed information for each function can be found in MATLAB's documentation.

3.2.3 Parameter estimation components for ensemble model

Data inspection and using information from the data. If biaxial mechanical data from an equibiaxial strain protocol is available, it can be used to determine parameters of the ensemble model separately. Data from the equibiaxial strain protocol was loaded and graphically inspected. Under equi-biaxial strain conditions, E_{11} equals E_{22}, and zero shear is assumed (E_{12}=0). Because of the symmetry of $R(\theta)$ and the fact that the fiber recruitment function ($D(x)$, see Chapter 2.0) does not depend on θ, the fiber ensemble stress-strain relationship could be obtained directly from the experimental data using $S_{ens} = S_{11} + S_{22}$, and $E^{ens}=E_{11}=E_{22}$ [86, 129]. To smooth small differences between the two directions, the fiber ensemble stretch values were calculated as $\lambda^{ens}=0.5*(F_{11}+F_{22})$, and the fiber ensemble strain was derived as $E^{ens}=0.5*(\lambda^{ens2}-1)$.

For each point along the S^{ens}-E^{ens} or P^{ens}-λ^{ens} curve (depending on the model choice, see below), the tangent modulus (TM) was calculated by performing a running linear regression of the curve with a window width determined specifically for each data set, based on visual inspection of the desired result. From this E^{ens}-TM curve, it could be observed that TM would eventually cease to increase with increased stretch. This is the point that all fibers are recruited and the fiber ensemble behaves linear elastically, with a stiffness value equal to the maximum tangent modulus (MTM). The corresponding strain at this point defines the upper bound strain (E_{ub}), and the value of MTM was used as an initial estimate for K. Next, the data sets were thinned to facilitate shorter fitting times, and S^{ens} values were scaled, because K was typically three or more orders of magnitudes larger than the other parameters.

Model choice. As described above and in section 2.1, two different models could be assumed for the fiber ensemble response. First, the choice was made between an exponential model and a structural model with recruitment. For the exponential model, two different forms could be chosen, *i.e.*, a simple exponential form with the two model parameters d_1 and d_2 (Eq. (2.4)) or an exponential form including a linear part, with the three model parameters d_1 and d_2 and E_{ub} (Eq.

(2.5)). For the structural model form, it needed to be decided which fiber relation was used, *i.e.* the linear *S*-*E* fiber model (the "original" model, Eq. (2.7)) or the linear *P*-λ fiber model (the "modified model", Eq. (2.43)). Depending on this choice, MTM was determined from either the S^{ens}-E^{ens} curve or the P^{ens}-λ^{ens} curve, respectively (section 3.2.3). Finally, one must choose between three forms of the recruitment function, *i.e.* exponential, beta distribution, or double beta distribution (Eqs. (2.10), (2.11), and(2.13), respectively). The parameters to be fit for the structural model with exponential recruitment are: K, E_{ub}, a, b, for the model with the unimodal beta recruitment function: K, μ,σ, E_{lb} (or λ_{lb}) and E_{ub} (or λ_{ub}), and for the model with the bimodal recruitment function K, μ_1, σ_1, γ, μ_2, σ_2, E_{lb} (or λ_{lb}) and E_{ub} (or λ_{ub}).

Determination of initial parameter estimates. Initial parameter estimates were determined from visual inspection of the ensemble model fit to the stress-strain data from an equibiaxial test, in a user-interactive, iterative process. Initial estimates for K and E_{ub} (or λ_{ub}) were determined from the MTM inspection. Parameters (including K and E_{ub}/λ_{ub}) were altered, until model stress-strain values were similar to data stress-strain values, as determined by visual inspection of the stress-strain curve.

Fitting settings. Parameter estimation is performed to minimize the sum of squared errors (SSE) between the experimental and model ensemble stress values

$$SSE = \sum_{i=1}^{N} \left(S_{\text{mod},i}^{ens} - S_{\text{exp},i}^{ens} \right)^2 , \tag{3.4}$$

subjected to lower and upper bounds and inequality constraints on the parameters. Before the actual fitting process is started, choices are made specific to the data set: the fitting algorithm is chosen ('fmincon', 'lsqcurvefit', 'GA', see section 3.2.2), values for the lower and upper bounds on the parameters are defined, and termination tolerance criteria of the objective function and of the change in parameter values are set, as well as the maximum allowable number of iterations and function evaluations. When the fitting is terminated and optimal parameters are determined, model stress values are calculated with these parameters, and the quality of the fit, defined by the r^2 value, is as calculated as

$$r^2 = 1 - \frac{SSE}{N \operatorname{var}\left(S_{\text{exp}}^{ens} \right)}, \tag{3.5}$$

where "var" represents variance in the data and N is the number of data points.

3.2.4 Parameter estimation methods for structural model

The same setting options and fitting components are available for the complete structural model as described above (section 3.2.3) for the ensemble model, *i.e.*, data inspection, model choice, iteratively determining initial parameter estimates, solver choice, parameter bounds, termination tolerance criteria. If fitting of the ensemble model is performed separately, settings such as model and solver choice, bound settings, and scaling and thinning factors, are transferred, and parameters found from this fitting are used as initial parameter estimates for the structural model. In addition to the ensemble model parameters, initial estimates for $R(\theta)$ are determined based on visual inspection. Parameter estimation was performed to minimize the sum of squared errors (SSE) between the experimental and model stress values in all directions including shear stresses:

$$SSE = \sum_{i=1}^{N} \left(S_{11}^{\text{mod},i} - S_{11}^{\text{exp},i} \right)^2 + \left(S_{22}^{\text{mod},i} - S_{22}^{\text{exp},i} \right)^2 + \left(S_{12}^{\text{mod},i} - S_{12}^{\text{exp},i} \right)^2 , \tag{3.6}$$

or only in the 11 and 22 directions, excluding shear terms

$$SSE = \sum_{i=1}^{N} \left(S_{11}^{\text{mod},i} - S_{11}^{\text{exp},i} \right)^2 + \left(S_{22}^{\text{mod},i} - S_{22}^{\text{exp},i} \right)^2 , \tag{3.7}$$

subjected to lower and upper bounds and inequality constraints on the parameters. If shear stress and strain in the data are negligible, Eq. (3.7) is optimized. However, if shear stress or strain was an essential component of the testing protocol and shear stress and strain values in the data are significant, Eq. (3.6) is optimized. When the fitting is terminated and optimal parameters are determined, model stress values are calculated with the fit parameters, and the quality of the fit defined by the R^2 value is calculated for each direction separately using Eq. (3.5).

The model modifications described in section 2.2 are implemented in the fitting process through the definition of the permanent set deformation gradient tensor ${}_0^1\mathbf{F}$. If values for ${}_0^1\mathbf{F}$ are detected by MATLAB other than the identity tensor, the appropriate calculations are carried out within the specific function files.

3.2.5 Additional GUI details

The fitting process of both the ensemble model and the structural model were implemented in a GUI (see Appendix B for images of the interface). All choices and settings described above are available here. In addition, both GUIs have the following options: setting of file paths where data is to be located and where fitting output is to be saved; saving and loading of settings; setting the numerical integration accuracy; saving the fitting output; setting the lower and upper bounds to values equal to the initial parameter estimate to exclude the parameter from the fitting process.

The structural model GUI also has some specific settings, based on the fact that the data to be fit consists of stress-strain data from multiple testing protocols that can either be handled individually, or simultaneously. Individual protocols are extracted from the loaded data set in order to handle the protocols individually in the fitting process as well as in creating plots. It is an option to perform the fitting process in steps, where the middle (equibiaxial) protocol is fit first, and in each subsequent step, the two protocols before and after are added. For each new step, the parameter values found in the previous step are used as initial estimates, and at the end of each step the parameters are saved to a temporary text file, allowing one to retain the intermediate parameter values if need. In addition, one or multiple specific protocols can be chosen to be fit. The option "pause" allows the user to inspect intermediate fitting results. The common number of protocols in biaxial mechanical data in our lab is five or seven, and hence, the maximum number of protocols to fit is either five or seven. The user has the option to include shear terms in the objective function or to exclude them (Eqs. (3.6) and (3.7)). An input field is available for the permanent set deformation gradient tensor ${}^{1}_{0}\mathbf{F}$. It is set standard at the identity tensor to represent no permanent set. If data was thinned and/or scaled for the fitting process, the setting "all data points" allows the user to calculate and plot the fitting results for all data points with unscaled stress values.

The ensemble model fitting process can be loaded individually but can also be called from the structural model GUI, where settings of the ensemble fitting will be transferred to the structural model fitting upon exiting the ensemble model GUI.

3.2.6 Validation of implementation of fitting process

The output of the discrete fiber simulations (section 3.1.4) are also used to validate the fitting process. Graphical results of all fits are presented in Appendix C, and results are summarized here. All data sets were fit well, and final parameters equaled the set parameters, even when initial estimates were not similar to the known parameter values. Nothing remarkable is noted from simulations 1-4 (Figure C1 and Figure C2). Introducing shear components in the loading and/or in the permanent set did not present any problems in the fitting routine (simulations 5-8, Figure C3 and Figure C4). It was noted that it was not necessary to include the shear components in the objective function to produce accurate parameter results (using Eq. (3.7) vs. (3.6). This can be visualized in an error plot of the objective function as a function of different values of σ_R and K, which are the two free parameters if a centered distribution function is assumed (Figure 3.11). For both objective functions, a perfect minimum was found at the given values of σ_R=15^o and K=1000. Note that the minimum value of the objective function did not equal zero, which suggested that the synthetic data was not perfect. For completeness, the fitting results of simulation 8-11 are depicted in Appendix C, Figure C5 - Figure C7.

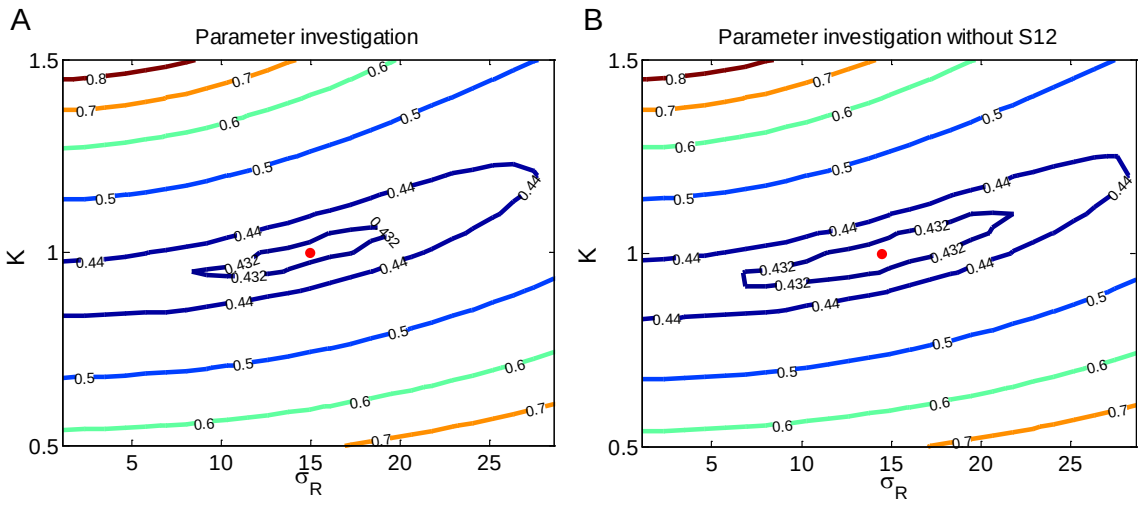

Figure 3.11. Contour plots of the objective function as function of different values of K and σ_R. A scaling factor of 1000 was used. The red dot denotes the minimum of the objective function. A) Objective function is given by Eq. (3.6); the minimum value of the objective function is 0.4307. B) Objective function is given by Eq. (3.7) and does not include shear terms; the minimum value of the objective function is 0.4300.

3.3 SUMMARY

In this chapter, it was shown that the structural model with its modifications was successfully implemented in MATLAB, including the two levels of numerical integration and the complete fitting process. The built-in MATLAB functions for numerical integration and parameter estimation have been shown reliable and effective. The complete process of parameter estimation was implemented within two separate user interfaces (GUIs), which provided full control over the data, fitting settings, and output, including data inspection, choices of model type and algorithms, setting parameter bound values, calculating model values, etc.

The modifications to the structural model, as well as the implementation of the model, were validated in three different steps. First, the fiber model formulation was validated by showing that the original linear *S*-*E* fiber model did not preserve the fiber effective modulus when slack was introduced in the fiber, which was solved by using the linear *P*-λ fiber model. Next, simulations with discrete fibers were performed and stress-strain behavior was compared to the continuous model formulation. This showed that the modifications to the model formulation were correct and that the implementation in MATLAB was correct. Finally, model stresses were calculated in both Ω_1 and Ω_0 for different sets of parameters and loading conditions to show that the modified model produces the correct stress strain behavior in Ω_1 as well as in Ω_0, with the same set of parameters. A thorough analysis of parameter covariance might be useful to obtain more insight in the model behavior. However, because of the strong nonlinear nature of the model, this is not a straightforward task. In conclusion, the structural model with its modifications of including permanent set effects and a new fiber stress-strain relation was implemented successfully in MATLAB and can be used to determine tissue-specific material parameters.

4.0 APPLICATION TO URINARY BLADDER TISSUE

4.1 BACKGROUND ON THE URINARY BLADDER

4.1.1 Bladder anatomy and structure

The urinary bladder (Figure 4.1) is a visceral (hollow) neuromuscular organ located anteriorly in the lower abdomen, just behind the pelvic bone. The two main functions of the urinary bladder are storage of large volumes of urine while maintaining a low intravesical pressure, and timely voiding. During urine storage, the bladder is relaxed while the urethra is closed by tonic contraction of the urethral sphincter. Normal voiding is accomplished by activation of the micturition reflex, where the bladder contracts with simultaneous relaxation of the urethral sphincter. The UBW consists of several layers: i) a mucosal layer, which consists of the urothelium and the basement membrane, ii) lamina propria, iii) detrusor, and iv) serosa [76, 104]. A network of nerves is found throughout all the layers of the bladder wall.

The urothelium is a mucosal layer of epithelial cells lining the inside of the bladder wall and isolates the toxic contents of the bladder from the rest of the body. The urothelial cells rest on a basement membrane. The lamina propria, also referred to as submucosal layer, consists of connective tissue and blood vessels. The detrusor layer, consisting of smooth muscle bundles, makes up the largest portion of the UBW (60-70%) [114] and contracts during bladder emptying. The serosa is the most outer layer consisting of a dense layer of collagen fibers. Bladders of different species consist of different numbers of smooth muscle layers with alternating orientation of the muscle fibers. The human bladder consists of three muscle layers and the rat bladder of two. During fetal development, fetal urine is emptied through the urachus instead of the urethra, which is a soft tissue tube that emanates from the dorsal part of the dome of the bladder. Fully developed bladders still contain a remainder of the urachus (Figure 4.2).

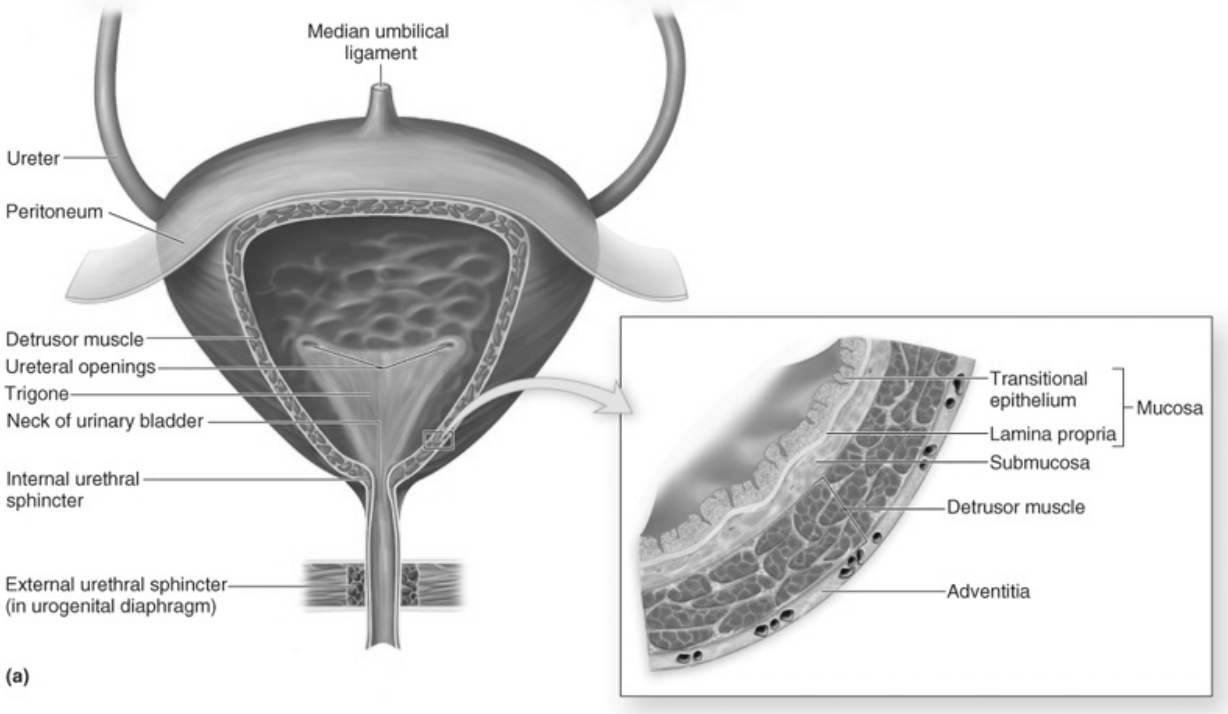

Figure 4.1. Schematic of the human urinary bladder.
Reproduced with permission from [99]. Copyright @ The McGraw-Hill Companies, Inc.

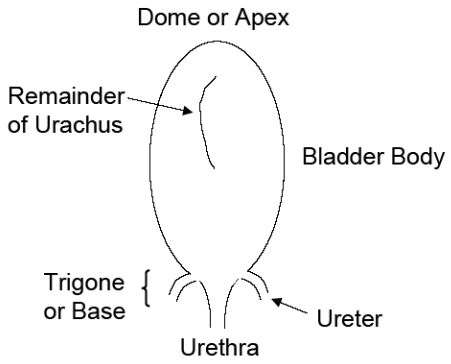

Figure 4.2. Schematic of a rat urinary bladder.

The SM cells in the detrusor form fascicles sheathed by collagen sheets and these SM fascicles are arranged into bundles that run in various directions [41, 42, 104, 157]. The collagen fiber network, consisting predominantly of fibrillar bundles of type I and type III collagen [16], serves to bind the SM together and provides resistance to high strains. In general, collagen structures are optimized to their specific function in each individual tissue type [112]. The collagen fibers exist in a coiled form when the urinary bladder is empty, and they straighten out during filling [16, 97, 104]. This suggests that the collagen structure in UBW tissue exhibits a unique multi-level hierarchy of coils, with super-coiled structures in addition to intrinsic fiber crimp, which allows for the accommodation of very large strains. Elastin in the normal UBW is found mainly in the vasculature, with small additional amounts in a loose network throughout the tissue [41, 77, 104, 125]. It has been suggested in arteries [37], and in the female reproductive organs [74, 92], that the elastic fibers keep the collagen in a more coiled state to enhance the extensibility of the collagen fiber network. The specific structures of collagen, elastin, and smooth muscle that the urinary bladder wall is made out of, are optimized for the organ's unique functions.

4.1.2 Bladder function

Normal bladder voiding is accomplished by activation of the micturition reflex, which is an autonomic spinal cord reflex. The bladder fills progressively until the tension in the wall rises above a threshold level. This happens either by the passive filling or by voluntary contracting the abdominal muscles. The stretch receptors in the bladder neck and the urethra are stimulated and elicit the micturition reflex, which is a coordinated neuromuscular event characterized by a sequence consisting of: 1) a sudden and complete relaxation of the striated sphincter muscles, 2) a decrease in urethral pressure, 3) an increase in detrusor pressure as the bladder and proximal urethra become isobaric, 4) opening of the bladder neck and urethra, and 5) voiding [13]. As the bladder fills, many superimposed micturition contractions begin to appear. When the bladder is only partially filled, these micturition contractions usually relax spontaneously after a fraction of a minute. As the bladder continues to fill, the micturition reflexes become more frequent and cause greater contractions of the detrusor muscle. The micturition reflex is self-generative. The micturition reflex also causes inhibition of the external sphincter of the urethra and hence gives

the possibility to void. Both voiding and urination can be controlled voluntary by contraction and relaxation of the external sphincter [13].

In the clinical field of urology cystometry is used to assess bladder function and health state. A cystometrogram (CMG) measures intravesical pressure (consists of abdominal pressure and detrusor pressure) as a function of bladder volume. The mechanically related parameters that can be derived from a CMG are bladder capacity and bladder compliance. Maximum cystometric capacity is defined as the volume at which the patient feels that he/she can no longer delay micturition. Bladder compliance is defined as change in volume divided by change in pressure (ml/cmH2O) [13].

Studies on the mechanical behavior of the bladder at the tissue and organ levels have provided useful information in assessment of the functional state of the organ [1, 2, 18, 19, 28, 33, 163]. These studies have included quasi-static uniaxial [1, 3, 26, 167], uniaxial viscoelastic [1, 18, 27, 162] and whole organ (in situ) [1, 20, 88, 124] studies. As an example of these mechanical studies, the influence of outflow tract obstruction on the mechanical properties of detrusor has been studied in an attempt to understand the reason for contractile abnormalities [165]. In this study, it was stated that the problem is to determine whether such abnormalities arise from defects in the contractile properties or whether they are due to changes in the extracellular matrix. The contribution made by both the resting properties and the active contraction to overall bladder wall compliance remains a controversial question.

From quasi-static and stress-relaxation planar biaxial mechanical testing the mechanical behavior of UBW tissue was characterized as anisotropic and highly time-dependent [47, 107] (see also section 4.2.2). In these studies, three different states were defined, *i.e.*, passive, active, and inactive-states, and the bladder wall tissue response was evaluated in the inactive state, where all smooth-muscle activity was abolished using a calcium-chelating agent. In another study, the stress-relaxation response was divided into the contributions of the ECM and SM separately, and it was shown that stresses are transferred from the SM at low strain values to the ECM at higher values [108]. Separation of the two components was experimentally achieved by decellularization of UBW tissue, through which the SM cells were removed. Histological analysis showed no visible damage of the ECM component after decellularization (Figure 4.3). The only attempt that has been made to develop a constitutive model of the complete bladder was by Damaser and Lehman [27, 29, 30]. Constitutive models, in combination with the

appropriate mechanical and clinical studies as mentioned, are essential in establishing the functional state of the urinary bladder, and in assessments of changes in function as a result of pathologies.

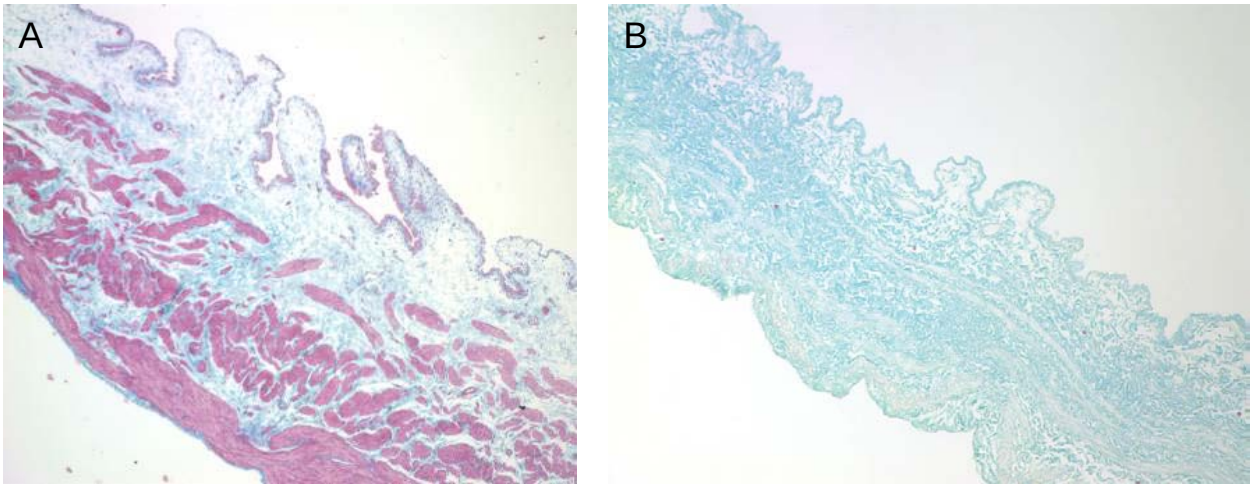

Figure 4.3. Histological assessment of intact and decellularized rat bladders.
Intact and decellularized rat bladders were fixed in Formalin and cross-sectional specimens were stained using Masson's Trichrome staining technique. A) Smooth muscle cells (stained in pink) were only present in the intact bladder specimens. With kind permission from Springer Science+Business Media: Biomech Model Mechanobiol, Contribution of the extracellular matrix to the viscoelastic behavior of the urinary bladder wall, Vol 7, 2008, p. 395-404, J. Nagatomi, K.K. Toosi, M.B. Chancellor, and M.S. Sacks, Figure 3A [108]. Copyright @ Springer-Verlag, 2007. B) Only collagenous ECM is present (stained in blue) that is no visibly affected by the decellularization process. Magnifications = 10x.

4.2 THE URINARY BLADDER WALL AND SPINALCORD INJURY

4.2.1 Clinical spinal cord injury

After spinal cord injury (SCI) above the lumbar level, the brain control is lost and the spinal cord undergoes tremendous plastic change. Approximately 250,000 to 400,000 individuals in the United States have spinal cord injuries, with urologic complications among the most common clinical conditions [32], which have an enormous influence on an individual's daily activities and physical function and can in some cases have an important impact on an individual's mental state

[111]. SCI can lead to severe lower urinary tract dysfunctions including bladder outlet obstruction (BOO), urinary retention (due to incomplete voiding), overactive bladders, and detrusor instability [35, 168]. A relationship has been shown to exist between treatment for several medical illnesses and suicide in elderly patients, including urinary incontinence [72].

In BOO specifically, the bladder is subjected to high stresses because of contractions against a closed sphincter, and high stretches due to overfilling. BOO leads to several structural and functional changes, including hypertrophy, in the detrusor muscle, regarded in part as a positive compensatory response aimed to overcome the resistance to bladder emptying [103]. After surgical relief of obstruction, bladder wall thickness and bladder weight are significantly reduced, suggesting reversibility of the remodeling processes [103]. BOO can result from many different pathologies, among others SCI and benign prostatic hyperplasia.

Bladder abnormalities as a result of SCI are characterized by an initial period of areflexia (*i.e.*, lack of contractions), followed by hyperreflexia (*i.e.*, bladder contracts frequently even at a relatively small volume), and detrusor-sphincter dysynergia (*i.e.*, the urethral sphincter and the bladder contract simultaneously) [134, 168] (Figure 4.4). In addition, they are accompanied not only by changes in the UBW tissue morphology, including increased thickness and hypertrophy [102], and fibrosis [34], but also by drastic changes in the mechanical properties (clinically reflected by compliance) of the wall [50, 137, 172]. Clinically, after the initial stabilization phase of the SCI patient where an indwelling catheter is placed, bladder management consists of roughly three types: continuous drainage through an indwelling Foley catheter (transurethral or suprapubic), clean intermittent catheterization, or spontaneous voiding. Regardless of the bladder management method, the lack of a normal micturition reflex leads to a decrease in compliance of the bladder [171, 172].

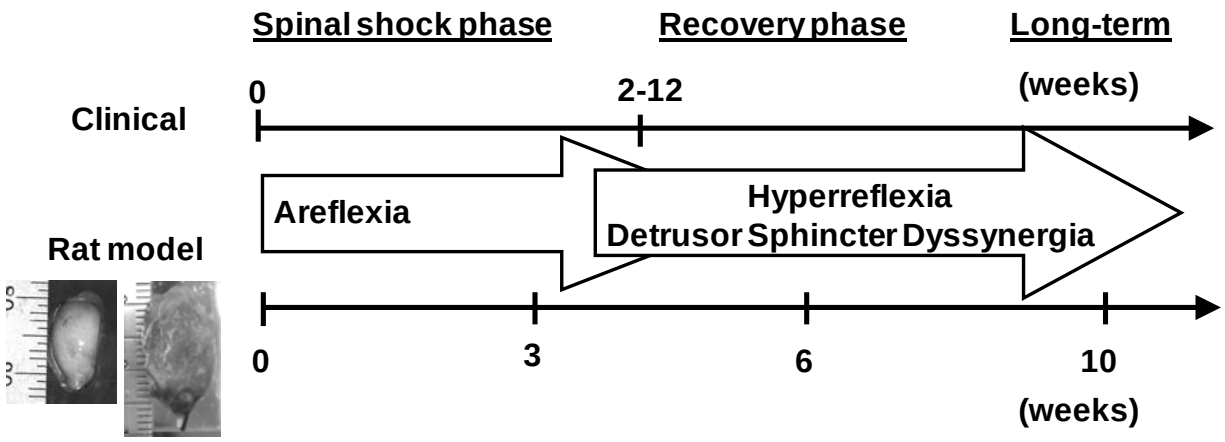

Figure 4.4. Time course of spinal cord injury, in a clinical setting and in the experimental rat model of SCI.

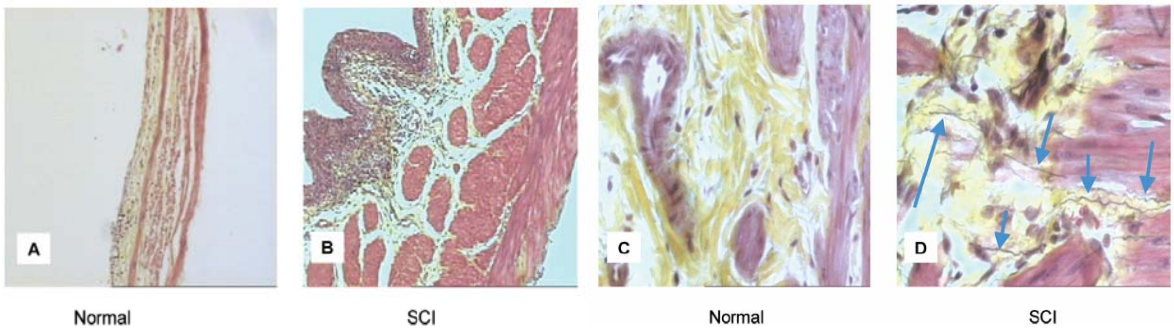

Figure 4.5. Morphology of normal and (10-day) SCI rat bladders.
Normal (A,C) and SCI (B,D) rat bladders were fixed in formalin and cross- and horizontal sections were stained using the Movat's pentachrome method. The SCI rat bladder (B) was much thicker and contained more smooth muscle (stained in red). Although comparable amounts of collagen (stained in yellow) were present in the sections of both normal (C) and SCI (D) bladders, there were significantly more elastic fibers (stained in black; indicated by arrows) in the SCI bladder compared to normal. Magnifications = 10× (Frames A and B); 40× (Frames C and D). With kind permission from Springer Science+Business Media: Ann Biomed Eng, Changes in the biaxial viscoelastic response of the urinary bladder following spinal cord injury, Vol 32, 2004, p. 1409-1419, J. Nagatomi, D.C. Gloeckner, M.B. Chancellor, W.C. Degroat, and M.S. Sacks, Figure 6 [107]. Copyright @ Biomedical Engineering Society, 2004.

4.2.2 Experimental SCI in a rat model

Our previous studies in a rat model of SCI have revealed that in the first ten days following injury during which the bladder is subjected to high levels of strain because of its inability tovoid, the UBW tissue became thicker, and significantly more compliant [47]. Using a novel image analysis software, Nagatomi *et al*. were first to quantify structural and compositional changes in the urinary bladder after spinal cord injury [107]. It was demonstrated that significant increases in smooth muscle and decreases in collagen area fractions in the 10-day SCI bladders existed, compared to the normal group. Furthermore, the SCI bladders exhibited significantly fewer cell nuclei per muscle area compared to the normal bladders. This indicated that hypertrophy rather than hyperplasia is the predominant mechanism that led to the overall increase in the wall tissue thickness and mass [107].

In addition to the smooth muscle hypertrophy, 10-day SCI rat bladders exhibited a different pattern of muscle orientation distribution compared to the normal rat bladders. Specifically, the orientation of smooth muscle bundles was bidirectional (*i.e.* in longitudinal and circumferential directions) post-SCI, while the orientation of smooth muscle bundles in normal bladders was predominantly longitudinal (Figure 4.6) [109]. This corroborated mechanical testing results, where bladders were shown to change its material class following spinal cord injury and behaved as an isotropic material while normal rat bladder was mechanically anisotropic. Additional biaxial mechanical testing to study the viscoelastic behavior of the bladder wall revealed that post-SCI bladder tissue exhibited a reduced stress-relaxation and a decreased rate of stress-relaxation compared to normal bladder [107]. It was suggested that this is due to different viscoelastic behaviors of smooth muscle, collagen, and elastin, where after SCI the tissue composition is different from normal.

Biochemical assays revealed that while the relative collagen concentration decreased, the relative elastin concentration of the post-SCI bladder was significantly greater compared to normal bladders, which was also confirmed by histological analysis (Figure 4.5) [107]. The production of elastin as a result of SCI [106, 107, 152] or in intravesical obstruction [127] is remarkable because elastin is generally assumed to be metabolically stable with negligible turnover rates [136]. The up-regulation of molecules related to remodeling, such as tropoelastin,

lysyl-oxidase, transforming growth factor-β1 (TGF-β1) and insulin-like growth factor-1 (IGF-1) was further confirmed by gene expression profiling techniques [106] (Figure 4.7).

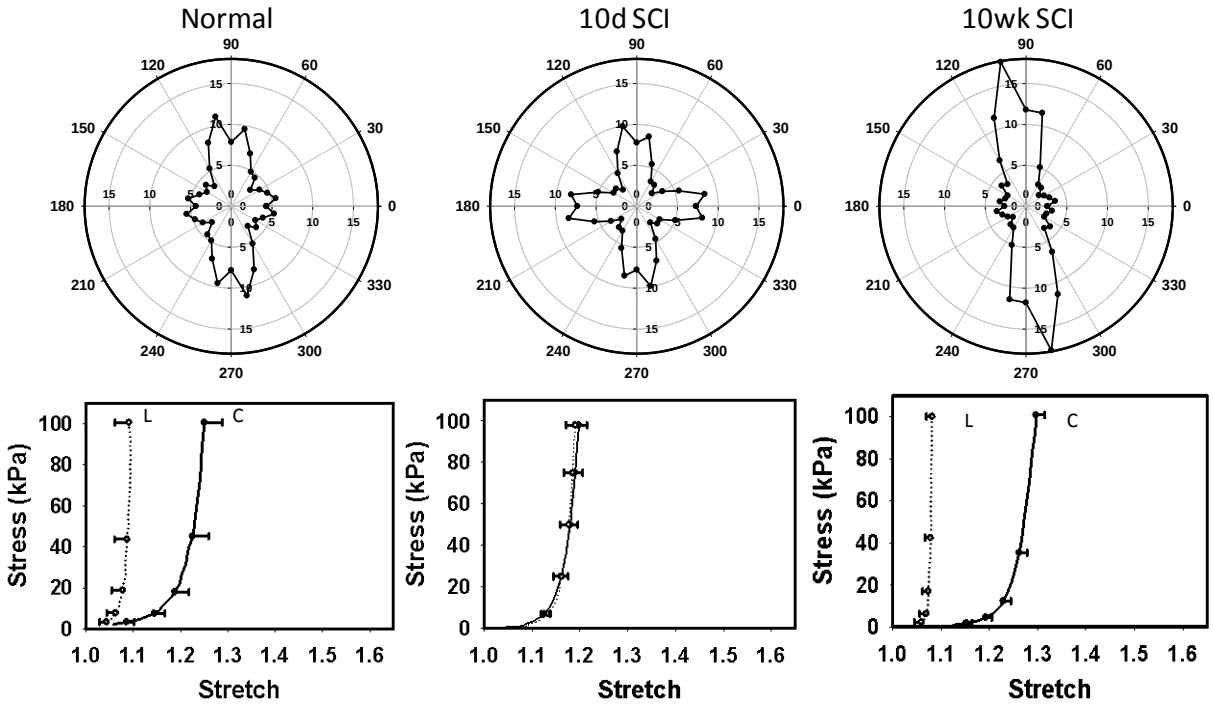

Figure 4.6. Time course changes in SM fiber orientation and biaxial mechanical behavior post-SCI. Upper panel: orientation distribution of smooth muscle bundles in normal (a), 1.5-week SCI (redrawn from [109] (b) and 10-week SCI (c) bladders. Lower panel: The longitudinal (○) and circumferential (●) stress-stretch curves representing data from equibiaxial stress protocol mechanical testing (mean ± SEM) in normal and SCI rat bladders. At all time points the changes in preferred muscle orientation corroborated the mechanical anisotropy data. With kind permission from Springer Science+Business Media: Ann Biomed Eng, The effects of long-term spinal cord injury on mechanical properties of the rat urinary bladder, Vol 36, 2008, p. 1470-1480, K.K. Toosi., J. Nagatomi, M.B. Chancellor, and M.S. Sacks, Figure 5 [152]. Copyright @ Biomedical Engineering Society, 2008.

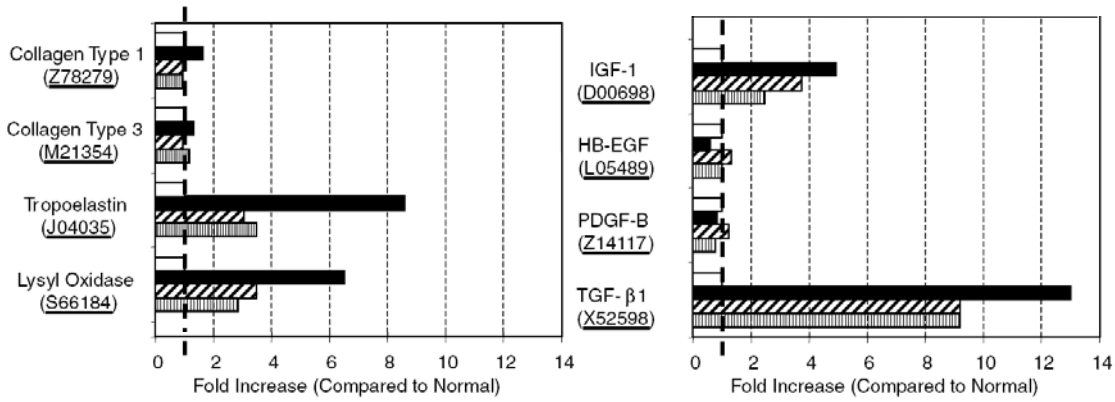

Figure 4.7. Microarray analysis (Affymetrix Gene Chip®) of detrusor RNA from normal and SCI rats. The transcription levels for tropoelastin and lysyl oxidase were as high as 8- and 6-fold in SCI at day 3 (■), day 7 (▨), and day 25 (▤) compared to normal (□). Furthermore, the transcription levels for TGF-b1 and IGF-1 in SCI rats increased to as high as 13- and 5-fold levels, respectively, following spinal cord injury. Reprinted from [106]. Copyright @ Elsevier Inc, 2005.

By examining time-course changes in mechanical behavior and tissue composition up to ten weeks post-injury, it was shown that there are significant differences between the areflexic (first ~4 weeks post-SCI, see also Figure 4.4) and the hyperreflexic phase (after about 4-6 weeks), in tissue structure, composition, as well as mechanical behavior [152]. The overall orientation of SM bundles changed from a predominantly longitudinal preference, to bidirectional after 10 days, and back to a longitudinal bias at 10 weeks post-SCI (Figure 4.6). Bladder tissue becomes more compliant in the areflexic phase, and stiffens again in the hyperreflexic phase (Figure 4.6, Figure 4.8). Furthermore, changes in elastin/collagen concentration ratio closely paralleled the change in compliance (Figure 4.8), with higher elastin content at all time-points post-SCI as compared to normal tissue [152]. In terms of composition, the 10-week SCI bladders exhibited significant increases in collagen area fractions compared to the 10-day SCI group, but similar to the normal bladders (Figure 4.9). These changes all eventually lead to the inability of the organ to normally fill and void.

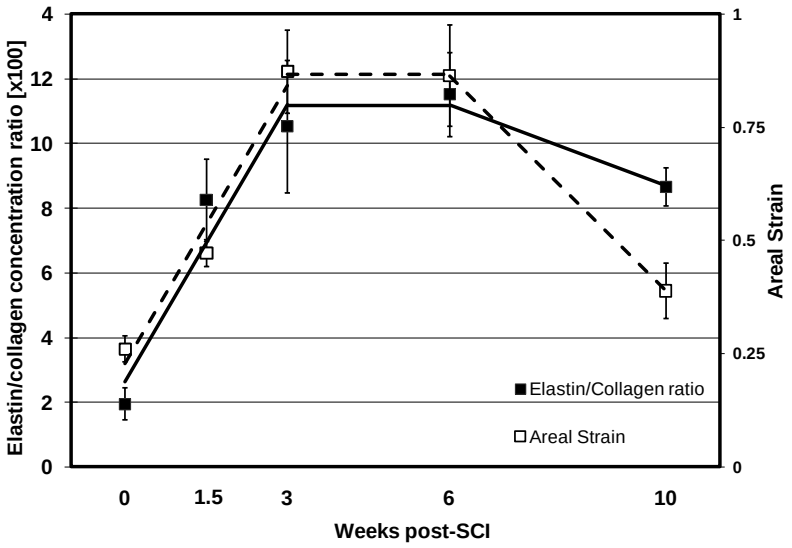

Figure 4.8. Time course changes in compliance post-SCI by two different measures.
Maximum areal strain values, and elastin/collagen ratio (both a measure for compliance) follow the same pattern as a function of time post-SCI. Data points from normal and 1.5-, 3-, 6-, and 10-week post-SCI rat bladders, shown as mean ± standard error of mean (SEM). Figure redrawn from data from [152].

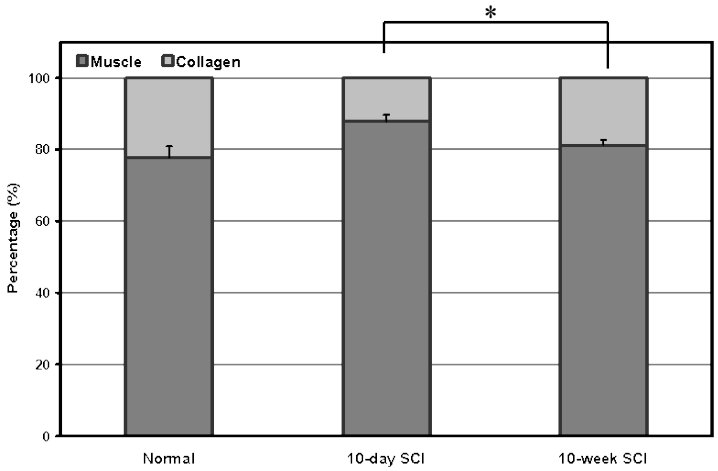

Figure 4.9. Area fractions of muscle and collagen in normal, 10-day (redrawn from [109]) and 10-week SCI rat bladders, fixed at 50% volume capacity.
The 10-week SCI bladders exhibited significant increases in collagen area fractions compared to the 10-day SCI group, but similar to the normal bladders. Data are mean ± SD; n = 3–5; analyzed by one-way ANOVA followed by the Student–Newman–Keuls post hoc test; with * indicating $p < 0.05$. With kind permission from Springer Science+Business Media: Ann Biomed Eng, The effects of long-term spinal cord injury on mechanical properties of the rat urinary bladder, Vol 36, 2008, p. 1470-1480, K.K. Toosi., J. Nagatomi, M.B. Chancellor, and M.S. Sacks, Figure 6 [152]. Copyright @ Biomedical Engineering Society, 2008.

4.3 THE URINARY BLADDER AS A REMODELING SYSTEM

All facts mentioned above indicate that there is strong correlation between the mechanical environment, tissue morphology, mechanical properties of the wall, and the health state of the bladder. Although extensive studies have been conducted on the effects of SCI on bladder function [35, 108, 152, 168, 177], the underlying mechanisms of the time-course changes, the specific driving force of UBW remodeling, and its end-goal, are not well understood. The post-SCI urinary bladder is subjected to high levels of strain during the first 4 weeks after SCI because of its inability to void (the areflexic phase), and to high levels of stress after about 6 weeks post-SCI due to re-innervation of the bladder resulting in uncontrolled contractions against a closed sphincter, *i.e.* the hyperreflexic phase. In the vascular literature, it is assumed that blood vessels remodel in response to an increase in blood pressure, by restoring the circumferential wall stress to a homeostatic value. This results in thickening of the wall and enlarging of the blood vessel. Instead of remodeling to restore homeostatic wall stresses, the bladder is most likely adapting to the functional demand of the organ, which means it is remodeling to restore function. Due to the fact that full physiological recovery is never achieved because of lack of full neural control, the remodeling results in a pathological process. In contrast to in blood vessels, the bladder will only fully recover with a "neural fix", *i.e.* after complete re-innervation. The available experimental data set of UBW remodeling post-SCI [47, 106-109, 152] provides us with a unique platform to specialize the proposed morphologically based constitutive model and to elucidate underlying remodeling mechanisms.

5.0 EXPERIMENTAL METHODS TO COMPLETE THE EXPERIMENTAL DATABASE

Experimental data is required to construct a constitutive model with physiological relevant model parameters. The necessary data is derived from the published results that were described in the previous chapter (Chapter 4.0), as well as from new experiments. This chapter describes the methods used to provide a complete experimental database needed for the model. This includes experimental methods to obtain new data, as well as analyses on the data presented in the previous chapter. The experimental data of healthy urinary bladder wall (UBW) is used to provide the constitutive model described in Chapter 2.0 with model parameters, and the data on remodeling processes in the UBW as a result of spinal cord injury (SCI) are used to guide the development of a model to simulate post-SCI remodeling.

The basis of the required experimental data is the notion that the mechanical behavior of the UBW is assumed to result from a combination of the two main load-bearing components, *i.e.*, collagen and smooth muscle (SM). In order to determine the physical and structural properties of these individual components, a decellularization technique was employed to separate the collagen component from the intact tissue in the form of extracellular matrix (ECM). The preparation of decellularized UBW specimens is described in section 5.1. This allowed us to obtain the following experimental data of the ECM component: Biaxial mechanical data (section 5.2); Collagen structure (sections 5.3.1and 5.3.2); ECM volume/mass fractions (section 5.3.3).

A significant amount of mechanical and structural data of healthy and post-SCI intact UBW was available from previous studies, as was introduced in Chapter 4.0. These data needed to be reanalyzed to make it suitable for the current constitutive model. The methods employed (including description of original methods) to create usable data on healthy intact UBW include the following: Biaxial mechanical testing of intact bladder wall (section 5.4.2); SM orientation (section 5.4.3). The methods to obtain usable experimental data on remodeling in the UBW as a

result of SCI comprise the following: Biaxial mechanical testing of intact bladder wall at multiple time points post-SCI (section 5.4.2); SM orientation at different time points post-SCI (section 5.4.3); Biochemical composition (collagen and elastin) at multiple time points post-SCI (section 5.4.4); Biaxial mechanical testing of post-SCI UBW ECM (section 5.4.5).

Parts of this chapter (specifically sections 5.1, 5.2, and parts of 5.3) are based on S. Wognum, D.E. Schmidt, M.S. Sacks, *On the mechanical role of de novo synthesized elastin in the urinary bladder wall*, J Biomech Eng, 2009, 131(10): 101018 [175], Copyright @ ASME.

5.1 URINARY BLADDER WALL ECM SPECIMEN PREPARATION

5.1.1 Tissue preparation

Urinary bladders were excised from 7 healthy, 2-3 months old, female Sprague-Dawley rats (150-300g), following euthanasia with CO_2. The bladders were placed immediately in modified Krebs solution (containing 113 mM NaCl, 4.7 mM KCl, 1.2 mM $MgSO_4 \cdot 7H_2O$, 25 mM $NaHCO_3$, 1.2 mM KH_2PO_4, 5.9 mM Dextrose, and 1 mM ethylene glycol tetraacetic acid (EGTA), pH 7.4) and refrigerated at 4 °C for up to 48 hours. The process provided an environment for complete SM cell relaxation. Bladders were then cut open longitudinally along the urachus and were trimmed down to make square test specimens by removing the dome and trigone sections of the organ [47, 152] (Figure 5.1). Dimensions (width, length and thickness) and wet weights of the specimens were measured. Thickness measurements were guided by assuming that the wet weight in grams equals the volume of the tissue specimen in cm^3 (tissue density = ~1 g/ml). To quantify tissue deformations, an array of four polypropylene discs (~0.4 mm in diameter, cut from 2-0 nonabsorbable surgical suture (Ethicon Inc., Somerville, NJ)) was affixed to the center portion of the intact bladder specimen's serosal surface with cyanoacrylate adhesive (Permabond, Somerset, NJ) [146]. This marker material was chosen because of its ability to securely adhere to the specimen surface through the specimen preparation, decellularization, and testing procedures (see sections 5.1 and 5.2). At each step in the testing process, marker positions were acquired.

5.1.2 Decellularization

To remove the SM component, the UBW specimens were treated in a series of detergent solutions following methods described in [14, 108]. Briefly, whole bladders were immersed in hypotonic tris-buffered saline (TBS; pH = 8.0) supplemented with a protease inhibitor (0.01mM phenylmethylsulphonyl fluoride (PMSF); Sigma, St Louis, MO) at room temperature with gentle agitation for ~28 h. This step was followed by incubation in 1.0% Triton X-100 (Sigma) for 44 h, in 0.1% SDS (BioRad, Hercules, CA) for 28 h, and finally the specimen was rinsed with standard phosphate buffered saline (PBS). Immersion times were shortened from the original protocol, as SM removal appeared to be complete after this amount of time as assessed by histological investigation. The dimensions and weight were measured and recorded, and the specimen was stored in PBS supplemented with PMSF until testing was performed.

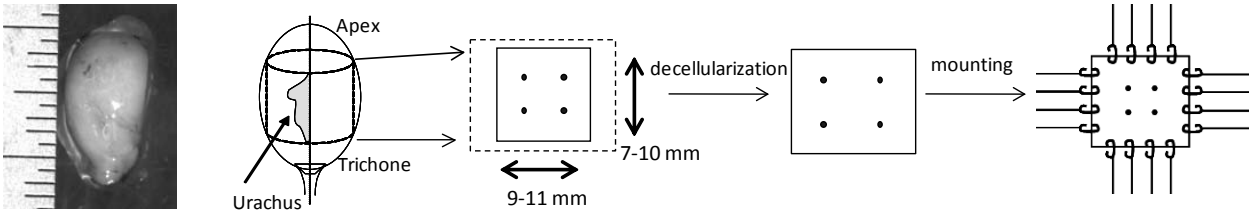

Figure 5.1. The process of specimen preparation from an intact rat urinary bladder to a mounted testing specimen. Rat bladders are cut open longitudinally along the urachus, and a testing specimen is prepared by trimming it and attaching markers onto the serosal surface. The specimen is decellularized, and suture hooks are attached for biaxial testing.

5.2 BIAXIAL MECHANICAL TESTING OF DECELLULARIZED SPECIMENS

5.2.1 Kinematics of a biaxial test and stress and strain calculations

Biaxial mechanical testing is used to determine the mechanical behavior of planar materials or membranes. UBW specimens can be considered planar since the thickness is several orders of magnitudes smaller than the length and width, and second-order effects such as bending and shear are negligible under physiological loading conditions. A plane stress state is assumed (stress in the perpendicular direction is zero), and the following homogeneous biaxial deformation is considered:

$$x_1 = \lambda_1 X_1 + \kappa_1 X_2, \qquad x_1 = \lambda_2 X_2 + \kappa_2 X_1, \qquad x_3 = \lambda_3 X_3, \tag{5.1}$$

where X and x are the locations of material particles in the reference and deformed states, respectively, and λ_i and κ_i are the components of the deformation gradient tensor $\mathbf{F}$ (*i.e.* λ_i are the stretch ratios and κ_i are measures of in-plane shear). The components of $\mathbf{F}$ are determined optically at each time point during the test by tracking the position of markers mounted on the upper specimen surface that delimit the central target region using optical tracking software. Finite element shape functions are used to approximate the position vector field within the central target regions. This can include linear and quadratic variations in strain. Since soft tissues are composed primarily of water, they can be considered incompressible so that $\det(\mathbf{F}) = 1$, and λ_3 is calculated from the components of $\mathbf{F}$.

Due to the highly distensible nature of the UBW ECM and the uncharacterized effects of decellularization and mechanical preconditioning, we defined each preparation step as separate deformation states (Ω) (Figure 5.2), where Ω_0 represents an initial (free floating) state. From the measured marker positions of each relevant testing state, the deformation gradient tensor $\mathbf{F}$ associated with each state was determined using standard methods [128]. As $\mathbf{F}$ is a two-point tensor, we utilized the notation ${}^{\beta}_{\alpha}\mathbf{F}$, where a bold capital represents a tensor quantity, and α and β represent the first and second state used, respectively. The corresponding Green-Lagrange strain tensor $\mathbf{E}$ was determined using $\mathbf{E} = \frac{1}{2}(\mathbf{F}^T\mathbf{F} - \mathbf{I})$. Under the assumption that the 0.1 g applied tare-load is small enough to be considered negligible (*i.e.* $\Omega_0=\Omega_3=\Omega_4$), the post-preconditioned tare-loaded state Ω_4 was used as the reference state in previous studies, and

dimension values from the initial free floating state Ω_0 were used. Note that the Ω_3 marker positions were not available for these data. In distensible tissues such as UBW ECM, the states cannot be considered equal, and the stress-free post-preconditioned unloaded reference state Ω_3 should be used for the stress and stretch calculations, and stress and stretch calculations are to be performed with respect to the same state. To facilitate comparison with previously obtained data sets (Table 5.1), newly obtained data were also referenced to Ω_4, in addition to Ω_3.

The components of Cauchy stress tensor **t** were calculated from the axial loads and the individual specimen dimensions at each time *t*, which were calculated from the initial measured specimen dimensions and the relevant deformation gradient tensor, assuming tissue incompressibility. The components of the Second Piola Kirchhoff stress and Lagrangian or first Piola Kirchhoff stress tensors (**S** and **P** respectively) were calculated from **t** using Eq. (1.2). This newly obtained stress-stretch data set is referred to as data set 1 (Table 5.1).

Note that it is impossible to fully characterize the three-dimensional mechanical properties of an anisotropic material through biaxial testing alone, unless extra assumptions are made about the dependence of the stress on specific strain components [58] (see also section 1.2). In general, the shear components of the deformation gradient and stress tensors can be considered negligible, and the two remaining components of the constitutive equation $S_{11}(E_{11}, E_{22})$ and $S_{22}(E_{11}, E_{22})$ can be determined from planar biaxial testing.

Table 5.1. Overview of mechanical data

Data set	1-a	1-b	2*	3*
animal model	normal		normal	SCI
specimen prep	decellularized specimen		decellularized bladder	decellularized bladder
tare-load	0.1 g		0.5 g	0.5 g
testing control	stretch		stress (load)	stress (load)
max level	specimen dependent		100 kPa	100 kPa
reference state	Ω_3	Ω_4	Ω_4	Ω_4

* Data obtained from [108]. Max level is defined with respect to initial free floating dimensions in Ω_0.

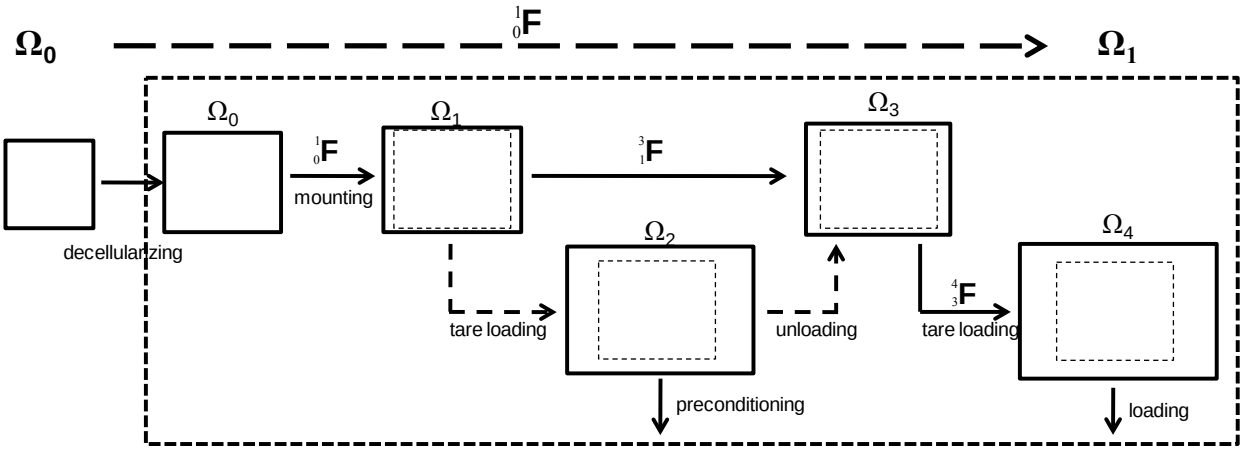

Figure 5.2. Schematic of all possible different reference states (Ω) encountered during biaxial mechanical testing. *Outside the dashed box*: Reference states as defined in the multi-component model. Ω_0 represents the free floating intact state, Ω_1 the post-preconditioned decellularized state. *Inside the dashed box*: Reference states as defined in the separate ECM model. Ω_0 represents the free floating decellularized tissue specimen, Ω_1 the state where the specimen is mounted in the biaxial testing device, Ω_2 the state where a tare-load is applied to the specimen and from which the specimen is preconditioned. After this, the specimen is unloaded, which is represented by Ω_3 (post-preconditioned un-loaded reference state). Before testing, a tare-load is applied, which is represented by Ω_4 (tare-loaded references state). The deformation between the different states is defined by the deformation gradient tensor ${}^{\beta}_{\alpha}\mathbf{F}$. Relative dimensions of the squares are representative of average specimen dimensions as measured. Initial specimen dimensions in Ω_0 were 12.7 x 9.76 x 0.832 mm, which are also depicted by the dashed lines in the other reference states.

5.2.2 Biaxial mechanical testing procedure

The decellularized tissue specimens were prepared for planar biaxial mechanical testing under stretch-control, and the four sides of each specimen were tethered using nylon suture and small stainless steel hooks (Figure 5.1), as described in detail in [47, 128]. The test specimen was then mounted onto a custom-made planar biaxial testing device (Figure 5.3). Each side of the square test specimen was connected to the motor carriages via sutures to apply four-point loads. The load on each axis was constantly monitored using force transducers (with a signal conditioner) and the applied load was controlled by adjusting the stepper motors using our custom software and a data acquisition board installed on a PC. Testing was performed at room temperature, in PBS, under stretch control, and starting from a preload of 0.1g. Throughout testing, in-plane axial stretches were determined from the two-dimensional deformation gradient tensor **F**,

determined from displacements of four markers affixed to the surface of the specimen, as described above.

The maximum testing stretch level was calculated for each specimen individually, from the maximum stretch levels of the rat urinary bladder as determined through whole organ strain studies, *i.e.* 2.8 (initial observations from[113]), divided by the axial stretch as a result of decellularization, preconditioning, and the 0.1 g tare-load, respectively. The maximum testing stretch was limited by the maximum load cell capacity (250g) in some specimens. Tissue specimens were preconditioned for 12 cycles under equi-biaxial strain, up to the determined maximum testing strain, and where equi-biaxial strain was defined with respect to Ω_4. The testing protocol utilized a constant ratio of the axial strains E_{11} :E_{22} = 1:1, 1:0.33, 1:0.5, 1:1, 0.5:1, 0.33:1. The specimen was placed in the device with the circumferential I direction aligned with x_1, and the longitudinal (L) direction with x_2, respectively. Each testing protocol consisted of 10-12 contiguous cycles with a period of 15 to 25 seconds, and after each cycle the specimen was returned to the state at the start of the protocol, *i.e.* the strain belonging to the initial tare load of 0.1 g. The loading portion of the data from the last cycle of the middle equi-biaxial stretch protocol (1:1) was used for analysis and model fitting in the ECM study (Chapter 6.0), and the loading portion of the data from the last cycle of each of the protocols was used for analysis and model fitting in the multi-component model study (Chapter 7.0).

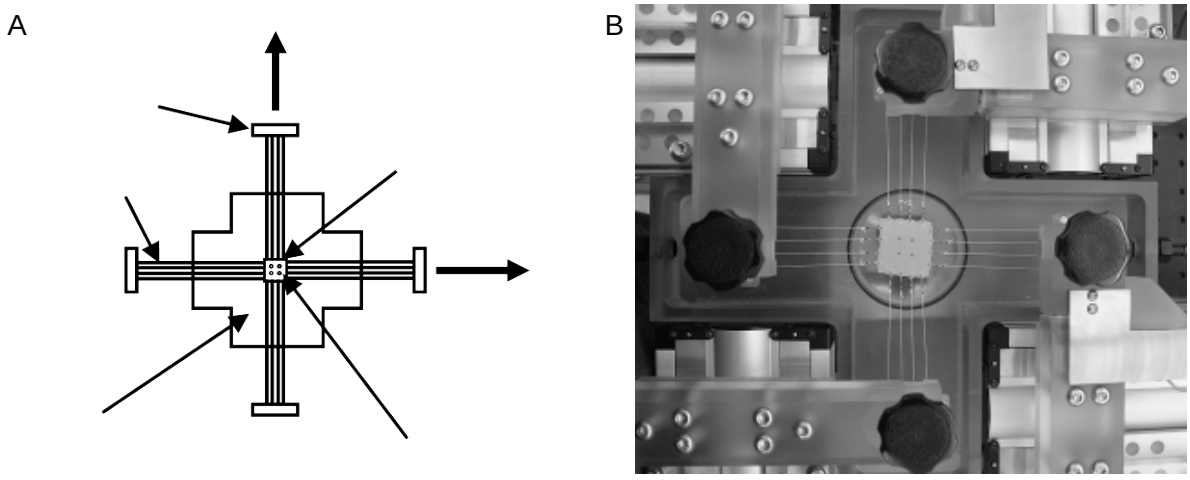

Figure 5.3. Biaxial mechanical experimental setup.
A) Schematic of the setup. B) Photo of the setup.

5.3 TISSUE STRUCTURE AND COMPOSITION

5.3.1 Structure of bladder ECM

To prepare for histology, tissue specimens were chemically fixed in 10% formalin and paraffin embedded. Next, the blocks were sectioned transversely along the longitudinal direction (cross-section) or parallel to the specimen surface (*en-face)* and individual sections were stained. All stained sections were investigated using a Nikon (Melville, NY) eclipse E600 bright field microscope under 40x magnification, and images were captured with a SPOT Rtslider 1.4MP camera and MetaView (Dowingtown, PA) software. Images were enhanced for visualization purposes using standard image analysis software.

The collagen structure of the intact bladder tissue was visualized at different filling volumes. Two normal and two post-SCI bladders (both intact; for spinalization procedures see section 5.4.1 below) were filled with 10% formalin at 25% and 100% capacity respectively (100% capacity being equal to 0.7 ml for normal and 1.4 ml for post-SCI). A rectangular piece from the posterior side of each bladder was excised, and cross-sectional sections were stained with Picro-Sirius red.

A post-SCI (28 days; for spinalization procedures see section 5.4.1 below) bladder tissue specimen obtained from an unrelated study was decellularized according to the above protocol. To verify that elastin was still present after decellularization of post-injury UWB specimens, and to assess the extent of elastin production, cross-sectional and *en-face* sections were stained with Verhoeff van Gieson and elastic trichrome.

Scanning electron microscopy (SEM) was also used to visualize the detailed collagen structure of decellularized bladder in cross-section. A normal decellularized bladder tissue specimen was cut into smaller sections, fixed in 10% formalin, and rinsed with PBS before further processing. The specimens were washed in sequential washes of 30%, 50%, 70%, 90%, and 100% ethanol, and subjected to critical point drying and gold sputter coating.

5.3.2 Collagen orientation

The small angle light scattering technique (SALS) was used to nondestructively quantify collagen fiber architecture of UBW ECM. A detailed description of the SALS technique has been previously presented [131]. Briefly, a 4 mW HeNe continuous unpolarized laser (λ = 632.8 nm) is passed through the tissue specimen. The spatial intensity distribution of the resulting scattered light represents the sum of all structural information within the light beam envelope. The angular distribution of scattered light pattern, which represents the distribution of fiber angles within the light beam envelope, is obtained, and the preferred fiber direction, as well as the orientation index, are derived from this. To prepare specimens for SALS measurements, intact bladders were decellularized according to the protocol described in section 5.1, with each step lasting 48 h instead of the 28/44/44 hours as described in section 5.1.2. Decellularized bladders were filled with 10% formalin at different filling volumes and placed in 10% formalin to fix the collagen structure. A rectangular piece from the posterior side of each bladder was excised and was dehydrated through subsequent glycerol-PBS solutions up to 100% glycerol, to clear the specimens. SALS measurements are conducted over the entire specimen surface.

5.3.3 Volume fractions

Bladder wall tissue is assumed to consist of water, collagen and smooth muscle, and the tissue volume is assumed to approximately equal the tissue mass because of the high water content. Hence, mass fractions can be used as approximation of volume fractions. Mass fractions of the components were determined through determination of wet and dry weights and use of lyophilization. Four intact bladders were cut into square specimens as described above and were each cut in half. One half was rinsed in distilled water to eliminate salt content from the buffered salt solution, frozen at -20 ^{o}C overnight, and placed in an FTS Systems Bulk Freeze Dryer Model 854 lyophilizer until all water was eliminated. The other half was decellularized according to the protocol described in section 5.1, rinsed in distilled water afterwards, frozen, and lyophilized. Left and right halves were randomized. Specimens were weighted at every step and dimensions (length, width, thickness) were measured of the wet specimens. ECM fraction based on dry weight was determined as dry weight ECM/dry weight intact, and ECM fraction based on wet

weight as dry weight ECM/wet weight intact. Volume fractions of water were determined for both intact and decellularized specimens as 1 – dry weight/wet weight. Mean and standard deviation (SD) were calculated for the four specimens. Average volume fractions were compared to histological area fractions from our previous study [109] (Figure 4.9, see methods in section 5.4.3) to determine appropriate model parameter values for component volume fractions.

5.4 REANALYSIS OF AVAILABLE DATA TO MAKE USABLE FOR MODEL

5.4.1 Methods of spinalization

Spinal cord defects were created according to established protocols, as described previously [47, 107, 108, 152]. Female Sprague-Dawley rats were subjected to complete 89ransaction of spinal cord at the T9-T10 level. Under anesthesia, the dura and spinal cord at the T9-T10 level were cut with scissors and a sterile sponge was placed between the severed ends of the spinal cord. The rat bladders were emptied manually two to three times a day and general animal care was given according to the protocol approved by the Institutional Animal Care and Use Committee (IACUC, University of Pittsburgh, Pittsburgh, PA). The urinary bladders were harvested at 10 days and 10 weeks post-SCI, respectively, and were immediately placed in modified Krebs solution and refrigerated at 4 °C for up to 48 hours following sacrificing of the animals.

5.4.2 Intact bladder biaxial mechanical data – normal and post-SCI

Biaxial mechanical data of intact UBW, both normal and post-SCI, were obtained from two previous studies [47, 152]. Bladder specimens were prepared and small carbon graphite particles were affixed on the luminal surface for strain measurements, and four sides of each specimen were tethered using suture and stainless steel hooks. Bladder specimens were mounted onto the biaxial testing device (Figure 5.3), and biaxial stress-controlled loading experiments were performed at room temperature, in modified Krebs solution, starting from a tare-load of 0.5 g, to a maximum stress level of 100 kPa (defined with respect to initial dimensions in Ω_0), after

preconditioning to the same stress level for 12 cycles. The testing protocols utilized a constant ratio of the Lagrangian stresses (in kPa) P_{11}:P_{22} = 50:100, 75:100, 100:100, 100:75, 100:50. These ratios were chosen to cover a wide range of stress states that encompass the known range of physiological responses. The specimen was placed in the device with the circumferential I direction aligned with x_1, and the longitudinal (L) direction with x_2, respectively (Figure 5.3). Each testing protocol consisted of 10-12 contiguous cycles with a period of 15 to 25 seconds, and after each cycle the specimen was returned to the tare-loaded state. The loading portion of the data from the last cycle of each protocol was used for analysis.

New stress-strain data was obtained using the calculations described in section 5.2.1. Stress and strain values were calculated with respect to the tare-loaded reference state, and additionally, the deformation gradient tensor (${}^{1}_{0}\mathbf{F}_{\text{int}}$) from free floating unloaded state (Ω_0) to tare loaded reference state (Ω_1) was calculated for each specimen. Areal strain ($\lambda_1\lambda_2 - 1$) was also calculated for each sample at each time point, which corresponds to net tissue mechanical compliance. Corresponding areal strain results were presented in Figure 4.8. After careful inspection of the available biaxial stress-strain data of normal intact UBW, four representative data sets were selected for further analysis. Data selection was based on consistency with average biaxial behavior as reported in [152] exhibiting significant anisotropy, as well as on relative consistency in ${}^{1}_{0}\mathbf{F}_{\text{int}}$ values. Data selection of 10-day post-SCI biaxial mechanical data was done based on similar criteria, and five representative data sets were selected. For the 10-week time-point, data sets were found to not be suitable for further analysis.

5.4.3 SM orientation and area fraction data at different post-SCI time points

Smooth muscle bundle orientation was quantified in the UBW tissue from 10-day and 10-week post-SCI rats, using a novel, custom-made, semi-automated image analysis method. Detailed methods have been described previously [109], and were summarized in [152]. For each bladder specimen, 12 histological sections (sectioned *en face*, stained with Movat's Pentachrome stain) from the detrusor layer were examined using light microscopy. On average, six fields per section were imaged capturing the entire section without any overlap between the image fields. Digital images of each captured field were obtained and used for detection of the edge of smooth muscle

bundles, via the image analysis software. The smooth muscle bundle orientation for each bladder was quantified by first grouping the muscle edge counts (obtained from 72 images per specimen) into 18 angular bins, such that each bin contained the number of edges that lay within an angle span of 10^o (*i.e.*, -5^o–4^o, 5^o–14^o, 15^o–24^o, ... 165^o–174^o). The muscle edge counts in each angular bin were then normalized by the total number of muscle edges for each bladder, and the data were reported as edge count percentages, plotted in the polar coordinate system. To provide a visual clarity, taking advantage of the rotational symmetry of muscle orientation about horizontal axis (e.g., $30^o = 210^o$), the 180^o-rotated image of the plot was added to the original graph to construct a 360^o polar plot [152]. The results were presented in Figure 4.6.

To make the data suitable for model implementation, the edge count percentage values were multiplied by 180 and divided by 1000*π, to normalize it by the area under the curve (AUC), in order to achieve an AUC equal to 1, consistent with the definition of $R_{SM}(\theta)$ (with θ in radians). Next, a symmetric continuous bimodal distribution function was defined as a combination of two beta functions (similar to the double beta recruitment function as described in Eqs. (2.11)-(2.13), with peaks centered around 0 rad (circumferential direction, C) and π/2 rad (longitudinal direction, L)

$$R_{SM}(\theta) = \gamma_{SMC} R_{SMC}(\theta) + [1 - \gamma_{SMC}] R_{SML}(\theta), \tag{2.54}$$

where R_{SMC} and R_{SML} are beta functions described by a mean and standard deviation. The SM orientation data was fit to this function to determine values for the standard deviations σ_{smC} and σ_{smL} and the scaling factor γ_{SM}. Γ_{SM} represents the relative fraction of SM fiber bundles running in circumferential direction, and hence the relative fraction of SM fiber bundles running in longitudinal direction equals $(1 - \gamma_{SM})$.

Additionally, to quantify the area fraction for tissue components using the image analysis software, the numbers of color-segmented pixels (*i.e.*, red for muscle and yellow for collagen) were counted for all samples. The individual pixel counts for each component were normalized by the total pixel counts of both components (sum of red and yellow pixels, representing the entire tissue section) for each specimen and the data were reported as bladder tissue composition, as presented in Figure 4.9.

5.4.4 Biochemical composition data

As described previously [152], 10-day, 6-week, and 10-week SCI bladder specimens were each cut into 12 strips (1 x 10 mm^2 each). These strips were weighed, and six of them were digested in 0.5 N acetic acid supplemented with 1 mg/ml pepsin (Sigma, St. Louis, MO, USA) at 4°C overnight. Acid-soluble collagen in the supernatant solution was quantified using a commercially available assay kit (Accurate Chemical, Westbury, NY, USA) and following the manufacturer's instructions. In order to digest elastin contents, the remainder six strips were treated with 0.25 M oxalic acid at 95^0C for 180 min (60 min x 3). Elastin concentrations in these supernatants were also quantified using a commercially available assay kit (Accurate Chemical) and following the manufacturer's instructions. The data were expressed in terms of mass (in mg or μg) per volume of tissue specimen (in cm^3). Results were compared to the areal strain results in Figure 4.8.

These data represent changes in component *fractions* as a result of SCI, not changes in absolute amounts. Unfortunately, bladder weights were not measured at the time of the experiments. To allow calculation of absolute mass changes of collagen and elastin, information about bladder weights at different time points post-SCI was compiled from the literature and weight measurements of individual bladders that were available from other experiments. Data points were compiled and an exponential fit through the data points was performed. It was assumed that bladder weights at 10 weeks post-SCI are not different from earlier time-points (derived from experimental observations; personal communication with K.K. Toosi). Interpolated values of bladder mass at the relevant time points were used to convert collagen and elastin concentration data into absolute mass data.

5.4.5 Mechanical data of post-SCI UBW ECM

As described previously [108], whole bladders were harvested from normal and spinalized (3-4 week post-injury) female Sprague–Dawley rats (170–200 g initial weight) and were decellularized according to the protocol described in section 5.1, with each step for 48 h. Square test specimens were prepared, and biaxial stress-relaxation experiments were performed. Before testing, a quasi-static equi-biaxial stress test was performed with 12 loading–unloading cycles in order to precondition the tissue at the maximum stress level of 100 kPa (defined with respect to

initial free floating dimensions). The last cycle of the equi-biaxial stress test was used for analysis, and stress values were re-calculated with correct dimension values in the post-preconditioned state. These data sets from normal and post-injury bladders are referred to as data set 2 and 3, respectively (Table 5.1). In addition to standard stress-stretch analysis, the data were expressed as average stress (average of P_{11} and P_{22} per data point) vs. areal strain, which is defined as $\lambda_1\lambda_2 - 1$, as an overall index of tissue compliance.

6.0 ON THE MECHANICAL ROLE OF DE NOVO SYNTHESIZED ELASTIN IN THE URINARY BLADDER WALL

This chapter is an extended version of the publication: S. Wognum, D.E. Schmidt, M.S. Sacks, *On the mechanical role of de novo synthesized elastin in the urinary bladder wall*, J Biomech Eng, 2009, 131(10): 101018 [175], Copyright @ ASME.

6.1 INTRODUCTION

Virtually all tissues continuously grow, remodel, and adapt to changes in their physiological environment, resulting in changes in structure and composition. In addition to adaptation within normal physiological ranges, pathologies and their subsequent adaptations also account for a large part of observable tissue-level changes. Remodeling has been defined as a change in structure resulting in altered material properties that is achieved by reorganizing existing constituents or by synthesizing new constituents of different organization [65, 150]. Growth and remodeling (G&R) in soft tissues has been studied most extensively in the vasculature [4, 8, 45, 62, 66]. Sustained changes in flow or pressure (e.g. hypertension), induce altered turnover of cells, collagen, and possibly elastin, and these changes may alter the material properties of the tissue as well as its geometry and biological function. It has been found that hemodynamically altered wall shear stresses and intramural stresses (or strains) correlate well with changes in the production of vasoactive, growth regulatory, inflammatory, degradatory, and adhesive molecules by vascular cells [66]. In the vascular field, it has been recognized that "there is a pressing need to predict growth and remodeling of arteries in response to altered mechanical environments and to elucidate the underlying mechanisms" [62], and because of the abundance of available literature on G&R in vasculature it may serve as a basis for studying G&R in other tissues.

In arteries, elastin fibers form densely packed, concentric fenestrated elastic sheets. As pointed out in a recent study [49], "the causal relationship between the microstructure of elastin in native tissues and its functional role remains relatively unexplored." The primary role of elastin in most blood vessels is thought to be to redistribute wall stresses. It is well-known that elastin degradation occurs during aging, and is accountable for the loss of compliance in many tissues, including arteries and heart valves [17, 49, 62]. In a recent study, a quantitative investigation of the time-course changes in porcine aortic media during hypertension showed that the relative elastin content in hypertensive animals decreased significantly after four weeks of hypertension [62]. Because arterial disease is associated with elastin loss, elastin digested tissues are used to investigate the effects of elastin loss [37, 71, 81]. Thus, in general, loss of elastin has been the focus of most investigations, in contrast to the possible relevance of production of elastin.

The driving mechanisms and the underlying processes for G&R are likely to be tissue-dependent, and hence a universal mechano-growth law likely does not exist [150]. However, general trends among tissues with similar compositions should be apparent. In a general sense, the constituents (smooth muscle (SM), collagen, and elastin) of the urinary bladder wall (UBW) are similar to those found in arterial tissue. Moreover, we have demonstrated that the UBW undergoes profound remodeling in response to different pathologies, which makes it a particularly attractive tissue model to study remodeling mechanisms. In particular, spinal cord injury (SCI) above the lumbar level can lead to severe lower urinary tract dysfunctions including bladder outlet obstruction and urinary retention [35, 168]. These dysfunctions are accompanied by changes in the UBW tissue morphology and fibrosis [34, 102], drastic changes in the mechanical properties (clinically reflected by compliance) of the wall [47, 50, 137, 152, 172], altered ECM components [47, 106, 107, 152], and hypertrophic and reorienting bladder SM cells [47, 109, 152]. By examining time-course changes, it was found that the changes in elastin/collagen concentration ratio closely paralleled the change in compliance, with higher elastin content at all time points post-SCI as compared to normal tissue [152]. These changes all eventually lead to the inability of the organ to normally fill and void. In the immediate period after injury, the bladder is subjected to prolonged periods of high strain, and as a result, bladder tissue remodels profoundly to compensate for the change in mechanical environment. We believe that the bladder aims to restore organ-level function, e.g., increased storage capacity at

low intravesical pressure, in contrast to other soft tissues such as blood vessels which are assumed to remodel in response to an increase in blood pressure, by restoring the circumferential wall stress to a homeostatic value.

As in other muscular tissues, the main load bearing structures in the UBW are SM and collagen fibers, where the collagen fiber network serves to bind the SM together and provides resistance to high strains. The collagen structure is optimized to function in each individual tissue type [112]. UBW mainly contains fibrillar bundles of type I and type III collagen, which are mainly found in the lamina propria and serosal layers, between the SM bundles in the detrusor and between individual muscle cells within the muscle fascicles [76, 104]. In addition, it has been shown that collagen fibers exist in a coiled form when the urinary bladder is empty, and they straighten out during filling [16, 97, 104]. This suggests that the collagen structure in UBW tissue exhibits a unique multi-level hierarchy of coils, with super-coiled structures in addition to intrinsic fiber crimp, which allows for the accommodation of very large strains. In contrast, elastin in the normal UBW is found mainly in the vasculature, with small additional amounts throughout the tissue [41, 77, 104, 125]. The production of elastin after intravesical obstruction [127] or as a result of SCI [106, 107, 152] is remarkable, primarily since elastin is generally assumed to be metabolically stable with negligible turnover rates [136]. It has been suggested in arteries that elastic fibers keep the collagen in a more coiled state to enhance the extensibility of the collagen fiber network, as was evidenced by stretching out of post-elastase treated artery specimens [37].

We have previously shown that the mechanical behavior of the ECM can be isolated from the rest of the tissue through testing of decellularized bladder tissue [108]. Extensive re-analysis of the mechanical data from this study warranted more thorough quantitative investigation of the effect of elastin on post-injury UBW ECM. Based on this, we hypothesize that the main effect of *de novo* produced elastin post-injury is to keep collagen in a more highly coiled state, thereby indirectly affecting the compliance of post-injury UBW tissue.

Thus, the goal of the present study is to investigate the effects of *de novo* synthesized elastin fibers on UBW ECM mechanical behavior, utilizing a structural approach incorporating a fiber recruitment function motivated by its unique super-coiled collagen structure. Biaxial mechanical stress-stretch data of normal UBW ECM were fit to a structural constitutive model to obtain the mechanical behavior of collagen fiber ensembles. The resulting fiber ensemble model

was combined with an experimentally derived fiber distribution function to determine the biaxial mechanical behavior of normal UBW ECM, from both newly and previously obtained data [108]. In addition, model parameters were modulated based on functional observations to quantify post-injury biaxial mechanical data from our previous study [108].

6.2 METHODS

6.2.1 Experimental methods

Detailed methods were described in Chapter 5.0 . Experimental methods of UBW ECM structural and mechanical analysis comprised the following components: tissue preparation and decellularization (section 5.1); structural analysis of UBW ECM (section 5.3.1); stress and strain calculations (section 5.2.1); biaxial mechanical testing of normal UBW ECM (section 5.2.2). With regards to analysis of mechanical testing results, the loading portion of the data from the last cycle of the middle equibiaxial stretch protocol (1:1) was used for analysis and model fitting. The stress-stretch data were presented as mean ± standard error of mean (SEM) of a representative subset of data points, for both stress and stretch. This newly obtained stress-stretch data set is referred to as data set 1 (Table 5.1). Equibiaxial stress data presented in the current study from decellularized normal and post-injury rat UBW tissue were obtained from a previous study and detailed methods were presented in [108]. The summary of these methods to obtain data on the mechanical effect of *de novo* elastin on UBW ECM was presented in section 5.4.5. These data sets from normal and post-injury bladders are referred to as data sets 2 and 3, respectively (Table 5.1) All data are presented as mean ± standard error of mean (SEM).

6.2.2 Constitutive model

The adopted model framework is based on a separate treatment of the mechanical behavior for the muscle and ECM components, as proposed in other tissue areas [59, 179]. The present study focuses on the model development for the collagen rich ECM constituent. Building upon the

theoretical work introduced by Lanir [60, 82, 84, 86], a structurally based modeling approach for planar collagenous tissues was developed in which the tissue-level response is related to the collective contribution of individual fiber ensembles. The term fiber ensemble refers to a collection of fibers sharing a common orientation. This modeling technique treats the fibrillar ECM component by homogenizing the fiber ensemble response. This approach was later extended in our lab by demonstrating that the complete planar biaxial mechanical response of the tissue could be simulated by combining the fiber ensemble stress-strain response, derived from a single equibiaxial test, with the experimentally determined fiber angular distribution [129]. It is this later method we exploit in the present study.

Detailed model equations were presented in sections 3-2.1.5 and the relevant equations and definitions are repeated here. The complete tissue-level (ECM) strain energy density function Ψ assumes the form

$$\Psi_{ECM}\left(\mathbf{E}\right)=\int_{\theta}R\left(\theta\right)\,\Psi_{col}^{ens}\left(E^{ens}\left(\theta\right)\right)d\theta\,, \tag{2.3}$$

where $R(\theta)$ is the fiber angular density function, Ψ^{ens} is the strain energy associated with an individual fiber ensemble, which in-turn equals the sum of individual fiber strain energies of the ensemble, and $E^{ens}=\mathbf{N}^{T}\mathbf{E}\mathbf{N}$ is the uniaxial Green-Lagrange strain acting in the ensemble direction. Assuming a pseudoelastic, hyperelastic model, the tissue-level 2nd Piola Kirchhoff stress **S** is given by

$$\mathbf{S}(\mathbf{E})=\frac{\partial\Psi\left(\mathbf{E}\right)}{\partial\mathbf{E}}-p\mathbf{C}^{-1}\,, \tag{2.2}$$

where the Lagrange multiplier p accounts for the incompressible nature associated with non-fibrillar components of the ECM. In the present study, p was eliminated as a result of the configuration of planar biaxial testing. The fiber ensemble stress-strain relation (S^{ens} – E^{ens}) is described in terms of a fiber recruitment function D as

$$S_{col}^{ens}(E^{ens})=K\int_{0}^{E^{ens}}D(x)\frac{E^{ens}-x}{\left[1+2x\right]^{2}}dx\,, \tag{2.7}$$

where the variable of integration x represents the slack strains E_s, and where for convenience the fiber volume fraction ϕ_f is absorbed into the fiber effective modulus such that $K=\phi_f\eta$. The recruitment function $D(E_s)$ is defined by a bimodal modified beta function (Eq. (2.13)), in terms of two means and standard deviations (μ_1, σ_1, μ_2, σ_1), a scaling factor γ, and the upper bound

strain that defines the point when all fibers are recruited (E_{ub}). Combining Eqs. (2.2), (2.3) and (2.7) leads to a complete formulation for stress in the ECM component

$$\mathbf{S}_{ECM}(\mathbf{E}) = K\int_{-\frac{\pi}{2}}^{\frac{\pi}{2}} R(\theta)\left\{\int_0^{E^{ens}(\theta)} D(x)\frac{E^{ens}(\theta)-x}{(1+2x)^2}dx\right\}\mathbf{N}\otimes\mathbf{N}\,d\theta\,. \tag{2.9}$$

6.2.3 Normal UBW ECM fiber ensemble model fitting

For each of the $S^{ens} - E^{ens}$ curves, the upper bound strain and stress (E_{ub}, S_{ub}) and the maximum tangent modulus (MTM) were directly determined from tangent modulus calculations by performing a running linear regression of the $S^{ens} - E^{ens}$ curve. Subsequently, the data sets were thinned to facilitate lower fitting times, and S^{ens} values were scaled with a factor $20\cdot\max(S^{ens})$, because K was typically three or more orders of magnitudes larger than the other parameters. Parameter estimation was performed using custom written files in MATLAB (v.7.6.0 R2008a), with a nonlinear constrained minimization algorithm (a sequential quadratic programming Quasi-Newton line-search method) to minimize the sum of squared errors (SSE) between the experimental and model stress values

$$SSE = \sum_i \left(S^{ens}_{\mathrm{mod},i} - S^{ens}_{\mathrm{exp},i}\right)^2 \tag{3.4}$$

subjected to lower and upper bounds and inequality constraints on the parameters. For the fiber ensemble model with a unimodal beta distribution, the bounds on the parameters were as follows: $0.75\cdot\mathrm{MTM} < K < 5\cdot\mathrm{MTM}$, $1\cdot10^{-4} < \mu < 0.9999$, $10^{-5} < \sigma < 0.577$, where $\sigma = 0.577$ is the maximum value where the beta function had a unimodal shape (Eq. (2.11), $s_1, s_2 > 1$). For the fiber ensemble model with a bimodal beta distribution, the bounds were $0.75\cdot\mathrm{MTM} < K < 5\cdot\mathrm{MTM}$, $10^{-4} < \mu_1 < 0.9999$, $10^{-5} < \sigma_1 < 0.577$, $10^{-10} < \gamma < 0.5$, $10^{-3} < \mu_2 < 0.9999$, $10^{-4} < \sigma_2 < 0.577$. The nonlinear constraints on μ and σ, for both models, were derived from $s_1, s_2 > 1$ (Eq.(2.13)), and for the bimodal model the linear constraint $\mu_1 - \mu_2 < 0$ was imposed.

Numerical integration was performed using recursive adaptive Lobatto quadrature ("quadl", see section 3.1.1). Fitting was performed in subsequent steps motivated by the tissue structure, to determine the parameters of the individual peaks in $D(E_s)$. For each fitting step, initial guess values for the parameters were determined by exploring the error function for a

range of parameter values (*i.e.*, error space). Data sets referenced to both reference states (data sets 1-a and 1-b) were each fit to determine model parameters. The parameters to be fit were K, μ and σ for the model with the unimodal recruitment function, and K, μ_1, σ_1, γ, μ_2 and σ_2 for the model with the bimodal recruitment function. Note that at this stage, E_{ub} was not included as a fit parameter.

To establish initial parameter values, the data were fit to the fiber ensemble model with a unimodal beta distribution first, with as initial guess values K = MTM and μ and σ from exploring the error space to estimate optimal values. The value of K (K_1) found from this fit was used as initial guess for the next steps. Secondly, to determine the initial values of the first peak of the bimodal beta distribution, the lower half of the data (up to a strain of $0.5 \cdot E_{ub}$) was fit separately to a unimodal model, with $K' = \gamma \cdot K_1$, and a guess value for γ. The error space (μ_1 vs. σ_1) was investigated for several values of K'. The resulting minimum values for μ_1, σ_1, and $\gamma = K_1/K'$ were used as guess values for the final fit. Next, the error space of μ_2 and σ_2 was explored for $K = K_1$ and $\gamma = K_1/K'$ to obtain guess values for μ_2 and σ_2. As the final step, all parameters were fit simultaneously to the fiber ensemble model with the bimodal recruitment model.

Average values for K and E_{ub} were determined from the 7 specimens, for each reference state. Average values for the recruitment function parameters (μ_j, σ_j, γ; j=1,2) could not simply be obtained through averaging because of the nonlinear nature of the function. The scaled nature of the beta function allowed for calculation of $D(y)$ for the normalized strain range of [0,1] for each individual specimen and for both reference states using the fit parameters. To obtain average parameters, Eq. (2.13) was fit to these results of all 7 specimens simultaneously.

6.2.4 Determination of normal UBW ECM mechanical behavior

The fiber ensemble response for UBW ECM with average model parameters from data set 1-b, was combined with an expression for the fiber distribution $R(\theta)$ to yield the full tissue model (Eq.(2.9)). Model stress values in both directions were calculated for each data set for the experimental stretch range up to the average maximum stretch, using Romberg integration as described before [129]. As in our studies on pericardium, $R(\theta)$ was derived from small angle light scattering (SALS) data (section 5.3.2). The results of a sample filled with 0.2 ml was used for analysis. Σ was determined (μ = 0) for a mean distribution of collagen fiber angles of 15

representative locations in the specimen. The resulting fiber distribution was modeled using a beta distribution with the mean μ_θ and standard deviation σ_θ [129, 131].

6.2.5 Normal and post-injury stress-stretch data analyses

In order to compare our previously obtained results with the data set of the current study (data sets 2 and 3 vs. data set 1-b), several features in the data needed to be altered. Firstly, average thickness values between the two studies were different. Data set 2 was re-analyzed using the average thickness value from the present study, and stresses were calculated with respect to the post-preconditioned tare-loaded dimensions (Ω_4). For data set 3, thickness values were corrected with the same factor, under the assumption that the same amount of error was introduced in the post-injury specimen thickness measurements as in the normal. Secondly, previous biaxial testing was performed starting from a tare-load of 0.5 g, as opposed to 0.1 g for the current testing. Since the tissue specimens exhibited high extensibility in the low stress range, the portion of the data between 0.1 and 0.5 g was absent in data set 2. In order to let the stress-stretch curve of data set 2 mimic the stress-stretch curve of data set 1-b, this difference in tare-load needed to be corrected for. As a result, the stress-stretch curve of data set 2 was shifted to the right, based on values from data set 1-b.

6.2.6 Determination of normal and post-injury UBW ECM mechanical behavior

The fiber ensemble response for UBW ECM was combined with $R(\theta)$, and model stress values were calculated for the experimental stretch range of data set 2, as described above for data set 1-b. The same procedure was performed for data set 3, with varied parameters to represent the effect of more highly coiled collagen fibers, *i.e.* a higher value for E_{ub}, and a smaller value for the stretch shift. These values were determined by systematically varying one parameter at a time until the model values were sufficiently similar to the experimental data. K and σ_R were not altered, under the assumption that intrinsic collagen properties and effective fiber distributions did not change substantially as a result of SCI. Note that the recruitment parameters were automatically scaled up due to a larger maximum strain value in data set 3.

6.3 RESULTS

6.3.1 General observations

Decellularization of the intact UBW tissue specimens resulted in specimen extensions, and the resulting decellularized bladder specimens were highly distensible (Figure 5.2, Table 6.1). The dimensions of the tissue specimens increased after each step in the specimen handling and mechanical testing process, e.g. due to mounting in the biaxial testing device and preconditioning ($^{3}_{0}\mathbf{F}$) and due to tare-loading ($^{4}_{3}\mathbf{F}$) (Figure 5.2, Table 6.1 B).

Table 6.1. Mean and SEM values of specimen observations (n = 7)

A. Dimensions and weight

	Width (mm)	Length (mm)	Thickness (mm)	Weight (mg)
Intact	10.0 ± 0.2	8.59 ± 0.49	0.781 ± 0.031	70.6 ± 4.9
decell	12.7 ± 0.3	9.76 ± 0.28	0.832 ± 0.043	92.4 ± 4.7

B. Stretch values

	$^{3}_{0}\mathbf{F}$	$^{4}_{3}\mathbf{F}$
Circumferential	1.25 ± 0.04	1.37 ± 0.05
Longitudinal	1.19 ± 0.03	1.22 ± 0.04

6.3.2 Structure of normal and post-injury UBW ECM

Cross-sections of normal bladder tissue stained with Picroirius red revealed a super-coiling structure of the collagen fibers (Figure 6.1). Under low tissue stretch, the collagen was densely coiled and individual collagen coils were difficult to identify. Under high stretch, the collagen fiber bundles were very elongated and therefore visible in a coiled configuration, and individual fibers were visible within the bundles. The same uncoiling process was visible post-injury, and additionally, at low stretch a denser and more highly coiled structure was visible, as compared to in the normal bladder. Furthermore, coils appeared more elongated in the fully stretched specimen.

SEM images of a cross-section of bladder ECM confirmed previous results [108] of full removal of SM cells after decellularization and confirmed that that fiber bundles still existed in a coiled form after decellularization (Figure 6.2). These coils were also visible in decellularized post-SCI UBW tissue (Figure 6.3A). Histology using Verhoeff van Gieson and elastic trichrome stains convincingly showed the presence and the abundance of elastin fibers in bladder ECM after decellularization both in cross-section (results not shown) and *en-face* (Figure 6.3).

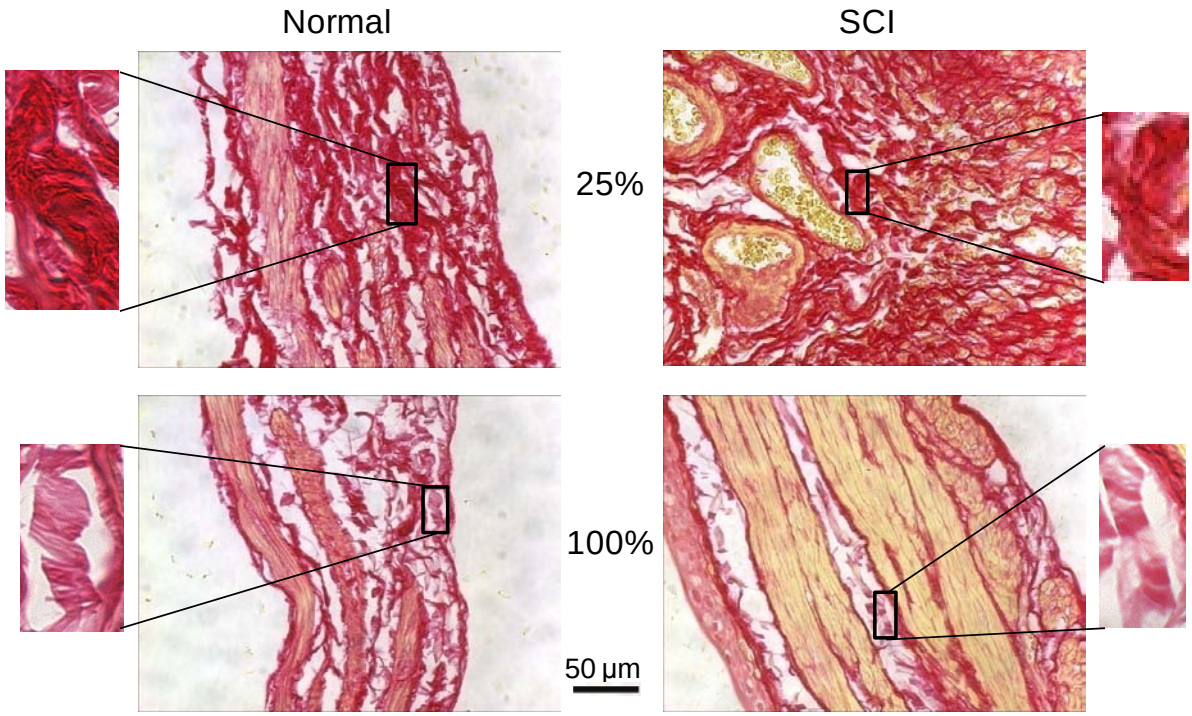

Figure 6.1. Cross-sections of intact bladder specimens, stained with Picro-Sirius red stain. Bladders were filled at 25% or 100% capacity with 10% formalin. Red is collagen, yellow is SM, and yellow discs are red blood cells. The more intense the red staining, the denser the collagen structure. Collagen fibers appear in a highly super-coiled configuration in tissue under low stretch, and collagen super-coils uncoil at higher stretches. Scale bar is 50 µm. Insets show close ups of representative coiling structures.

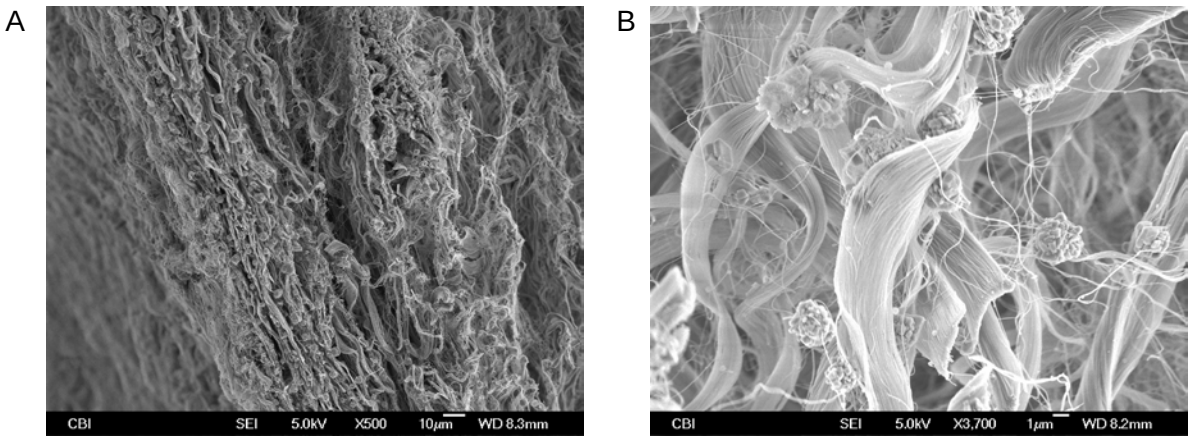

Figure 6.2. Structure of normal bladder ECM.
A) Cross-section of normal decellularized bladder visualized by SEM (magnification 500x, scale bar is 10 μm). Different layers are visible and collagen fibers appear in highly coiled configuration. B) A close-up showing the collagen coils and individual fibers in the coils (magnification 3700x, scale bar is 1 μm). Other visible structures are salt crystals from PBS.

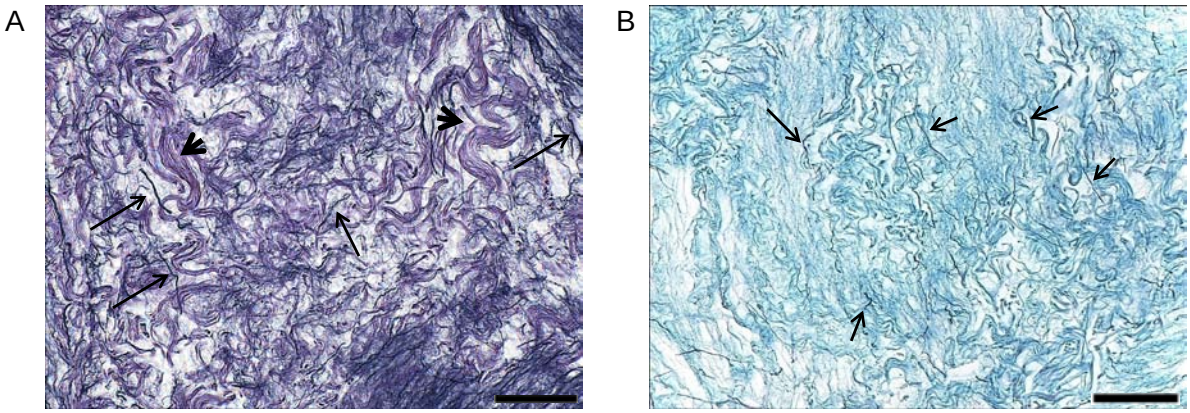

Figure 6.3. Structure of post-SCI bladder ECM.
A) *En-face* section of post-SCI decellularized bladder stained with Verhoef van Gieson stain to visualize elastin (black). Arrows point at examples of elastic fibers, and arrow heads point at collagen coils. Some remnants of SM tissue are visible. B) *En-face* section of post-SCI decellularized bladder stained with elastic trichrome stain to visualize elastin. Arrows point at examples of elastic fibers. Images were enhanced to better visualize the black elastic fibers; scale bar is 50 μm.

6.3.3 Biaxial mechanical testing results of normal UBW ECM

UBW ECM exhibited significant anisotropy (Figure 6.4). Referencing the stress-stretch data to Ω_4 showed lower maximum stresses in the longitudinal direction, suggesting that UBW ECM was more extensible in that direction (Figure 6.4 A). However, referencing the stress-stretch data to the Ω_3, revealed that the tissue was actually more extensible in the circumferential direction (Figure 6.4 B).

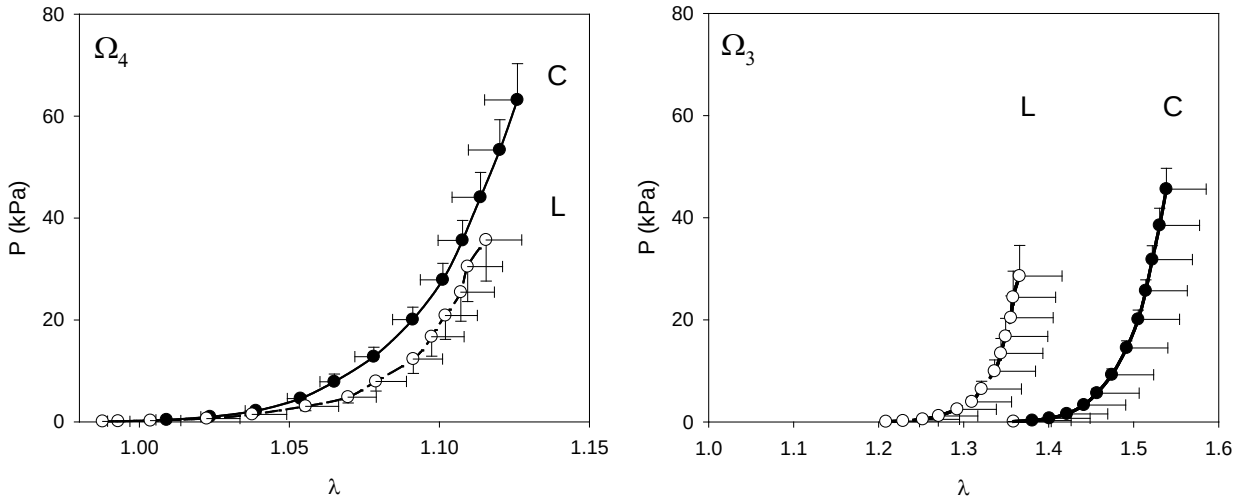

Figure 6.4. Stress-stretch results of biaxial mechanical testing of normal decellularized bladder specimens (mean ± SEM, n = 7), with respect to two different reference states.
P represents first Piola Kirchhoff stress, λ is stretch. Closed circles are circumferential data I, open circles are longitudinal (L). A) Data referenced to Ω_4. B) The same data, referenced to the stress-free state Ω_3, showing that bladder ECM is more compliant in the circumferential direction.

6.3.4 Mechanical effect of elastin on UBW ECM

Equibiaxial stress results of normal and post-injury UBW ECM from our previous study [108] (n = 4 each) revealed that that UBW ECM was more distensible post-injury as compared to normal (Figure 6.5 A). This became more apparent when the data were presented as average stress (average of two directions) vs. areal strain (Figure 6.5 B). Post-injury UBW ECM was significantly more compliant than normal ECM.

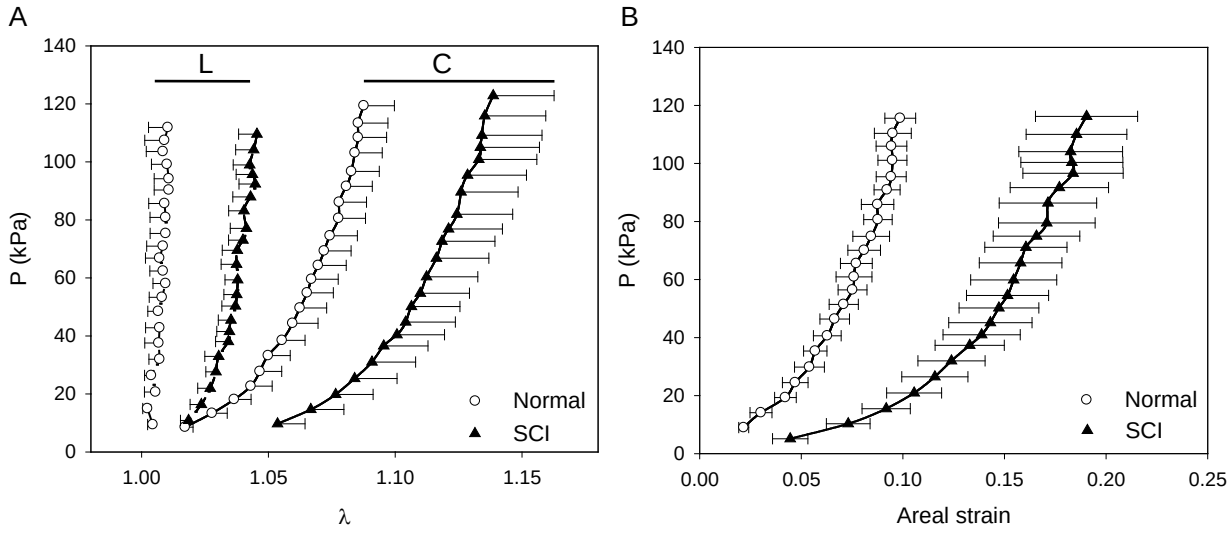

Figure 6.5. Comparing equibiaxial stress data of normal and post-injury decellularized UBW, referenced to Ω_4. (mean ± SEM, n = 4 for each group). P represents first Piola Kirchhoff stress, λ is stretch. Open circles are normal, closed triangles are post-injury. Both normal and post-injury UBW ECM specimens were more compliant in circumferential I direction than in longitudinal (L) direction. B) Average stress (P_{11}, P_{22}) vs. areal strain showing that bladder ECM was significantly more compliant than normal bladder ECM.

6.3.5 Fiber ensemble model fitting

E_{ub}, S_{ub}, and MTM values were determined directly from the experimental data, and average values are listed in Table 6.2. The equibiaxial stretch data of each specimen were fit to the fiber ensemble model with a bimodal beta recruitment function. The average resulting model parameters are listed in Table 6.2 for both reference states. The data referenced to Ω_3 (data set 1-a) were used to determine actual model parameters, and data referenced to Ω_4 to enable comparison with previously obtained data (data sets 2 and 3). Data from all specimens exhibited smooth and convex error surfaces at each fitting stage, which provided confidence in the parameter estimation results (Figure 6.6). Both the low and high stress ranges of the data were fit very well, with average r^2 values of 0.993 for Ω_3 and 0.992 for Ω_4 (Figure 6.8). MTM provided a lower bound of K, and was a good prediction of K for data set 1-b. MTM was lower for data set 1-a because more slack was present in that data. On average, K equaled approximately 3 Mpa, as found from both data sets using both the bimodal and the unimodal recruitment function (Table 6.2). MTM, E_{ub}, and S_{ub} for a representative specimen are presented in Figure 6.7 and Figure 6.8 A. The average recruitment model of the data with respect Ω_3 showed a large second peak and a small first peak (data not shown, parameters in Table 6.2), which was less pronounced than the peak in the data that were referenced to Ω_4 (Figure 6.9).

Table 6.2. Average model parameters.

A

Ref state	E_{ub}	S_{ub} (kPa)	MTM (Mpa)	unimodal model		bimodal model	
				η (Mpa)	r^2	η (Mpa)	r^2
Ω_4	0.115 ± 0.025	58.1 ± 18.6	2.67 ± 1.28	3.06 ± 1.74	0.988	3.38 ± 1.86	0.992
Ω_3	0.539 ± 0.158	32.6 ± 11.1	0.794 ± 0.251	2.95 ± 1.36	0.992	3.07 ±1.49	0.993

B

Ref state	μ_1 (-)	σ_1 (-)	γ (-)	μ_2 (-)	σ_2 (-)
Ω_4	0.581	0.276	0.243	0.864	0.119
Ω_3	0.874	0.107	0.611	0.962	0.0281

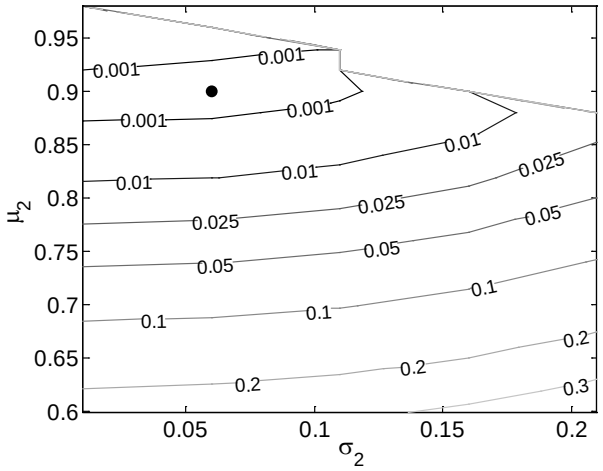

Figure 6.6. Representative error space plot of the fiber ensemble model with bimodal recruitment. The error space of μ_2 vs. σ_2 It shows a smooth and convex error surface with one clear minimum (black dot). The contour lines represent the values of the error function.

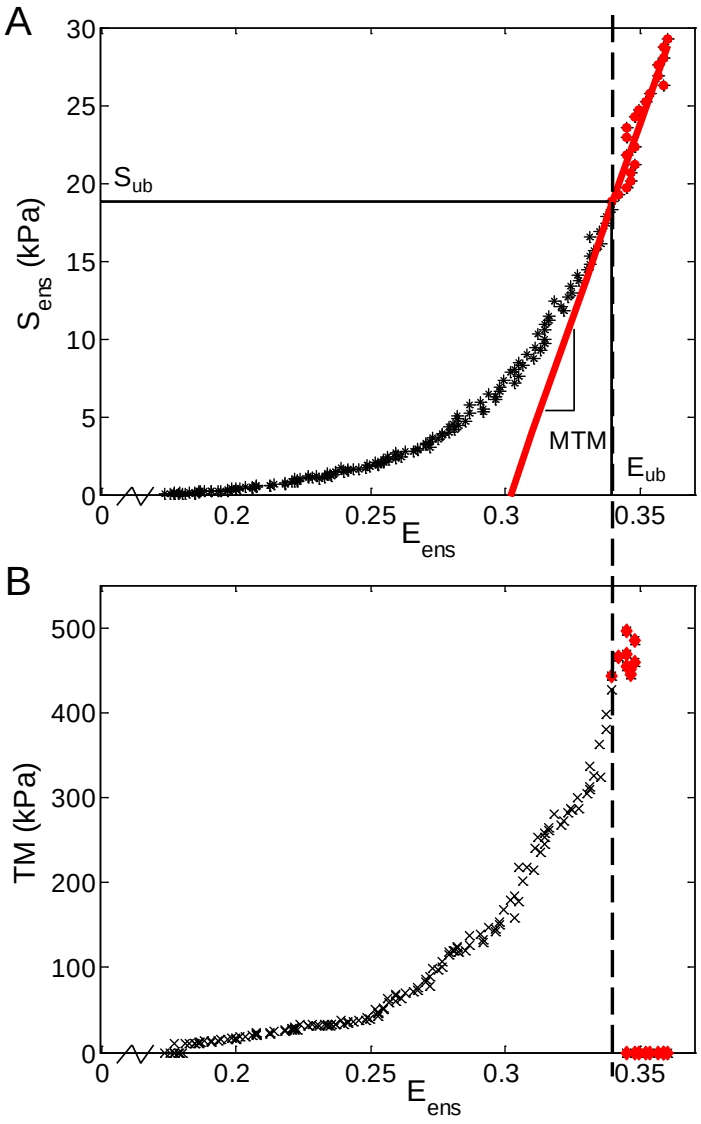

Figure 6.7. Representative plot of determining the maximum tangent modulus.
A) S^{ens} vs. E^{ens} plot with the part indicated where the data is assumed to be linear. B) Tangent modulus I plot indicating the point where it ceases to increase and trails off. This is the value of the maximum tangent modulus (MTM).

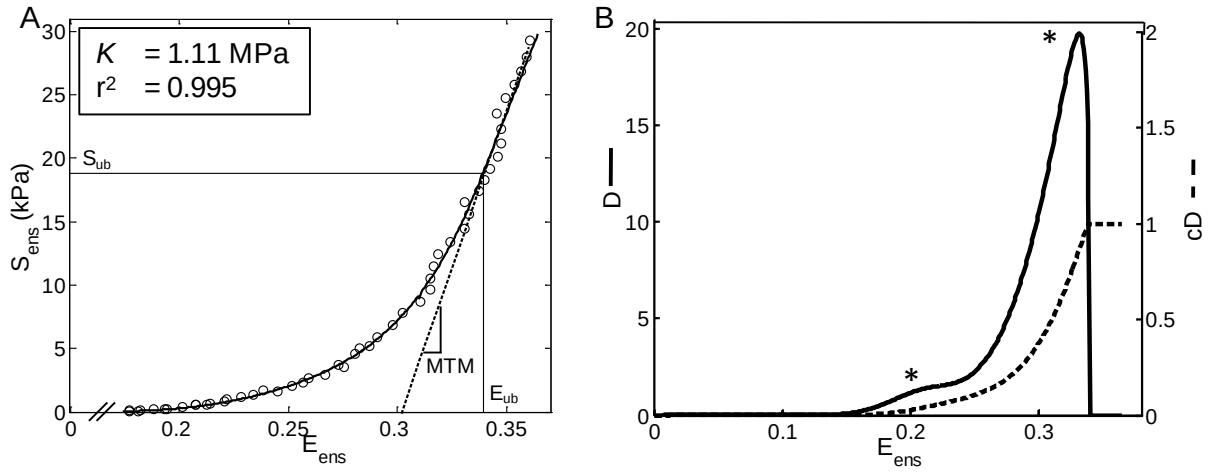

Figure 6.8. Model fitting results of one representative normal bladder ECM specimen (referenced to Ω_3). A) Representative fit of fiber ensemble stress-strain data of one bladder ECM specimen showing an excellent fit (r^2 = 0.995). The upper bound strain and stress are indicated (E_{ub} = 0.34, S_{ub} = 18.8), and MTM is defined as the slope of the line fit through the data points beyond E_{ub} (MTM = 495 kPa). The fiber effective modulus found from the fit is K = 1.11 Mpa. B) Representative recruitment function and cumulative distribution function, of the same specimen, showing two peaks (denoted by *).

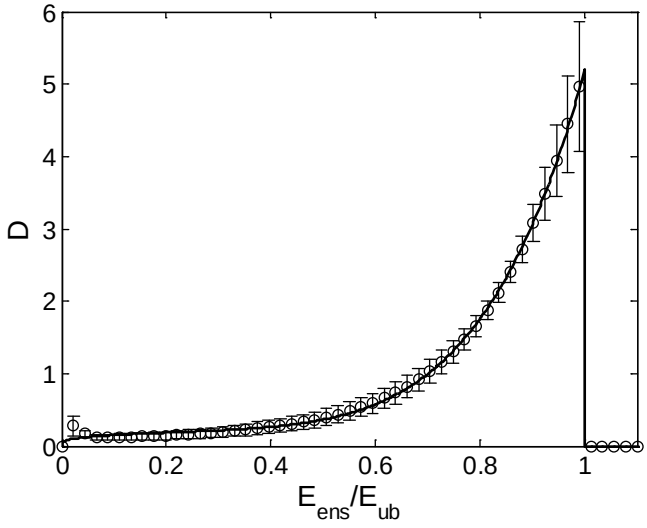

Figure 6.9. Average recruitment function of 6 samples.
Average recruitment function of 6 samples (average ± SEM) (referenced to Ω_4). The parameters are given in Table 6.1.

6.3.6 Determination of UBW ECM mechanical behavior

Combining the average fiber ensemble model determined from data set 1-b (Figure 6.9) with a fiber distribution function $R(\theta)$ (σ_R = 41 deg) (Figure 6.10 C) predicted the overall stress-strain behavior of normal UBW ECM very well (r_C^2 = 0.948, r_L^2 = 0.998, Figure 6.11). The average value of E_{ub} = 0.115 was used, which was a factor 0.86 of E_{max}. σ_R = 41 deg was slightly higher than the average value of 30 deg found from a representative tissue specimen examined with SALS (Figure 6.10 A, B).

To enable comparison of data set 2 with data set 1-b, stress values of data set 2 were recalculated with the average thickness value of data set 1, and stretch values in two directions were multiplied by λ_C = 1.035 and λ_L = 1.043 respectively. The fiber ensemble model as determined from data set 1-b was combined with a narrower $R(\theta)$ (σ_R = 34 deg), and a higher value for the fiber modulus K of 6.8 Mpa. These values deviated from the ones found from data set 1-b, and were determined by systematically varying one parameter at a time until the model values were qualitatively similar to the experimental data (r_C^2 = 0.967, r_L^2 = 0.988, data not shown). The value for K was within the experimental error, since it was equal to the highest value of K found from the fitting of data set 1.

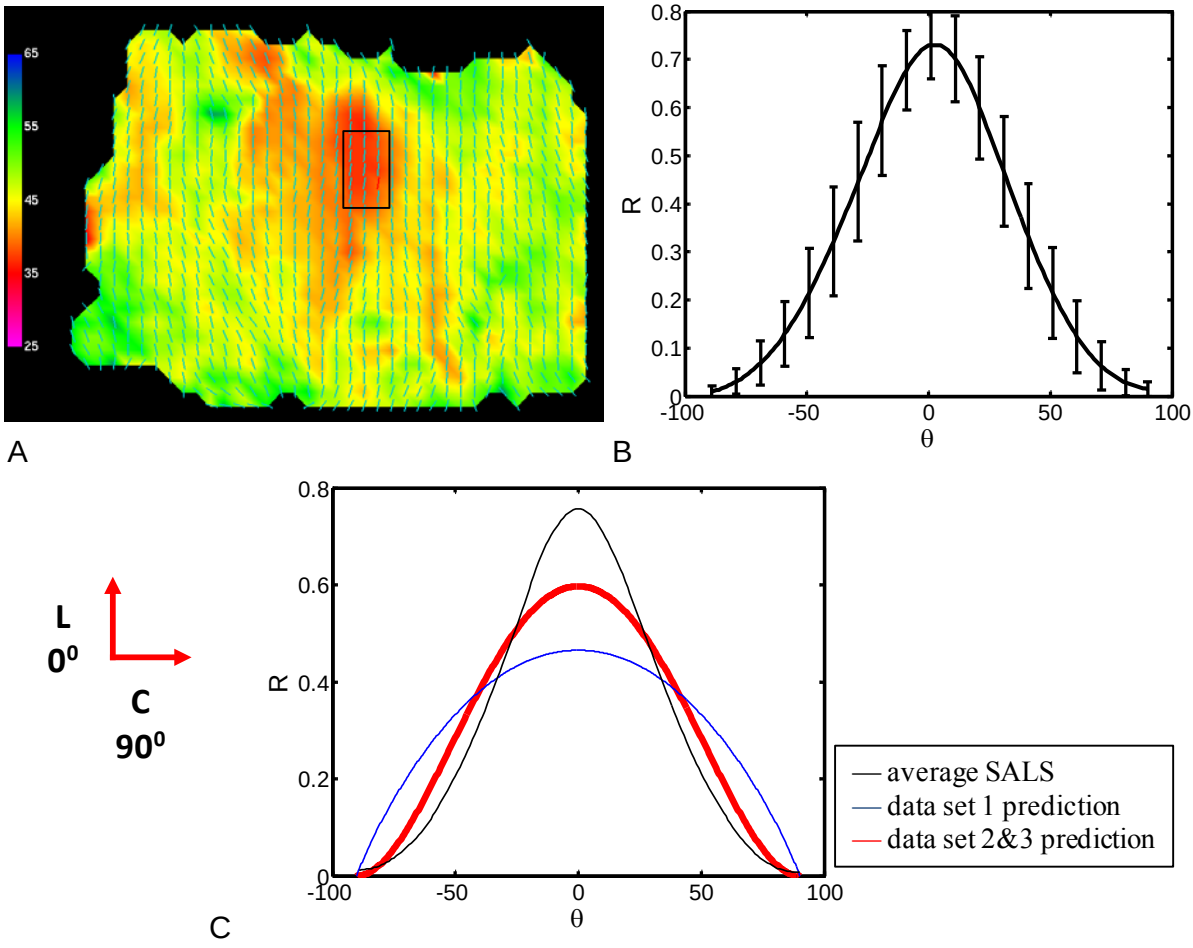

Figure 6.10. Collagen fiber orientation distribution in UBW ECM.
A) Representative result of a SALS test. Vectors indicate preferred direction of the collagen fibers and color is a measure of alignment (pink is high, blue low). Fibers are aligned predominantly in the longitudinal direction (L, 0^o). B) Average fiber distribution of 15 locations in SALS specimen, approximately indicated by box in panel A. C) Comparison of fiber distributions used. Black line is the fit of a beta distribution to the data in panel B, with σ_R =30^o. Blue line is the distribution used for tissue level stress-strain predictions for data set 1, σ_R = 41^o. Red line is the distribution used for tissue level stress-strain predictions for data set 2 and 3, σ_R = 34^o.

In data set 3, the factor E_{ub}/E_{max} was determined to be 0.9 instead of 0.86, which yielded E_{ub} = 0.133. The shift in stretch values was determined to be 1.01 for both directions. Recruitment parameters were automatically scaled up as a result of a higher E_{ub} value. A high correlation between the model with modified parameters and data set 3 was achieved (r_C^2 = 0.995, r_L^2 = 0.993, Figure 6.12 A). The final sets of model parameters for both normal and post-injury UBW ECM were used to calculate the effective fiber ensemble response (Figure 6.12 B). The ensemble responses demonstrated that the altered fiber recruitment post-injury, with a difference in maximum fiber ensemble strain of approximately 3%, resulted in effectively more compliant tissue with a change in areal strain of approximately 10% (Figure 6.5).

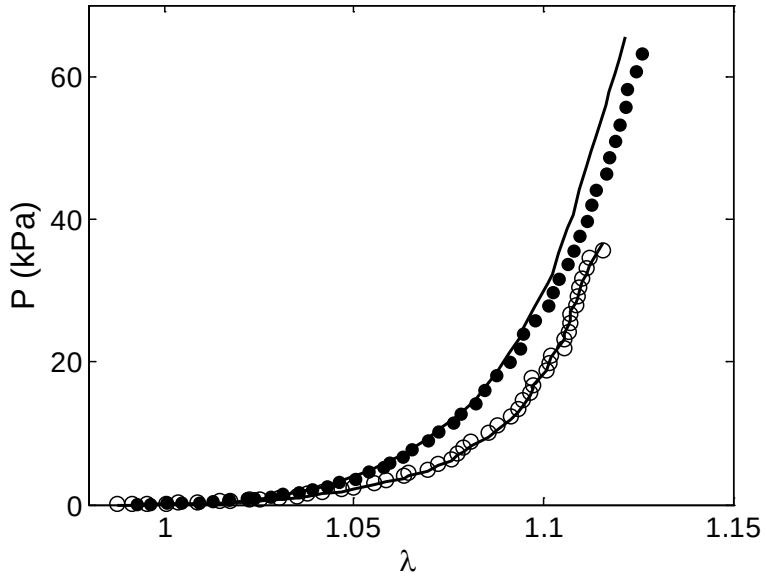

Figure 6.11. Average tissue-level model prediction.
Combining average fitting result of fiber ensemble function, with a fiber distribution function $R(\theta)$, with σ_R = 41 deg, predicted the equibiaxial stretch data very well.

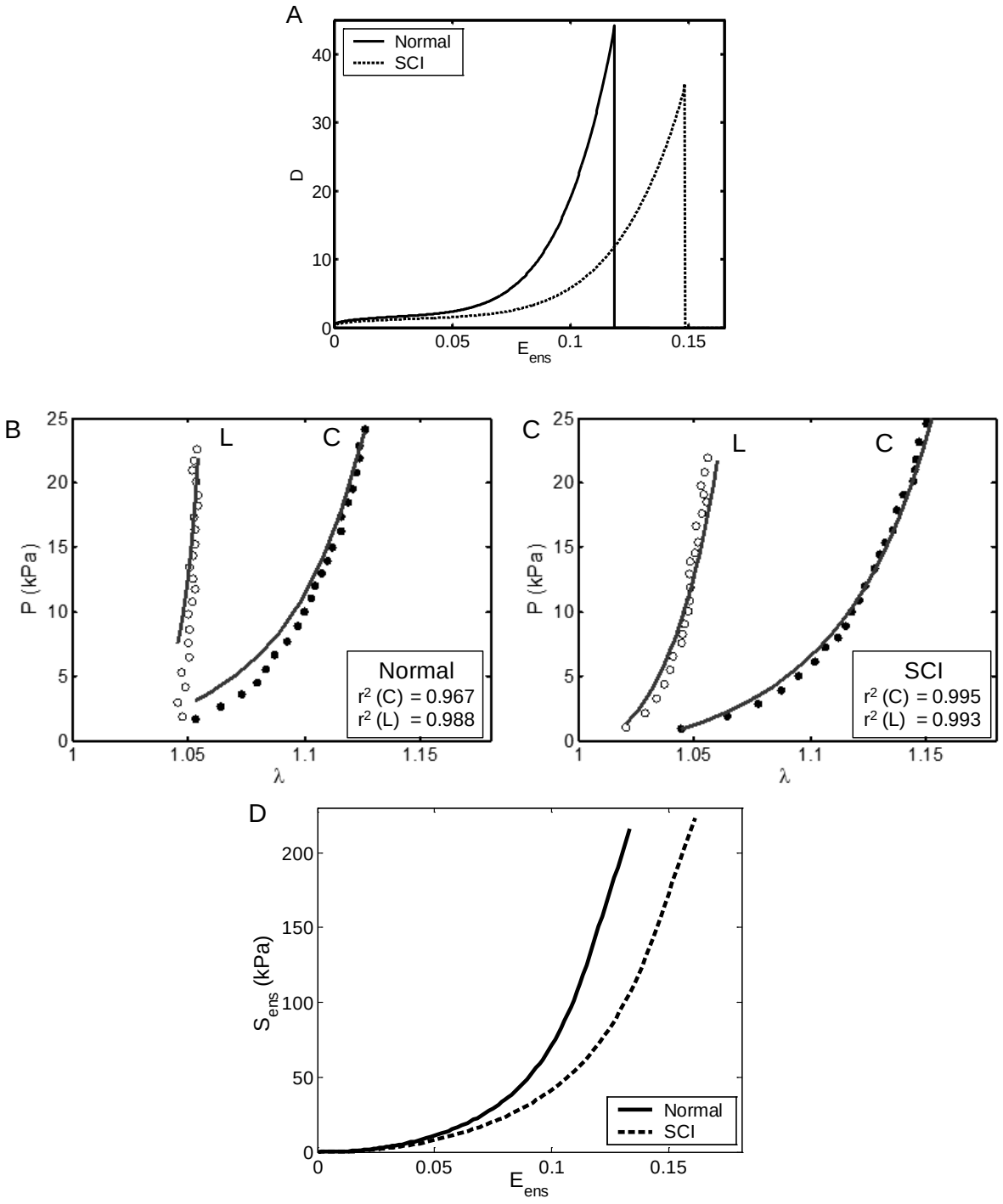

Figure 6.12. Prediction of behavior of normal and post-injury decellularized bladder tissue. Using an average fiber ensemble function (A) plus $R(\theta)$ with σ_R = 34 deg, equibiaxial stress data of normal decellularized bladder (B) and of post-injury decellularized bladder (C) is predicted. D) Prediction of effective fiber ensemble behavior of normal and SCI bladder ECM. Average model parameters from normal tissue, and modified parameters for post-injury tissue were used.

6.4 DISCUSSION

6.4.1 Summary

Removing the SM cells from bladder wall tissue allowed for the separate investigation of the effects of de novo produced fibrillar elastin on UBW ECM. The structural constitutive model of normal UBW ECM was based on a bimodal recruitment function representing the two levels of coiling in the collagen structure, and the correct stress-free reference state was used in the analyses. Key results of the study indicated that the presence of elastin fibers in the UBW ECM post-injury induces, indirectly, a distinct mechanical behavior with higher compliance (Figure 6.12). This was attributed to the presence of more highly super-coiled collagen fibers in post-injury UBW ECM. The present model also suggests two additive mechanisms (Figure 6.13):

1. Elastin fibers exert forces on the existing collagen fiber network resulting in tissue retraction and subsequently in a more highly coiled collagen fiber network in the empty organ.
2. De novo synthesized collagen fibers are produced in this more contracted reference state and thus may form in a more highly coiled configuration.

The results of both mechanisms are:

1. A net increase in ECM compliance allowing for a higher overall extensibility of the post-SCI UBW tissue and increased bladder storage capacity.
2. Continuation of ECM production until the ability of the tissue to extend equals the maximum filling ability.

The UBW G&R mechanism is thus an organ-level driven process which does not necessarily result in re-establishment of a homeostatic stress state, but instead attempts to achieve a degree of overall organ functional restoration.

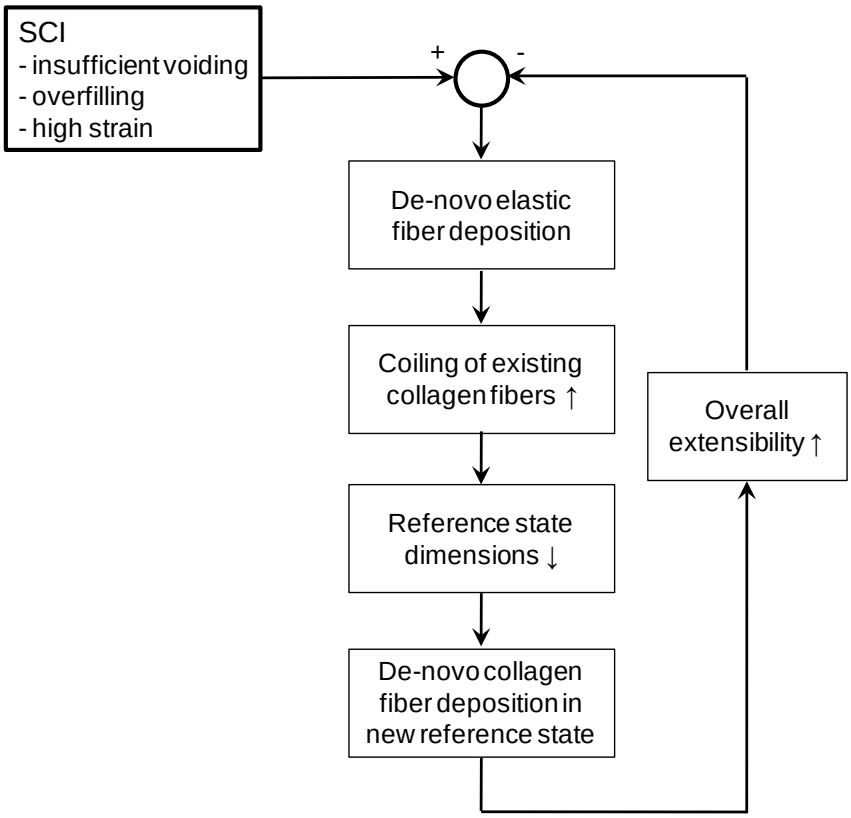

Figure 6.13. Schematic showing the effects of SCI on organ level storage function and UBW compliance. SCI induces overfilling of the bladder and increasing tissue strain, which stimulates elastin production. Elastin fibers pull in existing collagen and make the structure more super-coiled, which in turn decreases the reference state dimensions. *De novo* produced collagen is deposited in a more coiled configuration. This increases tissue compliance and overall extensibility, and eventually decreases the effective tissue strain.

6.4.2 Normal UBW ECM mechanical behavior

The mechanical behavior of decellularized UBW tissue under equibiaxial stretch was utilized to determine collagen mechanical behavior in UBW tissue. Collagen recruitment was shown to occur in a bimodal manner, which was consistent with histological evidence. Specifically, the small first peak represented unwinding of the super-coils, and the larger second peak represented uncrimping of the individual collagen fibers. The model proved to be sensitive to changes in the shape of the recruitment function. Small differences in D produced large effects in the fiber ensemble stress-strain behavior, *i.e.*, the presence of the subtle first peak in D was necessary to fit the experimental data in a satisfactory manner.

Combining the fiber ensemble model including an average recruitment function with an experimentally determined collagen distribution function allowed for simulation of the complete biaxial mechanical behavior of normal UBW ECM. However, because of the extensible nature of the specimens and a difference in tare-load between the data sets, the previously obtained experimental data had to be manipulated in order to be compared with current data. The model with altered collagen recruitment parameters was capable of simulating post-injury mechanical behavior data. Σ_R of the fiber distribution function $R(\theta)$ was slightly different for each analysis, and different from the SALS results, which was justified by the difference in initial stretch state between the data sets, which has an effect on the fiber alignment.

6.4.3 Reference states

The results of the present study emphasized the importance of the correct stress-free reference state to derive physically correct mechanical properties. However, it can also be concluded that in highly extensible soft tissues such as UBW ECM (Figure 6.1), this stress-free state is difficult to define. Traditionally, the tare-loaded state is assumed to be nearly stress-free and is hence used for stress and strain analyses. In robust tissues such as pericardium, the errors induced are negligible. However, stress and stretch values of UBW ECM calculated with respect to the tare-loaded state proved to be significantly different from those calculated with respect to the unloaded state (Figure 6.4), and different conclusions would be drawn from these. Note that the comparison between normal and post-injury tissue was done with data referenced to a tare-

loaded reference state, and hence, caution needs to be taken in interpreting the actual values of the model parameters. In addition, data set 2 and 3 were both referenced to their own individual reference state and not to a common normal reference state, *i.e.* before SCI was induced. This imposes challenges on investigating time-evolving changes.

6.4.4 Decellularization

In our laboratory we previously used decellularized bladder tissue to elucidate properties of the bladder ECM separate from the SM component, and this proved to be a valuable system [108]. Tissue specimens in the current study were decellularized for a shorter time period, which was found not to affect the extent of SM removal (results not shown). Decellularization affected the structure of the ECM, *i.e.*, it resulted in stretching of the tissue specimen and most likely uncoiling of the collagen fiber super-coils. This would also explain the small first peak in the recruitment function. This needs to be taken into account if the results are extended to a complete model of UBW tissue. ECM sheets have been used in different studies to isolate ECM properties and behavior from other, possibly confounding factors, and to assess the individual contribution of a component to the overall tissue mechanical behavior. In decellularized arteries, it has been shown that elastin is connected to vascular SM cells, and decellularization relieves the tension [126]. Elastin is also connected to collagen, and elastase digestion affects collagen recruitment properties [37].

6.4.5 ECM structure and composition

Intact bladder tissue clearly showed the presence of highly coiled collagen bundles (Figure 6.1), which confirmed earlier studies in other animal species [16, 97, 104], and this structure was maintained after decellularization, in both normal and post-injury bladder tissue (Figure 6.2). In addition, the collagen fibers appeared to be more highly coiled in post-injury bladder tissue. Furthermore, massive amounts of elastin are produced post-SCI [107, 152], and it was proven that elastin was still present after decellularization (Figure 6.2 C,D), which has not been observed this clearly in other tissues. In addition, the overall elastin morphology was different

from other tissues, where elastic fibers often appear in sheets. In post-SCI UBW, elastin fibers were sparsely distributed.

6.4.6 Collagen-elastin interaction

The model results indicated that elastin has an indirect mechanical role in post-SCI UBW tissue, resulting in effectively more compliant bladder tissue to allow for higher bladder filling capacity (Figure 6.5, Figure 6.13). Collagen recruitment in post-injury UBW ECM was different from normal (Figure 6.12 B), indicating that collagen fibers existed in a more coiled configuration post-injury. Existing collagen exists in a more coiled configuration, and in addition, *de novo* collagen fibers are produced in a more coiled state because of the retracted reference state of the tissue. The present study suggested that elastin was responsible for this, which has also been suggested previously in the opposite way. In a study comparing control to elastase treated arteries it was concluded that elastin degradation altered the collagen engagement properties, which contributed to functional stiffening of the wall [37]. The same functionality of elastin to keep collagen crimped has been shown in the female reproductive organs. These organs contain large amounts of elastic fibers, with pronounced elastin remodeling during pregnancy and birth [74, 92]. The rebuild of the elastic fiber system aids in maintaining structural and functional integrity of the female pelvic floor after partition, which makes elastin production essential during pregnancy [92].

6.4.7 Collagen fiber super-coiling

Both histological evidence and model results underscored the functional implications of a unique super-coiled collagen fiber structure in the UBW, as also observed in the literature [16, 97, 104]. The two levels of collagen unwinding were incorporated in the structural model by a bimodal beta recruitment function, suggesting a distinct bimodal behavior. However, the average recruitment function (Figure 6.11) showed a less clear distinction, suggesting a more gradual behavior where the coils and the normal crimp straighten out simultaneously after an initial period of just unwinding of the super-coils. Collagen coiling structures at different levels are present in other tissues, such as the heart. However, the level of super-coiling as observed in the

present study is unique to bladder tissue. The coils are present in the connective tissue layers of the bladder and act independently of the SM cells. In addition, the unwinding behavior was detectable mechanically. The collagen fibers in heart muscle, such as the perimysial fibers between myocytes and endomysial fibers connecting the myocytes [15, 98, 122], are all connected to the myocytes and act in concurrence with the muscle fibers.

6.4.8 Model extensions

The present study elucidated the indirect effects of elastin on pathological UBW ECM mechanical behavior. To further elucidate the possible direct mechanical effects of elastin, and possible changes in the SM component on intact bladder tissue, as well as to completely describe time-course G&R events in intact bladder tissue as a result of SCI, the structural model needs to be expanded. Our ultimate goal is to develop a concise structurally based model for soft tissues consisting of collagen, SM and elastin, which simulates tissue-level time-course remodeling events. The first step to model intact tissue is to add a SM component. Similar models have been developed for other muscle containing tissues such as the heart and blood vessels, including structural information of the different tissue components [59, 179].

Our approach to separate the ECM from the tissue will allow us to define the properties of the smooth muscle component more accurately. However, an appropriate common reference state is required for each tissue component, which is the normal intact tissue state before decellularization and before SCI induction. This includes using a correct reference state for newly deposited collagen, which we suggested is deposited in a more highly coiled state. Humphrey and colleagues developed a constrained mixture theory to take this into account [45, 65, 66], which could possibly be used.

Another challenge is to include interaction between the tissue components, since it is becoming recognized that the assumption that the tissue components act in parallel and independently is an oversimplification [37, 126]. As elucidated in the present study, the interaction between elastin and collagen fibers is especially important, and an elastin component needs to be added to the model in some form. Modeling elastin as a simple elastic isotropic network as is done in models of the vasculature [49, 81, 126], will not be sufficient.

6.4.9 Conclusion

We have shown that instead of remodeling to restore wall stress to a homeostatic value, the urinary bladder responds to the prolonged period of high strain due to overfilling by increasing its effective compliance through the interaction between collagen and *de novo* deposited elastic fibers. Thus, bladder tissue is adapting to the functional demand at the organ level. Due to the fact that full physiological recovery is never achieved because of lack of full neural control, the remodeling ultimately results in an irreversible pathological process. Our general modeling framework has the potential to elucidate tissue- and pathology-specific mechanisms in various tissues.

7.0 A STRUCTURAL CONSTITUTIVE MODEL FOR A MUSCLE–CONNECTIVE TISSUE COMPOSITE

7.1 INTRODUCTION

Many different formulations of constitutive models have been developed for many different soft tissues. Soft tissues are generally nonlinear, anisotropic, inhomogeneous, and undergo finite strains. Constitutive models, in particular structural constitutive models, allow for clarifying the relation between tissue mechanical behavior, tissue morphology, the organ's functional state, and related pathologies. Due to the complexity in determining multi-constituent tissue properties, most structural constitutive models for soft tissues focus on a single constituent. However, many tissues contain multiple load-bearing constituents. In connective tissues the main load bearing constituent is assumed to be collagen fibers, whereas in myocardium or skeletal muscle it is muscle cells. Tissues such as the urinary bladder, esophagus, intestines, and arteries contain collagen fibers as well as smooth muscle (SM) cells, which together are considered to provide the tissue with its mechanical strength and stability.

The most advanced constitutive models that explicitly take into account both structural components (collagen and muscle) are those of arterial wall tissue. In these models the total tissue strain energy is assumed to be the sum of the strain energy of the individual tissue components, weighted by their respective volume fractions [37, 121, 178, 180]. Typically in these types of models, collagen fibers are represented by fiber families that run at a specific angle with respect to the center axis. In contrast, a structurally based modeling approach that accounts for the intrinsic mechanical behavior of collagen fibers was originally introduced by Lanir [60, 82, 84, 86], and has been used more recently in several studies [25, 121, 129, 178, 179]. The structural approach, where each model parameter has physiological significance, allows for separate investigation of the contribution of each individual tissue component to the

tissue's mechanical behavior, and eventually will provide the ability to elucidate changes as a result of pathological processes.

Traditionally, collagenous soft tissues are subjected to preconditioning cycles to obtain a reproducible loading-unloading response. The effect of preconditioning itself is usually not included in the mechanical description of tissue behavior, and pseudoelastic stress and strain analyses are performed using the post-preconditioned tare-loaded state, which is assumed to be nearly stress-free. The time-dependent effects of preconditioning have been integrated into comprehensive material characterization of tendons and skin by Lanir and coworkers [93, 94, 149]. This is currently the most sophisticated technique available to include preconditioning effects. Related to the effects of preconditioning is the definition of a correct and experimentally-attainable stress-free reference state. This is an important aspect of developing a finite deformation constitutive model. While the true stress-free state exists in the intact organ, specific experimental methods might call for alternate approaches to define a suitable reference state. In highly extensible soft tissues a true stress-free state is difficult to define (Chapter 6.0), and when combining separate data sets of individual tissue constituents, a common reference state might not be available. In addition, the issue of choosing the optimal reference length is especially important in smooth muscle-rich tissue, because smooth muscle does not have a unique length-tension relationship nor an optimal length at which maximum contraction is performed [161]. Smooth muscle exhibits mechanical plasticity in which the smooth muscle cells constantly adapt to changes in length by actin cytoskeleton modifications leading to shifts in force-displacement curves and peak forces [135].

An excellent example application that underscores these issues is the urinary bladder wall (UBW), which undergoes profound remodeling in response to different pathologies such as spinal cord injury (SCI) [34, 47, 50, 102, 106-109, 137, 152, 172]. UBW tissue is able to undergo large deformations during the filling phase and exhibits highly nonlinear and anisotropic mechanical behavior, as quantified by our laboratory through both quasi-static and stress-relaxation planar biaxial mechanical testing [47, 107, 108]. To elucidate how observed structural and functional changes of individual tissue components are related to altered mechanical behavior and altered organ function, a structural constitutive model of the UBW is needed. As stated in a recent review by Spirka and Damaser [145], "physiological models of the lower urinary tract are in their infancy, but they have the long-term potential to improve our

understanding of physiological mechanisms." In early studies, the bladder typically has been modeled as an elastic sphere under passive stretching conditions, simulating bladder filling. The only attempt that has been made to develop a constitutive model of the complete bladder was by Damaser and Lehman [27, 29, 30]. In this study an incompressible, isotropic and homogeneous model was used to study the effect of bladder shape, mass, and distension on whole bladder mechanics. One of their conclusions was that the shape of the bladder is not as important in modeling of the bladder as are the actual mechanical properties of the wall [29].

To provide a constitutive model with physiologically relevant model parameters, experimental data is required. Our available experimental database contains planar biaxial mechanical data of intact, inactivated UBW (without contribution of SM tone) [47, 152]; SM orientation data [109, 152]; and planar biaxial mechanical data of decellularized UBW and collagen structure data (Chapter 6.0). We have previously shown that the mechanical behavior of the extracellular matrix (ECM) can be isolated from the smooth muscle component through the use of a decellularization technique [108], and we utilized this method to further elucidate the mechanical behavior of UBW ECM by means of a structural constitutive model. This also allowed for separate investigation of the effects of *de novo* produced fibrillar elastin on UBW ECM (Chapter 6.0). Under the assumption that the main load-bearing components of the UBW are SM and collagen, a combination of mechanical data of intact UBW and UBW ECM, together with structural information of both SM and collagen, is sufficient to fully characterize UBW mechanical behavior, including the explicit behavior of each of the two components.

SM contributes significantly to UBW mechanical behavior, especially in the early stages of filling, both under passive and inactivated conditions [113]. Under physiological conditions SM is characterized by basal tone or passive tension that is independent of neural inputs and can lead to spontaneous contractions through myogenic activity [33], which we refer to as the passive state. The basal tone is abolished by subjecting the tissue to a calcium-free saline solution with a calcium chelating agent, which allows for a focus on the inactive behavior of the SM component. In general, it is believed that inactivated SM cells do not contribute to the mechanical behavior of tissues such as the vasculature, and are generally not included in constitutive formulations (*e.g.* [56, 126, 178, 179]), with the exception of one recent study where smooth muscle cells were represented by discrete fiber families [158]. No commonly accepted formulation is yet available for SM in any state and only recently, models describing the

mechanical contribution of SM tone have been developed [78, 142, 179]. However, it is recognized that the material properties in inactive, passive, and active state are different [39, 48].

In the present study, a two-phase structural continuum constitutive model is developed. The two phases are ECM and SM, with the unique feature that both constituents are expressed to a common, intact tissue reference state, while ECM mechanical behavior is determined in decellularized tissues. This is achieved by explicitly defining the net resulting effect of decellularization and preconditioning in the model description by introducing a permanent set term. The model is applied to the inactivated urinary bladder wall. Under the assumption that inactivated SM contributes significantly to the UBW mechanical behavior, it is hypothesized that including the mechanical response of inactivated SM is essential for a complete constitutive model of UBW. The model for the ECM component is extended from our previously developed UBW ECM model (Chapter 6.0), and the functional form of SM is derived from the difference between the strain energy of intact UBW tissue and UBW ECM. The model parameters of UBW ECM and SM are determined separately and both a continuous and a discrete SM fiber distribution are investigated [12]. The two-component structural constitutive model will provide the basis for a growth and remodeling framework that will elucidate mechanical and structural changes in the urinary bladder wall in several pathologies.

7.2 CONSTITUTIVE MODEL

Detailed model equations were presented in Chapter 2.0 and the relevant equations and definitions are repeated here. The schematic representation of the model (Figure 2.6) is repeated in Figure 7.1. The tissue level strain energy density function Ψ is assumed to result from the contribution of SM and ECM, weighted by their respective volume fractions ϕ, and is defined in terms of the Green-Lagrange strain tensor ($\mathbf{E}$) as

$$\Psi\left(\mathbf{E}\right) = \sum_i \phi_i \Psi\left(\mathbf{E}\right) = \phi_{ECM}\,\Psi_{ECM}\left(\mathbf{E}\right) + \phi_{SM}\,\Psi_{SM}\left(\mathbf{E}\right). \tag{2.1}$$

The tissue level 2nd Piola Kirchhoff stress $\mathbf{S}$ is derived from the strain energy density function Ψ as

$$\mathbf{S}(\mathbf{E}) = \frac{\partial \Psi(\mathbf{E})}{\partial \mathbf{E}} - p\mathbf{C}^{-1} = 2\frac{\partial \Psi(\mathbf{C})}{\partial \mathbf{C}} - p\mathbf{C}^{-1}, \tag{2.2}$$

where **C** is the Right Cauchy-Green tensor and p a Lagrange multiplier (see also Chapters 1.0 and 2.0).

The ECM constitutive model was modified from the original formulation that was outlined in section 2.1 and summarized in section 6.2.2. The model modifications were described in sections 2.2 and 2.3 and included introducing a permanent set effect and a correct linear fiber model. The resulting ECM constitutive model, defined in state Ω_1, and expressed in component form, is

$$S_{ECM,11} = \eta\phi_f \int_{-\pi/2}^{\pi/2} R_1(\theta')\, {}_0^1\lambda(\theta')^2 \left\{ \int_1^{{}_1^t\lambda^{ens}(\theta')} D_1(x,\theta') \left(1 - \frac{x}{{}_1^t\lambda^{ens}(\theta')}\right) dx \right\} \cos^2(\theta')\, d\theta'$$

$$S_{ECM,22} = \eta\phi_f \int_{-\pi/2}^{\pi/2} R_1(\theta')\, {}_0^1\lambda(\theta')^2 \left\{ \int_1^{{}_1^t\lambda^{ens}(\theta')} D_1(x,\theta') \left(1 - \frac{x}{{}_1^t\lambda^{ens}(\theta')}\right) dx \right\} \sin^2(\theta')\, d\theta' \tag{2.46}$$

$$S_{ECM,12} = \eta\phi_f \int_{-\pi/2}^{\pi/2} R_1(\theta')\, {}_0^1\lambda(\theta')^2 \left\{ \int_1^{{}_1^t\lambda^{ens}(\theta')} D_1(x,\theta') \left(1 - \frac{x}{{}_1^t\lambda^{ens}(\theta')}\right) dx \right\} \cos(\theta')\sin(\theta')\, d\theta'$$

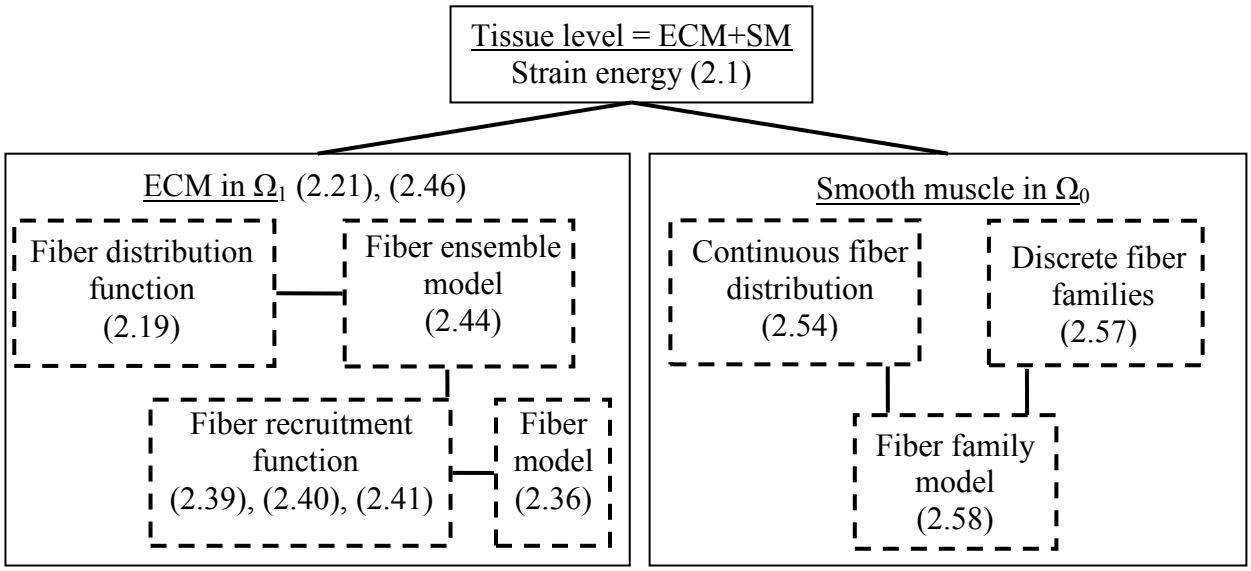

Figure 7.1. Schematic overview of the interrelations of the components of the multi-phase structural constitutive model. The numbers refer to the equations.

In this, the following definitions are used.

- The permanent set ensemble stretch ($ {}^{1}_{0}\lambda\left(\theta'\right)$) is derived from the deformation gradient tensor $ {}^{1}_{0}\mathbf{F}$ as

$$ {}^{1}_{0}\lambda\left(\theta'\right) = \mathbf{N}^{T}\left[\theta\left(\theta', {}^{1}_{0}\mathbf{F}\right)\right] {}^{1}_{0}\mathbf{F}^{T}\, {}^{1}_{0}\mathbf{F}\ \mathbf{N}\left[\theta\left(\theta', {}^{1}_{0}\mathbf{F}\right)\right] \tag{7.1}$$

- The fiber distribution function $R_1(\theta')$, where θ' is the fiber angle in Ω_1, is defined via $ {}^{1}_{0}\mathbf{F}$ in terms of the fiber distribution function $R_0(\theta)$ in Ω_0, and is given by

$$R_1\left(\theta'\right) = R_0\left[\theta\left(\theta', {}^{1}_{0}\mathbf{F}\right)\right]\frac{ {}^{1}_{0}\lambda\left(\theta'\right)}{ {}^{1}_{0}J}. \tag{2.19}$$

- The fiber ensemble model ($ {}^{t}_{1}S^{ens}\left({}^{t}_{1}\lambda^{ens}\right)$, *ens* = ensemble), in terms of a recruitment function ($D(\lambda_s)$) and with η the collagen fiber modulus and ϕ_f the fiber volume fraction, is defined by

$$ {}^{t}_{1}S^{ens}\left({}^{t}_{1}\lambda^{ens}\right) = \eta\phi_f\, {}^{1}_{0}\lambda^{2}\int_{1}^{ {}^{t}_{1}\lambda^{ens}} D_1\left(x\right)\left(1-\frac{x}{ {}^{t}_{1}\lambda^{ens}}\right)dx, \tag{2.44}$$

- The function $D({}_1\lambda_s,\theta')$, which describes the distribution of slack stretches ${}_1\lambda_s$ is given by

$$D_1\left({}_1\lambda_s,\theta',\mu,\sigma\right) = \begin{cases} \dfrac{B\left(y,s_1,s_2\right)}{ {}_1\lambda_{\mathrm{lb}}\left(\theta\left(\theta', {}^{1}_{0}\mathbf{F}\right)\right) - {}_1\lambda_{\mathrm{ub}}\left(\theta\left(\theta', {}^{1}_{0}\mathbf{F}\right)\right)} & {}_1\lambda_{lb} \le {}^{t}_{1}\lambda_s \le {}_1\lambda_{ub} \\ 0 & \text{otherwise} \end{cases}, \tag{2.39}$$

with the lower and upper bound stretch, respectively, defined as

$${}_1\lambda_{\mathrm{lb}} = \frac{ {}_0\lambda_{\mathrm{lb}}}{ {}^{1}_{0}\lambda_{\mathrm{ens}}\left(\theta\left(\theta', {}^{1}_{0}\mathbf{F}\right)\right)}, \quad {}_1\lambda_{\mathrm{ub}} = \frac{ {}_0\lambda_{\mathrm{ub}}}{ {}^{1}_{0}\lambda_{\mathrm{ens}}\left(\theta\left(\theta', {}^{1}_{0}\mathbf{F}\right)\right)}, \tag{2.40}$$

and y a scaled variable:

$$y\left({}_1\lambda_{\mathrm{s}}\right) = \frac{ {}_1\lambda_{\mathrm{s}}\left(\theta'\right) - {}_1\lambda_{\mathrm{lb}}\left(\theta\left(\theta', {}^{1}_{0}\mathbf{F}\right)\right)}{ {}_1\lambda_{\mathrm{ub}}\left(\theta\left(\theta', {}^{1}_{0}\mathbf{F}\right)\right) - {}_1\lambda_{\mathrm{lb}}\left(\theta\left(\theta', {}^{1}_{0}\mathbf{F}\right)\right)}. \tag{2.41}$$

Two models are proposed for the smooth muscle component, as introduced in section 2.4, one with a continuous fiber distribution and one with two discrete orthogonal families of fiber bundles. When investigating both models, it was observed that two different functions for the two different fiber families were required. For the continuous model, two beta functions were used for the fiber distribution function, one with the mean at 0 deg (circumferential direction, C),

and one with the mean at 90 deg (longitudinal direction, L), resulting in the following modified equation for the continuous smooth muscle model (compare to Eq. (2.53)):

$$ {}^{t}_{0}\mathbf{S}_{SM}\left({}^{t}_{0}\mathbf{E}\right)=\int_{-\pi/2}^{\pi/2}\left\{\begin{array}{l}\gamma_{SMC}\cdot R_{SMC}\left(\theta\right)\cdot s_{SMC}\left(E_{SMb}\left(\theta\right)\right)\\ +\left[1-\gamma_{SMC}\right]\cdot R_{SML}\left(\theta\right)\cdot s_{SML}\left(E_{SMb}\left(\theta\right)\right)\end{array}\right\}\mathbf{N}\otimes\mathbf{N}\,d\theta \tag{7.2} $$

R_{smC} and R_{smL} together represent the bimodal distribution given by

$$ R_{SM}\left(\theta\right)=\gamma_{SMC}\cdot R_{SMC}\left(\theta\right)+\left[1-\gamma_{SMC}\right]\cdot R_{SML}\left(\theta\right). \tag{2.54} $$

The model with two discrete families of fiber bundles oriented at $\theta = 0^0$ and 90^0, weighted by a fraction γ, is given as follows:

$$ \mathbf{S}_{SM}\left(\mathbf{E}\right)=\sum_{\theta=0,1/2\pi}s_{SM}\left(E_{SMb}\right)=\gamma\cdot s_{SMC}\left(E_{SMbC}\right)+\left[1-\gamma\right]\cdot s_{smL}\left(E_{SMbL}\right). \tag{2.57} $$

A phenomenological exponential expression is proposed for each SM fiber (bundle) model, for both the continuous and the discrete model:

$$ s_{SMb}\left(E_{SMb}\right)=\mathrm{d}_1\cdot\left[\exp\left(d_2\cdot E_{SMb}\right)-1\right]. \tag{2.58} $$

The corresponding strain energy for the continuous model is subsequently given by

$$ \Psi_{SM}=\int_{-\pi/2}^{\pi/2}\left\{\begin{array}{l}\gamma\cdot R_{SMC}\left(\theta\right)\cdot\left[\dfrac{d_{1C}}{d_{2C}}\exp\left(d_{2C}\cdot E_{SMb}\left(\theta\right)\right)-d_{2C}\cdot E_{SMb}\left(\theta\right)-1\right]\\ +\left[1-\gamma\right]\cdot R_{smL}\left(\theta\right)\cdot\left[\dfrac{d_{1L}}{d_{2L}}\exp\left(d_{2L}\cdot E_{SMb}\left(\theta\right)\right)-d_{2L}\cdot E_{SMb}\left(\theta\right)-1\right]\end{array}\right\}d\theta, \tag{7.3} $$

and for the discrete model by

$$ \begin{aligned}\Psi_{SM}=&\frac{d_{1C}}{d_{2C}}\cdot\left[\exp\left(d_{2C}\cdot E_{SMbC}\left(\theta_C\right)\right)-d_{2C}\cdot E_{smbC}\left(\theta_C\right)-1\right]\\ &+\frac{d_{1L}}{d_{2L}}\cdot\left[\exp\left(d_{2L}\cdot E_{SMbL}\left(\theta_L\right)\right)-d_{2L}\cdot E_{SMbL}\left(\theta_L\right)-1\right]\end{aligned}. \tag{7.4} $$

7.3 METHODS

7.3.1 Summary of experimental methods

Detailed experimental methods were described in Chapter 5.0. Experimental methods related to UBW ECM comprised the following subjects: preparation of UBW ECM tissue samples (section 5.1); stress and strain calculations, including determination of the permanent set deformation ${}^{1}_{0}\mathbf{F}$ (section 5.2.1); biaxial mechanical testing of normal UBW ECM (section 5.2.2); and collagen fiber orientation (section 5.3.2). Related to the composition of intact UBW, the calculation of collagen and SM volume fractions was described in section 5.3.3. Reanalysis of previously obtained data on intact UBW comprised the following: smooth muscle fiber orientation (section 5.4.3) and biaxial mechanical testing of normal intact UBW tissue (sections 5.2.2, 5.4.2). From the available biaxial mechanical data sets of normal intact UBW from two separate studies, four representative data sets were chosen.

7.3.2 Parameter estimation methods for ensemble model

Ensemble model parameters determined in Chapter 6.0 could not be used directly for the full structural model because the model was modified and the biaxial mechanical data was reanalyzed. The fitting process of the ensemble model was performed again, where the upper bound strain/stretch parameter λ_{ub} was included as a fitting parameter, and an initial estimate for λ_{ub} was determined from the ensemble stress strain curve (P^{ens}-λ^{ens} in this case). The fitting of the ensemble model was performed similarly to the procedure described in section 3.2.3, where it was now implemented in a graphical user interface (GUI). Parameter estimation was performed with the MATLAB (Mathworks Inc, Release 2009a) function "fmincon" (a sequential quadratic programming Quasi-Newton line-search method, see section 3.2.2) to minimize the sum of squared errors (SSE) between the experimental and model stress values (in 11 and 22 directions, excluding shear terms), as defined in Eq. (3.4). The minimization was subjected to lower and upper bounds and (in)equality constraints on the parameters. Numerical integration was performed using the MATLAB "quad" function (Adaptive Simpson Quadrature, see section

3.1.1). Termination criteria of the fit were set at a tolerance of 10^{-15}, except for where noted otherwise.

First, initial estimates for K and ${}_1\lambda_{ub}$ were determined from tangent modulus calculations by performing a running linear regression of the un-thinned ensemble stress-strain data calculated from the equi-biaxial strain protocol. Based on the value of the maximum tangent modulus, the stress-values were scaled to decrease the parameter value of K to ~1. Next, the fitting was performed. Initial parameter estimates were set by using μ and σ determined in our previous study, as well as K and ${}_1\lambda_{ub}$ from step 1. The ensemble data were then fit to the fiber ensemble model with a unimodal beta distribution. The beta function was restricted to a unimodal shape with a lower bound of zero, by enforcing $s_1, s_2 > 1$, ${}_1\lambda_{lb}$ was set to value of one, and bounds on the remaining parameters were defined as follows: $0.1 \cdot K_{guess} < K < 3 \cdot K_{guess}$, $1 < {}_1\lambda_{ub} < \lambda_{max}$, $0.1 < \mu < 0.9999$, $0.01 < \sigma < 0.5772$, where $\sigma = 0.577$ is the maximum value where the beta function maintained a unimodal shape. To determine the initial parameter values of the first peak of the bimodal beta distribution, the lower half of the data (up to a strain of $0.5 \cdot {}_1E_{ub}$) was fit separately to a unimodal model with $K' = \gamma \cdot K$ and an initial estimate for γ from the first study (Chapter 6.0). Bounds on the parameters were defined as: $0.01 < K' < 0.5$, $0.01 < \mu < 0.9999$, $0.01 < \sigma < 0.5772$, and ${}_1\lambda_{ub}$ was fixed to a value of one. Fitting termination criteria were set at a tolerance of 10^{-18} for this step. Finally, all parameters of the fiber ensemble model were fit simultaneously with the bimodal recruitment function.

7.3.3 Parameter estimation methods for structural model

The recruitment parameters found from the ensemble model fit were used as initial estimates for the structural model fitting process. Thinned, multiprotocol, biaxial mechanical data in Ω_1, as well as specimen-specific values of ${}^1_0\mathbf{F}$ were loaded into the user interface. Data was further thinned to every fifth data point to speed up the fitting process and was fit to the modified model. The fiber distribution function was assumed to be centered around a mean of zero degrees (longitudinal direction) ($\mu_R = 0$). Values of K, ${}_0\lambda_{lb}$, ${}_0\lambda_{ub}$ and σ_R were explored manually by inspecting the model stress-strain results of the equibiaxial protocol. K had to be increased significantly from the value found in the ensemble model fit because of the scaling artifact introduced by the permanent set. To aid in this process, the stress-strain data in Ω_0 was loaded as

well and appropriateness of values of K, ${}_0\lambda_{lb}$, ${}_0\lambda_{ub}$ and σ_R was assessed. This was alternated until reasonable initial estimates for K, ${}_0\lambda_{lb}$, ${}_0\lambda_{ub}$ and σ_R were obtained. Specifically, when σ_R was altered, ${}_0\lambda_{lb}$, ${}_0\lambda_{ub}$ had to be altered because of their dependency on θ. These initial parameter estimates were used in the fitting process. At every fitting step parameters found from the previous step were used as initial estimates.

During the first fitting step recruitment parameters were kept fixed at the values determined from the ensemble fit, μ_R was set to a value of zero, and the bounds on σ_R were defined as $1 \cdot 10^{-5} < \sigma_R < 0.95978$ (rad), where $\sigma_R = 0.95978$ is the maximum possible value to ensure a unimodal shape for $\mu_R = 0$. Bounds on ${}_0\lambda_{lb}$ and ${}_0\lambda_{ub}$ were set for each data set individually. This first fitting step with extra thinned data determined parameter values for K, ${}_0\lambda_{lb}$, ${}_0\lambda_{ub}$ and σ_R, while keeping the other parameters constant. In the next fitting step, ${}_0\lambda_{lb}$ was set at the value found from the previous step, μ_R was still set at zero, and the rest of the parameters were included in the fit to optimize the recruitment behavior simultaneously with K, ${}_0\lambda_{ub}$ and σ_R. As the final step, the thinning factor was reset to 1 and all parameters were fit simultaneously (with $\mu_R = 0$). To check if the assumption of $\mu_R = 0$ was appropriate, another fit was performed with the bounds $-0.1 < \mu_R < 0.1$.

7.3.4 ECM strain energy in Ω_1 and transforming ECM strain energy in Ω_1 to Ω_0

Parameters as determined from the model fit were used to calculate the ECM strain energy for each individual specimen (Eq.(2.49)) for a relevant generalized strain range in Ω_1 (50x50 data points, assuming shear effects were negligible) that encompassed all specimen specific experimental strain ranges.

To calculate the strain energy of the ECM component in Ω_0 from the strain energy in Ω_1, the changes in volume due to removal of cells as well as retaining of water (swelling) that occurred during decellularization needed to be taken into account. Because of the occurrence of swelling, the stress borne by the ECM as determined in the decellularized state is not the same as the stress that would have been borne by the same ECM component in the intact state. This is demonstrated by a 1D uniaxial tension example using a continuum damage mechanics analogy in 1D [87]. This theory is used to calculate a “swelling factor”.

A bar containing voids ('damage') is subjected to a uniaxial tensile force f on the side with area A, with uniaxial stress defined as $\sigma = f/A$ (state 1, Figure 7.2). This state is equivalent to a UBW specimen consisting purely of ECM, with voids where the SM would be located. In continuum damage mechanics, a fictitious, intermediate (i), undamaged configuration is considered (state 2, Figure 7.2) with a damage factor φ representing the fraction of damage in terms of the undamaged volume. We assume the undamaged state to be equivalent to a UBW specimen consisting purely of ECM. Note that this configuration is theoretical and is not equal to the decellularized configuration. The third configuration (state 3, Figure 7.2) is obtained by theoretically adding water to the intermediate configuration and is equal to the decellularized state.

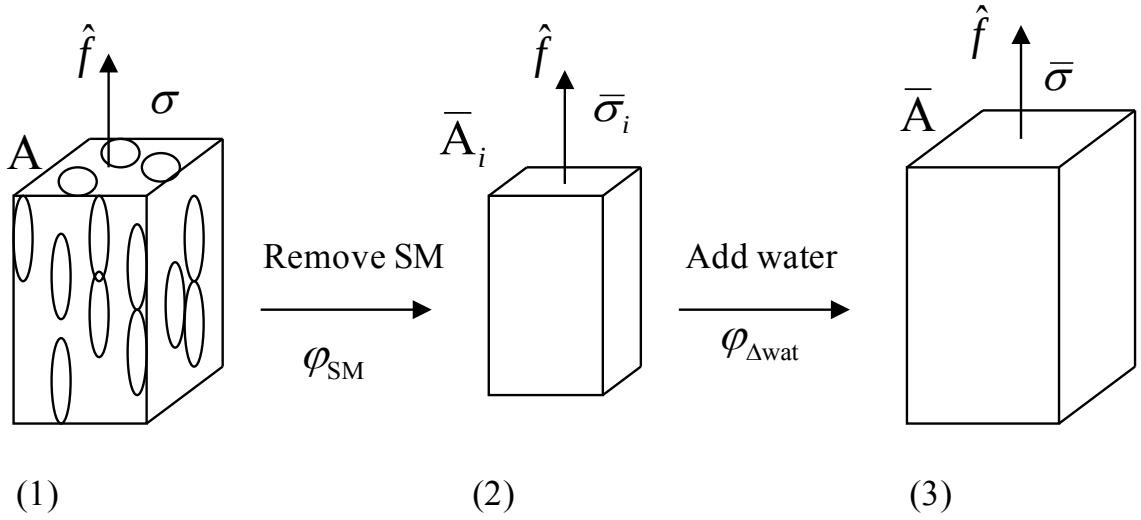

Figure 7.2. Schematic of a bar subjected to uniaxial tension.
State (1) represents a fictitious bladder specimen with voids where the SM cells are supposed to be located. State (2) represents a fictitious intermediate (i) configuration with the SM cells removed. State (3) is obtained by adding water to state (2) and represents a decellularized bladder specimen. A = area, σ = stress, f = force, φ = volume fraction.

The different areas in each configuration are subjected to the same force *f*. This is used to express stresses in each state in terms of known variables. If φ_{SM} is the volume fraction of smooth muscle in state 1 (equivalent to the damage variable φ [87]), then the uniaxial tensile stress in state 2 ($\bar{\sigma}_i$) is expressed in terms of the stress in the intact state (σ) as $\bar{\sigma}_i = \frac{1}{1-\varphi_{SM}}\sigma$. Next, we define the "change of water fraction" between states 2 and 3 in terms of the volume in state 3. Under the assumption that there was no water change between states 1 and 2, it is defined as $\varphi_{\Delta w} = \frac{V_{w3} - V_{w1}}{V_3}$. Using this definition, the stress in state 3 is now defined as $\bar{\sigma} = \bar{\sigma}_i\left(1-\varphi_{\Delta w}\right)$. Combining the two stress relations results in $\sigma = \frac{1-\varphi_{\Delta w}}{1-\varphi_{SM}}\bar{\sigma}$.

Extrapolating this 1D example to a UBW specimen subjected to planar biaxial loading, and noting that the term σ can be seen as equivalent to the 1st Piola Kirchhoff stress borne by the ECM in the intact state ($\mathbf{P}_{\mathrm{ECM}}$), this results in

$$\mathbf{P}_{ECM} = \frac{(1-\varphi_{SM})}{(1-\varphi_{\Delta w})}\mathbf{P}_{decell}, \tag{7.5}$$

where $\frac{1-\varphi_{SM}}{1-\varphi_{\Delta w}}$ is named the "swelling factor". Incorporating this definition in Eq.(2.2) results in

$$\mathbf{P} = \frac{(1-\varphi_{SM})}{(1-\varphi_{\Delta w})}\phi_{ecm}\mathbf{P}_{decell} + \phi_{SM}\mathbf{P}_{SM}. \tag{7.6}$$

Accurate specimen volumes in Ω_1 were calculated from a combination of 1) measured dimensions in Ω_0, 2) dimension changes represented by ${}^{1}_{0}\mathbf{F}$, and 3) measured thickness in Ω_1, resulting in the relation $V_1 = V_0 \cdot \det\left({}^{1}_{0}\mathbf{F}\right) \cdot \frac{t_1}{t_0}$.

Each value of ${}_1\Psi_{\mathrm{ecm,I}}({}_1E_{11,\mathrm{I}}, {}_1E_{22,\mathrm{i}})$ was multiplied with the calculated swelling factor to calculate true strain energy in Ω_0. Note that ${}_1\Psi_{\mathrm{ecm,I}}({}_1E_{11,\mathrm{I}}, {}_1E_{22,\mathrm{i}})$ multiplied by the swelling factor equals ${}_0\Psi_{\mathrm{ecm,I}}({}_0E_{11,\mathrm{I}}, {}_0E_{22,\mathrm{i}})$, and that no parameter transformations were needed because of the model modifications.

7.3.5 Average ECM parameters

Average ECM strain energy in terms of Ω_0 (*i.e.*, including the swelling factor for each data set) was calculated for each point ($_1E_{11}$,$_1E_{22}$) of the generalized strain range, creating an "average" strain energy data set. Average $^1_0\mathbf{F}$ was calculated by taking the average of each of the four components of $^1_0\mathbf{F}$ for each specimen. Note that this yielded the same values as an average $^1_0\mathbf{F}$ calculated from deforming a unit square by each individual $^1_0\mathbf{F}$ and averaging deformed coordinates. In order to obtain "true" average model parameters, the average strain energy data set was fit to Eq. (2.49) using the average $^1_0\mathbf{F}$. Initial parameter estimates were determined as follows. Average values of K, $_0\lambda_{lb}$ and $_0\lambda_{ub}$ were calculated from the individual parameter values. An "average" value for σ_R was determined by fitting the individual R functions simultaneously to a beta distribution function. Average recruitment parameters were obtained in the same manner as described in section 6.2.3. Briefly, the scaled nature of the beta function allowed for calculation of $D(y)$ for the normalized strain range of [0,1] for each individual specimen using the fit parameters. To obtain "average" parameters, the recruitment function was fit to the results of all specimens simultaneously.

The model strain energy results were explored for this set of model parameters; and K, $_0\lambda_{lb}$, $_0\lambda_{ub}$, and σ_R were adjusted to better represent the strain energy data set. With initial fitting attempts, it was noted that different combinations of initial estimate values of K and $_0\lambda_{lb}$ yielded good fitting results. To investigate this and optimize the initial estimates, an error plot was created for a range of K and $_0\lambda_{lb}$ values with values for $_0\lambda_{ub}$ and σ_R based on initial fit inspection, and with fixed values for the other parameters as described above. Values of K and $_0\lambda_{lb}$ that yielded a minimum value of the objective function were used as initial estimates for the fitting process. In the first fitting step, recruitment parameters were kept fixed at the average values, while K, $_0\lambda_{lb}$, $_0\lambda_{ub}$, and σ_R were optimized in the fitting process using the MATLAB function "fmincon" in the same manner as the fitting process of the stress-strain data. In the second fitting step, all parameters were included as fitting parameters to further optimize the fit. M_R was assumed to equal zero for both fitting steps. The resulting parameter values represented the average ECM mechanical behavior.

7.3.6 Intact tissue strain energy

Strain energy of intact UBW was calculated by calculating the work (W) for each (E_{11}, E_{22}) data point of the individual stress-strain data sets in Ω_1 (the intact post-preconditioned tare-loaded state) from biaxial mechanical testing of normal intact UBW tissue. It was assumed that shear was negligible and that there was no dependence on the strain path. The latter results from the hyperelasticity assumption, and also implies that the calculated work equals the strain energy. To eliminate noise, strain data was first smoothed using a 5-point moving average with a span value of 30 (via the MATLAB "smooth" function). Next, for each smoothed data point $(E_{11}, E_{22})_I$ the x- and y-component of the shortest distance between $(E_{11}, E_{22})_{i+1}$ and $(E_{11}, E_{22})_I$ was calculated, and the work for each point $(E_{11}, E_{22})_I$ was calculated using the relation [22, 23]

$$dW = S_{11}dE_{11} + S_{22}dE_{22}\,. \tag{7.7}$$

The set of data points $W(E_{11}, E_{22})$ in all data sets combined formed the strain energy surface for each data set.

A mathematical description of this surface was obtained by fitting all data points to a Fung-type model following Eq. (1.21). The 9-parameter model chosen was previously used to interpolate stress components of bladder data [152] and is given by

$$\begin{gathered}\Psi = \tfrac{1}{2}c_0 \exp(Q) \\ Q = c_1E_{11}^2 + c_2E_{22}^2 + 2c_3E_{11}E_{22} + c_4E_{11}^2E_{22} + c_5E_{22}^2E_{11} + c_6E_{11}^2E_{22}^2 + c_7E_{11}^4 + c_8E_{22}^4\end{gathered} \tag{7.8}$$

Parameters c_i (I = 0,1,…8) were determined from the fit of work data. Since no strain energy is involved with the deformation from Ω_0 to Ω_1, the work for each point $({}_1E_{11}, {}_1E_{22})$ is the same as for the corresponding point $({}_0E_{11}, {}_0E_{22})$. In order to eliminate the high variability in ${}^1_0\mathbf{F}$ values for the different data sets, an average state Ω_0 was defined from calculating an average ${}^1_0\mathbf{F}$. ${}_0E_{11}$ and ${}_0E_{22}$ were calculated from the average ${}^1_0\mathbf{F}$ and ${}_1E_{11}$ and ${}_1E_{22}$, respectively. The result was a strain energy surface of intact UBW with respect to strain in Ω_0. The Fung fit parameters resulting from the strain energy fit were checked against the equibiaxial stress-strain data.

7.3.7 Smooth muscle strain energy and constitutive model

Eq. (2.1) states that the intact tissue strain energy is the sum of the strain energy of its two components (SM and ECM), weighted by their respective volume fractions. Having available the strain energy in intact UBW (section 7.3.6), the strain energy of UBW ECM (section 7.3.4, 7.3.5), as well as values for the volume fractions of ECM and SM (ϕ_{ECM}, ϕ_{SM}) (Figure 4.9), the SM strain energy Ψ_{sm} is calculated as

$$\Psi_{SM}(\mathbf{E}) = \frac{\Psi_{intact}(\mathbf{E}) - \phi_{ECM}\Psi_{ECM}(\mathbf{E})}{\phi_{SM}}. \tag{7.9}$$

Ψ_{ecm} is calculated for the intact tissue strain range using the average model parameters obtained from the strain energy fit (section 7.3.5). For each point ($_0E_{11}$, $_0E_{22}$) in the defined strain range, Ψ_{sm} is calculated with Eq. (7.9), yielding a strain energy surface for the smooth muscle component.

The resulting strain energy surface was fit to the two proposed models for smooth muscle (Eqs. (7.3) and (7.4)), using the MATLAB function "lsqcurvefit". Initial parameters for the continuous distribution function were determined by fitting the proposed bimodal beta distribution function to the available experimental distribution data (Figure 4.6A). The ratio parameter γ for the discrete model was assumed to be the same as for the continuous model. Different sets of initial parameter values were tried with γ fixed to the value determined from the distribution fit, and the fitting result with the lowest value of the objective function was taken as the final result. Resulting parameter values for d_{1C}, d_{2C}, d_{1L}, d_{2L} were used as initial estimates for the discrete model. The two resulting fits were compared.

7.4 RESULTS

7.4.1 Volume fractions general specimen observations

Like all tissues, normal UBW tissue consists of mostly water in addition to SM and collagen (Figure 7.3). Volume fractions of the different UBW constituents were calculated from UBW

specimen measurements, of which half of each specimen was decellularized. The average volume fraction of water in intact specimens was found to be 0.84 ± 0.01 and in decellularized specimens 0.94 ± 0.004 (Figure 7.3). Note that the standard deviation of these measurements was very low. Comparing dry weights of intact specimens and decellularized specimens showed that the average volume fraction (based on dry weight) of ECM in intact specimens was 0.55 ± 0.15. Finally, combining all measurements yielded average volume fractions based on wet weight of smooth muscle (0.08 ± 0.01) and ECM (0.1 ± 0.01).

As described in section 6.3.1, the dimensions of the tissue specimens that were mechanically tested increased after each step in the specimen handling and mechanical testing process. Average specimen dimensions and weights were presented in Table Table 6.1. From this specimen-specific data, combined with the average intact water volume fraction as determined from the lyophilization study (Figure 7.3), relevant individual specimen volume fractions were determined (Table 7.1).

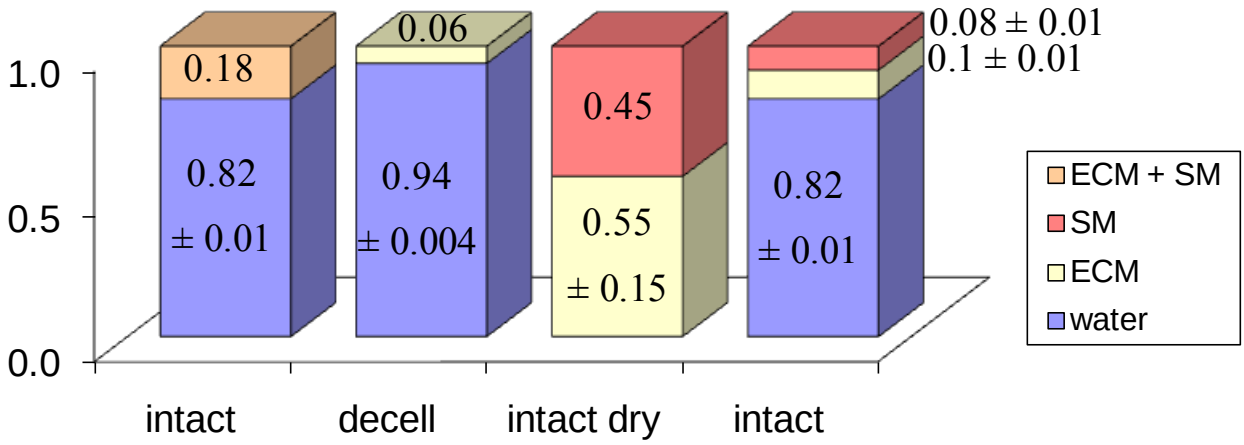

Figure 7.3. Volume fractions of tissue constituents as determined through lyophilization of UBW specimens. Intact and decellularized UBW tissue specimens were lyophilized and wet and dry weights of specimens were determined.

Table 7.1. UBW ECM specimen information.

	F01				Volume intact	Volume decell	fraction ECM	φ_sm	φ_Δwat	swelling factor
	11	12	21	22						
ECM2	1.79	-0.08	0.35	1.37	0.059	0.112	0.540	0.083	0.460	1.70
ECM6	2.41	-0.08	-0.17	1.72	0.053	0.067	0.528	0.085	0.306	1.32
ECM7	2.30	-0.16	-0.18	1.80	0.065	0.077	0.508	0.088	0.369	1.44
ECM8	2.23	0.21	-0.14	1.88	0.067	0.102	0.479	0.094	0.327	1.35
ECM9	1.94	-0.16	0.01	1.34	0.085	0.081	0.278	0.130	0.031	0.90
ECM10	1.97	-0.16	-0.06	1.44	0.081	0.080	0.280	0.130	0.273	1.20
ECM11	1.87	-0.16	0.21	1.61	0.079	0.086	0.341	0.119	0.384	1.43
mean	2.073	-0.086	0.003	1.596	0.070	0.086	0.422	0.104	0.307	1.33
std	0.236	0.135	0.205	0.214	0.012	0.015	0.118	0.021	0.136	0.25
mean (4)	2.065	-0.050	0.011	1.600	0.069	0.093	0.451	0.099	0.296	1.35
std (4)	0.240	0.174	0.241	0.280	0.011	0.017	0.118	0.021	0.186	0.335

Mean (4) and std (4) refer to calculations of data sets ECM2, 7, 8, 9.

A total ECM fraction based on dry weight was calculated from the four values of the lyophylization study plus the seven values from the tested samples, yielding an overall ECM volume fraction based on dry weight of 0.47 ± 0.14 (compared to a value of 0.55 as shown in Figure 7.3). Table 7.1 also lists the four components of the permanent set tensor ($^{1}_{0}\mathbf{F}$), for all seven specimens that were mechanically tested. From the combination of volume fraction data and permanent set values, a "swelling factor" was calculated for each specimen, to be used in calculation of ECM strain energy in Ω_0 (Table 7.1). Averages were also calculated of the four data sets that were chosen for further analysis (see section 7.4.2).

An ECM/collagen volume fraction of 0.47 did not match with the collagen area fraction of 0.22 found from the histomorphometric study (Figure 4.9 and Figure 7.4). This can be explained by considering that it is likely that decellularized specimens did not consist of 100% collagen, but they might also have contained remnants of smooth muscle and other ECM proteins. This information was used to determine the volume fraction of collagen fibers in the decellularized specimens (Figure 7.4). The collagen volume fraction ϕ_f, which appears as a model parameter in the structural model (Eq. 2.41), was calculated from the ECM volume fraction of 0.47, the intact collagen volume fraction of 0.22, and the average swelling factor of the four samples as: $\phi_f = 0.22/0.47/1.35 = 0.35$ (Figure 7.4).

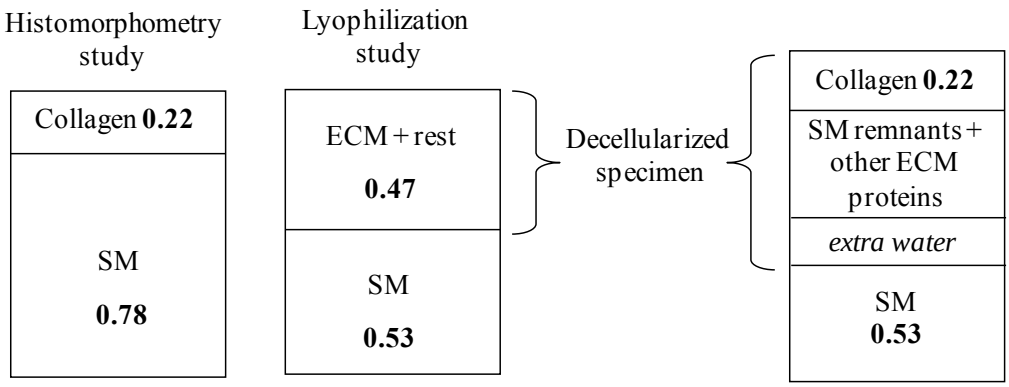

Figure 7.4. Schematic of UBW volume fractions from two different sources and the integration of information. The collagen and smooth muscle area fractions from the histomorphometry study (Figure 4.9) are compared to the volume fractions of ECM and smooth muscle found from the lyophilization of intact and decellularized UBW specimens. Combining this information yields information about the collagen fiber volume fraction in decellularized UBW specimens (see text).

7.4.2 ECM model fitting results

The stepwise process of parameter estimation yielded satisfactory results for all seven data sets. Figure 7.5 shows a representative fitting result for one data set with good quality of fit values (r^2 = 0.956 for the circumferential direction and r^2 = 0.986 for the longitudinal direction). The parameter results for all seven specimens are listed in Table 7.2. All parameter values are expressed with respect to Ω_0, as the model modifications allowed. Three of the seven data sets each exhibited their own problems, either in the fitting or in the original data set and were excluded from the following analyses. The stress-strain data of specimen ECM6 in Ω_1 was referenced such that the stress at the first data point was significantly larger than zero, which resulted in a non-realistically narrow and tall first peak in the recruitment function. The fits of ECM10 and ECM11 yielded an unrealistic high value for *K*. One of the model assumptions stated that ${}_0\lambda_{lb} \geq {}_0^1\lambda(\theta)$ (see also Chapter 3.0). The lower bound stretch ${}_0\lambda_{lb}$ was larger than the cut-off stretch for 95% of the fibers for all data sets, except for the excluded ECM11, and was also larger than the cut-off stretch for 99% of the fibers for most data sets (Table 7.3).

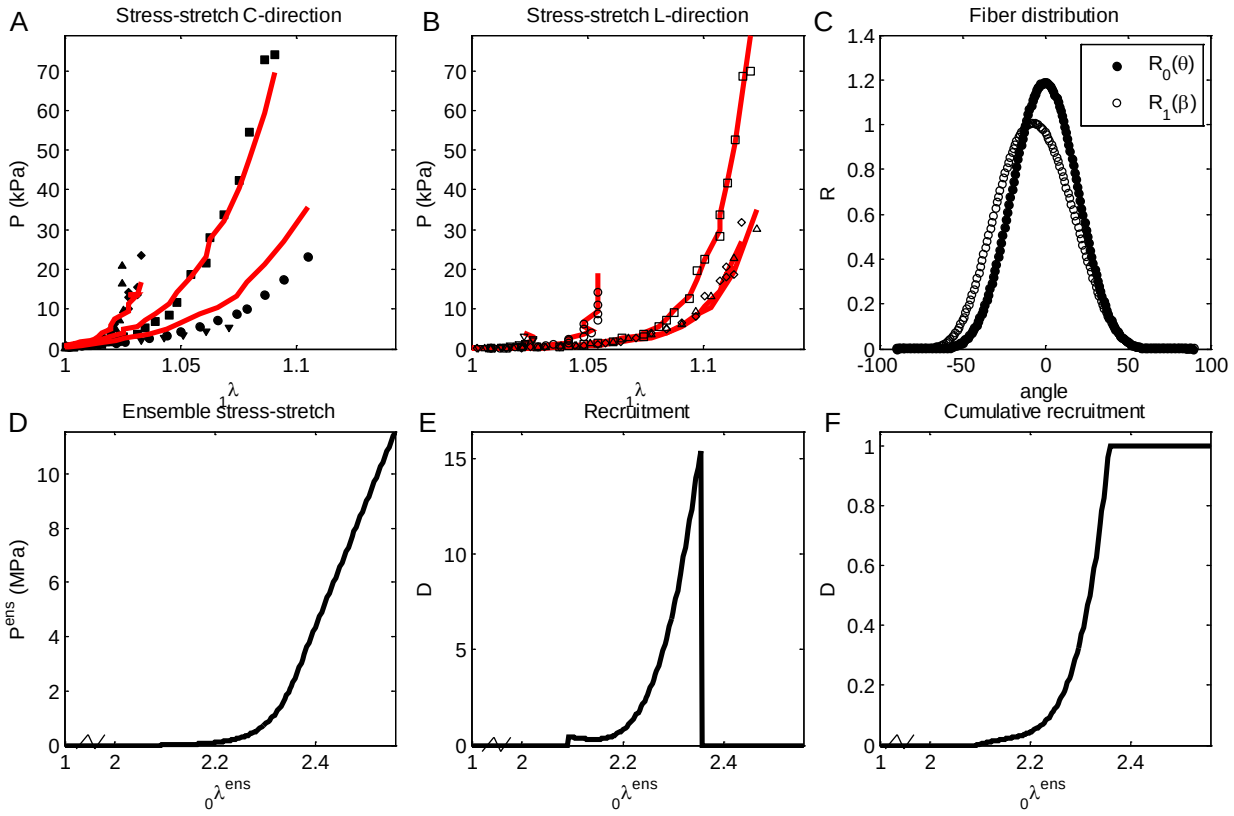

Figure 7.5. Representative results of bladder ECM fitting.
Results are shown for sample ECM8 (model parameters and r^2 values are shown Table 7.2). A) 1st Piola Kirchhoff stress vs. stretch in the circumferential I direction, in Ω_1 for 5 testing protocols. Black circles are data, red line is fit. $R^2 = 0.956$. B) 1st Piola Kirchhoff stress vs. stretch in the longitudinal (L) direction, in Ω_1 for 5 testing protocols. Black circles are data, red line is fit. $R^2 = 0.986$. C) Resulting fiber distribution function $R(\theta)$ and the corresponding $R(\beta)$. $\Sigma_R = 18.6^o$. Zero degrees is aligned with the longitudinal direction. D) Resulting ensemble stress-stretch behavior, in Ω_0. $K = 45$ Mpa. E) Resulting collagen fiber recruitment behavior ${}_0\lambda_{lb} = 2.09$ ${}_0\lambda_{ub} = 2.36$. F) Corresponding cumulative recruitment function.

Table 7.2. ECM model parameters defined in Ω_0.

	K (kPa)	μ_1 (-)	σ_1 (-)	γ (-)	μ_2 (-)	σ_2 (-)	λ_{lb}(-)	λ_{ub}(-)	σ_R (deg)	r^2_C	r^2_L
ECM2	12,228	0.286	0.151	0.103	0.801	0.163	1.77	2.01	23.3	0.963	0.976
ECM6	34,163	0.050	0.043	0.098	0.764	0.178	2.12	2.44	15.6	0.942	0.856
ECM7	85,373	0.188	0.140	0.028	0.870	0.109	2.34	2.59	22.3	0.967	0.949
ECM8	45,573	0.215	0.172	0.033	0.819	0.150	2.09	2.36	18.6	0.956	0.986
ECM9	60,064	0.200	0.150	0.002	0.836	0.128	1.80	2.04	20.2	0.940	0.861
ECM10	150,023	0.148	0.120	0.026	0.860	0.120	1.88	2.05	18.1	0.933	0.818
ECM11	9,727	0.590	0.185	0.277	0.909	0.048	1.76	2.34	34.7	0.912	0.964
mean	56,735.7						1.97	2.26	21.9	0.945	0.916
std	48,919.2						0.22	0.23	6.25	0.019	0.068
mean (4)	50,809.3	*0.406*	*0.239*	*0.075*	*0.841*	*0.131*	2.00	2.25	*21.0*	0.957	0.943
std (4)	30,530.0						0.27	0.27		0.012	0.057

Model parameters are shown for each individual specimen, as well as mean parameters for all specimens, mean parameters for the best four specimens, and recruitment and fiber distribution parameters found from the simultaneous distribution fits (in italic).

Table 7.3. Comparison of the lower bound stretch values from the model fit with calculated cut-off values.

$\lambda_{01\_cutoff95\%}$	$\lambda_{01\_cutoff99\%}$	λ_{lb}(-)
1.44	1.53	1.77
2.00	2.13	2.12
2.19	2.28	2.34
1.97	2.03	2.09
1.64	1.76	1.80
1.72	1.82	1.88
1.79	1.84	1.76

7.4.3 Average ECM parameters and strain energy

The resulting average recruitment and distribution functions are shown in Figure 7.6, and the corresponding parameters are listed in Table 7.2. The shape of the recruitment function is very similar to the function determined in the previous study (Chapter 6.0), which suggests that expression of the recruitment function in terms of stretch is not fundamentally different from expression of it in terms of strain. The average fiber distribution function (Figure 7.6 B) with a standard deviation of $\sigma_R = 21$ deg is different from the distribution function measured by small angle light scattering (SALS) with a standard deviation of $\sigma_{Rm} = 30$ deg (Figure 6.10). However, these distributions were each defined in a different state. The model distribution function was defined in Ω_0, *i.e.*, the intact free floating state, whereas the experimental fiber distribution was measured in specimens that were cut from decellularized bladders fixed in a filled state. Comparing the average dimensions of intact free floating specimens to the dimensions of filled decellularized bladders yields approximate values for the stretch in 11 and 22 directions respectively, of ${}^{1}_{0}\lambda_{11} = 2.37$ and ${}^{1}_{0}\lambda_{22} = 1.65$. Applying these values to an $R(\theta)$ with $\sigma_R = 30$ deg (Eq. (2.19)), yielded an $R(\beta)$ with $\sigma_R = 22$ deg, which is close to $\sigma_R = 21$deg.

Strain energy was calculated for each ECM specimen over a generalized strain range defined by a circle with a radius of $E_{11} = E_{22} = 0.16$ in Ω_1 (Figure 7.7 A). This range was chosen such that the strain ranges of all specimens were represented without extrapolating too far. The strain energy values were multiplied by the swelling factor determined for each individual specimen (Table 7.1). For each point (E_{11},E_{22}), the strain energy values of four data sets were averaged, resulting in an average ECM strain energy surface (Figure 7.7 B).

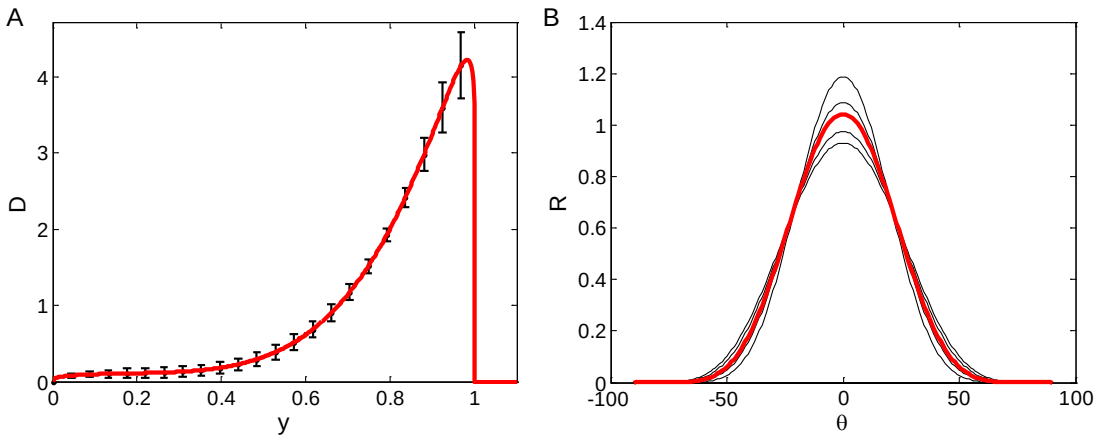

Figure 7.6. Average fiber recruitment and distribution.
A) A double beta distribution was fit to four recruitment functions in terms of the scaled parameter *y*. The red line is the fit and the error bars represent the standard error of the average of the four recruitment functions. B) A beta distribution was fit to four distribution functions. The red line is the fit ($\sigma_R = 21$ deg) and the black lines are the individual distribution functions. Zero degrees is aligned with the longitudinal direction.

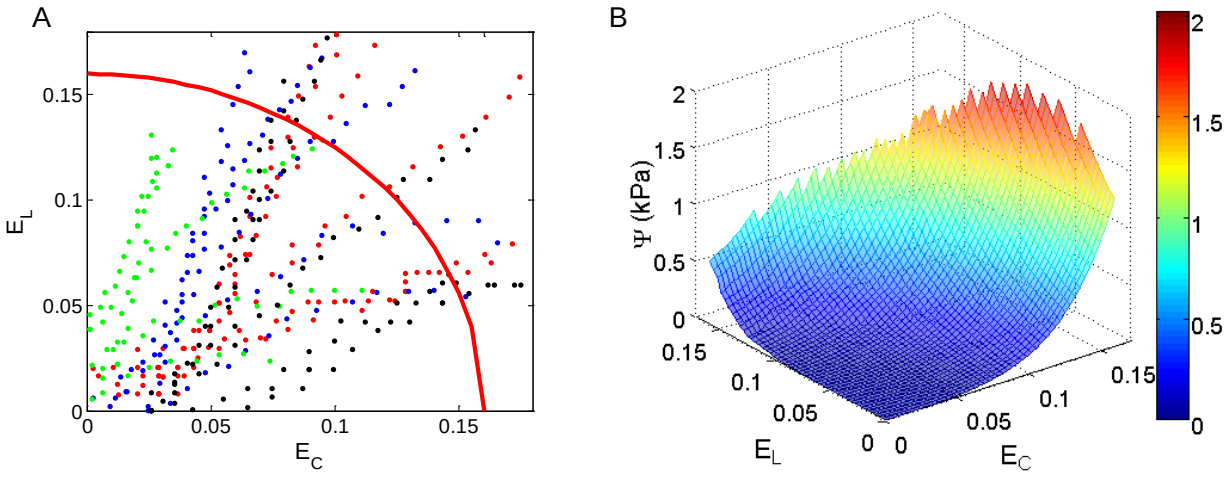

Figure 7.7. Strain range and average ECM strain energy.
A) Strain data points of four ECM specimens are depicted together with the strain range defined by a circle with radius 0.16 that encompassed the strain range of all data sets. B) Average ECM strain energy calculated for the strain range depicted in panel A.

The average strain energy data was fit to the structural model to obtain average ECM model parameters. With initial fitting attempts, it was noted that different combinations of K, λ_{lb}, λ_{ub} produced good fitting results, suggesting a strong correlation between these parameters. To explore this effect, the objective function was explored for a range of values of K and λ_{lb}, for serveral different values of λ_{ub}. The resulting parameter space plot for a fixed value of σ_R = 19 deg, λ_{ub} = 2.18, and average recruitment parameters (Figure 7.6 A) is depicted in Figure 7.8 A.

This combination of parameters yielded the lowest minimum objective function value of $4.03 \cdot 10^{-9}$ for λ_{lb} = 1.83 and K = 57,600 (note that this "K" includes the swelling factor and is different from the K values in Table 7.2). Higher values of λ_{ub}, and hence higher values of K, yielded higher minimum objective function values. Using the parameter values of the parameter space investigation as initial estimates for the fit resulted in a fit quality with r^2 = 0.981(Figure 7.8 B). The resulting parameter values were η = 105,761 kPa (assuming ϕ_f = 0.35), μ_1 = 0.421, σ_1= 0.239, γ = 0.047, μ_2 = 0.834, σ_2 = 0.130, λ_{lb} = 1.80, λ_{ub} = 2.15, σ_R = 19.08 deg and the corresponding recruitment function, ensemble response and distribution function are depicted in Figure 7.8 C-E.

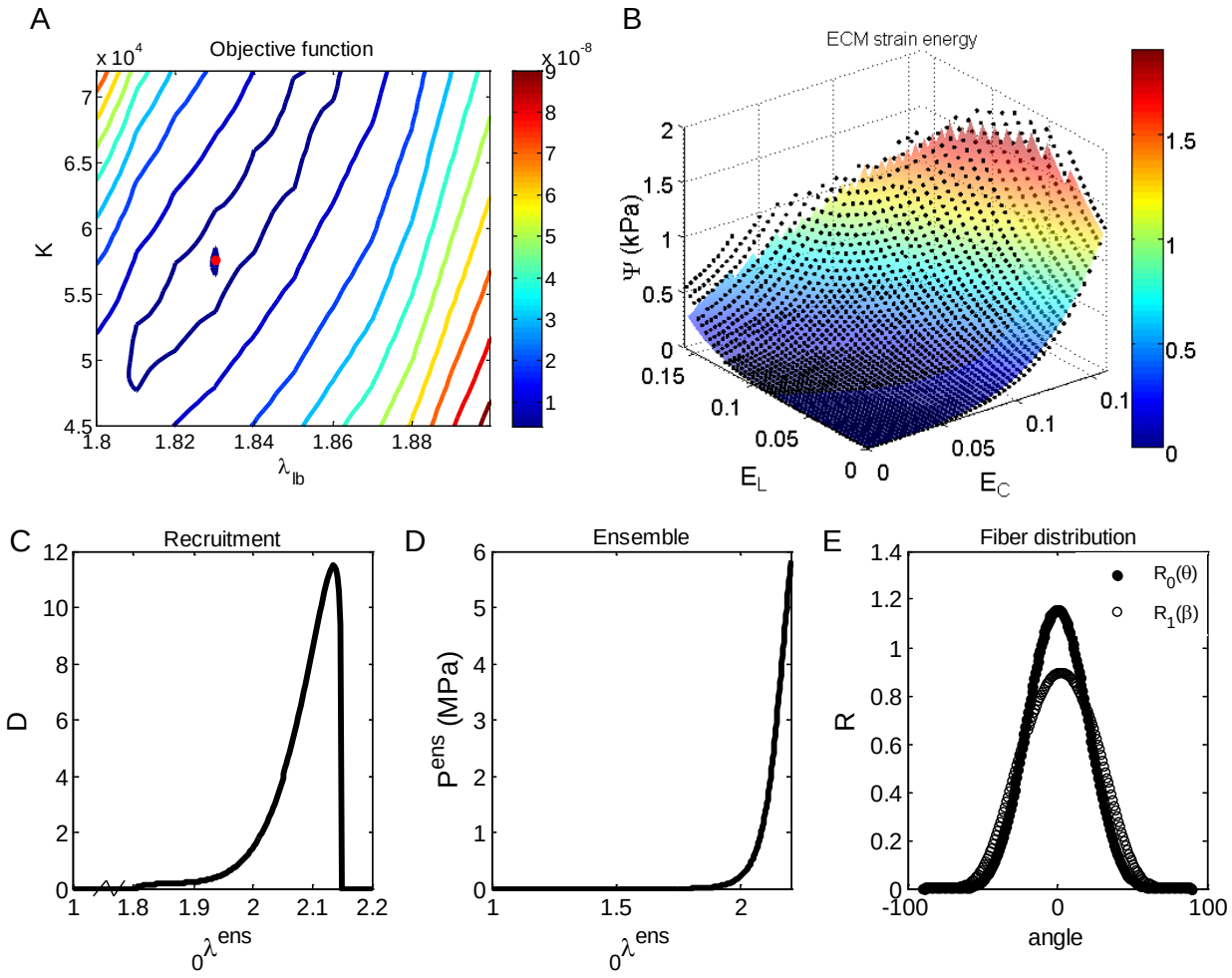

Figure 7.8. Fitting of average ECM strain energy data to obtain average ECM parameters. A) Contour plot of the objective function as function of K and λ_{lb}, for "average" recruitment parameters and λ_{ub} = 2.18. The minimum value of the objective function (red dot) equals 4.03e-009, for K = 57,600 and λ_{lb} = 1.83. B) Fit of the average ECM strain energy surface. Black dots represent the average strain energy calculated from four samples, and the meshed surface represents the fit. r^2 = 0.981. C) Resulting recruitment function with parameters μ_1=0.421, σ_1 = 0.239, γ = 0.047, μ_2 = 0.834, σ_2 = 0.130, λ_{lb} = 1.80, λ_{ub} = 2.15. D) Resulting ensemble model with η = 105,761 kPa and ϕ_f = 0.35. E) Resulting fiber distribution function with σ_R = 19.08 deg. Zero degrees is aligned with the longitudinal direction.

7.4.4 Intact UBW and smooth muscle strain energy

Work was calculated from the smoothed intact UBW stress-strain data (Eq. (7.7)) in Ω_1, and it was observed that the work values for all protocols from all four data sets laid approximately on one surface (Figure 7.9). This data was fit simultaneously to a Fung-type strain energy function (Eq. (7.8)), resulting in a decent fit with $r^2 = 0.84$. Subsequently, the work data and the strain energy surface were expressed in terms of a general Ω_0 by multiplying the stretch data points with an average deformation between Ω_0 and Ω_1 (ignoring shear terms) of ${}^{1}_{0}F_{11} = 1.89$ and ${}^{1}_{0}F_{22} = 1.72$ (Figure 7.9 A). Comparing the average fit strain energy surface with the individual data sets resulted in r^2 values of 0.793, 0.957, 0.739, 0.730, for the four respective samples. Model stress calculations with the Fung fit parameters compared reasonably well with the individual specimen stress-strain data from the equibiaxial stress protocol (Figure 7.9 B).

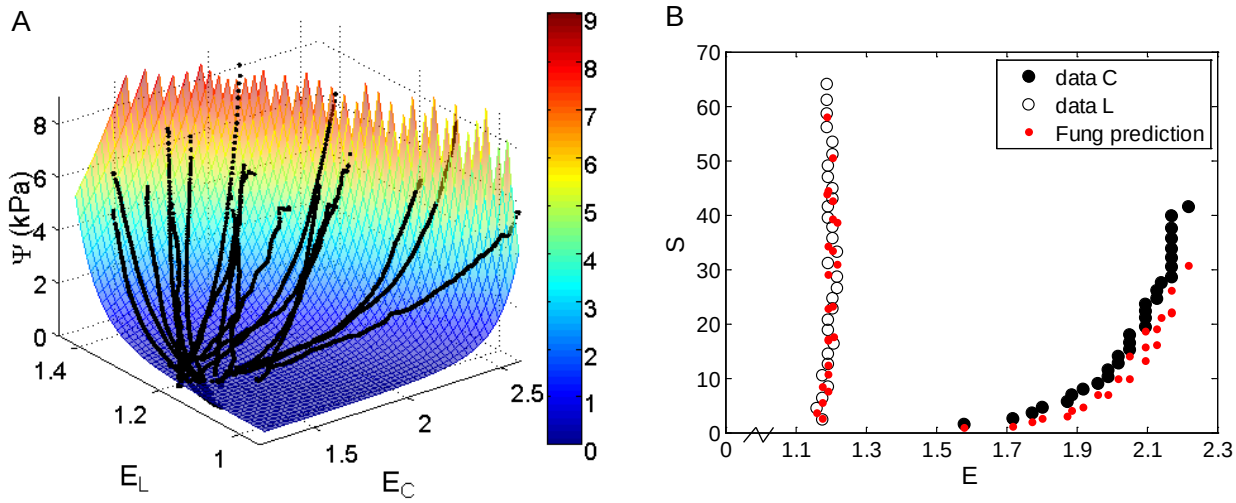

Figure 7.9. Fit of work data of intact UBW in Ω_0 to Fung model and comparison to stress-strain data. A) Data points of $W(E_C,E_L)$ for four specimens were simultaneously fit to a Fung-type strain energy function.($r^2 = 0.84$) and a general surface was created. Note that the strain axes do not start at zero. B) The Fung model with fit parameters (red dots) predicted the individual equibiaxial stress data in Ω_0 (black circles) reasonably well.

ECM strain energy was calculated for the strain range of the intact data sets and subtracted from the intact strain energy, taking into account the volume fractions of ECM and SM (Eq. (7.9), ϕ_{ecm} = 0.22, Figure 7.10). The resulting data set represented the strain energy attributed to the smooth muscle component (Figure 7.10 C). Note that in Figure 7.10 the relative contribution of strain energy is depicted, which includes the respective volume fractions.

Smooth muscle orientation was represented in the constitutive model by a bimodal beta function (Eq. (2.54)) with peaks at θ = 0 deg (circumferential direction) and θ = 90 deg (longitudinal direction). Initial parameters for this function were determined by fitting the bimodal beta function to previously obtained SM orientation data, redrawn from the previously published polar plot (Figure 4.6 A) to a regular plot as a function of angle θ (Figure 7.11). The standard deviations of the circumferential and longitudinal peaks were σ_{RC} = 26.3 deg and σ_{RL} = 24.8 deg, respectively, with the ratio of the areas of the peaks γ_{SMC} = 0.38 (Figure 7.11).

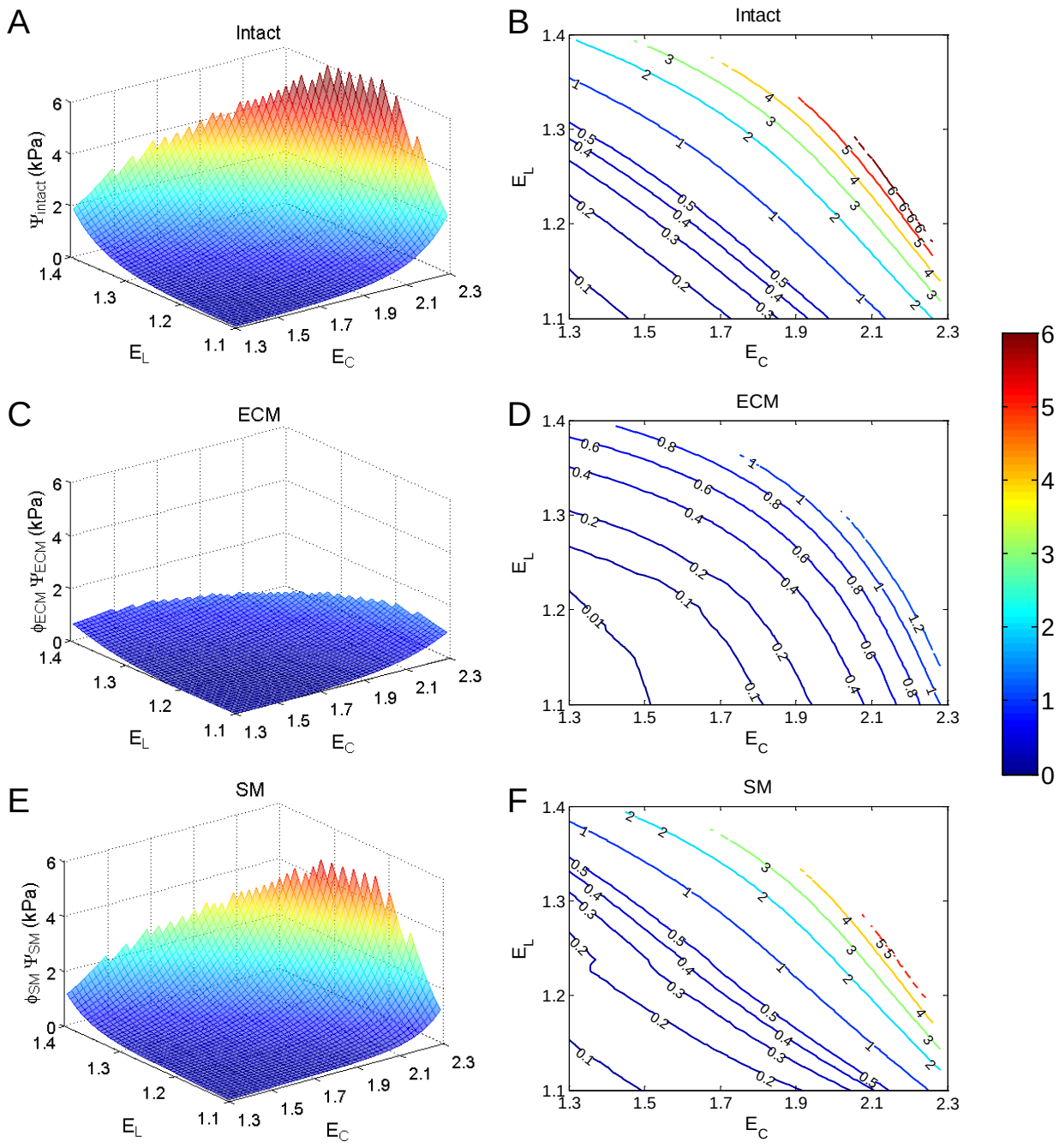

Figure 7.10. Strain energy surface and contour plots for intact UBW and its two components ECM and SM. A,B) Intact UBW strain energy. These represent the same data as Figure 7.9. C,D) Strain energy attributed to the ECM (including the ECM volume fraction). E,F) The difference in strain energy between intact UBW (panel A) and ECM (panel B) yields the strain energy attributed to SM (including the SM volume fraction). Note that the strain axes do not start at zero, and that the strain energy axes and the color levels are all at the same scale.

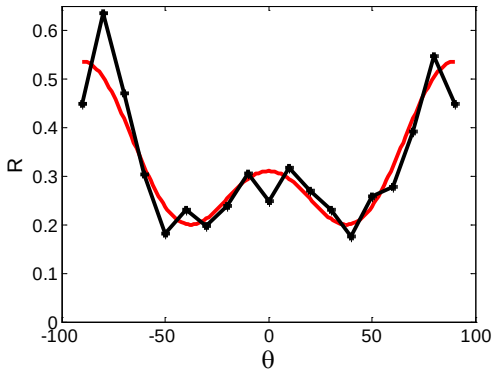

Figure 7.11. Smooth muscle orientation data and fit.
Black dots and line represent the experimental SM orientation data shown in Figure 4.6 A. Red line is the fit of a double beta function with two peaks at 0 and 90 degrees. The standard deviation of the peak at 0 deg is 26.3 deg, and of the peak at 90 deg, 24.8 deg. The ration between the two peaks (γ) is 0.38. Zero degrees is aligned with the circumferential direction to be consistent with the published SM orientation data.

The smooth muscle strain energy data was fit to a constitutive model with either a continuous fiber distribution (Eq. (7.3)) or with two discrete orthogonal fiber families (Eq. (7.4)). Figure 7.12 represents the optimal fit result within the constraint of γ_{SMC} = 0.38 after investigating different sets of initial parameter values. Two families of fibers were maintained, which was comparable to the experimentally determined fiber distribution (Figure 7.11), although with narrower peaks (represented by lower values for the standard deviations).

The constitutive model with two discrete orthogonal fiber families at 0 and 90 deg was not able to fit the data (Figure 7.13 A, B, r^2 = 0.497). Note that the maximum stress values in the fiber families are higher than for the continuous model because each curve represents all fibers in that direction, whereas in the continuous model, it represents a fiber bundle at a specific angle. Four and six families located at different angles around the circumferential and longitudinal direction (thereby still representing the general distribution as found experimentally) were also investigated, but the result never came close to the fit quality of the continuous distribution model (Figure 7.13 C,D, r^2 = 0.76 for 6 families). It is clear that if a discrete model would be used, an extra term needs to be added to the model, *i.e.*, a set of randomly distributed fibers or additional fiber families at off-center axes.

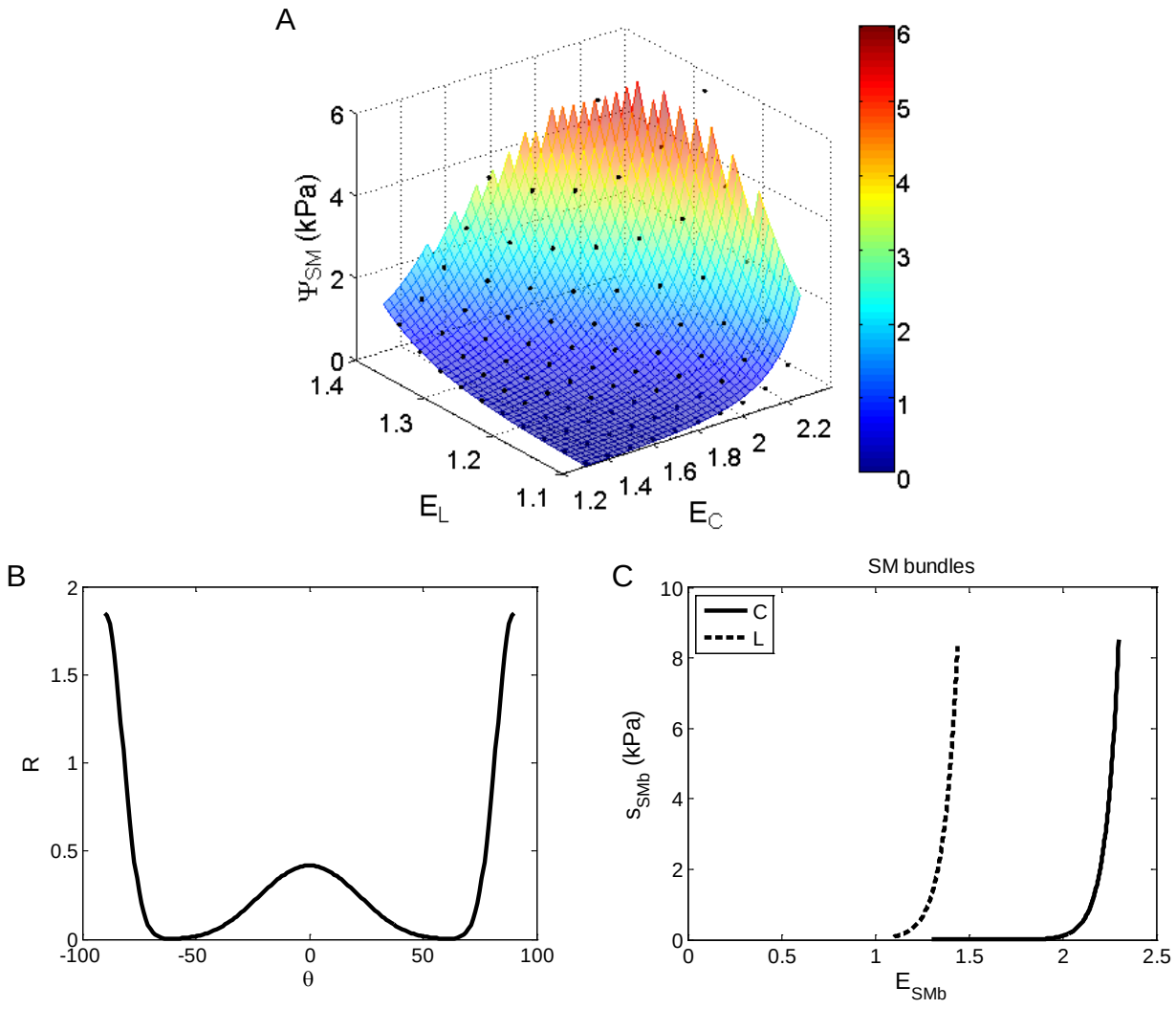

Figure 7.12. Fit result of the smooth muscle strain energy for a model with a bimodal continuous distribution. A) Smooth muscle strain energy data (black dots, see also Figure 7.10 C) is fit to the continuous SM constitutive model (Eq. (7.3)), resulting in good agreement between the data and the model ($r^2 = 0.988$). Note that the strain axes do not start at zero. B) The resulting continuous SM distribution function. The standard deviation of the peak at 0 deg is 20 deg (circumferential), and at 90 deg, 7.6 deg. The ratio between the two peaks, γ_{SMC}, was set to 0.38. C) The resulting stress-strain relations of the smooth muscle bundles in the circumferential direction (0 deg) and longitudinal direction ((90 deg). Parameters: $d_{1C} = 2.3 \cdot 10^{-14}$, $d_{2C} = 14.58$, $d_{1L} = 2.6 \cdot 10^{-8}$, $d_{2L} = 13.59$.

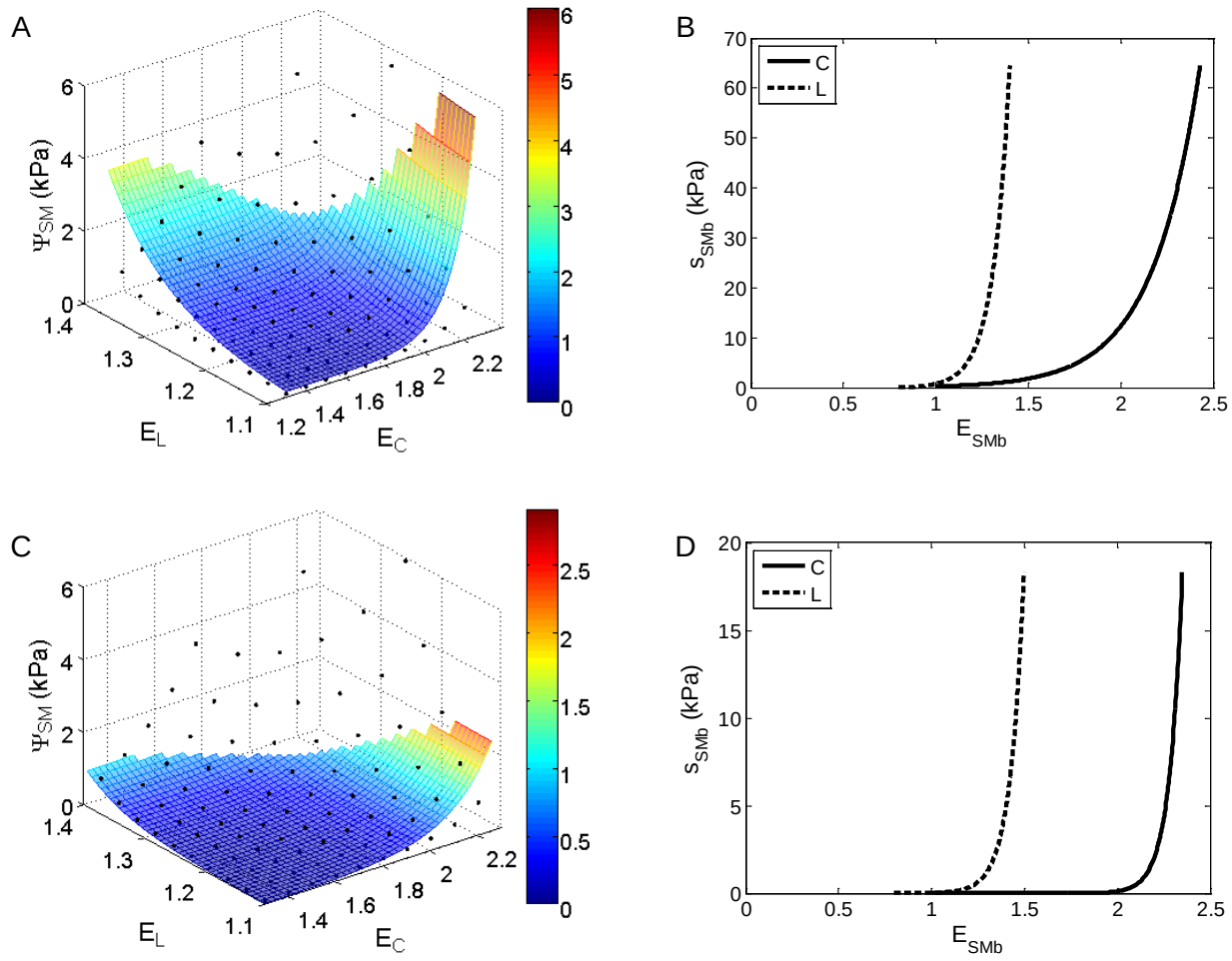

Figure 7.13. Fit result of the smooth muscle strain energy for the model with discrete orthogonal SM bundles. Smooth muscle strain energy data (black dots, see also Figure 7.10 C) is fit to the discrete SM constitutive model (Eq.(7.4)), resulting in poor agreement between data and model. The resulting stress strain relations of the smooth muscle bundle aligned along the circumferential direction (0 deg) and the longitudinal direction (90 deg) are also shown. A,B) Model with 2 discrete families at 0 and 90 deg ($r^2 = 0.497$ $d_{1C} = 5.47 \cdot 10^{-3}$, $d_{2C} = 3.86$, $d_{1L} = 1.11 \cdot 10^{-5}$, $d_{2L} = 11.1$, $\gamma_{SMC} = 0.46$.). C,D) Model with 6 discrete families at 0, -20, 20, -85, 85, and 90 deg ($r^2 = 0.758$, $d_{1C} = 6.3 \cdot 10^{-5}$, $d_{2C} = 5.9$, $d_{1L} = 9.6 \cdot 10^{-9}$, $d_{2L} = 15.6$) . Note that the strain axes of panel A and C do not start at zero.

7.5 DISCUSSION

7.5.1 Summary

A two-phase structural constitutive model was successfully established taking into account multiple referential configurations and was successfully applied to UBW tissue. Model parameters of the collagen phase and the smooth muscle phase were determined separately using mechanical and structural data of intact UBW and of decellularized UBW (UBW ECM). To our knowledge, this is the first time that the mechanical behavior of two load-bearing constituents was determined separately with model parameters expressed in the same state, whereas mechanical and structural data was obtained in different states. The two proposed modifications to the existing structural model included introducing a fiber stress-strain relation linear in P-λ instead of S-E and explicitly taking into account the permanent set effect of decellularization and preconditioning. This allowed for successful and reliable parameter estimation of the collagen phase of this specific tissue application of UBW.

The tissue components were not only successfully separated physically but also in terms of strain energy, allowing for determination of the model parameters of the smooth muscle phase. Using previously determined SM fiber architecture data, the functional form of the SM model constitutive equation was determined from subtracting ECM from intact data. It was found that a model with two discrete orthogonal fiber families was unable to fit the strain energy data. The current study underscores that developing a model and setting model parameters is one thing, but applying it to an actual tissue system is a challenge that is not thoroughly addressed in the literature. In addition, this is the first non-phenomenological constitutive model of urinary bladder tissue that is more sophisticated than one other existing constitutive model developed by Damaser and coworkers [27, 29, 30].

7.5.2 Reference state, preconditioning and permanent set

The novel feature of the current modeling approach is that model parameters of two different constituents were expressed in the same reference state, while structural and mechanical properties were obtained in other states. Each of the available mechanical data sets was obtained

in a different reference state. Decellularization allowed for separate investigation of the collagen constituent and subtraction of this behavior from known intact tissue behavior. To our knowledge, this approach has not been employed before in its current form. A somewhat similar approach involves using elastase to break down elastin in arterial tissue and determine the mechanical properties of the remaining tissue separately [37]. However, this does not provide information about the elastin component itself.

The only commonly available reference state for both tissue constituents was the intact unloaded reference state before preconditioning. It is common practice in mechanical testing of soft tissues to use the post-preconditioned reference state to reference stresses and strains to (see also Chapter 6.0). In the case of decellularized tissues as were investigated in the current study, however, this state had no meaning with respect to the intact tissue. Decellularization and preconditioning caused large deformations in the tissue specimens, which were permanent set-like deformations assumed to have occurred without change in internal energy (see Chapter 2.0). During mechanical testing, the tissue reverts to the post-preconditioned state when unloaded, and the strain energy density function should be defined in this state. This essentially results in a reference configuration wherein the tissue's strain energy function is defined that is different from the initial state. The explicit inclusion of the permanent set in the constitutive model allowed for expressing ECM model parameters in the common intact reference state. However, the question of what the true correct stress-free reference state is still remains.

Preconditioning is utilized in mechanical testing of soft tissues, which are generally considered viscoelastic, in order to reach a pseudoelastic steady state, so that the cyclic loading and unloading curves are repeatable and stable. Preconditioning might only be suitable for dense collagenous tissues and the concept of preconditioning should be revisited for highly deformable tissues such as the UBW. One solution, proposed by Lanir, is to explicitly include the time-dependent effects of preconditioning in the constitutive model [93, 94, 149]. We chose not to model the direct effects of preconditioning, but to include only the end result of it by introducing the measurable permanent set term into the model.

The results of the current study must be interpreted within the light of at least one important limitation. The study is built on the assumption that the ECM component can be separated from a soft tissue without affecting the mechanical and structural properties. Previous results from our laboratory have qualitatively shown that the ECM structure was not visibly

damaged and the collagen structure appeared intact (Figure 4.3) [108]. Decellularization most likely affected the extent of collagen crimp, as observed from the large dimensional increase of the specimens (see also Chapter 6.0), suggesting it caused collagen fibers to uncoil or uncrimp to a certain extent. However, this is assumed to not affect the overall tissue mechanical behavior, as given by two main model assumptions. Firstly, it is assumed that collagen fibers do not bear load until fully uncrimped, and secondly, fibers that were crimped in the initial state remain crimped in the reference state, after the permanent set deformation (Chapter 2.0).

7.5.3 Parameter estimation

Model parameters of the ECM component were obtained through fitting of biaxial mechanical data of decellularized bladder specimens to the collagen structural constitutive model. A step-wise fitting procedure was successfully established. First, an estimate of the parameters describing collagen recruitment were obtained, followed by all model parameters of the collagen component including the collagen fiber modulus and fiber orientation distribution. All parameters were defined in the initial reference state. This step-wise fitting procedure worked well and acceptable final fits were obtained for seven data sets, of which four were optimal. Considering the high variability in the data, relatively consistent parameter values were obtained. The MATLAB optimization algorithm "fmincon" was successful in finding an optimal solution, provided that good initial estimates were provided. The solutions converged for every fitting step. The fitting process revealed that one cannot rely purely on curve-fitting alone. Knowledge of the structural meaning of parameters to guide the choice of initial parameter estimates and to restrict the parameter values to reasonable physiological ranges is essential. Note in this light the questionable parameter values of two recent constitutive models of tissue engineered blood vessels and of esophageal tissue. In both studies, parameters were obtained by unconstrained parameter fitting [25, 110].

The transition from the fiber ensemble parameters obtained in Ω_1 from the equibiaxial strain data to initial estimates for the parameters in Ω_0 (*e.g.*, ${}_0\lambda_{lb}$, ${}_0\lambda_{ub}$ and K) was not trivial. A strong correlation between the parameters was observed with the linear S-E fiber model. Use of the modified model with the linear P-λ fiber model solved many of those problems. Initial values for ${}_0\lambda_{lb}$ and ${}_0\lambda_{ub}$ were successfully estimated by comparing the model predictions of the model

without a permanent set to the data of the equibiaxial protocol expressed in Ω_0. σ_R was estimated by inspecting the degree of anisotropy in the equibiaxial protocol, either in Ω_0 or Ω_1. K was increased to yield corresponding maximum stress values in both directions. This was all performed while keeping the recruitment parameters fixed to their respective values obtained from the ensemble model fit. Based on observations from SALS measurements, it was assumed that all fibers were aligned along the longitudinal direction, and hence a value of $\mu_R = 0$ was forced throughout all fitting steps.

The addition of the permanent set to the model allowed for all parameters to be expressed to the intact reference state before any preconditioning, *i.e.*, the reference state that was also available for the experimental data on intact UBW. This was especially important for the collagen modulus parameter K. It speaks for itself that the collagen modulus is defined in the intact tissue, in its most natural state. However, this would not have been possible without the inclusion of the permanent set in the model. The value of K is much lower when expressed in Ω_1, thereby not representing the real collagen modulus. Note that this is generally not accounted for, nor recognized in the current state of the literature (*e.g.* [11, 129] and Chapter 6.0). Parameter K, for convenience, included the collagen fiber fraction ϕ_f ($K = \phi_f \eta$). The collagen fiber fraction in decellularized tissues was established to equal 0.35, which yielded an average collagen fiber modulus η = 105,761 kPa. This value of roughly 100 MPa is very similar to the collagen fiber stiffness found in X-ray diffraction studies [90].

The average collagen modulus and other average parameter values for the collagen component were obtained by fitting the average strain energy of four ECM data sets to the model. The advantage of using strain energy vs. stress-strain data to obtain average parameters, is that a regular strain grid could be defined over which strain energy was calculated for all four data sets, using the model parameters. Other methods to obtain average parameters exist but are usually inferior. One commonly used method is to simply average the parameter values of all specimens. However, because of the nonlinear nature of the parameters, this is not desirable. Another method is to calculate average multi-protocol stress-strain data and fit the model to the average data sets, or to fit the model to all data sets simultaneously [130]. Because of the highly variable strain ranges in the current study, neither method was feasible. A method to determine average parameters of the fiber ensemble model is to average the model ensemble stress-strain

behavior calculated with individual specimen model parameters [11], but this is only useful in comparing different groups.

Average strain energy data was obtained by defining an average permanent set deformation ${}^{1}_{0}\mathbf{F}$ from the individual ${}^{1}_{0}\mathbf{F}$ of the four data sets. This allowed for defining an average Ω_0 state, thereby eliminating the variability in the effect of decellularization and preconditioning, as well as the variability in the initial inactivated tissue state (see also next section 7.5.4).

7.5.4 Application to multiple experimental data sets of UBW

The newly developed structural constitutive model was applied to our extensive UBW data set to provide the model with physical parameters [47, 108, 109, 152]. Data had to be reanalyzed to make it suitable for model implementation. Biaxial mechanical data and smooth muscle orientation data of intact UBW was originally obtained without model application in mind, which imposed some challenges on the reanalysis procedures. From the biaxial mechanical data of many available, intact tissue specimens, four data sets were selected that represented the average reported behavior in Ω_1, and that exhibited relatively consistent permanent set values (where the intact permanent set is defined between the free floating state Ω_0 and the post-preconditioned tare-loaded reference state Ω_1). Intact tissue specimens were most likely not all in the same fully inactivated state, indicated by the high variability in ${}^{1}_{0}\mathbf{F}$ values when comparing all available data sets. To reduce variability even further, stress-strain data was expressed in an average state Ω_0 by using an average ${}^{1}_{0}\mathbf{F}$. In future experiments involving UBW tissue, full inactivation of SM cells needs to be better controlled and assessed.

It has been recognized in bladder smooth muscle that it exhibits a dynamic passive length-tension relationship [119, 140-142]. Speich *et al*. established that rabbit detrusor smooth muscle displays passive stiffness that is adjustable because it is dependent on both strain history and muscle activation history. In these studies “passive” is defined as the state where cross-bridges are not cycling to produce active force because tissues are maintained in calcium-free solution. Upon addition of calcium, the tissue regains its ability to contract. This is slightly different from our “inactive” state where EGTA is added to the solution to chelate all calcium present in the SM cells as well and restoration of the active state is not possible. The passive

length-tension curve for rabbit SM shifts to the right as a result of strain softening (with increasing deformations) and to the left following muscle activation [141]. Comparing this to the high variability in ${}^{1}_{0}\mathbf{F}$ suggests that the SM cells in the current study were indeed not in the same state of inactivation.

The overall strain range in Ω_0 of the intact UBW data sets did not completely overlap with the strain range of the decellularized bladder specimens, which made defining a general strain range to calculate strain energy challenging. In essence, preconditioning intact and ECM tissues yielded a different equilibrium state. The main difference between the biaxial mechanical data sets of intact and decellularized specimens was that intact specimens were subjected to stress-controlled testing, whereas decellularized specimens were subjected to strain-controlled testing. It appeared that UBW tissue responds to stress-history in an inconsistent way. This might suggest that the accepted pseudo-elastic approach to model soft tissues may need to be extended or even abandoned to accommodate the peculiar stress or strain-path dependency observed when dealing with bladder wall tissue (see also [113]). It was assumed that it was justified to extrapolate the ECM model prediction beyond the testing strain range, to the overall strain range of the intact data sets, because the model parameters have structural meaning and should not be expected to depend on the specific strain range chosen.

Volume or mass fractions of tissue components are usually obtained from general histological measures when used for modeling purposes, for example in modeling studies of the vascular wall. Similar data was also available for the UBW from our previous histomorphometric study [109]. It was anticipated that the collagen volume fraction by that measure would not necessarily represent the fraction of ECM as represented by the decellularized tissue specimens. For this reason, intact and decellularized specimens were lyophilized, and dry and wet weights were measured. Indeed, it was found that both measures of volume fractions were not the same (Figure 7.3, Figure 7.4). The information was combined to determine the collagen fiber volume fraction in the decellularized specimens ϕ_f. This allowed for using the collagen fraction found from the histomorphometric study as ϕ_{ECM} in the overall tissue model.

By introducing the permanent set in the model formulation, ECM model parameters were automatically expressed in terms of the intact tissue. To fully express the ECM mechanical data (or more specifically, the ECM strain energy) in the intact state, an extra transformation had to take place to account for the higher water content of decellularized specimens. This was

accounted for by multiplication of the strain energy by the so-called "swelling factor", determined from deformation changes based on a damage analogy theory (Figure 7.2) [87].

Most challenges in making the experimental data suitable for model implementation was the fact that it was obtained by different investigators with multiple different underlying goals, and more importantly, without modeling in mind. A suggestion to overcome this problem and to modify the current experiments would be to first perform mechanical testing on intact tissue specimens, followed by decellularization and mechanical testing of the ECM, where both tests are done under strain control. However, the effects of preconditioning and mechanical testing on the tissue structure in general and on smooth muscle cells in particular are unknown, which would pose other challenges on analysis of the biaxial mechanical data of decellularized specimens.

7.5.5 Smooth muscle

In the current study, the mechanical behavior of smooth muscle was indirectly determined from the difference between the mechanical behavior of intact UBW tissue and of UBW ECM. The implicit assumption here is that there is no interaction between the two tissue components of collagen and smooth muscle. The analysis was performed via strain energy, not via the traditionally accepted approach of stress-strain data. Strain energy of intact tissue was estimated by calculating the work produced during biaxial testing [22, 23]. This is only a reliable method if the hyperelasticity assumption is valid. To test this, work was calculated for the decellularized specimens using the same method and this was compared to the model strain energy calculations. Work and strain energy values were found to be very similar. This assumption could not be verified for the intact tissue, because of the nature of the study. Work calculations were used to derive a constitutive model for inactive smooth muscle, whereas a complete tissue-level constitutive model would be needed to calculate tissue (and hence smooth muscle) strain energy.

To our knowledge, this is the first attempt to derive a mechanical description of smooth muscle based on mechanical data that can be attributed solely to the smooth muscle component. It needs to be noted, however, that only the inactive behavior of SM was modeled, and basal tone or active contraction were not considered. In general, especially in the vascular literature, it is assumed that the inactive component of smooth muscle does not contribute to the mechanical

behavior (*e.g.* [56, 126, 178, 179]). The current results show that a significant amount of tissue strain energy is attributed to smooth muscle even in inactivated state (Figure 7.10). The present results suggest that the assumption used in vascular studies might need to be revisited, or at the least it suggests that bladder smooth muscle is different from vascular smooth muscle.

In the one study where inactive behavior of smooth muscle was included, it was modeled as one discrete family of fibers running circumferentially [158]. Depending on the specific blood vessel, the majority of the smooth muscle fibers runs along the circumferential direction, and hence modeling the SM behavior as one discrete family of fibers is justified. However, in the urinary bladder, histomorphometric data has shown that SM is distributed along all directions, with two predominant directions, longitudinal and circumferential (Figure 7.11). Following Bishoff [12], both a continuous and a discrete fiber distribution were explored and compared, and it was found that two orthogonal fiber families were not able to represent the SM strain energy surface (Figure 7.13), whereas a constitutive model with a continuous distribution with two peaks at 0 deg and 90 deg was able to fit the SM strain energy very well (Figure 7.12). This suggests that studies based on the theory of composites using strain-based invariants, such as a recent model of esophageal tissue [110], should be interpreted with caution (see Chapter 2.0).

During the fitting process of the SM strain energy surface, it was noticed that when the parameters were not restricted and the standard deviation values of the experimental distribution were used as initial estimates, the optimal solution predicted a single fiber family aligned along the longitudinal direction. A longitudinal peak that was too wide overruled the contribution of circumferential fibers completely. When the ratio of the two peaks was restricted to $\gamma = 0.38$, and the longitudinal peak was estimated more narrow (lower standard deviation), this was prevented, and the peak along the circumferential direction was maintained. This shows again that brute-force parameter estimation has no meaning, and morphological information is required to restrict parameter values to physiologically relevant values (*cf.* [25, 110]).

As an extension to the model, to fully describe the mechanical behavior of UBW in physiological state, passive tone and active contraction should be added to the model. However, determination of the mechanical behavior of UBW in passive or active state is complicated by spontaneous contractions (preliminary experimental observations). Furthermore, no generally accepted model description of smooth muscle tone and activation is currently available in the literature. Models that are available use phenomenological expressions [78, 142, 179].

7.5.6 Conclusion

A morphologically-driven multi-phase constitutive model was successfully developed based on the separate treatment of the ECM and SM constituents. The presence of multiple referential configurations was accounted for and a physically correct linear fiber model was included. Physiologically relevant model parameters were defined in the same referential configuration and the mechanical behavior of the SM component was derived via a strain energy-based approach. It was found that a model formulation based on a finite number of strain invariants was not sufficient to capture the strain energy of the SM component.

The model will form the basis for a growth and remodeling framework that will explain tissue remodeling of individual tissue constituents in different pathologies. Specifically, it will elucidate if mechanical changes in the UBW post-SCI are due to changes in constituent fractions or intrinsic properties. In addition, the model will have the potential to be utilized in remodeling predictions in a tissue engineering setting.

8.0 TOWARDS A MODEL TO SIMULATE SOFT TISSUE REMODELING AND ELUCIDATE MECHANICSMS

8.1 INTRODUCTION

Growth and remodeling (G&R) is involved in many pathological as well as normal physiological processes, such as tissue maintenance and aging; adaptations to altered loads, e.g. in exercise; wound healing in responses to injury or clinical treatment; and progression of disease [6]. All tissues in the human body continuously grow, remodel, and adapt to changes in their physiological environment, resulting in changes in structure and composition. G&R involves production, degradation, and reorientation of tissue constituents such as collagen, elastin and muscle, and newly produced constituents can exhibit different mechanical and/or structural properties, resulting in changes in wall thickness, tissue mass, and tissue structure. The specific remodeling processes are tissue specific and are aimed at maintaining the unique tissue-specific function. Hence, the driving mechanisms and the underlying processes for G&R are tissue-dependent, and a universal mechano-growth law likely does not exist [150]. On the other hand, general trends among tissues with similar compositions should be apparent. Theoretical models of G&R will allow for elucidation of the underlying mechanisms of specific remodeling processes. There is a need for models that describe the fundamental process by which G&R occurs, i.e. the continual production and removal of constituents, and not just consequences of G&R, i.e. mass growth.

Mixture theory, which combines continuum theories for the motion and deformation of solids and fluids, with general principles of chemistry, might be a good platform to model G&R [5]. Humphrey and coworkers have developed what could perhaps be called the most extensive modeling framework for tissue remodeling utilizing the so-called constrained mixture approach, where the tissue is assumed to be a mixture of multiple (solid) constituents, which are

constrained to deform together [65]. This theory has mainly been applied in studies on the vascular wall, but might provide a good basis for developing G&R models in other applications, such as the urinary bladder wall (UBW). This dissertation has laid the basis for developing a new theoretical description of remodeling, applied to the UBW after spinal cord injury (SCI). It was shown that the urinary bladder wall tissue appears to remodel to compensate for the change in mechanical environment that exists as a result of the specific pathology, and attempts to restore normal organ-level function. This is in contrast to what is believed in the vascular field where blood vessels remodel to restore homeostatic wall stress, which calls for extensions to currently available G&R theories.

We hypothesize that the altered tissue mechanical behavior at different post-SCI time points is a result of structural changes in the tissue components such as fiber orientation and mass fraction. This implies that the intrinsic constituent properties, such as collagen fiber modulus, collagen recruitment, and smooth muscle (SM) fiber mechanical behavior, do not change with time, and that newly produced material exhibits the same properties as original material. This hypothesis will be explored in the current chapter. First, a literature review is presented of currently available G&R theories that may serve as a basis for a new theoretical description of remodeling. This is followed by an overview of the available experimental data on structural changes in the UBW at different time points post-SCI. Based on known responses from the this experimental data, remodeling hypotheses are formulated in terms of possible regulatory parameters and model inputs. Next, a parametric investigation is performed with the multi-phase structural constitutive model that was developed as an initial step to predict altered mechanical behavior as a result of changes in constituent structure. Using the obtained knowledge, key remodeling parameters are identified and the mechanical behavior of UBW at 10 days post-SCI is predicted in terms of strain energy. Finally, preliminary kinetic equations describing time-course changes in model parameters are suggested.

8.2 LITERATURE REVIEW OF AVAILABLE G&R MODELS

The theory of mixtures is used to account for the separate contributions of each constituent, and homogenization is done through a rule-of-mixtures model for the stress response. Formal ideas

of mixture theory for mass balance are melded with the less stringent concept of rule-of-mixtures for linear momentum balance. Two classes of constituents are considered, soluble and structurally not significant constituents (e.g. cytokines and chemokines), and insoluble but structurally significant constituents (e.g. collagen, muscle) [6]. Each constituent is produced and degraded, which can be represented in the model by kinetic relations for the mass or mass density production [66]. Constituent turnover involves complex chemical reactions, but first order kinetics can often provide reasonable descriptions [46]. The net density production is the difference between the true density production and the true density removal [66]. It has also been assumed that there are two groups of each tissue constituent, i.e. old and new [45, 46], for which a production equation was formulated for new material and a degradation equation for old material, using first order type kinetics.

Production and degradation together can be represented by a survival function including a heredity integral, which defines how much of a produced constituent is still present at time *t*. With continual turnover, material produced in the recent past will contribute more to load bearing than material produced in the distant past [7, 63]. The mass density of a component is described in terms of a survival function, where the production rate (rate of mass change), and the survival function (which describes the fraction of a constituent surviving) need to be prescribed through constitutive equations that depend on a physiological measure (e.g. magnitude or rate of stress or strain, depending on the specific hypothesis, as pointed out before [118]) that guides the remodeling, i.e. the critical regulatory parameter [7, 63, 118]. The specific form of the kinetic relations will be dictated by experimental data [118]. With these types of expressions, a new equilibrium state is reached when the stress is equal again to the homeostatic value, and the production rate is zero.

The rate of mass change has been defined in different ways in the vascular remodeling theories: it can be kept constant [4]; can depend on a regulatory parameter such as stress [7, 118]; be a function of the number of cells by which the constituent is produced, and the stress experienced by the cells via the local collagen matrix [7]; or depend on the deviation of ratio of constrictors and dilators from its normal value [8, 63]. In the vasculature, SM cells are assumed to maintain circumferential muscle stress and endothelial fluid shear stress at homeostatic values, via a combination of growth and active contraction, which makes circumferential stress in the SM the critical regulatory parameter in a model [4]. For the survival function, the two main

parameters to define are the length of time that a newly produced constituent is present, and its decay, which accounts for changes in removal rates during periods of G&R [118]. Different forms of the survival function can be used, depending on the physiological remodeling process, see examples in [7, 8, 65, 68, 118].

In traditional continuum mechanics, a stress-free reference state is defined where all other (loaded) configurations are mapped to. However, with the continuous turnover of material occurring in G&R, there is no such configuration in the traditional sense. Instead, the focus is on neighborhoods defined by an identifying location (i.e., a mathematical point), that define the geometry of the tissue. In addition, there are three main assumptions in the constrained mixture theory [6]. First, each structurally significant constituent k is assumed to move with the body as a whole. Second, each structurally significant constituent k can possess an individual natural configuration, which is defined by the time τ that the constituent is incorporated within the tissue or cell. Third, the material properties at each point are assumed to result from the properties of all constituents that co-exist within a neighborhood at a particular G&R time point. In the vascular remodeling studies, three configurations are defined, denoted by $\kappa(0)$, $\kappa(\tau)$, and $\kappa(s)$, where s denotes the current G&R time. G&R starts at $s = 0$ and new constituents are deposited at $\tau \in [0, s]$. For convenience a fourth configuration can be introduced, which is a geometrically fixed reference configuration that does not necessarily have to physically exist, such as an unloaded configuration at $s = 0$.

Even though multiple constituents co-reside within one point, each constituent k possesses a unique natural configuration $\kappa^k(\tau)$. Moreover, this constituent is deposited and integrated within configuration $\kappa(\tau)$ at a preferred (homeostatic) value of stretch given by the linear transformation $\mathbf{G}^k(\tau)$. Each constituent can experience a different deformation in the current configuration $\kappa(s)$, relative to its individual natural configuration, denoted by $\mathbf{F}^k(s)$. This deformation experienced by an individual constituent, which was produced at time τ and exists at time s, is defined in terms of tissue deformation $\mathbf{F}(s)$ and the "deposition stretch" as $\mathbf{F}^k(s) = \mathbf{F}(s)\left(\mathbf{F}^{-1}(\tau)\mathbf{G}^k(\tau)\right)$. This allows one to relate deformations experienced by individual constituents, relative to individual natural configurations, to those experienced by the mixture as a whole [7]. Deposition stretches cannot be measured, but reasonable values can be bounded by experimentally available information. Simulations have suggested that biologically bounded,

stable G&R requires depositions stretches larger than a value of 1, which implies that new constituents are likely incorporated within the matrix at a pre-stress [159]. Moreover, this study showed that also the combined effects of changing mass density turnover and vasoactivity, in combination with the pre-stretch, are essential to capture salient features of bounded arterial G&R [159].

The constrained mixture approach has been applied successfully by Humphrey and coworkers to various questions and open problems in vascular mechanics. The most recent examples are: Investigating the effects of axial extension and stress on vascular remodeling [64, 160]; Enlarging intracranial fusiform aneurysms [7]; The resolution of cerebral vasospasm [8]; The complementary effect of vasoactivity and matrix remodeling in response to altered flow and pressure [158]; Quantification of cloth formation and evolving mechanical properties of intraluminal thrombus in aneurysms [75].

Variations of the mixture approach, sometimes in combination with other approaches, have been implemented by other groups and have been used in different applications [52, 79, 80, 115, 117, 154-156, 170]. Holzapfel and coworkers initially modeled the process of arterial remodeling as collagen fiber reorientation in response to stress [52]. More recently, they have been applying this theory in an extended form to the growth of saccular cerebral aneurysms [79, 80, 170]. They have included expressions for collagen fiber turnover [79], and explicitly included fibroblasts in the model, which produce the collagen [80]. Collagen production rate was made dependent on the magnitude of the cyclic deformation of fibroblasts, caused by the pulsating blood pressure during the cardiac cycle [80]. And finally, they included in the model that newly deposited collagen fibers are acted on by fibroblast cells to attach them to the ECM in a state of stretch [170]. This analysis was aimed at guiding the selection of suitable functional forms for the fiber concentration evolution equations.

The group of Stergiopulos, in collaboration with Rachev, utilizes a more simplified global growth approach. This approach couples explicit geometric remodeling with the constrained mixture theory and can be seen as an intermediate approach between the volumetric growth approach and constrained mixture models. It is based on the assumption that remodeling manifests as a continuous change in the dimensions of the zero-stress configuration driven by local arterial stresses. Their studies focus on the time-course arterial remodeling events in

response to hypertension and increased blood flow [115, 117, 154-156]. The most recent study in this line of research included mechanical and structural inhomogeneity in the model [116].

The currently available G&R models require different types of constitutive relations, i.e., strain energy functions, rates of mass density production, and survival functions for constrained mixture models specifically, all for each family of structurally significant constituents. Current functional forms are in a state of infancy, and appropriate constitutive relations need to be derived based on experimental data. Each of these constitutive equations will need to be derived uniquely for each new application. All available studies in the literature make mention of the lack of suitable experimental data. For the current dissertation, experimental data on remodeling in the urinary bladder wall (UBW) as a result of spinal cord injury (SCI) was available. In addition, the required strain energy functions were developed. As a next step, rates of mass density production and survival functions will need to be defined. To enable this, remodeling hypotheses are first formulated based on known responses from the available experimental data.

8.3 URINARY BLADDER WALL REMODELING

8.3.1 Constituent data

Methods of obtaining area fraction and biochemical concentration data of the individual UBW constituents were described in sections 5.4.3 and 5.4.4. The area fraction values for collagen and smooth muscle are used as volume fractions ϕ_{ECM} and ϕ_{SM} in the constitutive model. Histomorphometric analysis at different time points post-SCI revealed that the fraction of collagen decreased with respect to the amount of SM 10 days after injury (ϕ_{ECM} = 0.22 for normal tissue, and ϕ_{ECM} = 0.12 at 10 days post-SCI), and at the 10-week time point, UBW tissue exhibited significant increases in collagen area fractions compared to the 10-day SCI group (ϕ_{ECM} = 0.19 at 10 weeks post-SCI), but similar to the normal bladders (Figure 8.1, see also Figure 4.8). This suggests that the collagen fraction recovered towards the end suggesting that collagen production was going up after a couple of weeks. The fraction of SM did not change significantly (Figure 8.1 B) ((ϕ_{SM} = 0.78, 0.88, and 0.81, at the respective time points).

Biochemical concentration of collagen followed the same trend as the area fraction data (Figure 8.2 A). This data represented the concentration of soluble collagen, which is different from the total amount of collagen. However, considering the similarity in trend it can be assumed that the total amount of collagen follows the trend of soluble collagen. The lowest collagen concentration was found 6 weeks after injury. Note that area fraction data of intermediate time points was not available for comparison. The most remarkable result from this data was that the fraction of elastin increased drastically within a couple of days after injury (Figure 8.2 B). As was suggested in Chapter 6.0, this amount of elastin does most likely not contribute to the mechanical properties directly, but could indirectly influence the mechanical behavior of the collagen component.

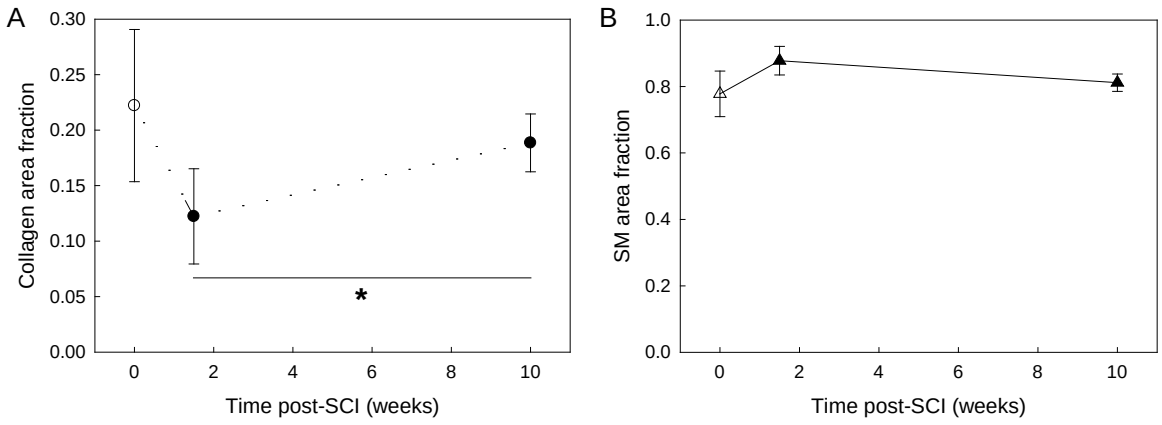

Figure 8.1. Collagen and smooth muscle area fraction data from histomorphometry.
A) Histological area fraction of collagen component. * Indicates significant difference in collagen fraction between the 10-day and 10-week time point. B) Histological area fraction of smooth muscle component. Data presented as average +/- standard deviation. Data is redrawn from [152], and is the same as presented in Figure 4.8.

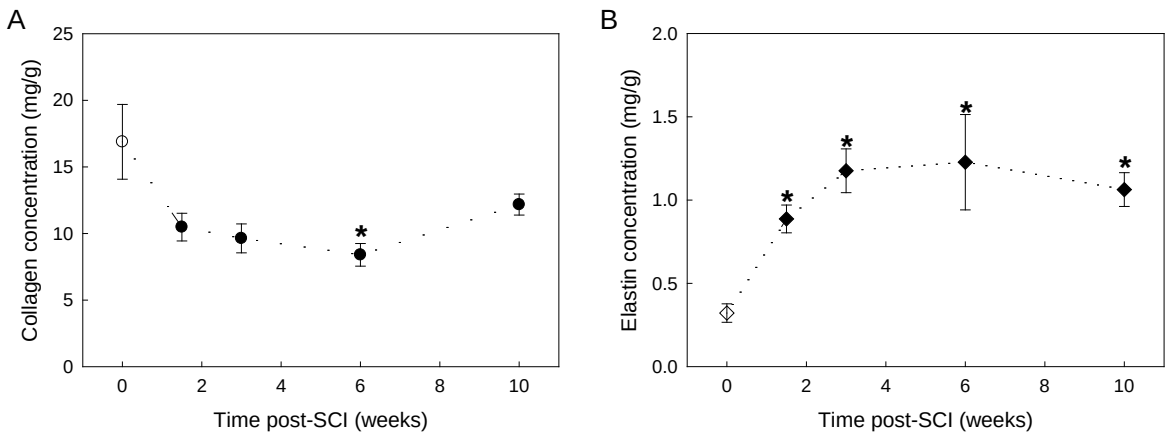

Figure 8.2. Mass fraction changes of soluble collagen and elastin in UBW tissue as a result of SCI. A) Mass fractions of soluble collagen at different time-points post-SCI, determined by SirCol assay. Specimen numbers for the different data points were n = 7, 5, 7, 5, 4, respectively. B) Mass fractions of elastin at different time-points post-SCI, determined by Fastin Elastin assay (n = 10, 5, 6, 5, 4, respectively). Data presented as average +/- standard error of mean for both panels. * Indicates significantly different from normal. Data reanalyzed from [152]. This data was also presented in terms of relative ratios in Figure 4.8.

It would be interesting to relate the concentration data to changes in absolute mass of the individual constituents. Unfortunately, absolute bladder weights were not measured at the time of the experiments. To determine absolute mass changes of different components, rat bladder weight data was compiled from the literature and from some preliminary measurements of bladders that were available (Figure 8.3). This showed how drastically bladder mass changes with SCI. It was assumed that bladder weight at 10 weeks post-SCI would not be different from earlier time points (derived from experimental observations; personal communication with K.K. Toosi). Values from an exponential fit through these bladder weight values were used to transform the concentration values from Figure 8.1 and Figure 8.2 into absolute mass changes of the different constituents, to get an idea of the trends (Figure 8.4). Trends were obtained by tentatively fitting exponential or linear lines through the data points. These trends will be used in future studies to derive hypotheses on production and degradation of the constituents in the two separate phases post-SCI.

◆

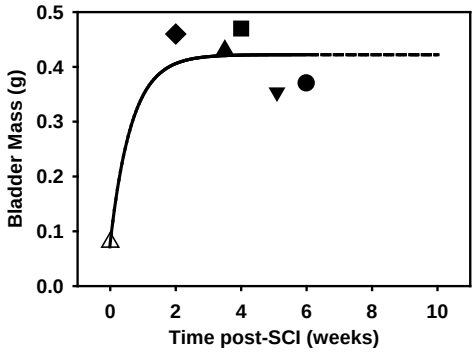

Figure 8.3. Bladder weight at different time-points post-SCI.
Data derived from literature and new experimental measurements. Legend: ▲ literature values from [134]. ♦ average value of 2 bladder measurements. ■ average of 2 literature values [134, 166] combined with average of 5 bladder measurements. ● measurement of 1 bladder. Black line is an exponential fit through the data points; the dashed line is extrapolated. Bladder mass goes up drastically (from 80 mg to ~400 mg) within the first two weeks after injury, but appears to stabilize after that.

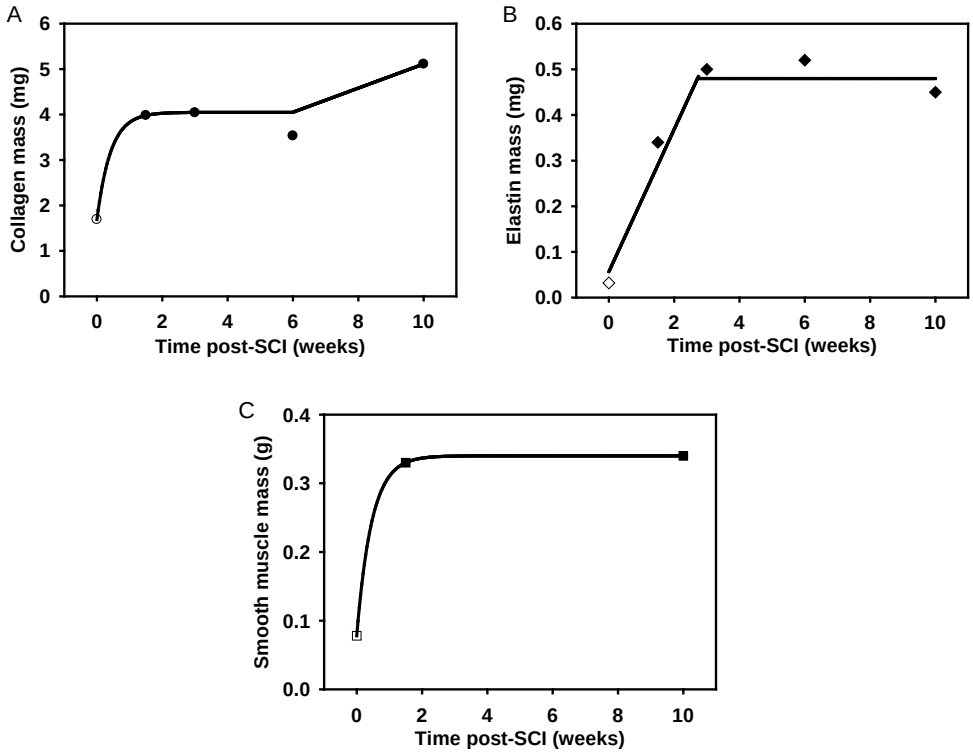

Figure 8.4. Collagen, elastin, and SM mass changes as a function of time post-SCI.
Data points are calculated from data in Figure 8.1and Figure 8.2, using data in Figure 8.3. A) Collagen production goes up but stabilizes at the end of the first phase, and there is a strong increase in collagen production in the later phase. B) Elastin production goes up in the first phase. C) The increase in bladder mass is almost entirely due to increase in smooth muscle mass.

Smooth muscle orientation data from histomorphometric analysis (Figure Figure 4.5) was redrawn and fit to a bimodal distribution function (Eq.(2.54)) (Figure 8.5)). The parameters of the fit reflect the (an)isotropic distribution of the two fiber families. The SM fiber distribution of normal UBW was also shown in Figure 7.11. At 10 days post-SCI, an equal bimodal distribution of fibers is found, with a ratio between the two directions of $\gamma_{SM} = 0.54$ and approximately equal standard deviations fir the two peaks of 21-24^o. At the 10-week time point, the circumferential fiber family has practically disappeared ($\sigma_{RC} = 56.63^o$) and a relatively narrow peak is found along the longitudinal direction ($\sigma_{RC} = 14.6^o$). This distribution appears to be equal to a unimodal distribution combined with a random distribution of fibers.

Figure 8.5 might be misleading, in the sense that the fibers are not actually rotating, but merely hypertrophying in specific directions. Direction-specific hypertrophying of SM cells can lead to an effective reduction of the fraction of cell edges, and hence a smaller number of cells, in a specific direction.

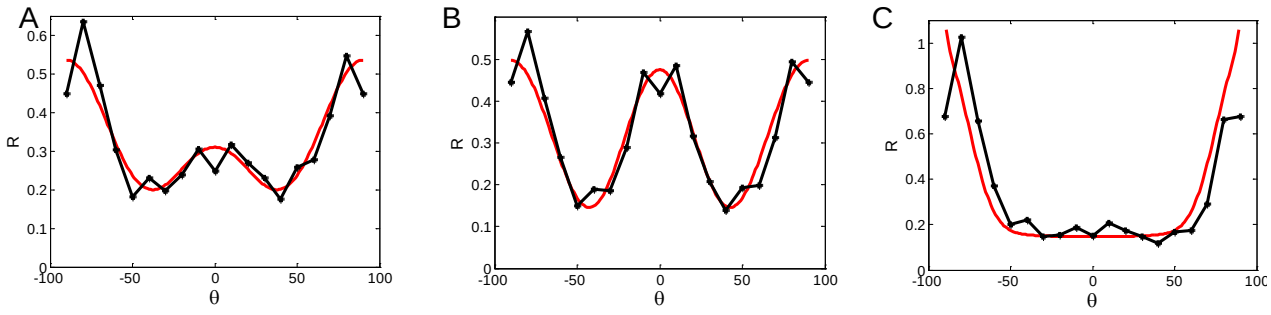

Figure 8.5. Smooth muscle orientation for normal UBW and at two time points post-SCI. Black lines represent data points from Figure Figure 4.6., red line represents the fit with a bimodal beta distribution. 0 deg represents circumferential direction (C), 90 degrees longitudinal direction (L). A) Normal UBW: $\sigma_{RC} = 26.26^o$, $\sigma_{RL} = 24.84^o$, $\gamma_{SM} = 0.38$. This is the same figure as Figure 7.11. B) UBW 10 day post-SCI: $\sigma_{RC} = 21.14^o$, $\sigma_{RL} = 23.85^o$, $\gamma_{SM} = 0.46$. C) UBW 10 weeks post-SCI: $\sigma_{RC} = 56.63^o$, $\sigma_{RL} = 14.60^o$, $\gamma_{SM} = 0.45$.

8.3.2 Intact tissue strain energy at the 10-day post-SCI time point

Strain energy of 10-day post-SCI UBW tissue (n = 5) was calculated the same way as for intact UBW tissue (section 7.3.6) by calculating the work (W) for each (E_{11}, E_{22}) data point of the individual stress-strain data sets in Ω_1 (the intact post-preconditioned tare-loaded state) from biaxial mechanical testing data, and fitting all data simultaneously to a 9-parameter Fung model (Eq. (7.8)). A good fit was obtained (r^2 = 0.93), although the surface was not monotonically increasing for the complete strain range (Figure 8.6 A). For this reason, a pie-shaped section of the strain range was selected for further analysis (Figure 8.6 B). The strain energy surface was transformed from Ω_1 to Ω_0 with the average deformation gradient tensor for these five data sets given by ${}^1_0F_{11} = 1.72$ and ${}^1_0F_{22} = 1.62$). The resulting 10-day SCI strain energy surface in Ω_0 was compared to normal (Figure 8.7) showing a marked difference in (an)isotropy (*cf*. Figure 4.6).

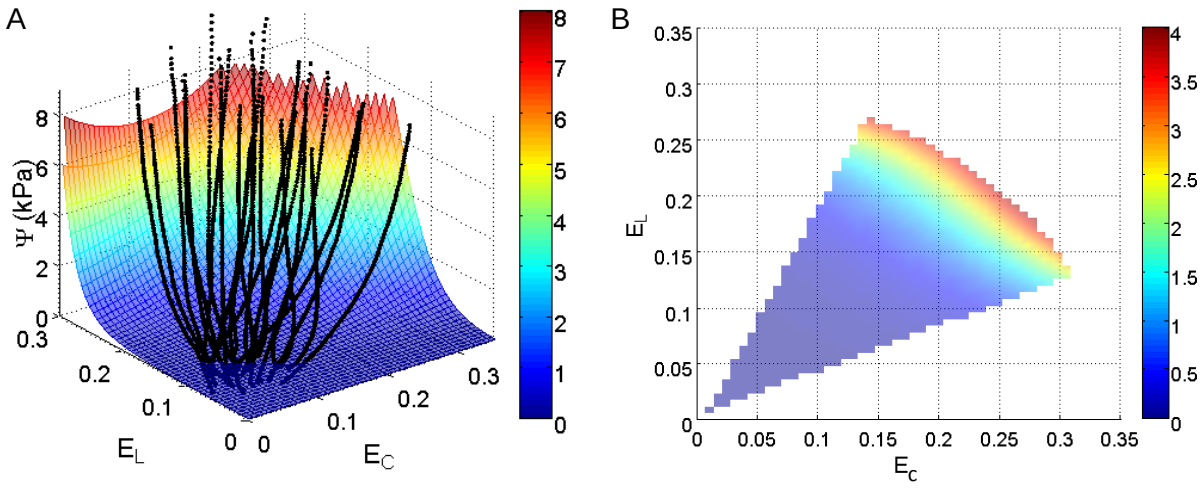

Figure 8.6. Fit of work data of intact UBW at 10 days post-SCI in Ω_1 to Fung model.
A) Data points of $W(E_C,E_L)$ for five specimens were simultaneously fit to a Fung-type strain energy function (r^2 = 0.93) and a surface was created for a general strain range. B) A general strain range was determined representing the relevant data strain range and a monotonically increasing surface. The surface fit is shown as a 2D color plot.

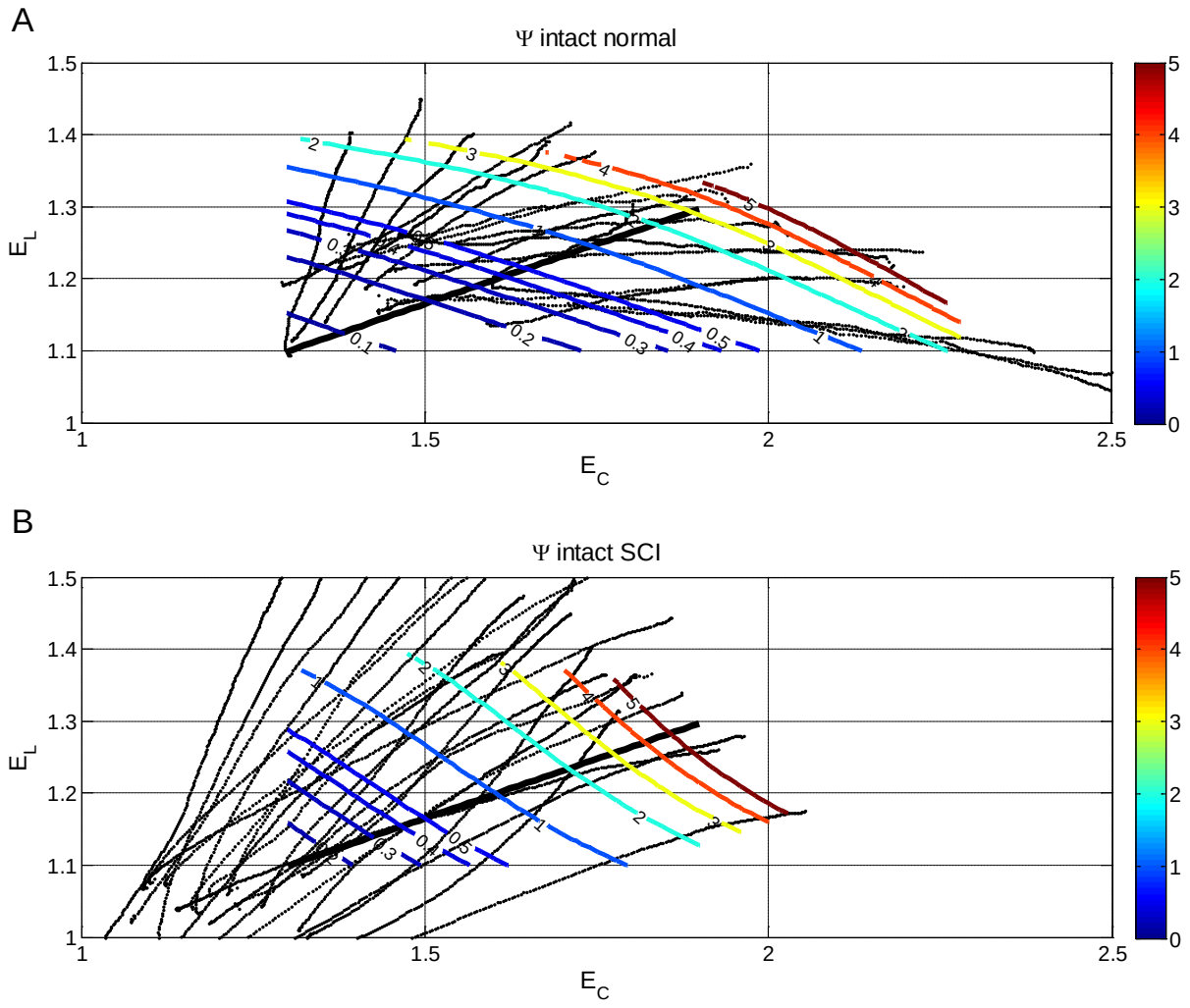

Figure 8.7. Comparison of intact tissue strain energy of normal and 10-day post-SCI data sets in Ω_0. Individual protocol strain paths are shown by black dots and strain energy surface fits are shown by contour lines. The black line indicates a general strain path defining a cross section. Note that the strain axes do not start at zero. A) Normal. B) 10-days SCI.

8.3.3 Parametric investigation

In order to determine what model parameters are representative of the mechanical behavior of UBW at 10 days post-SCI, a parametric investigation was performed on the tissue level model in terms of strain energy with the model parameters determined in Chapter 7 as a starting point. The hypothesis was that the mechanical behavior of post-SCI UBW tissue can be explained completely by changes in tissue structure. Thus, the effect of alterations in structural parameters on the constituent strain energy was first investigated. Parameters related to the ECM component were as follows: ECM volume fraction (ϕ_{ECM}); lower and upper bound ensemble stretch ($_0\lambda_{lb}$, $_0\lambda_{ub}$); and standard deviation of the collagen fiber distribution function (σ_R). A combination of changes in σ_R, $_0\lambda_{lb}$, and $_0\lambda_{ub}$ was also investigated because $_0\lambda_{lb}$ and $_0\lambda_{ub}$ are dependent on angle and hence depend indirectly on σ_R (section 3.1.5). A wider collagen fiber distribution (increase in σ_R) should be accompanied by higher values of $_0\lambda_{lb}$ and $_0\lambda_{ub}$ for the same permanent set deformation. Furthermore, the effect of introducing a second collagen fiber family along the circumferential direction was investigated. Parameters related to the SM component were the ratio of circumferential SM fibers to longitudinal fibers (γ_{SM}), the widths of the circumferential and longitudinal fiber distributions (σ_{SMC}, σ_{SML}). ECM strain energy, SM strain energy, and the weighted sum of these was calculated for two specific strain paths in order to facilitate 2-dimensional plot. The results are summarized, and all graphical results are listed in Appendix D.

It was found that the model was insensitive to changes in ϕ_{ECM}, suggesting that the mechanical contribution in normal UBW was relatively low. Changes in σ_R had a larger effect, especially on the ECM strain energy in direction 2. A moderate difference in anisotropy was observed at the tissue level. Note, that with a value of $_0\lambda_{lb}$ = 1.8 and an unchanged permanent set deformation, σ_R cannot be larger than 24^o (section 3.1.5). The effect of increasing the value of $_0\lambda_{lb}$ or decreasing $_0\lambda_{ub}$ was a pronounced decrease of ECM strain energy and tissue-level strain energy in both directions. Note, that with a value of σ_R = 19^o and an unchanged permanent set deformation, $_0\lambda_{lb}$ needs to be larger than ~1.73.

Several combinations of the three parameters (σ_R, $_0\lambda_{lb}$, $_0\lambda_{ub}$) were also investigated, and it was found that a wider collagen distribution (σ_R = 30) combined with higher values for the lower and upper bound stretch ($_0\lambda_{lb}$ = 1.88, $_0\lambda_{ub}$ = 2.23) yielded a strain energy behavior that came close to the post-SCI tissue-level strain energy. Introducing a second collagen fiber family along the

circumferential direction (with the same standard deviation ($\sigma_{RC} = \sigma_{RL} = 19$), yielded a significant increase in ECM and tissue-level strain energy, especially in direction 1. Even a small circumferential peak resulted in a significant increase in strain energy. The resulting anisotropic behavior of the tissue-level strain energy resembled that of post-SCI tissue. Note, that when more fibers are oriented in the direction of the largest permanent set, ${}_0\lambda_{lb}$ should be increased (section 3.1.5).

With respect to model parameters of the smooth muscle component, different values of the ratio of circumferential SM fibers to longitudinal fibers (γ_{SMC}) did not have a large effect on the SM and tissue strain energy. Changing the width of the distribution of circumferential SM fiber (σ_{smc}) did not show any visible effect. This is most likely due to the fact that mechanical contribution of circumferential SM fibers is low at lower strains (Figure 7.12). On the contrary, the effect of changing the width of the distribution of longitudinal fiber family (σ_{SML}) was large. In fact, the SM strain energy reached unrealistically high values with a broader distribution. This is most likely because the longitudinal fiber family overpowered the circumferential family.

8.3.4 Predicting altered UBW mechanical behavior at 10 days post-SCI

The results of the parametric investigation were used to guide the prediction of the mechanical behavior of UBW tissue at 10 days post-SCI. First, it was assumed that intrinsic material properties had not changed and the changes in mechanical behavior could be completely attributed to morphological changes such as constituent volume fractions and fiber orientation. The intact strain energy (Figure 8.6 B) for 37 data points was fit to the tissue-level constitutive model (Eq. (2.1), (2.21), (2.44), (2.53), (2.58)) with fixed values as found from the normal data fit for the following parameters: K, μ_1,σ_1,γ, μ_2,σ_2, μ_R for the ECM component, and d_{1C},d_{2C}, d_{1L},d_{2L} for the SM component. Based on the assumption that collagen fibers are produced by SM cells and are hence expected to follow a similar distribution as SM, a bimodal distribution was assumed for the ECM component in the same way as for SM. The fit parameters were: ${}_0\lambda_{lb}$, ${}_0\lambda_{ub}$, σ_{RC}, σ_{RL} and γ_{RC} for the ECM component and σ_{SMC}, σ_{SML} and γ_{SMC} for the SM component. As initial estimates for ${}_0\lambda_{lb}$ and ${}_0\lambda_{ub}$, values from the normal data were used, and initial estimates for the distribution parameters were based on experimental SM orientation data (Figure 8.5).

It was found impossible to fit the strain energy surface of intact post-SCI UBW without allowing the contribution of the circumferential family of SM fibers to reach unrealistically high values (*i.e.*, high values for σ_{RL} and γ_{SMC}), to the extent that the longitudinal family of fibers almost completely disappeared (results not shown). A good fit was obtained ($r^2 = 0.98$), but this has no meaning with unphysiological model parameters.

As a result, it was deemed necessary to include the intrinsic SM parameters (d_{1C}, d_{2C}, d_{1L}, d_{2L}) as fit parameters. When setting appropriate bounds on the parameters during the fitting procedure, this yielded good fitting results. During initial fitting attempts, it was found that the anticipated circumferential collagen peak was not predicted (low value γ_{RC}) and it was decided to fix the value of γ_{RC} to zero in the final fitting attempt.

A good fit of the intact strain energy was obtained (Figure 8.8 A, $r^2 = 0.996$). Figure 8.8 also depicts the resulting ECM and SM strain energy surfaces for the same strain range. The resulting parameters are listed in Table 8.1 where they are compared to the model parameters of normal UBW. The most remarkable result is the high value of ${}_0\lambda_{ub}$ combined with a lower value of ${}_0\lambda_{lb}$ (see also Figure 8.10 A).). This resulted in a more compliant fiber ensemble behavior (Figure 8.10 B). This corroborates the findings of Chapter 6.0 of the presence of more coils and crimp in the collagen fibers. A slightly wider collagen distribution as compared to normal was predicted (Figure 8.9 A, Figure 8.11 C), which can be explained by assuming that newly produced collagen fibers post-SCI are deposited in a more random manner. Note, that it was not needed to include the collagen modulus as a fitting parameter, *i.e.*, the collagen fiber modulus was not altered as a result of SCI. The predicted SM distribution was very similar to the experimental distribution (compare Figure 8.9 B and Figure 8.11 B with Figure 8.5 B). The mechanical behavior of individual SM fibers was significantly different post-SCI as compared to normal, especially in the circumferential direction (Figure 8.11 A; see also parameter values in Table 8.1).

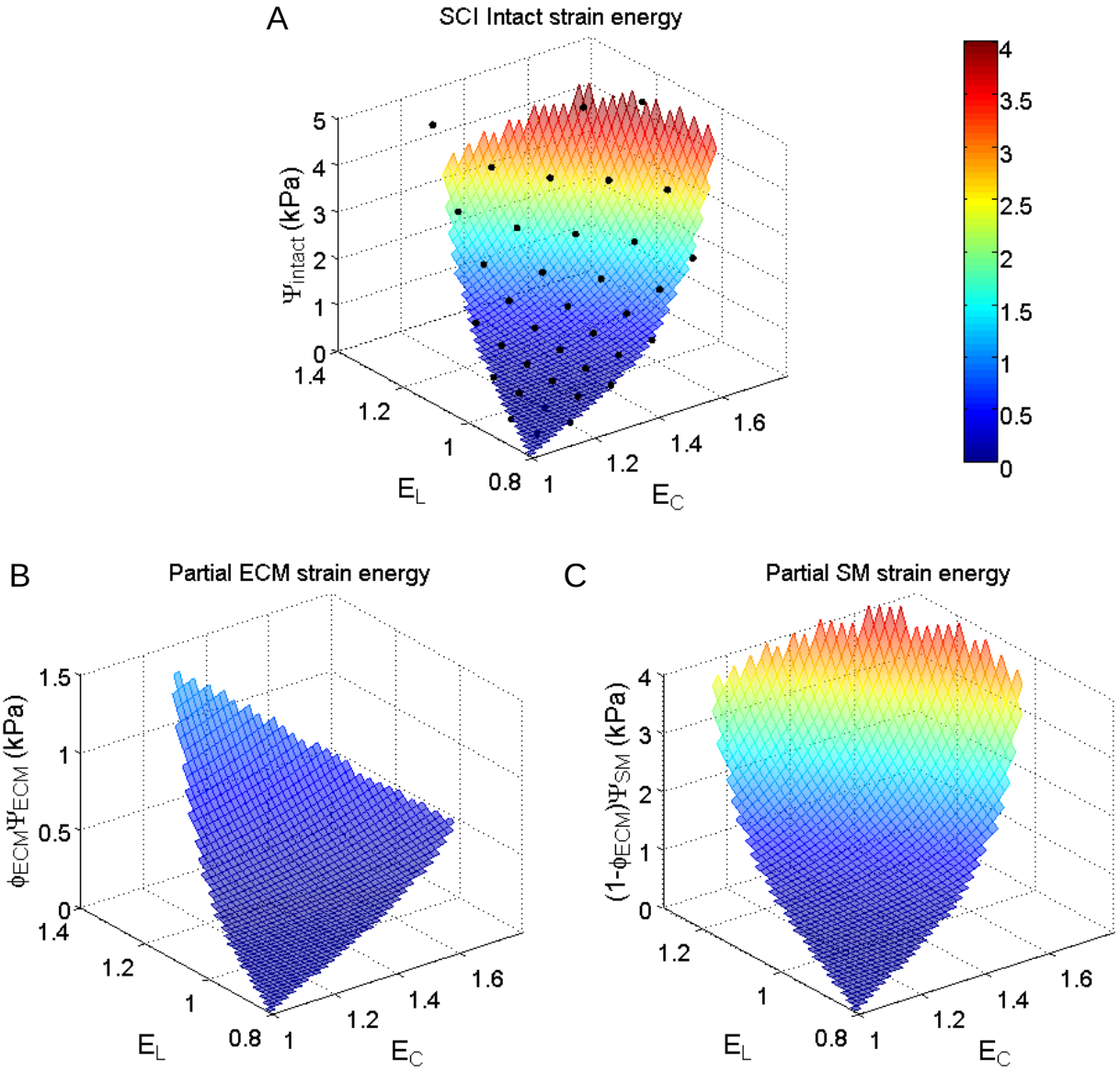

Figure 8.8. Strain energy of 10-day post-SCI UBW.
A) Intact tissue strain energy for 37 data points (black dots) was fit to the tissue-level structural model and a good fit was obtained ($r^2 = 0.996$). B,C) For the same strain values, ECM strain energy (panel B) and SM strain energy (panel C) were calculated with the resulting model parameters. Note that the strain axes do not start at zero and that the strain energy axes are not the same for the three panels. The color levels are at the same scale.

Table 8.1. Comparison of model parameters of UBW at 10 days post-SCI to normal

	ECM			SM						
	λ_{lb}	λ_{ub}	σ_{RL}	σ_{SMC}	σ_{SML}	γ_{RSM}	d_{1C}	d_{2C}	d_{1L}	d_{2L}
Normal	1.80	2.15	19.08	20	7.6	0.38	$2.3 \cdot 10^{-14}$	14.58	$2.6 \cdot 10^{-8}$	13.59
SCI	1.74	2.45	21.82	23.56	22.9	0.47	$1.77 \cdot 10^{-6}$	3.77	$1.57 \cdot 10^{-5}$	8.08

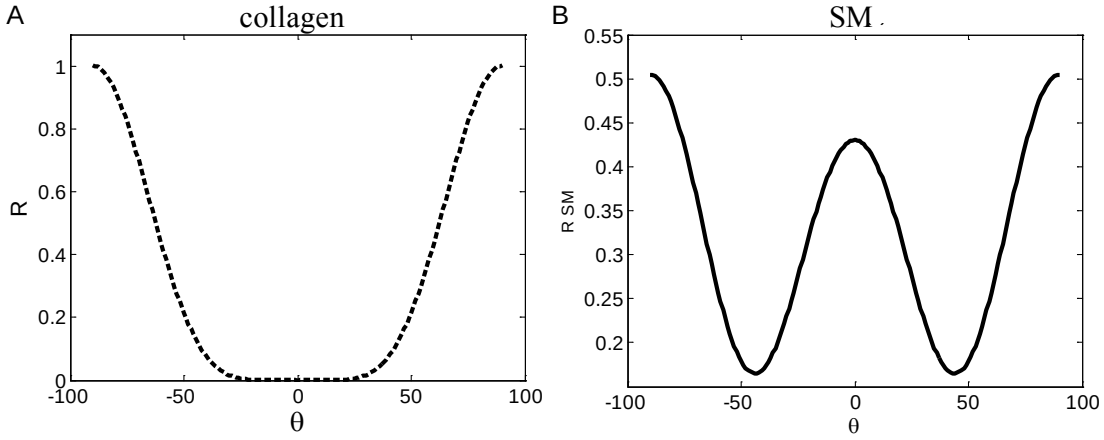

Figure 8.9. Collagen and SM fiber distribution post-SCI.
A) Collagen fiber distribution. B) SM fiber distribution. $\theta = 0$ represents the circumferential direction.

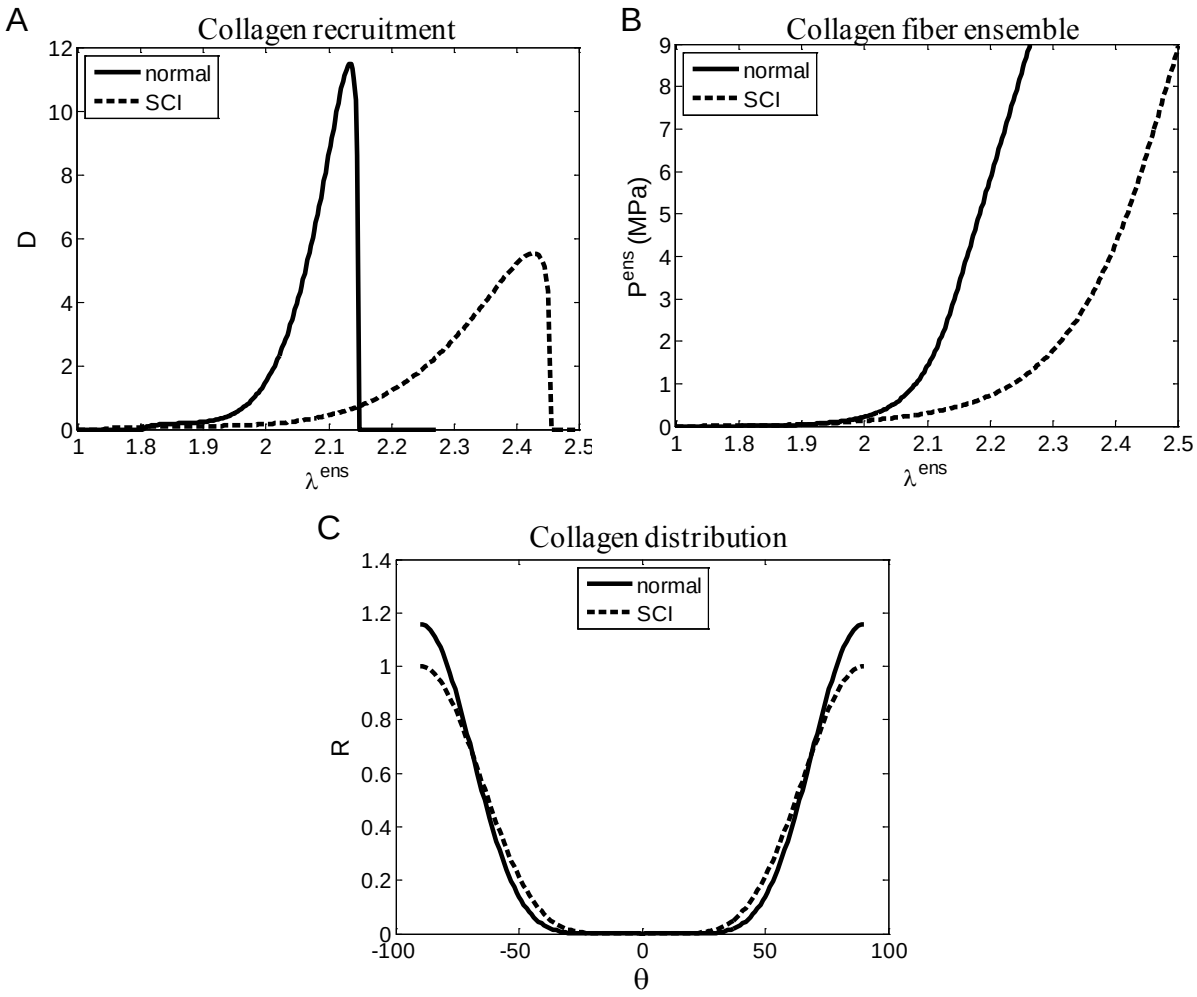

Figure 8.10. Normal and post-SCI Comparison for collagen component.
A) Collagen fiber distribution for normal and post-SCI UBW. B) Collagen fiber ensemble stress-strain for normal and post-SCI UBW. C) Collagen fiber recruitment for normal and post-SCI UBW. . $\theta = 0$ represents the circumferential direction

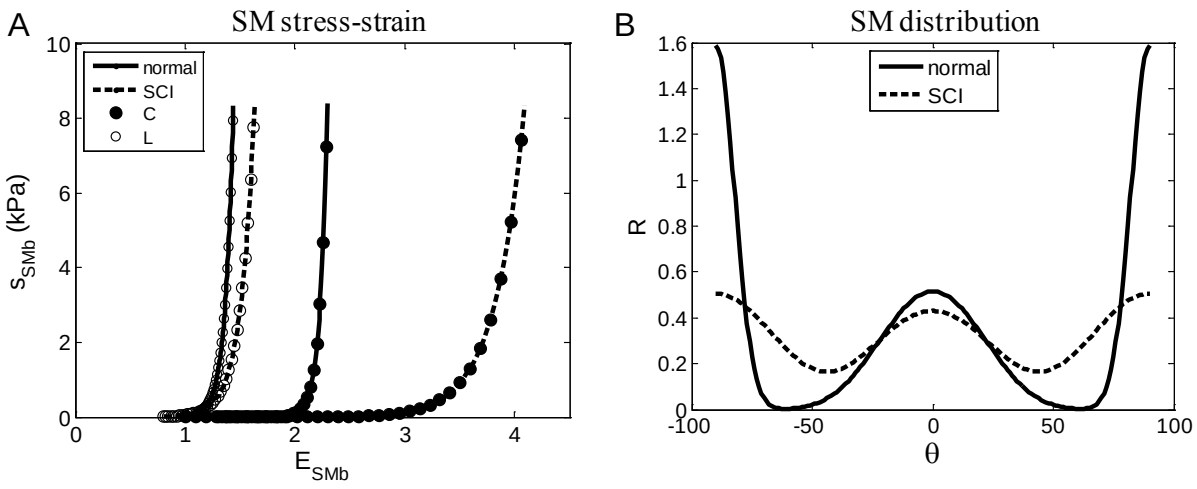

Figure 8.11. Normal and post-SCI Comparison for smooth muscle component.
A) Mechanical behavior of SM fibers for normal and post-SCI UBW. B) SM fiber distribution for normal and post-SCI UBW. $\theta = 0$ represents the circumferential direction.

The general strain path as defined in Figure 8.7 was used to compare cross sections of the strain energy surfaces of the different tissue components, in normal and post-SCI UBW (Figure 8.12, Figure 8.13). Changes in constituent mass fractions, as well as changes in the individual constituents contributed to the altered mechanical behavior post-SCI. The partial contribution of SM strain energy to the total tissue strain energy increased post-SCI due to the higher volume fraction and this was opposite for the ECM component (Figure 8.12). However, by absolute measure, both ECM and SM strain energy increased post-SCI (Figure 8.13). The individual SM fiber families became more compliant (Figure 8.11 A), but the different fiber distribution resulted in an overall higher strain energy (Figure 8.13 B).

The combined results suggest that the observed mechanical changes at 10 days post-SCI are due to a combination of factors. With respect to the ECM component, those are purely structural changes, *i.e.*, changes in the collagen fiber distribution and in the collagen crimp behavior. The collagen fiber modulus remained unaltered. For the SM component, this involved both structural as intrinsic changes. The SM orientation distribution was different from normal, as was also shown experimentally, but also the mechanical behavior of the fiber families changed.

The results of this study in its current state should be interpreted with some caution. Although the fitting process was carefully guided by enforcing physiologically realistic bounds on the parameters, there was still flexibility in the fit. For example, the relative contributions of the two components were not controlled for. A penalty method could be used in the fitting process to ensure that each constituent has a significant contribution to the mechanical behavior, as was used by Hansen *et al*. [51]. However, some knowledge on the expected contribution is required for this, which is not necessarily available for the post-SCI UBW application.

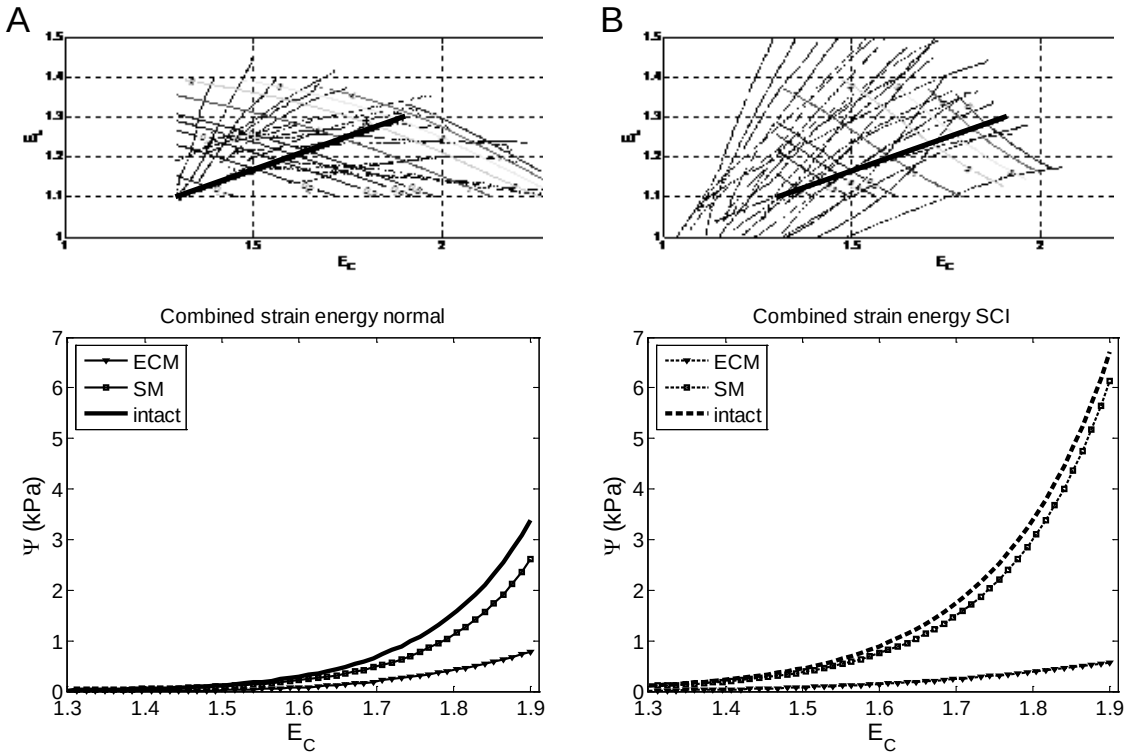

Figure 8.12. Comparison of cross sections through the strain energy surfaces for individual tissue components. The strain path (Figure 8.7) that was used for the calculations is shown as a reference. Intact, partial ECM ($\phi_{ECM}\Psi_{ECM}$), and partial SM strain energy ($(1-\phi_{ECM})\cdot\Psi_{SM}$) are plotted vs. circumferential strain E_c for normal UBW (panel A) and 10-day SCI UBW (panel B). Note that the strain axes do not start at zero.

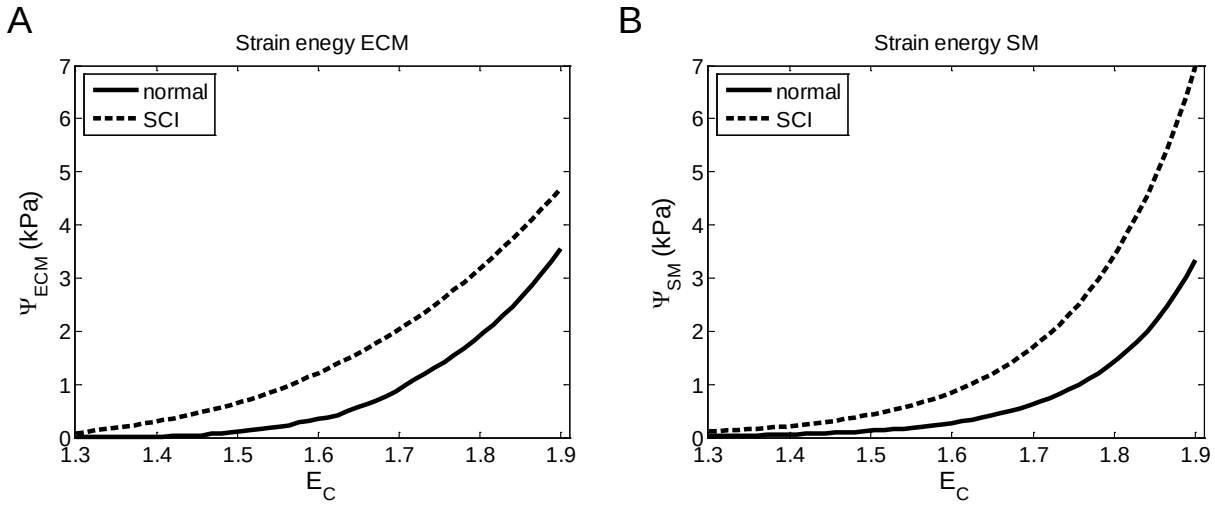

Figure 8.13. Comparison of cross sections through the strain energy surfaces for A) ECM and B) SM. A) ECM strain energy is higher post-SCI, but the slope is lower. B) SM strain energy is higher post-SCI. Note that the strain axes do not start at zero.

8.4 CONCLUSION

A first step has been taken to elucidate the remodeling process in the UBW at 10 days post-SCI using a multi-phase structural constitutive model and available experimental data on mechanical and structural time-course changes. The parameters of the constitutive model of normal UBW were inspected and systematically altered to guide the fitting of post-SCI strain energy data to that same constitutive model. Model parameters of post-SCI UBW were determined and it was shown that UBW mechanical behavior post-SCI was predicted without any intrinsic changes in collagen properties, but with changes in the SM bundle properties. Observed changes in UBW mechanical behavior as a result of SCI can now be attributed to structural changes in the ECM component, and both structural and intrinsic properties of the SM component. It remains to be elucidated what the changes in SM bundle properties are due to.

This is the first time that explicit changes in individual tissue constituents have been elucidated using a constitutive model combined with experimental data. Studies currently available in the literature either show sophisticated models but mention a lack of experimental

data to validate the model, or show a vast amount of experimental remodeling data not suitable for model implementation.

Now that the changes in model parameters have been identified at the discrete time point of 10 days post-SCI, this knowledge can be used in combination with the time-course constituent data to guide the derivation of time-dependent remodeling equations. The known structural and intrinsic changes can be represented in these equations by expressing certain model parameters as a function of time or as a function of a regulatory remodeling parameter (such as stress or strain). The results obtained in the present study are the first essential step in the development of a full G&R model. The available literature on G&R as presented in section 8.2 will serve as a guideline to develop such a model.

9.0 SUMMARY AND CONCLUSIONS

The original aim of this dissertation was to develop a generalized multi-phase constitutive model to simulate soft tissue remodeling and to apply it to a specific tissue system, in order to elucidate mechanisms of urinary bladder wall (UBW) remodeling as a result of spinal cord injury (SCI). The hypothesis was that distinct mechanical stimuli, such as prolonged periods of high strain or stress, or frequent short-term intermittent loading, induce different remodeling events to compensate for the change in mechanical environment and to restore normal organ-level function. Before remodeling could be studied, a reliable morphologically driven constitutive model was needed, and hence, an important component of this aim was to develop a morphologically driven multi-phase constitutive model that would allow for separate investigation of the contribution of individual tissue components to the tissue-level remodeling process. In fact, it was found that developing a reliable constitutive model was crucial and more challenging than anticipated and a large emphasis of this dissertation was put on developing this model and on creating an appropriate experimental data set to derive physically realistic model parameters, rather than simulating soft tissue remodeling. However, it is emphasized that the developed model laid the basis for a generalized modeling framework of remodeling in a multi-phase soft tissue.

The objectives of this dissertation were as follows: The first objective was to formulate an ECM constitutive model to elucidate the mechanical role of *de novo* synthesized elastin on urinary bladder ECM. The second objective was to develop a morphologically driven constitutive model of a multi-phase tissue, applied to the urinary bladder wall. To achieve this objective, the structural constitutive model as used for the first objective was extended with two necessary modifications; one to account for multiple tissue components existing in different reference states and the second to include a physically realistic fiber model. The third objective was to obtain insights into UBW remodeling as a result of SCI. More specifically, to elucidate if

mechanical changes in UBW tissue after spinal cord injury could be explained by changes in tissue structure, *e.g.*, mass fractions and fiber orientation, without intrinsic changes in constituent properties. The main findings from these objectives are summarized in the following sections.

9.1 SUMMARY OF MAIN FINDINGS

9.1.1 On the mechanical role of de novo synthesized elastin in the urinary bladder wall

A structural constitutive model was used to elucidate basic remodeling mechanisms of ECM. Removing the smooth muscle (SM) cells from bladder wall tissue allowed for the separate investigation of the effects of *de novo* produced fibrillar elastin on UBW ECM. It was shown that the presence of elastin fibers in the UBW ECM post-SCI induced, indirectly, a distinct mechanical behavior with higher compliance. This was attributed to the presence of more highly super-coiled collagen fibers in post-SCI UBW ECM. The result was a net increase in ECM compliance allowing for a higher overall extensibility of the post-SCI UBW tissue and increased bladder storage capacity.

The urinary bladder responds to the prolonged period of high strain due to overfilling by increasing its effective compliance through the interaction between collagen and *de novo* deposited elastic fibers. UBW tissue adapts to the functional demand at the organ level. The UBW G&R mechanism is thus an organ-level driven process which does not necessarily result in re-establishment of a homeostatic stress state, but instead attempts to achieve a degree of overall organ functional restoration. Due to the fact that full physiological recovery is never achieved because of lack of full neural control, the remodeling ultimately results in an irreversible pathological process.

9.1.2 A structural constitutive model for a muscle–connective tissue composite

A novel morphologically-driven multi-phase constitutive model was successfully developed based on the separate treatment of the ECM and SM constituents and successfully implemented

in the software package MATLAB. The structural constitutive model for planar collagenous tissues as used for the first objective was extended to be able to apply it to a multi-component tissue with individual model components existing in different reference states. The two necessary modifications to the existing structural model included introducing a fiber stress-strain relation linear in terms of 1st Piola Kirchhoff stress (P) vs. stretch (λ) instead of 2nd Piola Kirchhoff stress (S) vs. Green's strain (E) and explicitly taking into account the permanent set effect of decellularization and preconditioning such that all model components and parameters were expressed in the same reference state. This allowed for successful and reliable parameter estimation of the collagen phase of this specific tissue application of UBW.

The structural model with its modifications was successfully implemented in MATLAB, including the two levels of numerical integration and the complete fitting process. The built-in MATLAB functions for numerical integration and parameter estimation have been shown reliable and effective. The complete process of parameter estimation was implemented within two separate user interfaces (GUIs), which provided full control over the data, fitting settings, and output, including data inspection, choices of model type and algorithms, setting parameter bound values, calculating model values, etc.

The modifications to the structural model, as well as the implementation of the model, were successfully validated. It was shown that the original linear S-E fiber model did not preserve the fiber effective modulus when slack was introduced in the fiber, which was solved by using the linear P-λ fiber model. Comparison of discrete fiber simulations and of synthetic data to the continuous model formulation showed that the modifications to the model formulation were correct and that the implementation in MATLAB was correct.

Physically realistic parameters for the multi-phase constitutive model were determined form UBW experimental data through an extensive parameter estimation procedure. Available experimental data on intact UBW was reanalyzed to make it suitable for model implementation. This was extended and combined with new data on the ECM component specifically. The tissue components were not only successfully separated physically but also in terms of strain energy, allowing convenient averaging of parameters as well as determination of the smooth muscle constitutive behavior. It was found that a model with two discrete orthogonal fiber families derived from invariant theory was insufficient to accurately represent the strain energy data. A continuous fiber distribution was required to model the SM constitutive behavior. This multi-

phase structural constitutive model with physically realistic parameters will be used to take a first step at elucidating remodeling in multi-phase muscular soft tissues, specifically UBW post-SCI, in the next objective.

9.1.3 Towards a model for soft tissue remodeling

UBW tissue remodels significantly as a result of SCI. Previously obtained experimental data on structural and mechanical changes in the rat UBW 10 days after initiation of SCI was reanalyzed to make it suitable for model implementation. Specifically, mass fraction data of collagen and SM, SM orientation data, and biaxial mechanical data were utilized. The mechanical data of the 10-day time point was analyzed in the same manner as mechanical data of normal UBW, yielding an average strain energy surface for intact tissue. The parameters of the constitutive model of normal UBW formed the baseline from which model parameters of post-SCI UBW were determined.

Through fitting of intact post-SCI strain energy data to the constitutive model, it was shown that UBW mechanical behavior post-SCI could be predicted without any intrinsic changes in collagen properties (*i.e.* collagen modulus and recruitment parameters), but with changes in the SM bundle properties. The ECM was found to be significantly more compliant, thereby corroborating the results of the first objective. Observed changes in UBW mechanical behavior as a result of SCI can now be attributed to structural changes in the ECM component, and both structural and intrinsic properties of the SM component. The identified changes in model parameters combined with the time-course constituent data can be used next to guide the derivation of time-dependent remodeling equations. Remodeling hypotheses will first need to be formulated based on known responses from the available experimental data. The developed model has the potential to explain underlying remodeling mechanisms of individual constituents in muscular tissues in several pathologies (*e.g.* UBW post-SCI), and predict remodeling events in a tissue engineering setting of muscular tissues. The general nature of the remodeling framework will allow for applications to a variety of native and engineered tissues, to investigate and predict individual, tissue specific, remodeling mechanisms.

9.2 FUTURE STUDIES

9.2.1 Simulating time-course UBW remodeling

The multi-phase structural constitutive model needs to be extended with kinetic remodeling equations to be able to elucidate UBW-specific remodeling mechanisms as a result of SCI. In order to derive kinetic equations, remodeling hypotheses, regulatory parameters, and model inputs need to be defined. In the areflexic phase (the initial phase after initiation of SCI) of the post-SCI rat bladder, the bladder is over-distended because it is filled over a longer period of time compared to a healthy bladder. The bladder is manually expressed every 12 hours, whereas normally a rat voids every hour. The time of urine expression is short in comparison to the filling time, so emptying time can be ignored, and UBW stretching can be represented by one high stretch value. A step increase in a strain measure could be considered as the input to the model in the areflexic phase. Areal stretch could be taken as the strain measure to eliminate direction dependencies. Normal maximal filling stretches can be determined from the whole-organ strain experiments [113], and an areal strain value can be calculated from this.

As an initial step, the remodeling model expressions will be represented in its most general form as a function of time; this should be replaced by a meaningful expression as a function of the regulatory remodeling parameter, such as tissue stretch or stress. As elucidated in Chapter 8.0 , the parameters that will need to be expressed as a kinetic equation are the constituent mass or volume fractions ϕ_{ECM} and $\phi_{SM.}$. The form of these equations will be determined from the time-course constituent data (Figure 8.1 and Figure 8.2). Newly produced families of collagen fibers exhibit a different level of coiling, which is represented by a different value of λ_{lb} and λ_{ub}, as was confirmed by the 10-day SCI fitting results (section 8.3.4) The shape of the collagen recruitment function will be assumed remain unaltered; only the onset of recruitment and the endpoint will be different. Based on the results from Chapter 6.0, this effect can be introduced as a result of elastin production, and hence the change of λ_{lb} and λ_{ub} can be made a function of elastin production via the elastin mass fraction: $\lambda_{lb}(\phi_{el}(t)), \lambda_{ub}(\phi_{el}(t))$. Another option is to make the change in reference state (via the permanent set deformation ${}^{1}_{0}\mathbf{F}$) a function of a remodeling parameter, similarly to Watton [169, 170]. Changes in SM orientation (Figure

4.6 and Figure 8.5 as further quantified by fitting the data to a bimodal distribution function) could be made a function of a directional change in tissue strain to represent directional hypertrophy.

Time-course data of constituent mass-fraction, specifically of SM, can be described by exponential rise-to-maximum functions, possibly combined with a limiting factor. These types of equations are the response of a linear system to an input of a unit step function. The unit step function can be multiplied with a linear factor, which could represent a measure of stretch or stress, or another regulatory parameter. Next, it will be assumed that larger SM cells or a higher number of SM cells are able to produce more collagen and hence the rate of production of collagen can be represented as a linear function of the amount of smooth muscle (*e.g.* [7]). A limiting factor could be introduced to the maximum amount of collagen that the SM cells can produce. With respect to the elastin component, as a simple initial step it will be assumed that elastin is produced in response to high tissue strain, with a linear relation as function of time or as a function of the strain input, wherein it is assumed that elastin is not degraded. The resulting kinetic equations will be combined with the constitutive model to simulate UBW remodeling as a function of time post-SCI.

9.2.2 Modeling UBW in physiological state

The constitutive model developed in the current dissertation describes UBW tissue in inactive state, which means that no passive tone or active contractions were taken into account and hence the bladder was not modeled in its full physiological state. The physiological state of the smooth muscle cells is characterized by basal tone and the ability to contract upon electrical or chemical stimulation. To derive a model of the tissue in its full physiological state, the mechanical behavior of UBW tissue should be determined in passive and active states, respectively. However, this is complicated by the occurrence of spontaneous contractions as was found from preliminary biaxial mechanical experiments. In addition, an appropriate method of smooth muscle activation to elicit controlled contractions needs to be developed. Currently, no generally accepted model of smooth muscle tone and active contraction is available. The challenge will be to develop such a model, applied specifically to UBW smooth muscle. What also will need to be addressed is the question if it is justified to add inactive, passive, and active behavior, and what

effect preconditioning has on each of these. Speich *et al.* [140-142] addressed this by stating that detrusor preconditioning involves elements of both viscoelastic softening (reversible) and strain softening (cross-link breakage). They suggested that even inactive stiffness is variable, which challenges the assumption that muscle force is the sum of inactive and active forces and inactive force is a constant value at a given muscle length.

To fully validate the model and evaluate the predictive capabilities of the constitutive model, it needs to be extended to the organ level. This will allow for investigation of the relationship between *in vivo* organ level loading patterns and tissue level changes. In clinical urology and in urology research, a common technique to evaluate bladder function is the cystometrogram (CMG), which measures the pressure-volume relation upon controlled bladder filling. To simulate the full 3D bladder organ behavior, the constitutive model together with the remodeling theories would need to be implemented in a Finite Element Method (FEM) framework, together with accurate 3D bladder geometry. In addition, it is relevant to know the exact geometry of the organs of the urinary tract and of the entire pelvic floor in their physiological environment, because surrounding organs impose external pressure on the bladder, which is not taken into account in in vitro testing of the organ. As an initial step, a spherical or spheroidal geometry could be implemented without surrounding organs, combined with membrane theory (i.e., ignoring tissue thickness) and a simple nonlinear phenomenological constitutive model in FEM software such as Comsol Multiphysics®. The next steps would involve implementing the complete 3D rat bladder geometry including a 3D fiber orientation distribution function, implanting the multi-phase structural constitutive model as developed in this dissertation, and to calibrate this with experimental pressure-volume data from rat CMG and with *ex vivo* organ-level strain data [113].

In preparation of the organ level simulations, a 3D surface map of collagen fiber orientation will to be determined, mapped to an accurate 3D bladder geometry. Following methods described by Smith *et al*. [139], an array of 2D markers is mapped to the 3D geometry. An array of white polymer markers dividing the surface in eight sections will be applied to decellularized rat urinary bladders filled with opaque silicone. Bladders will be scanned with a FARO laser arm to obtain the 3D geometry outlining the marker positions. After scanning, the bladders will be cut into sections, and these tissue specimens will be cleared for Small Angle Light Scattering measurements to obtain the planar collagen fiber architecture (see section 5.3.2).

2D SALS measurements are then mapped to the 3D bladder geometry through the following procedure. The 3D point cloud from the FARO scan is converted to spherical coordinates, the marker coordinates are obtained, and the point cloud is divided into eight finite triangular elements based on the marker locations. A general 3D surface is defined by a surface fitting function. Each finite element is related to one of the eight SALS specimens. 2D marker coordinates are determined in the SALS scans and the SALS fiber orientation data is mapped to the 3D surface through the use of an intermediate natural coordinate system. The possibly heterogeneous fiber orientation that is obtained in this manner is incorporated in the Finite Element implementation.

9.2.3 Simulating remodeling in a tissue engineering setting of (smooth) muscle-rich tissues

The field of tissue engineering and regenerative medicine is aimed at replacing injured tissues with functional tissue equivalents. However, the current understanding of the factors that control the functional outcome of the remodeling process that is required for successful tissue engineering is extremely limited. Very few quantitative, systematic studies are available that determine the effect of controllable factors such as mechanical forces, and even fewer studies have focused on (smooth) muscle-rich tissues such as the UBW and the esophagus. The primary function of smooth muscle organs is mechanical in nature (storage, voiding, and transport) and hence mechanical stimuli are important in its tissue formation. The fundamental quantitative principles that guide constructive remodeling of smooth muscle tissue have not been systematically investigated.

In vitro studies at two different levels are currently underway to address the relationship between mechanical forces and tissue remodeling in the context of smooth muscle tissue regeneration. The first level focuses on the effect of loading patterns on *in vitro* remodeling of UBW ECM scaffolds seeded with smooth muscle cells and the second level on how the SM cell seeded ECM scaffolds affect local tissue remodeling events in an *in vitro* organ culture system. Previous *in vitro* organ culture studies on rat UBW tissue have shown a similar remarkable remodeling capability in response to different strain protocols as was observed in the UBW post-SCI. The general nature of the developed multi-phase constitutive model provides the potential to be applied in this setting of tissue engineering. The model can be modified for the specific

characteristics of the *in vitro* systems and underlying mechanisms of *in vitro* strain-induced remodeling can be elucidated in both the ECM scaffold and the combined tissue system of tissue and cell populated ECM scaffold. A scaffold component will need to be added to the various tissue components in the model. And in addition to tissue constituent production, degradation of the scaffold will need to be explicitly modeled.

Adding a different methodology, the remodeling events such as the production and degradation of ECM components and fiber reorientation could also be modeled using a bioinformatics approach, such as the Agent Based Modeling (ABM) technique [89]. This technique adds a stochastic component to the model, and is based on rules rather than equations.

9.2.4 Simulating right ventricle remodeling in response to pulmonary hypertension

Pulmonary hypertension involves chronic pressure overload on the right ventricle (RV), which makes the RV an important focus of treatment of this specific type of hypertension. Central to RV function is the underlying mechanical behavior of the RV myocardium. Current stu0dies are underway to elucidate RV myocardium mechanical behavior in the inactive and active states to evaluate the effects of disease and treatment. Morphological and mechanical behavior of intact, active, RV myocardium from a rat model of pressure overload will be determined. In this study, it is hypothesized that there will be a difference in mechanical behavior between normal and pressure-overloaded RV myocardium, and this will be mostly due to remodeled ECM in combination with increased myocyte mass. The biaxial mechanical behavior of RV myocardium will be quantified in the inactive and actively contracting states, and the relative contribution of ECM is determined by using the same decellularization technique as described in the current dissertation. The same testing will be performed on RV myocardium after remodeling and failure have been induced in the rat by pulmonary artery banding, and results will be compared to the normal behavior.

This situation of RV myocardium remodeling as a result of hypertension is very similar to UBW remodeling as a result of SCI as was covered in the present dissertation, and hence the developed model will be easily applied to this new tissue system. It is anticipated that the ECM component of myocardium can be modeled in the same way as UBW ECM. However, a novel constitutive model for the myocyte component will need to be developed based on the observed

mechanical behavior of intact myocardium, where the ECM behavior is subtracted. The strain energy based approach as utilized in the present dissertation will be a useful technique in this. Simulation of the remodeling process in RV myocardium as a result of pulmonary hypertension will lay the basis for developing new treatments, specifically focused on the RV myocardium tissue.

APPENDIX A

SCHEMATIC OF MODEL EQUATIONS

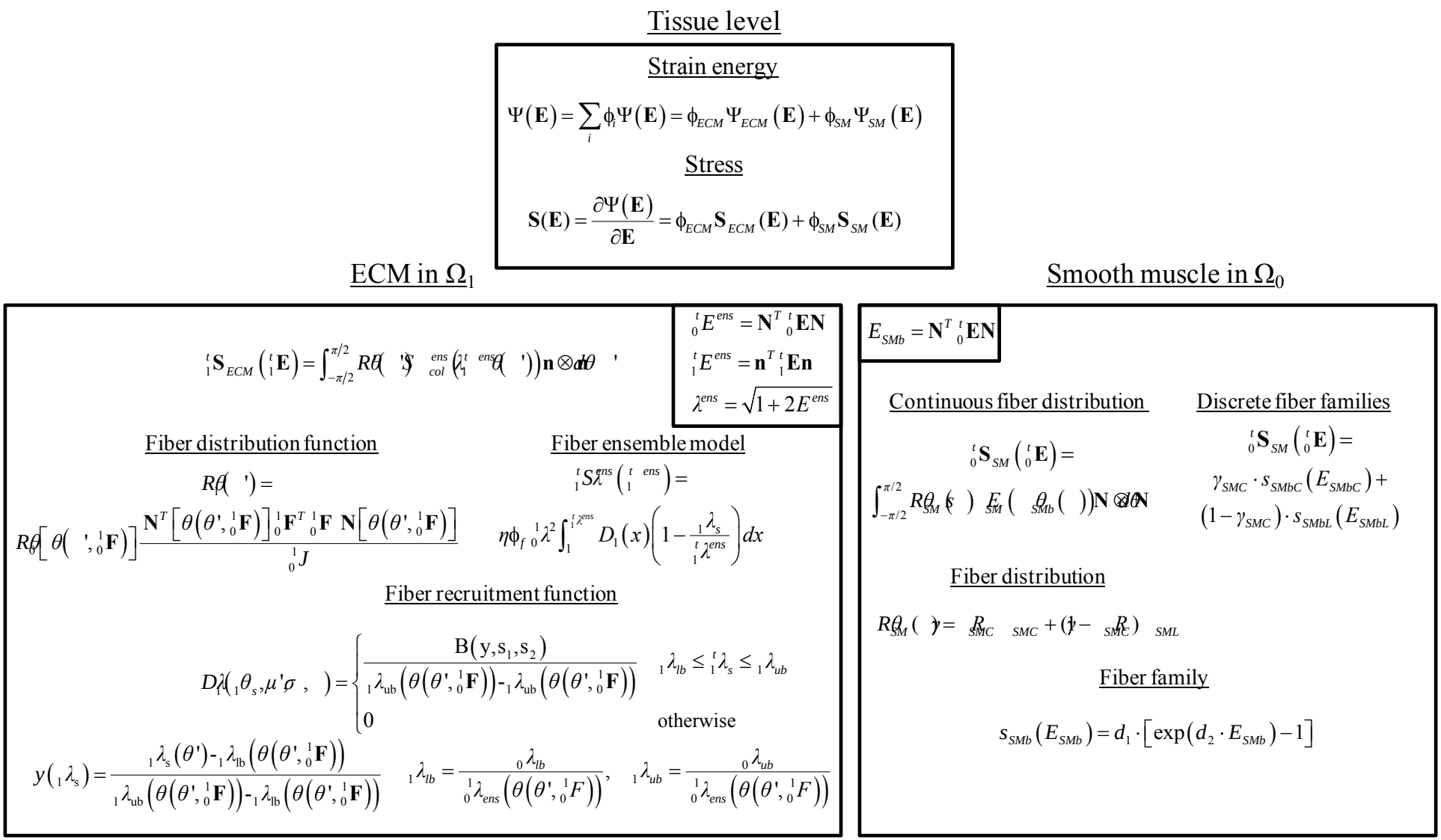

Figure A1. Schematic overview of the relevant equations of the multi-phase structural constitutive model.

APPENDIX B

MATLAB GRAPHICAL USER INTERFACES

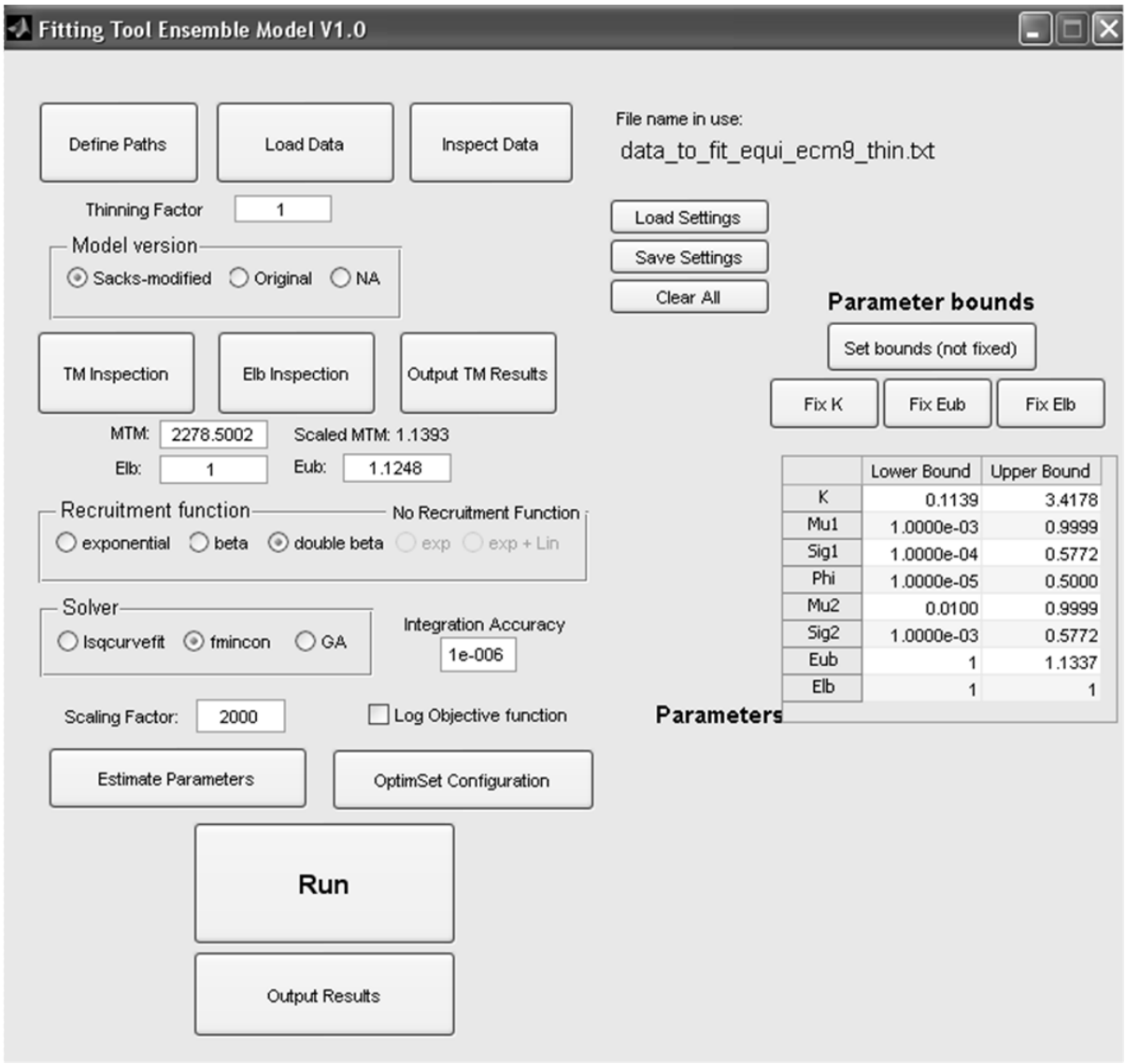

Figure B1. Graphical User Interface of the ensemble model fitting process.

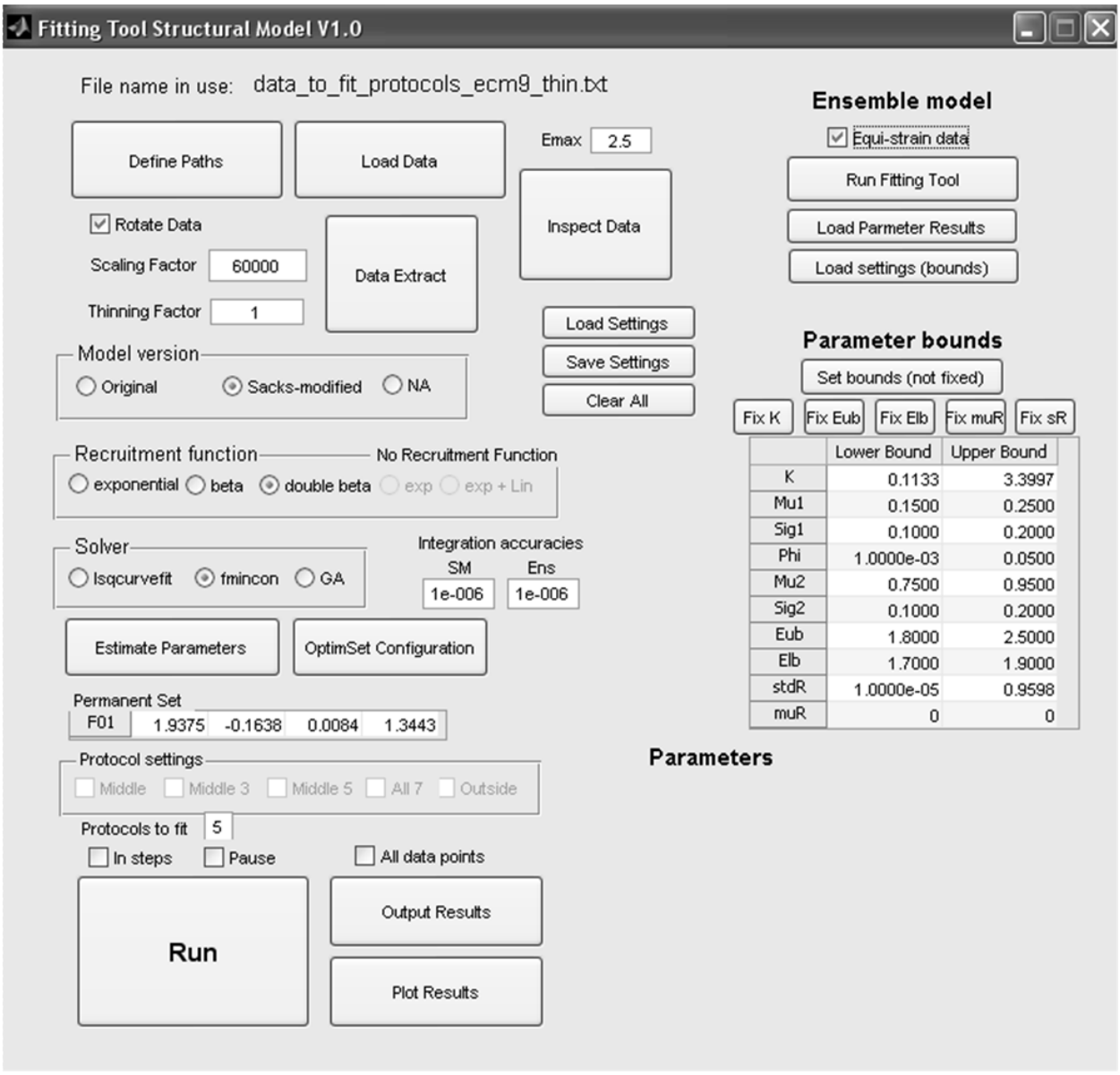

Figure B2. Graphical User Interface of the structural model fitting process.

APPENDIX C

RESULTS OF SYNTHETIC FIBER SIMULATIONS IN MATLAB

Table B1. Overview of settings discrete fiber simulations (see also Table 3.1).

sim.	fiber		F01					maxU1t			
no.	model	λs	descr.	11	12	21	22	descr.	11	12	22
1	S-E	0	none	1	0	0	1	equibiaxial	2	0	2
2		1.5	none	1	0	0	1	equibiaxial	2	0	2
3		1.5	equibiaxi	1	0	0	1	equibiaxial	2	0	2
4		1.5	unequal	1.2	0	0	1	equibiaxial	2	0	2
5		1.5	unequal	1.2	0	0	1	shear	2	0.1	2
6		1.5	shear	1.2	0.10	0.00	1	shear	2	0.1	2
7		1.5	shear	1.2	0.15	0.15	1	shear	2	0.15	2
8	P-λ	1	none	1	0	0	1	equibiaxial	2	0	2
9		1.5	none	1	0	0	1	equibiaxial	2	0	2
10		1.5	equibiaxi	1.1	0	0	1.1	equibiaxial	2	0	2
11		1.5	unequal	1.4	0	0	1.1	equibiaxial	2	0	2

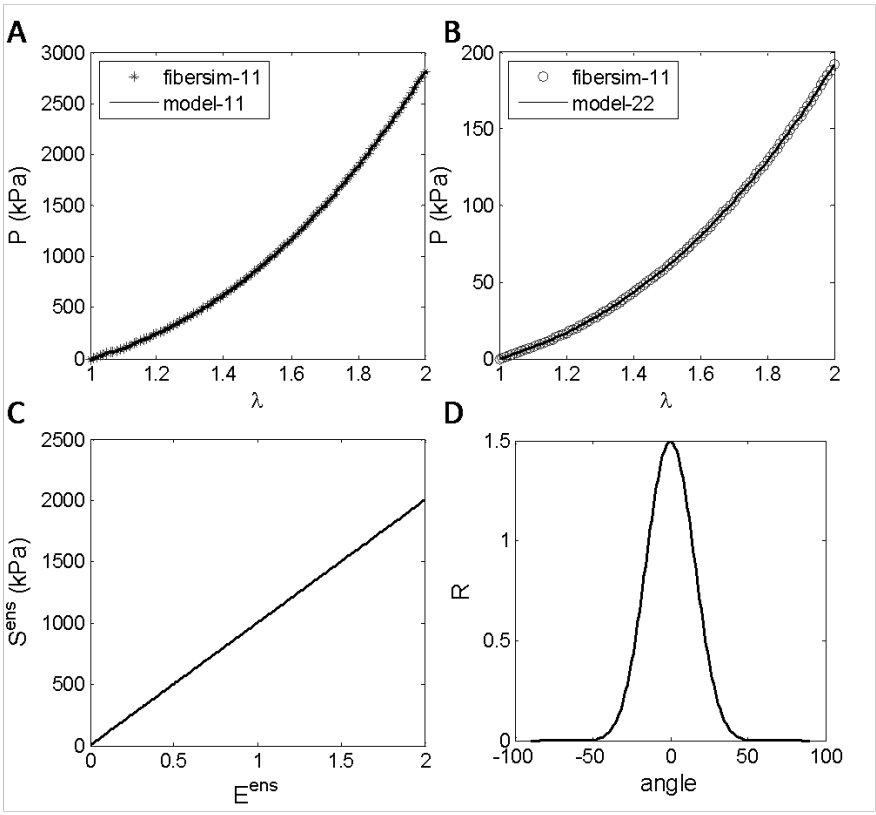

Figure C1. Comparison of model stress calculations with results of discrete fiber simulation 1 with the linear S-E fiber model without slack (Table B1). A) 1st Piola Kirchhoff Stress vs. stretch in the 11 direction. B) 1st Piola Kirchhoff Stress vs. stretch in the 22 direction. C) Fiber ensemble stress vs. fiber ensemble strain. D) Fiber distribution function in Ω_0

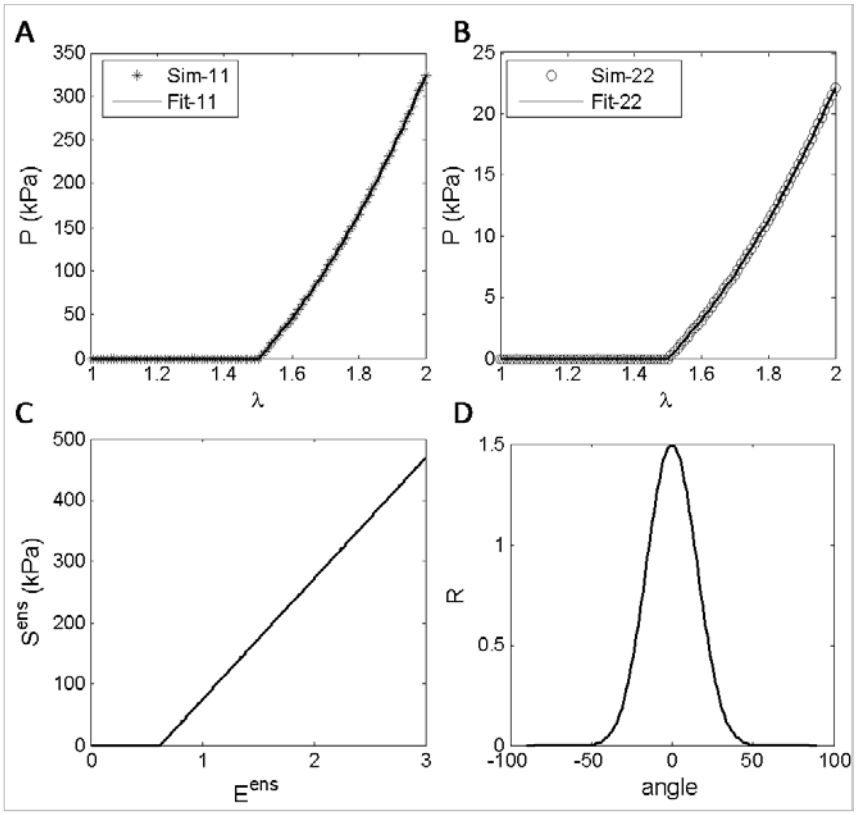

Figure C2. Comparison of model stress calculations with results of discrete fiber simulation no. 2 with the linear S-E fiber model with slack (Table B1). A) 1st Piola Kirchhoff Stress vs. stretch in the 11 direction. B) 1st Piola Kirchhoff Stress vs. stretch in the 22 direction. C) Fiber ensemble stress vs. fiber ensemble strain. D) Fiber distribution function in Ω_0.

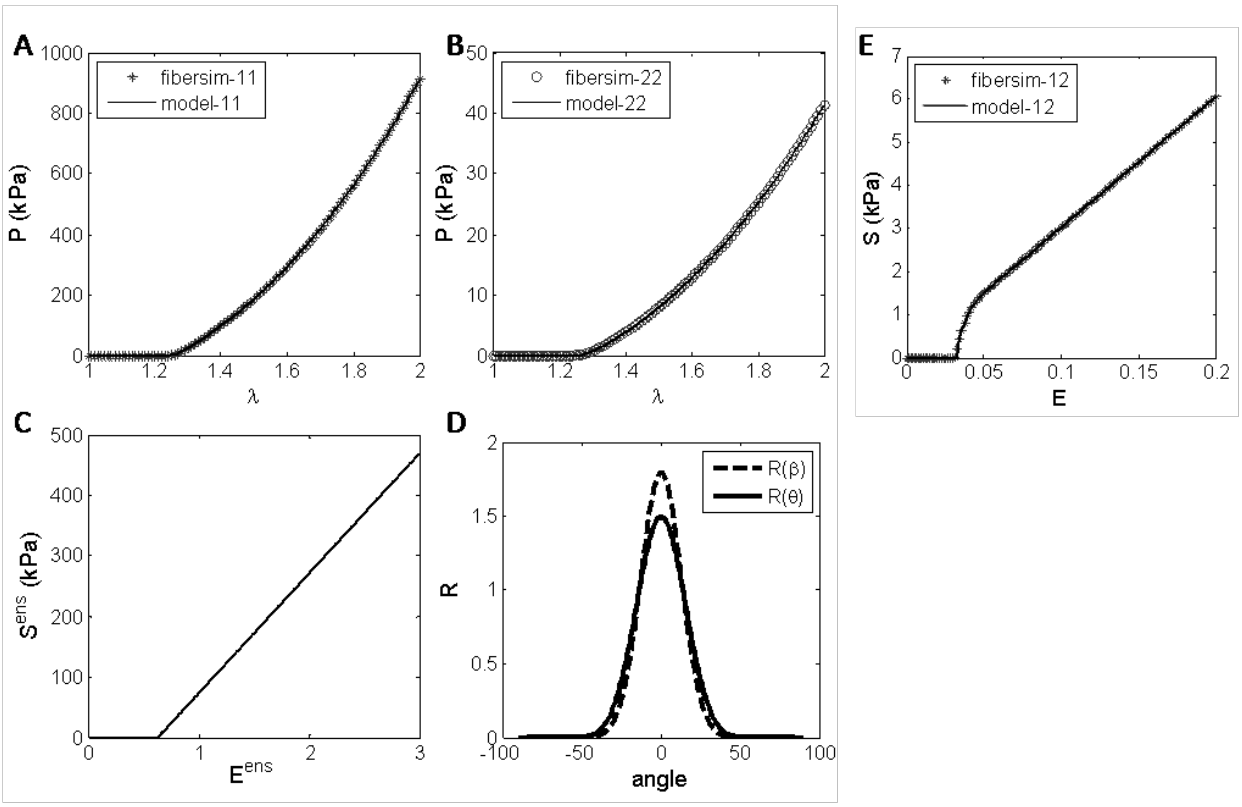

Figure C3. Comparison of model stress calculations with results of discrete fiber simulation no. 5 with the linear S-E fiber model with slack, permanent set and shear deformation (Table B1). A) 1st Piola Kirchhoff Stress vs. stretch in the 11 direction. B) 1 st Piola Kirchhoff Stress vs. stretch in the 22 direction. C) Fiber ensemble stress vs. fiber ensemble strain. D) Fiber distribution function in Ω0 and Ω1. E) 2nd Piola Kirchhoff shear stress vs. shear strain.

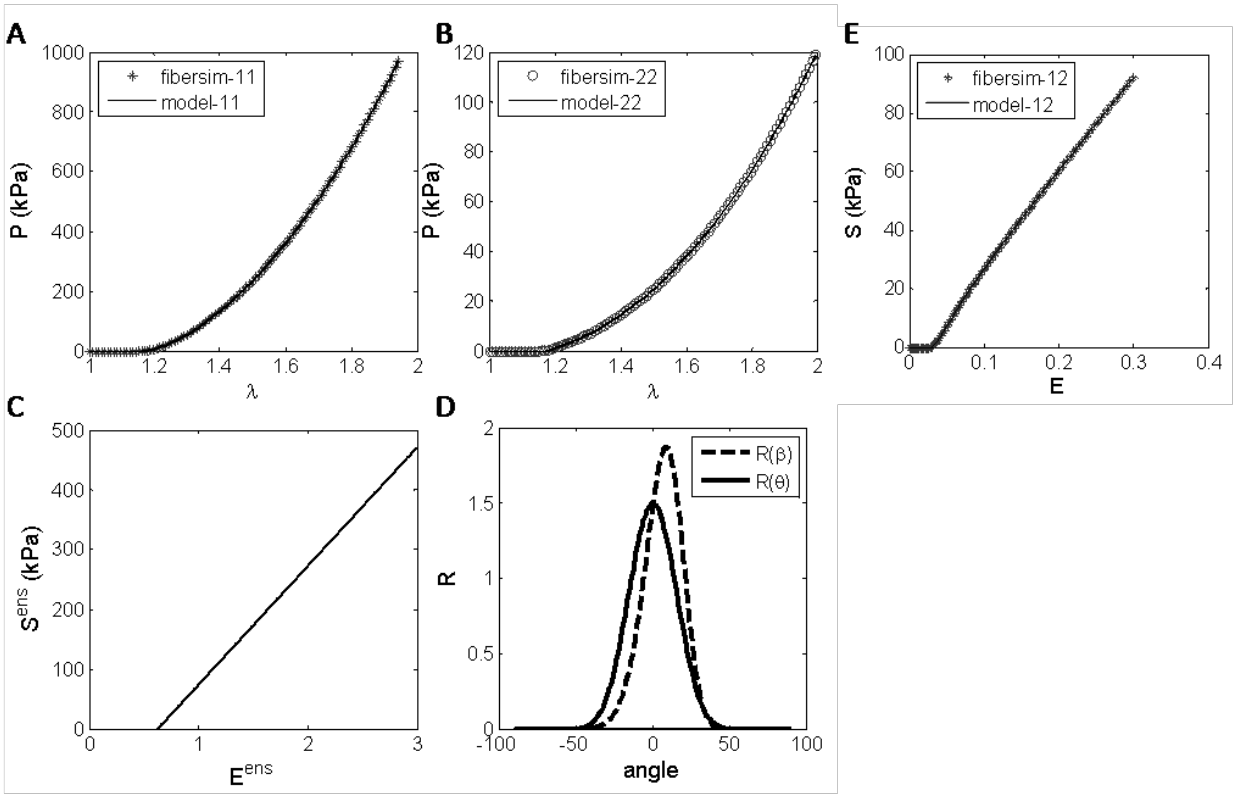

Figure C4. Comparison of model stress calculations with results of discrete fiber simulation no. 7 with the linear S-E fiber model with slack, permanent set including shear and shear deformation (Table B1, Figure 3.7). A) 1st Piola Kirchhoff Stress vs. stretch in the 11 direction. B) 1st Piola Kirchhoff Stress vs. stretch in the 22 direction. C) Fiber ensemble stress vs. fiber ensemble strain. D) Fiber distribution function in Ω_0 and Ω_1. E) 2nd Piola Kirchhoff shear stress vs. shear strain.

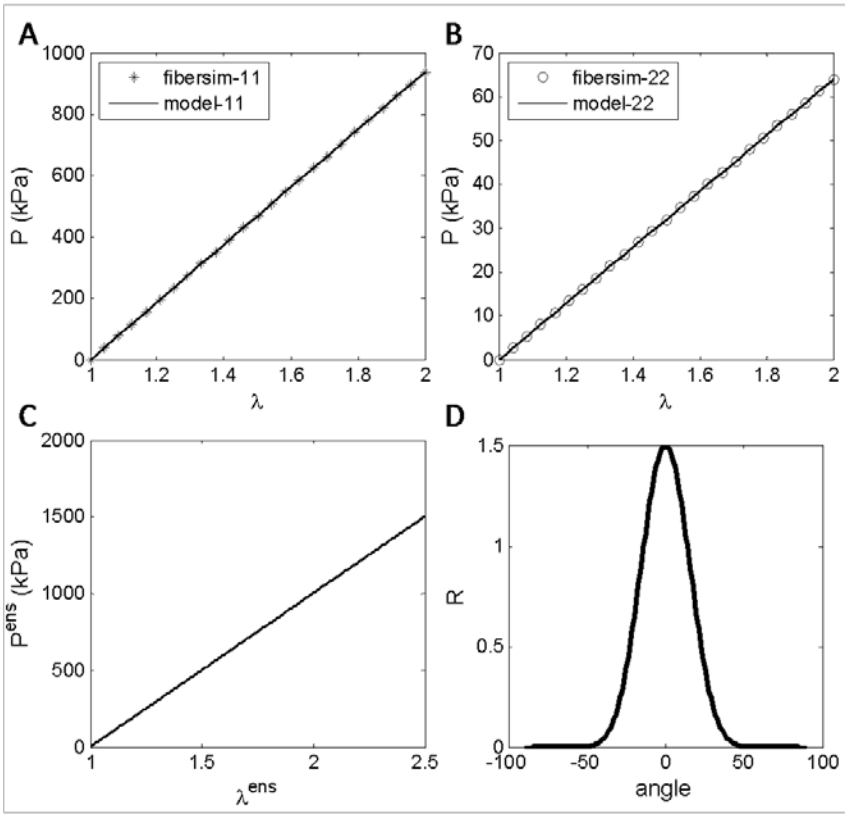

Figure C5. Comparison of model stress calculations with results of discrete fiber simulation 8 with the linear P-λ fiber model without slack (Table B1). A) 1st Piola Kirchhoff Stress vs. stretch in the 11 direction. B) 1st Piola Kirchhoff Stress vs. stretch in the 22 direction. C) Fiber ensemble stress vs. fiber ensemble strain. D) Fiber distribution function in Ω_0.

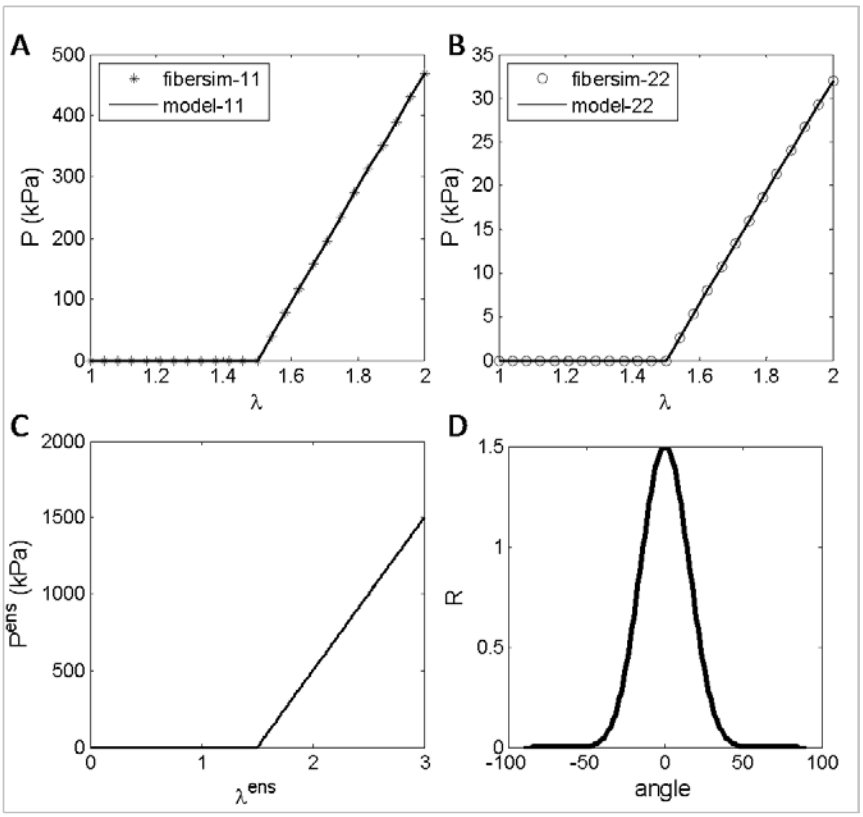

Figure C6. Comparison of model stress calculations with results of discrete fiber simulation 9 with the linear P-λ fiber model with slack (Table B1). A) 1st Piola Kirchhoff Stress vs. stretch in the 11 direction. B) 1st Piola Kirchhoff Stress vs. stretch in the 22 direction. C) Fiber ensemble stress vs. fiber ensemble strain. D) Fiber distribution function in Ω_0.

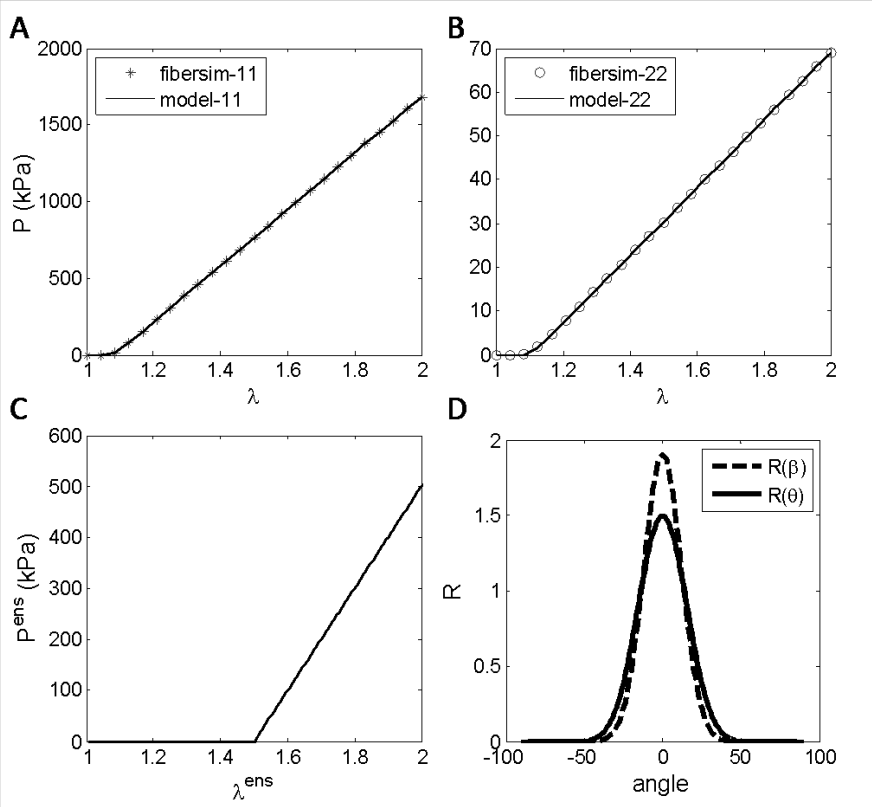

Figure C7. Comparison of model stress calculations with results of discrete fiber simulation 11 with the linear P-λ fiber model with slack and permanent set deformation (Table B1). A) 1st Piola Kirchhoff Stress vs. stretch in the 11 direction. B) 1st Piola Kirchhoff Stress vs. stretch in the 22 direction. C) Fiber ensemble stress vs. fiber ensemble strain. D) Fiber distribution function in Ω_0 and Ω_1.

APPENDIX D

PARAMETRIC INVESTIGATION OF THE MULTI-PHASE CONSTITUTIVE MODEL

Two linear strain paths were defined that encompassed a general strain range representative for both data sets and showing anisotropic effects (Figure D1). These strain paths were used in preliminary parametric studies to facilitate plotting of result). For these two strain paths, ECM and SM strain energy of normal intact UBW were calculated using the model parameters determined in Chapter 7.0, as well as the weighted sum of ECM and SM strain energy (Eq.(2.1). These were plotted as function of the circumferential strain E_C (Figure D2 A-C). Post-SCI intact strain energy (from Figure 8.6) was calculated for the same strain paths for comparison (Figure D2 D).

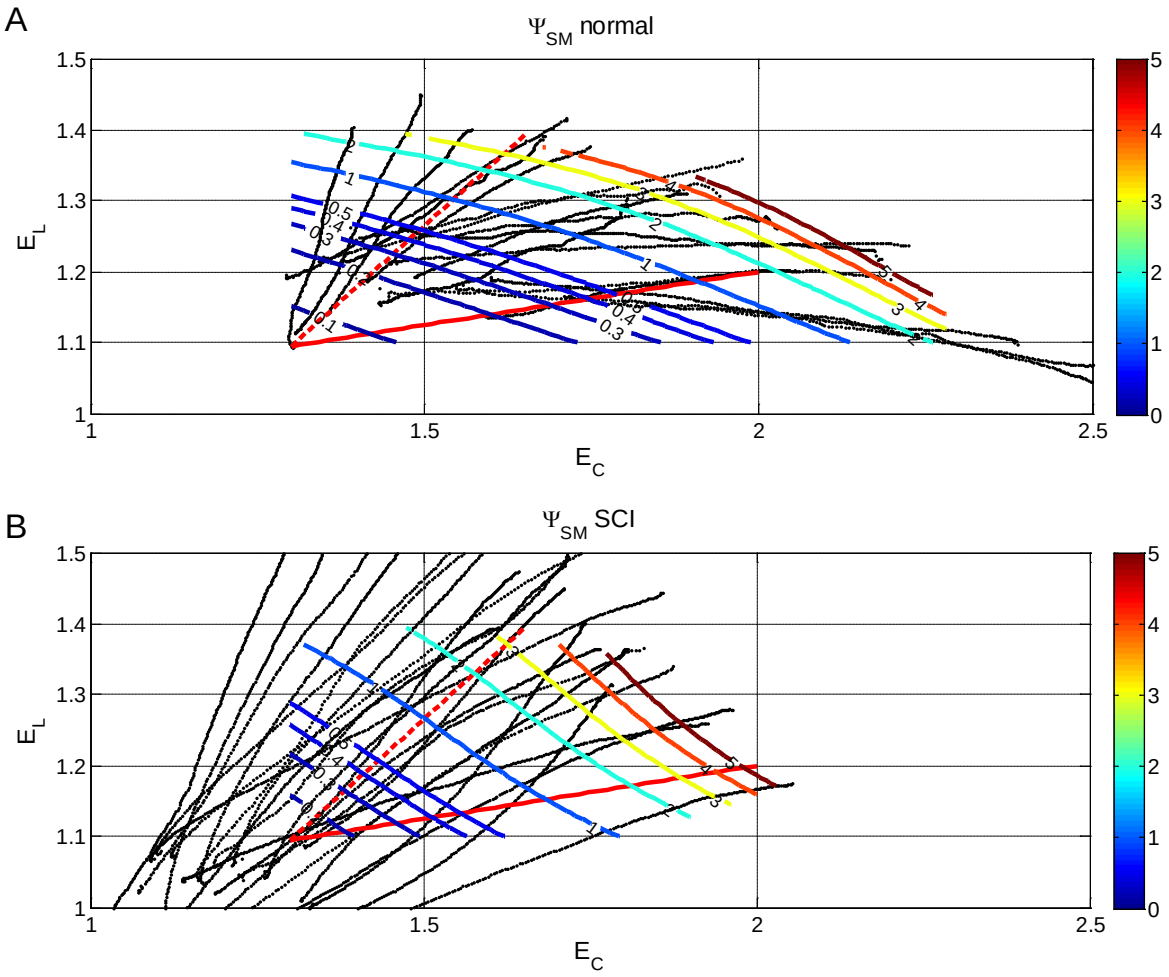

Figure D1. Comparison of intact tissue strain energy of normal and 10-day post-SCI data sets. Individual protocol strain paths are shown by black dots and strain energy surface fits are shown by contour lines. The red lines indicate two general strain paths to use for parametric investigation. The straight line is referred to as "direction 1" and the dashed line as "direction 2". 1 A) Normal. B) 10-days SCI.

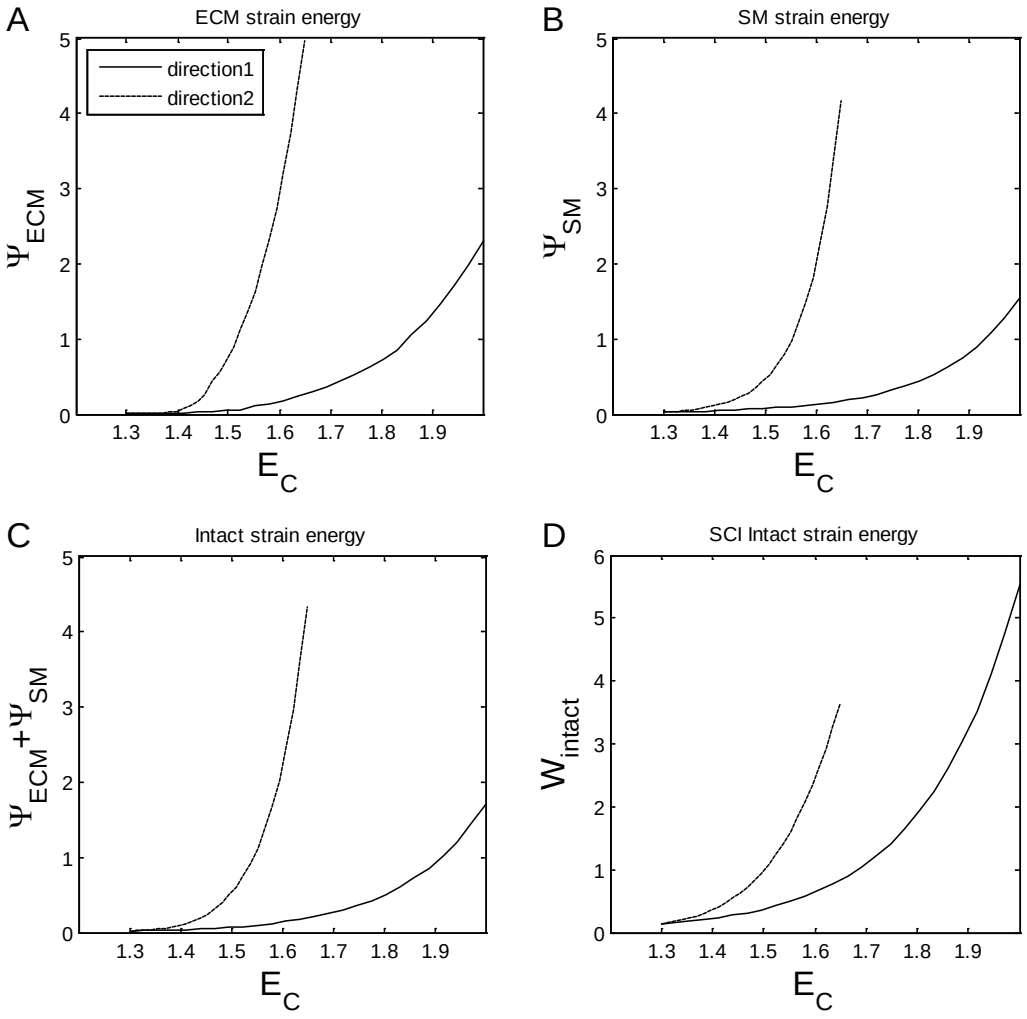

Figure D2. Strain energy of normal ECM, SM and intact, as well as post-SCI intact, for two linear strain paths. The black lines represent "direction 1" and the dashed lines "direction 2" as defined in Figure 8.7. A) Normal ECM strain energy calculated using the model fit parameters (Chapter 7.0). B) SM strain energy calculated using model fit parameters (Chapter 7.0); C) Weighted sum of normal ECM and SM strain energy. D) Post-SCI intact strain energy calculated using the Fung model fit parameters. This is the same data as Figure 8.7

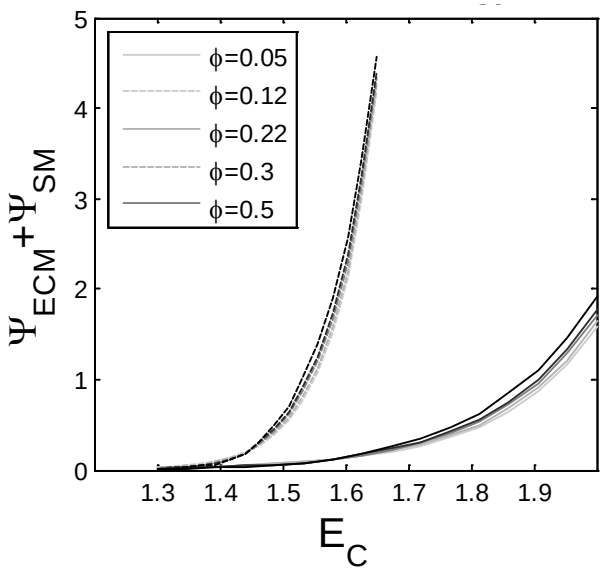

Figure D3. Effect of changes in ECM volume fraction parameter on strain energy of intact tissue. The weighted sum of ECM and SM strain energy was calculated for different values of ϕ_{ECM}. Dashed lines are direction 2. The model is very insensitive to values of ϕ_{ECM}.

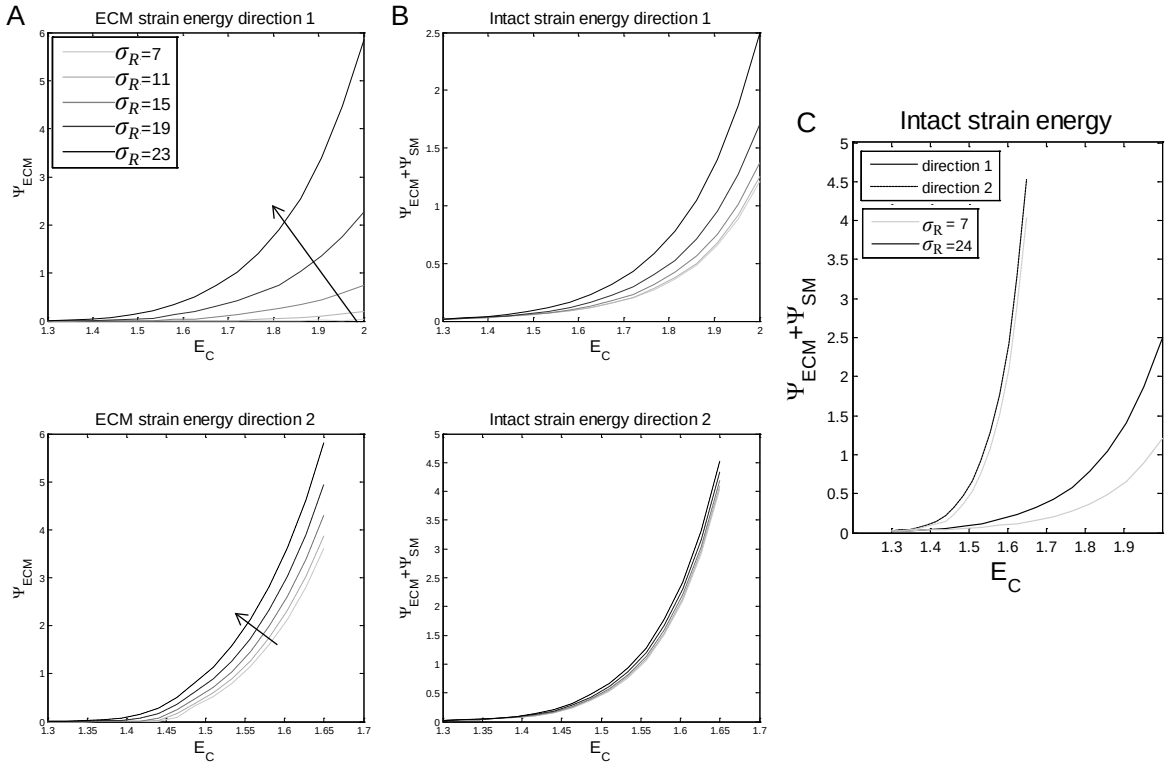

Figure D4. Effect of changes in collagen distribution width on strain energy of ECM and intact tissue. A,B) ECM strain energy (panel A) and the weighted sum of ECM and SM strain energy (panel B) were calculated for different values of σ_R, along two different strain directions. Arrows indicate the direction of parameter increase. σ_R = 19 represents normal behavior. The effect was larger in direction 1 (which is close to the circumferential direction) than in direction 2. C) Comparing the two extreme values of σ_R shows that the overall effect on the intact tissue strain energy is minimal in direction 2.

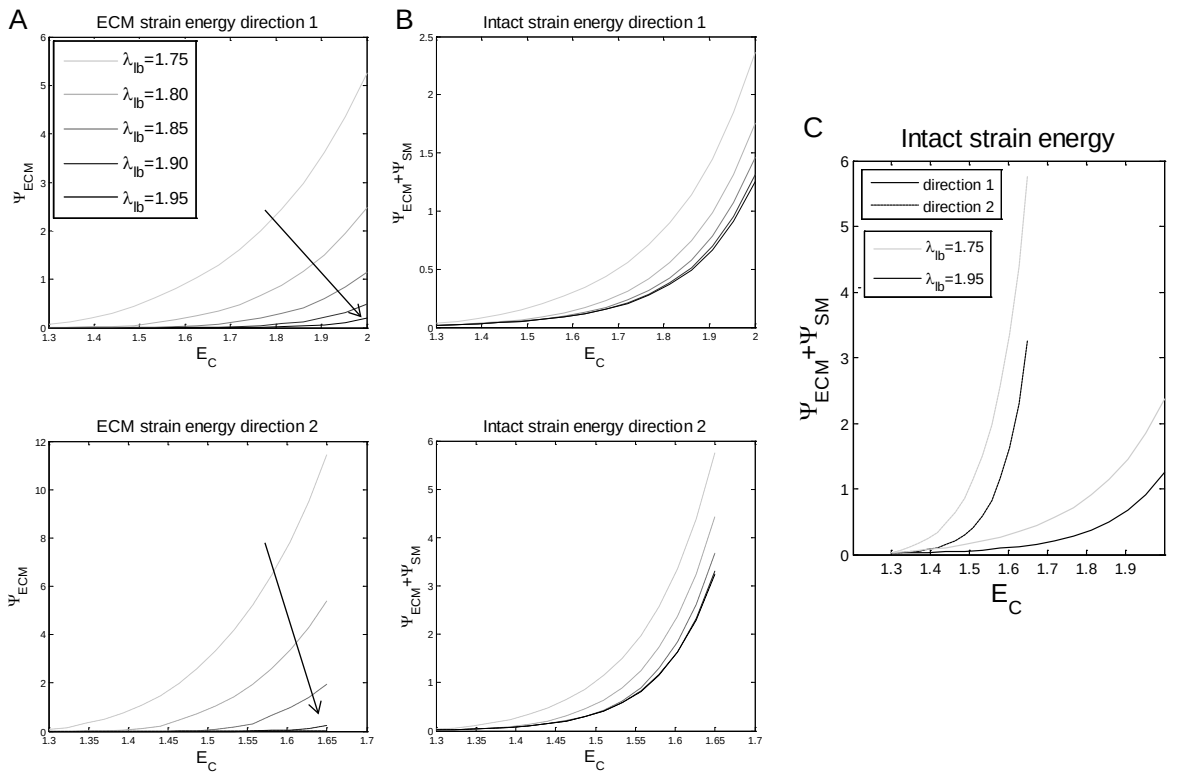

Figure D5. Effect of changes in collagen lower bound strain on strain energy of ECM and intact tissue. A,B) ECM strain energy (panel A) and the weighted sum of ECM and SM strain energy (panel B) were calculated for different values of ${}_0\lambda_{lb}$ along two different strain directions. Arrows indicate the direction of parameter increase. ${}_0\lambda_{lb}$ = 1.8 represents normal behavior. Higher values of ${}_0\lambda_{lb}$ yielded a pronounced decrease of ECM strain energy in both directions resulting in lower tissue-level strain energy in both directions (panel C).

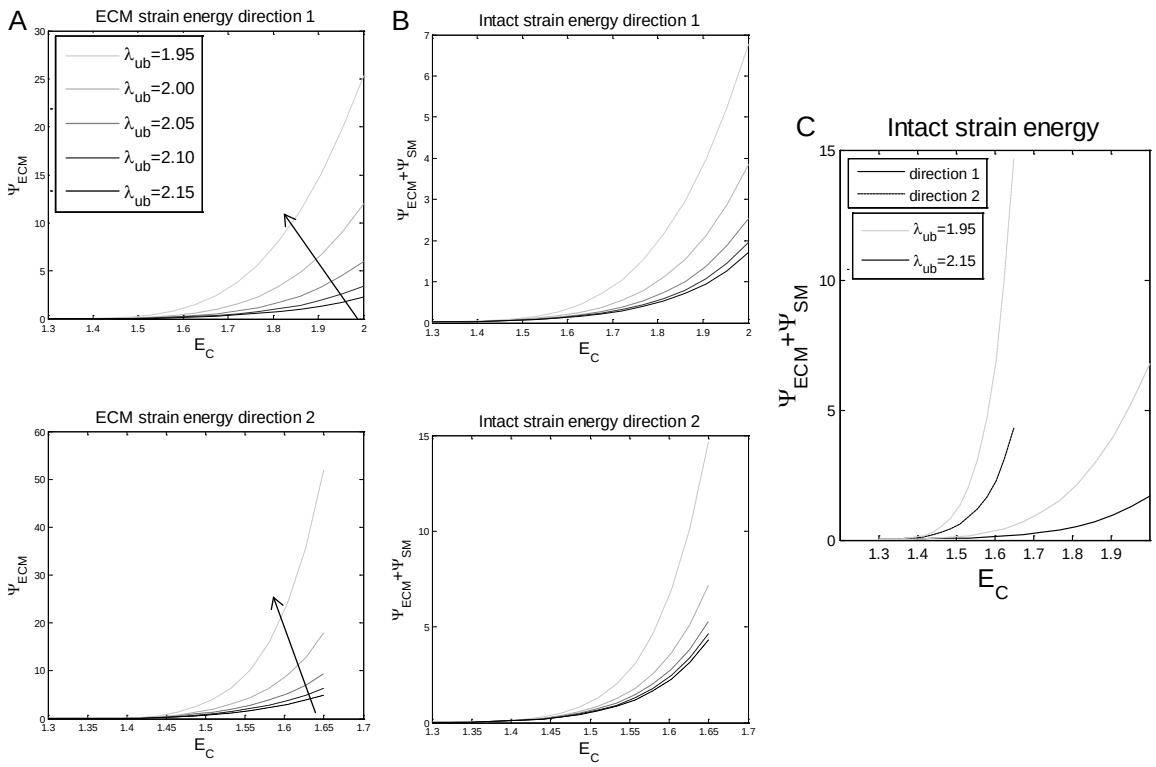

Figure D6. Effect of decreasing the collagen upper bound strain on strain energy of ECM and intact tissue. A,B) ECM strain energy (panel A) and the weighted sum of ECM and SM strain energy (panel B) were calculated for different values of ${}_0\lambda_{ub}$ along two different strain directions. Arrows indicate the direction of decrease in ${}_0\lambda_{ub}$ compared to a normal value of ${}_0\lambda_{ub} = 2.15$. Lower values of ${}_0\lambda_{ub}$ yielded a pronounced increase in ECM strain energy in both directions resulting in higher tissue-level strain energy in both directions (panel C).

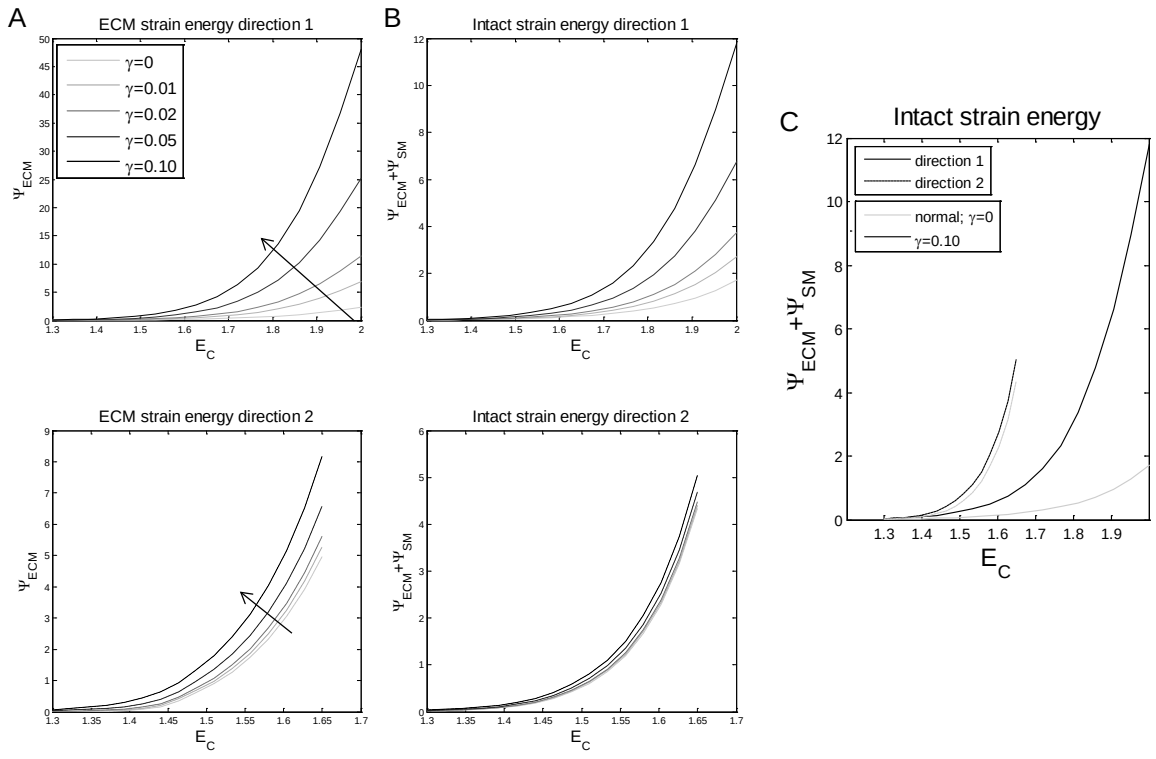

Figure D7. Effect of introducing a second collagen fiber family on strain energy of ECM and intact tissue. A,B) ECM strain energy (panel A) and the weighted sum of ECM and SM strain energy (panel B) were calculated for different values of γ along two different strain directions. Arrows indicate the direction of increase in γ compared to a normal value of $\gamma = 0$. The presence of a collagen fiber family along the circumferential direction yielded a pronounced increase in ECM strain energy in direction 1 resulting in different anisotropic behavior at the tissue level (panel C).

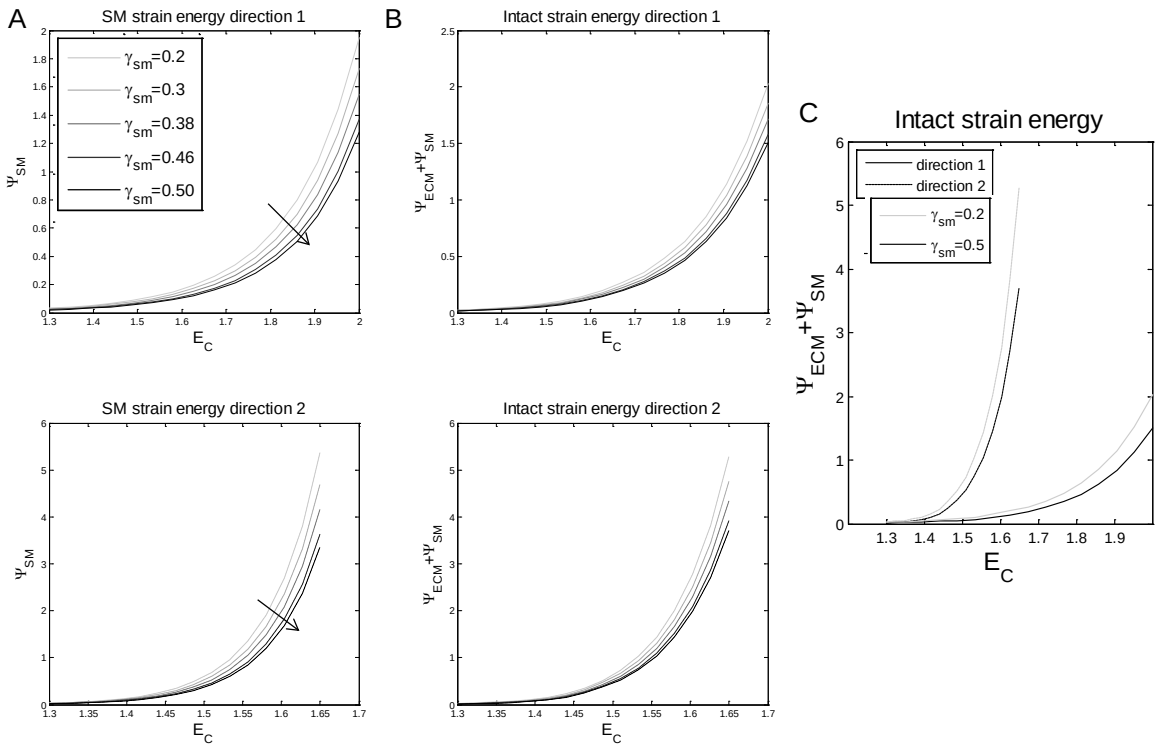

Figure D8. Effect of altering the ratio of circumferential to longitudinal SM fibers on strain energy of SM and intact tissue.

A,B) SM strain energy (panel A) and the weighted sum of ECM and SM strain energy (panel B) were calculated for different values of γ_{SM} along two different strain directions. Arrows indicate the direction of increase in γ_{SM} (normal value: $\gamma_{SM} = 0.38$). C) Comparing the two extreme values shows that the effect on the intact tissue strain energy is moderate.

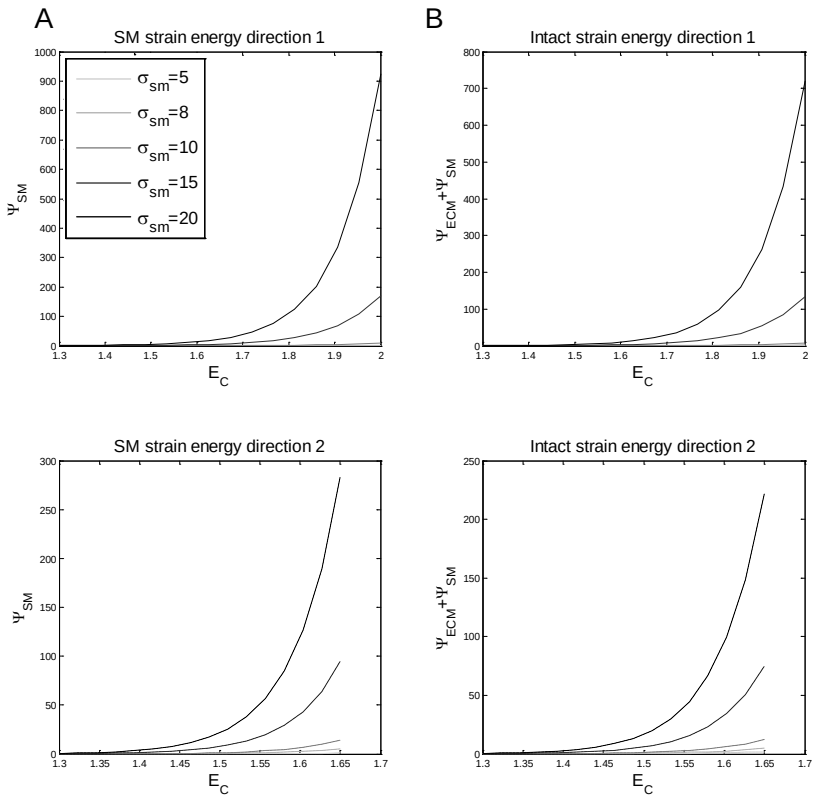

Figure D9. Effect of the width of the distribution of longitudinally oriented SM fibers on strain energy of SM and intact tissue.

A,B) SM strain energy (panel A) and the weighted sum of SM and tissue strain energy (panel B) were calculated for different values of σ_{SML} along two different strain directions. Arrows indicate the direction of increase in σ_{SML} (normal: $\sigma_{SML} = 7.6^{o}$). Note the unrealistically high strain energy values.

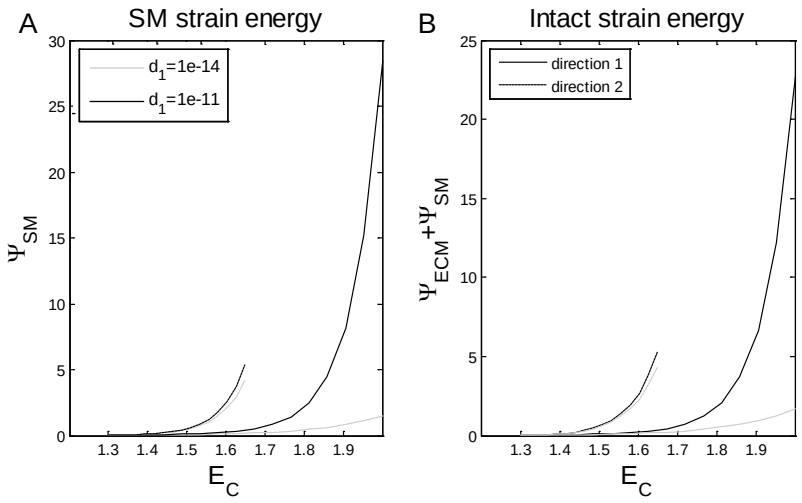

Figure D10. Comparing the effect of two different values of the parameter d_1 of the circumferential fiber family on strain energy of SM and intact tissue.
A higher value of d_1 resulted in significantly higher strain energy values in direction 1 (normal: $d_{C1}= 2.3 \cdot 10^{-14}$).

BIBLIOGRAPHY

1. Alexander, R.S., Mechanical properties of urinary bladder. American Journal of Physiology, 1971. 220(5): p. 1413-1421.

2. Alexander, R.S., Viscoplasticity of smooth muscle of urinary bladder. Am J Physiol, 1973. 224(3): p. 618-622.

3. Alexander, R.S., Series elasticity of urinary bladder smooth muscle. Am J Physiol, 1976. 231(5 Pt. 1): p. 1337-1342.

4. Alford, P.W., J.D. Humphrey, and L.A. Taber, Growth and remodeling in a thick-walled artery model: Effects of spatial variations in wall constituents. Biomech Model Mechanobiol, 2008. 7(4): p. 245-262.

5. Ateshian, G.A., On the theory of reactive mixtures for modeling biological growth. Biomech Model Mechanobiol, 2007. 6(6): p. 423-445.

6. Baek, S. and J.D. Humphrey, Computational modeling of growth and remodeling in biological soft tissues: Application to arterial mechanics, in *Computational modeling in biomechanics*, D. Suvranu, F. Guilak, and M.R.K. Mofrad, Editors. 2010, Springer: Dordrecht Heidelberg London New York.

7. Baek, S., K.R. Rajagopal, and J.D. Humphrey, A theoretical model of enlarging intracranial fusiform aneurysms. J Biomech Eng, 2006. 128(1): p. 142-149.

8. Baek, S., A. Valentin, and J.D. Humphrey, Biochemomechanics of cerebral vasospasm and its resolution: Ii. Constitutive relations and model simulations. Ann Biomed Eng, 2007. 35(9): p. 1498-1509.

9. Billiar, K.L. and M.S. Sacks, Biaxial mechanical properties of the native and glutaraldehyde-treated aortic valve cusp: Part ii--a structural constitutive model. J Biomech Eng, 2000. 122(4): p. 327-335.

10. Billiar, K.L. and M.S. Sacks, Biaxial mechanical properties of the natural and glutaraldehyde treated aortic valve cusp--part i: Experimental results. Journal of Biomechanical Engineering, 2000a. 122(1): p. 23-30.

11. Billiar, K.L. and M.S. Sacks, Biaxial mechanical properties of the native and glutaraldehyde-treated aortic valve cusp: Part ii--a structural constitutive model. Journal of Biomechanical Engineering, 2000b. 122(4): p. 327-335.

12. Bischoff, J.E., Continuous versus discrete (invariant) representation of fibrous structures for modeling non-linear anisotropic soft tissue behavior. International Journal of Non-Linear Mechanics, 2006. 41: p. 167-179.

13. Blaivas, J. and M.B. Chancellor, Atlas of urodynamics. 1996, Baltimore: Williams and Wilkins.

14. Brown, A.L., T.T. Brook-Allred, J.E. Waddell, J. White, J.A. Werkmeister, J.A. Ramshaw, D.J. Bagli, and K.A. Woodhouse, Bladder acellular matrix as a substrate for studying in vitro bladder smooth muscle-urothelial cell interactions. Biomaterials, 2005. 26(5): p. 529-543.

15. Caulfield, J.B. and T.K. Borg, The collagen network of the heart. Lab Invest, 1979. 40(3): p. 364-372.

16. Chang, S.L., P.S. Howard, H.P. Koo, and E.J. Macarak, Role of type iii collagen in bladder filling. Neurourol Urodyn, 1998. 17(2): p. 135-145.

17. Christie, G.W. and B.G. Barratt-Boyes, Age-dependent changes in the radial stretch of human aortic valve leaflets determined by biaxial stretching. Annals of Thoracic Surgery, 1995. 60: p. S156-159.

18. Coolsaet, B.L.R.A., W.A. Van Duyl, R. Van Mastrigt, and J.W. Schouten, Viscoelastic properties of bladder wall strips. Investigative Urology, 1975. 12(5): p. 351-355.

19. Coolsaet, B.L.R.A., R. Van Mastrigt, W.A. Van Duyl, and R.E.F. Huygen, Viscoelastic properties of bladder wall strips at constant elongation. Investigative Urology, 1976. 13(6): p. 435-440.

20. Coplen, D.E., E.J. Macarak, and R.M. Levin, Developmental changes in normal fetal bovine whole bladder physiology. J Urol, 1994. 151(5): p. 1391-1395.

21. Cowin, S.C., The mechanical and stress adaptive properties of bone. Ann Biomed Eng, 1983. 11(3-4): p. 263-295.

22. Criscione, J.C., M.S. Sacks, and W.C. Hunter, Experimentally tractable, pseudo-elastic constitutive law for biomembranes: I. Theory. J Biomech Eng, 2003. 125(1): p. 94-99.

23. Criscione, J.C., M.S. Sacks, and W.C. Hunter, Experimentally tractable, pseudo-elastic constitutive law for biomembranes: Ii. Application. J Biomech Eng, 2003. 125(1): p. 100-105.

24. Dafalias, Y.F., Orientation distribution function in non-affine rotations. Journal of the Mechanics and Physics of Solids, 2001. 49: p. 2493-2516.

25. Dahl, S.L., M.E. Vaughn, J.J. Hu, N.J. Driessen, F.P. Baaijens, J.D. Humphrey, and L.E. Niklason, A microstructurally motivated model of the mechanical behavior of tissue engineered blood vessels. Ann Biomed Eng, 2008. 36(11): p. 1782-1792.

26. Dahms, S.E., H.J. Piechota, R. Dahiya, T.F. Lue, and E.A. Tanagho, Composition and biomechanical properties of the bladder acellular matrix graft: Comparative analysis in rat, pig and human. Br J Urol, 1998. 82(3): p. 411-419.

27. Damaser, M.S., Whole bladder mechanics during filling. Scand J Urol Nephrol Suppl, 1999. 201: p. 51-58.

28. Damaser, M.S., A. Arner, and B. Uvelius, Partial outlet obstruction induces chronic distension and increased stiffness of rat urinary bladder. Neurourol Urodyn, 1996. 15(6): p. 650-665.

29. Damaser, M.S. and S.L. Lehman, The effect of urinary bladder shape on its mechanics during filling. J Biomech, 1995. 28(6): p. 725-732.

30. Damaser, M.S. and S.L. Lehman, Two mathematical models explain the variation in cystometrograms of obstructed urinary bladders. J Biomech, 1996. 29(12): p. 1615-1619.

31. Davol, A., M.S. Bingham, R.L. Sah, and S.M. Klisch, A nonlinear finite element model of cartilage growth. Biomech Model Mechanobiol, 2008. 7(4): p. 295-307.

32. De Groat, W.C., A neurologic basis for the overactive bladder. Urology, 1997. 50(6A Suppl): p. 36-52; discussion 53-36.

33. Dean, G.E., R.S. Cargill, 3rd, E. Macarak, H.M. Snyder, J.W. Duckett, and R. Levin, Active and passive compliance of the fetal bovine bladder. J Urol, 1997. 158(3 Pt 2): p. 1094-1099.

34. Deveaud, C.M., E.J. Macarak, U. Kucich, D.H. Ewalt, W.R. Abrams, and P.S. Howard, Molecular analysis of collagens in bladder fibrosis. J Urol, 1998. 160(4): p. 1518-1527.

35. Drake, M.J., P. Hedlund, I.W. Mills, R. Mccoy, G. Mcmurray, B.P. Gardner, K.E. Andersson, and A.F. Brading, Structural and functional denervation of human detrusor after spinal cord injury. Lab Invest, 2000. 80(10): p. 1491-1499.

36. Engelmayr, G.C. and M.S. Sacks, A structural model for the flexural mechanics of nonwoven tissue engineering scaffolds. J Biomech Eng, 2006. 128: p. 610-622.

37. Fonck, E., G. Prod'hom, S. Roy, L. Augsburger, D.A. Rufenacht, and N. Stergiopulos, Effect of elastin degradation on carotid wall mechanics as assessed by a constituent-based biomechanical model. Am J Physiol Heart Circ Physiol, 2007. 292(6): p. H2754-2763.

38. Fung, Y.C., Biomechanics: Mechanical properties of living tissues. 1981, New York: Springer-Verlag.

39. Fung, Y.C., Biomechanics: Mechanical properties of living tissues. 2nd ed. 1993, New York: Springer Verlag. 568.

40. Fung, Y.C.B., Biorheology of soft tissues. Biorheology, 1973. 10: p. 139-155.

41. Gabella, G. and B. Uvelius, Urinary bladder of rat: Fine structure of normal and hypertrophic musculature. Cell Tissue Res, 1990. 262(1): p. 67-79.

42. Gabella, G. and B. Uvelius, Structural changes in the rat bladder after acute outlet obstruction. Scand J Urol Nephrol Suppl, 1999. 201: p. 32-37.

43. Garikipati, K., E.M. Arruda, K. Grosh, H. Narayanan, and S. Calve, A continuum treatment of growth in biological tissue: The coupling of mass transport and mechanics. Journal of the Mechanics and Physics of Solids, 2004. 52(7): p. 1595-1625.

44. Garikipati, K., H. Narayanan, E.M. Arruda, K. Grosh, and S. Calve, Material forces in the context of biotissue remodelling, in *Material forces in the context of biotissue remodelling*, P. Steinmann and G.A. Maugin, Editors. 2003, Kluwer Academic Publishers.

45. Gleason, R.L., Jr. and J.D. Humphrey, A 2d constrained mixture model for arterial adaptations to large changes in flow, pressure and axial stretch. Math Med Biol, 2005. 22(4): p. 347-369.

46. Gleason, R.L., L.A. Taber, and J.D. Humphrey, A 2-d model of flow-induced alterations in the geometry, structure, and properties of carotid arteries. J Biomech Eng, 2004. 126(3): p. 371-381.

47. Gloeckner, D.C., M.S. Sacks, M.O. Fraser, G.T. Somogyi, W.C. De Groat, and M.B. Chancellor, Passive biaxial mechanical properties of the rat bladder wall after spinal cord injury. J Urol, 2002. 167(5): p. 2247-2252.

48. Gregersen, H., Biomechanics of the gastrointestinal tract. 2003, London: Springer-Verlag.

49. Gundiah, N., B.R. M, and A.P. L, Determination of strain energy function for arterial elastin: Experiments using histology and mechanical tests. J Biomech, 2007. 40(3): p. 586-594.

50. Hackler, R.H., M.K. Hall, and T.A. Zampieri, Bladder hypocompliance in the spinal cord injury population. J Urol, 1989. 141(6): p. 1390-1393.

51. Hansen, L., W. Wan, and R.L. Gleason, Microstructurally motivated constitutive modeling of mouse arteries cultured under altered axial stretch. J Biomech Eng, 2009. 131(10): p. 101015.

52. Hariton, I., G. De Botton, T.C. Gasser, and G.A. Holzapfel, Stress-driven collagen fiber remodeling in arterial walls. Biomech Model Mechanobiol, 2007. 6(3): p. 163-175.

53. Holzapfel, G.A., Nonlinear solid mechanics : A continuum approach for engineering. 2000, Chichester ; New York: Wiley. xiv, 455.

54. Holzapfel, G.A., Determination of material models for arterial walls from uniaxial extension tests and histological structure. J Theor Biol, 2006. 238(2): p. 290-302.

55. Holzapfel, G.A. and T.C. Gasser, A new constitutive framework for arterial wall mechanics and a comparative study of material models. Journal of Elasticity, 2000. 61: p. 1-48.

56. Holzapfel, G.A., T.C. Gasser, and R.W. Ogden, Comparison of a multi-layer structural model for arterial walls with a fung-type model, and issues of material stability. J Biomech Eng, 2004. 126(2): p. 264-275.

57. Holzapfel, G.A. and R.W. Ogden, Constitutive modelling of passive myocardium: A structurally based framework for material characterization. Philos Transact A Math Phys Eng Sci, 2009. 367(1902): p. 3445-3475.

58. Holzapfel, G.A. and R.W. Ogden, On planar biaxial tests for anisotropic nonlinearly elastic solids. A continuum mechanical framework. Mathematics and Mechanics of Solids, 2009. 14(5): p. 474-489.

59. Horowitz, A., Y. Lanir, F.C. Yin, M. Perl, I. Sheinman, and R.K. Strumpf, Structural three-dimensional constitutive law for the passive myocardium. J Biomech Eng, 1988. 110(3): p. 200-207.

60. Horowitz, A., Y. Lanir, F.C.P. Yin, M. Perl, I. Sheinman, and R.K. Strumpf, Structural three dimensional constitutive law for the passive myocardium. Journal of Biomechanical Engineering, 1988. 110: p. 200-207.

61. Hsu, F.H., The influences of mechanical loads on the form of a growing elastic body. J Biomech, 1968. 1(4): p. 303-311.

62. Hu, J.J., A. Ambrus, T.W. Fossum, M.W. Miller, J.D. Humphrey, and E. Wilson, Time courses of growth and remodeling of porcine aortic media during hypertension: A

quantitative immunohistochemical examination. J Histochem Cytochem, 2008. 56(4): p. 359-370.

63. Humphrey, J.D., S. Baek, and L.E. Niklason, Biochemomechanics of cerebral vasospasm and its resolution: I. A new hypothesis and theoretical framework. Ann Biomed Eng, 2007. 35(9): p. 1485-1497.

64. Humphrey, J.D., J.F. Eberth, W.W. Dye, and R.L. Gleason, Fundamental role of axial stress in compensatory adaptations by arteries. J Biomech, 2009. 42(1): p. 1-8.

65. Humphrey, J.D. and K.R. Rajagopal, A constrained mixture model for growth and remodeling of soft tissues. Mathematical models and methods in applied sciences, 2002. 12(3): p. 407-430.

66. Humphrey, J.D. and K.R. Rajagopal, A constrained mixture model for arterial adaptations to a sustained step change in blood flow. Biomech Model Mechanobiol, 2003. 2(2): p. 109-126.

67. Humphrey, J.D., R.K. Strumpf, and F.C. Yin, Determination of a constitutive relation for passive myocardium: I. A new functional form. J Biomech Eng, 1990. 112(3): p. 333-339.

68. Humphrey, J.D., P.B. Wells, S. Baek, J.J. Hu, K. Mcleroy, and A.T. Yeh, A theoretically-motivated biaxial tissue culture system with intravital microscopy. Biomech Model Mechanobiol, 2007.

69. Humphrey, J.D. and F.C.P. Yin, On constitutive relations and finite deformations of passive cardiac tissue: I. A pseudostrain-energy function. Journal of Biomechanical Engineering, 1987. 109: p. 298-304.

70. Itskov, M., A.E. Ehret, and D. Mavrilas, A polyconvex anisotropic strain-energy function for soft collagenous tissues. Biomech Model Mechanobiol, 2006. 5(1): p. 17-26.

71. Jesudason, R., L. Black, A. Majumdar, P. Stone, and B. Suki, Differential effects of static and cyclic stretching during elastase digestion on the mechanical properties of extracellular matrices. J Appl Physiol, 2007. 103(3): p. 803-811.

72. Juurlink, D.N., N. Herrmann, J.P. Szalai, A. Kopp, and D.A. Redelmeier, Medical illness and the risk of suicide in the elderly. Arch Intern Med, 2004. 164(11): p. 1179-1184.

73. Kabla, A. and L. Mahadevan, Nonlinear mechanics of soft fibrous networks. Journal of the Royal Society Interface, 2007. 4(12): p. 99-106.

74. Karam, J.A., D.V. Vazquez, V.K. Lin, and P.E. Zimmern, Elastin expression and elastic fibre width in the anterior vaginal wall of postmenopausal women with and without prolapse. BJU Int, 2007. 100(2): p. 346-350.

75. Karsaj, I. and J.D. Humphrey, A mathematical model of evolving mechanical properties of intraluminal thrombus. Biorheology, 2009. 46(6): p. 509-527.

76. Kim, K.M., B.A. Kogan, C.A. Massad, and Y.C. Huang, Collagen and elastin in the normal fetal bladder. J Urol, 1991. 146(2 (Pt 2)): p. 524-527.

77. Korossis, S., F. Bolland, E. Ingham, J. Fisher, J. Kearney, and J. Southgate, Review: Tissue engineering of the urinary bladder: Considering structure-function relationships and the role of mechanotransduction. Tissue Eng, 2006. 12(4): p. 635-644.

78. Kroon, M., A constitutive model for smooth muscle including active tone and passive viscoelastic behaviour. Math Med Biol, 2009. 27(2): p. 129-155.

79. Kroon, M. and G.A. Holzapfel, A model for saccular cerebral aneurysm growth by collagen fibre remodelling. J Theor Biol, 2007. 247(4): p. 775-787.

80. Kroon, M. and G.A. Holzapfel, A theoretical model for fibroblast-controlled growth of saccular cerebral aneurysms. J Theor Biol, 2009. 257(1): p. 73-83.

81. Lammers, S.R., P.H. Kao, H.J. Qi, K. Hunter, C. Lanning, J. Albietz, S. Hofmeister, R. Mecham, K.R. Stenmark, and R. Shandas, Changes in the structure-function relationship of elastin and its impact on the proximal pulmonary arterial mechanics of hypertensive calves. Am J Physiol Heart Circ Physiol, 2008. 295(4): p. H1451-1459.

82. Lanir, Y., A structural theory for the homogeneous biaxial stress-strain relationships in flat collageneous tissues. Journal of Biomechanics, 1979. 12: p. 423-436.

83. Lanir, Y., Constitutive equation for the lung tissue. Journal of Biomechanical Engineering, 1983. 105: p. 374-380.

84. Lanir, Y., Constitutive equations for fibrous connective tissues. journal of biomechanics, 1983. 16: p. 1-12.

85. Lanir, Y. and Y.C. Fung, Two-dimensional mechanical properties of rabbit skin. Ii. Experimental results. J Biomech, 1974. 7(2): p. 171-182.

86. Lanir, Y., O. Lichtenstein, and O. Imanuel, Optimal design of biaxial tests for structural material characterization of flat tissues. J Biomech Eng, 1996. 118(1): p. 41-47.

87. Lemaitre, J., A course on damage mechanics. 2nd ed. 1996, Berlin Heidelberg New York: Springer-Verlag.

88. Levin, R.M., P. Horan, and S.P. Liu, Metabolic aspects of urinary bladder filling. Scand J Urol Nephrol Suppl, 1999. 201: p. 59-66.

89. Li, N.Y.-K., S. Wognum, K. Ravin, and Y. Vodovotz, Agent-based simulation of urinary tract infection leading to renal scarring. Journal of Critical Care, 2007. 22(4): p. 336-336.

90. Liao, J., L. Yang, J. Grashow, and M.S. Sacks, The relation between collagen fibril kinematics and mechanical properties in the mitral valve anterior leaflet. J Biomech Eng, 2007. 129(1): p. 78-87.

91. Lin, D.H. and F.C. Yin, A multiaxial constitutive law for mammalian left ventricular myocardium in steady-state barium contracture or tetanus. J Biomech Eng, 1998. 120(4): p. 504-517.

92. Liu, X., Y. Zhao, B. Pawlyk, M. Damaser, and T. Li, Failure of elastic fiber homeostasis leads to pelvic floor disorders. Am J Pathol, 2006. 168(2): p. 519-528.

93. Lokshin, O. and Y. Lanir, Micro and macro rheology of planar tissues. Biomaterials, 2009. 30(17): p. 3118-3127.

94. Lokshin, O. and Y. Lanir, Viscoelasticity and preconditioning of rat skin under uniaxial stretch: Microstructural constitutive characterization. J Biomech Eng, 2009. 131(3): p. 031009.

95. Lubarda, V.A., Constitutive theories based on the multiplicative decomposition of deformation gradient: Thermoelasticity, elastoplasticity, and biomechanics. Applied Mechanics Reviews, 2004. 57(2): p. 95-108.

96. Lubarda, V.A. and A. Hoger, On the mechanics of solids with a growing mass. International Journal of Solids and Structures, 2002. 39: p. 4627-4664.

97. Macarak, E.J. and P.S. Howard, The role of collagen in bladder filling. Adv Exp Med Biol, 1999. 462: p. 215-223.

98. Mackenna, D.A., J.H. Omens, and J.W. Covell, Left ventricular perimysial collagen fibers uncoil rather than stretch during diastolic filling. Basic Res Cardiol, 1996. 91(2): p. 111-122.

99. Mckinley, M. and V.D. O'loughlin, Human anatomy. 2nd ed. 2008: McGraw Hill.

100. Mendenhall, W. and T. Sincich, Statistics for the engineering and computer sciences. 1988, San Francisco: Dellen. 1036.

101. Menzel, A., A fibre reorientation model for orthotropic multiplicative growth. Configurational driving stresses, kinematics-based reorientation, and algorithmic aspects. Biomech Model Mechanobiol, 2007. 6(5): p. 303-320.

102. Mimata, H., F. Satoh, T. Tanigawa, Y. Nomura, and J. Ogata, Changes of rat urinary bladder during acute phase of spinal cord injury. Urol Int, 1993. 51(2): p. 89-93.

103. Mirone, V., C. Imbimbo, N. Longo, and F. Fusco, The detrusor muscle: An innocent victim of bladder outlet obstruction. Eur Urol, 2007. 51(1): p. 57-66.

104. Murakumo, M., T. Ushiki, K. Abe, K. Matsumura, Y. Shinno, and T. Koyanagi, Three-dimensional arrangement of collagen and elastin fibers in the human urinary bladder: A scanning electron microscopic study. J Urol, 1995. 154(1): p. 251-256.

105. Nadler, B., P. Papadopoulos, and D.J. Steigmann, Multiscale constitutive modeling and numerical simulation of fabric material. International Journal of Solids and Structures, 2006. 43(2): p. 206-221.

106. Nagatomi, J., F. Demiguel, K. Torimoto, M.B. Chancellor, R.H. Getzenberg, and M.S. Sacks, Early molecular-level changes in rat bladder wall tissue following spinal cord injury. Biochem Biophys Res Commun, 2005. 334(4): p. 1159-1164.

107. Nagatomi, J., D.C. Gloeckner, M.B. Chancellor, W.C. Degroat, and M.S. Sacks, Changes in the biaxial viscoelastic response of the urinary bladder following spinal cord injury. Ann Biomed Eng, 2004. 32(10): p. 1409-1419.

108. Nagatomi, J., K.K. Toosi, M.B. Chancellor, and M.S. Sacks, Contribution of the extracellular matrix to the viscoelastic behavior of the urinary bladder wall. Biomech Model Mechanobiol, 2008. 7(5): p. 395-404.

109. Nagatomi, J., K.K. Toosi, J.S. Grashow, M.B. Chancellor, and M.S. Sacks, Quantification of bladder smooth muscle orientation in normal and spinal cord injured rats. Ann Biomed Eng, 2005. 33(8): p. 1078-1089.

110. Natali, A.N., E.L. Carniel, and H. Gregersen, Biomechanical behaviour of oesophageal tissues: Material and structural configuration, experimental data and constitutive analysis. Med Eng Phys, 2009. 31(9): p. 1056-1062.

111. Noonan, V.K., J.A. Kopec, H. Zhang, and M.F. Dvorak, Impact of associated conditions resulting from spinal cord injury on health status and quality of life in people with traumatic central cord syndrome. Arch Phys Med Rehabil, 2008. 89(6): p. 1074-1082.

112. Ottani, V., M. Raspanti, and A. Ruggeri, Collagen structure and functional implications. Micron, 2001. 32(3): p. 251-260.

113. Parekh, A., A.D. Cigan, S. Wognum, R.L. Heise, M.B. Chancellor, and M.S. Sacks, Ex vivo deformations of the urinary bladder wall during whole bladder filling: Contributions of extracellular matrix and smooth muscle. J Biomech, 2010. 43(9): p. 1708-1716.

114. Pitre, D.A., T. Ma, L.J. Wallace, and J.A. Bauer, Time-dependent urinary bladder remodeling in the streptozotocin-induced diabetic rat model. Acta Diabetol, 2002. 39(1): p. 23-27.

115. Rachev, A., Theoretical study of the effect of stress-dependent remoding on arterial geometry under hypertensive conditions. Journal of Biomechanics, 1997. 8: p. 819-827.

116. Rachev, A. and R.L. Gleason, Jr., Theoretical study on the effects of pressure-induced remodeling on geometry and mechanical non-homogeneity of conduit arteries. Biomech Model Mechanobiol.

117. Rachev, A., N. Stergiopulos, and J.J. Meister, Theoretical study of dynamics of arterial wall remodeling in response to changes in blood pressure. J Biomech, 1996. 29(5): p. 635-642.

118. Rao, I.J., J.D. Humphrey, and K.R. Rajagopal, Biological growth and remodeling: A uniaxial example with possible application to tendons and ligaments. Computer Modeling in Engineering Science, 2003. 4(3&4): p. 439-455.

119. Ratz, P.H. and J.E. Speich, Evidence that actomyosin cross bridges contribute to "Passive" Tension in detrusor smooth muscle. Am J Physiol Renal Physiol, 2010. 298(6): p. F1424-1435.

120. Redaelli, A., S. Vesentini, M. Soncini, P. Vena, S. Mantero, and F.M. Montevecchi, Possible role of decorin glycosaminoglycans in fibril to fibril force transfer in relative mature tendons--a computational study from molecular to microstructural level. J Biomech, 2003. 36(10): p. 1555-1569.

121. Rezakhaniha, R. and N. Stergiopulos, A structural model of the venous wall considering elastin anisotropy. J Biomech Eng, 2008. 130(3): p. 031017.

122. Robinson, T.F., S.M. Factor, J.M. Capasso, B.A. Wittenberg, O.O. Blumenfeld, and S. Seifter, Morphology, composition, and function of struts between cardiac myocytes of rat and hamster. Cell Tissue Res, 1987. 249(2): p. 247-255.

123. Rodriguez, E.K., A. Hoger, and A.D. Mcculloch, Stress-dependent finite growth in soft elastic tissues. J Biomech, 1994. 27(4): p. 455-467.

124. Rohrmann, D., S.A. Zderic, J.W. Duckett, Jr., R.M. Levin, and M.S. Damaser, Compliance of the obstructed fetal rabbit bladder. Neurourol Urodyn, 1997. 16(3): p. 179-189.

125. Rosenbloom, J., H. Koo, P.S. Howard, R. Mecham, and E.J. Macarak, Elastic fibers and their role in bladder extracellular matrix. Adv Exp Med Biol, 1995. 385: p. 161-172.

126. Roy, S., A. Tsamis, G. Prod'hom, and N. Stergiopulos, On the in-series and in-parallel contribution of elastin assessed by a structure-based biomechanical model of the arterial wall. J Biomech, 2008. 41(4): p. 737-743.

127. Rubinstein, M., F.J. Sampaio, and W.S. Costa, Stereological study of collagen and elastic system in the detrusor muscle of bladders from controls and patients with infravesical obstruction. Int Braz J Urol, 2007. 33(1): p. 33-39; discussion 39-41.

128. Sacks, M.S., Biaxial mechanical evaluation of planar biological materials. Journal of Elasticity, 2000. 61: p. 199-246.

129. Sacks, M.S., Incorporation of experimentally-derived fiber orientation into a structural constitutive model for planar collagenous tissues. J Biomech Eng, 2003. 125(2): p. 280-287.

130. Sacks, M.S. and C.J. Chuong, Orthotropic mechanical properties of chemically treated bovine pericardium. Ann Biomed Eng, 1998. 26(5): p. 892-902.

131. Sacks, M.S., D.B. Smith, and E.D. Hiester, A small angle light scattering device for planar connective tissue microstructural analysis. Ann Biomed Eng, 1997. 25(4): p. 678-689.

132. Sasaki, N. and S. Odajima, Elongation mechanism of collagen fibrils and force-strain relations of tendon at each level of structural hierarchy. J Biomech, 1996. 29(9): p. 1131-1136.

133. Sasaki, N. and S. Odajima, Stress-strain curve and young's modulus of a collagen molecule as determined by the x-ray diffraction technique. Journal of Biomechanics, 1996. 29: p. 655-658.

134. Seki, S., K. Sasaki, M.O. Fraser, Y. Igawa, O. Nishizawa, M.B. Chancellor, W.C. De Groat, and N. Yoshimura, Immunoneutralization of nerve growth factor in lumbosacral spinal cord reduces bladder hyperreflexia in spinal cord injured rats. J Urol, 2002. 168(5): p. 2269-2274.

135. Seow, C.Y., Myosin filament assembly in an ever-changing myofilament lattice of smooth muscle. Am J Physiol Cell Physiol, 2005. 289(6): p. C1363-1368.

136. Shapiro, S.D., S.K. Endicott, M.A. Province, J.A. Pierce, and E.J. Campbell, Marked longevity of human lung parenchymal elastic fibers deduced from prevalence of d-aspartate and nuclear weapons-related radiocarbon. J Clin Invest, 1991. 87(5): p. 1828-1834.

137. Shin, J.C., C.I. Park, H.J. Kim, and I.Y. Lee, Significance of low compliance bladder in cauda equina injury. Spinal Cord, 2002. 40(12): p. 650-655.

138. Skalak, R., G. Dasgupta, M. Moss, E. Otten, P. Dullumeijer, and H. Vilmann, Analytical description of growth. J Theor Biol, 1982. 94(3): p. 555-577.

139. Smith, D.B., M.S. Sacks, P.M. Pattany, and R. Schroeder, Fatigue-induced changes in bioprosthetic heart valve three-dimensional geometry and the relation to tissue damage. J Heart Valve Dis, 1999. 8(1): p. 25-33.

140. Speich, J.E., L. Borgsmiller, C. Call, R. Mohr, and P.H. Ratz, Rok-induced cross-link formation stiffens passive muscle: Reversible strain-induced stress softening in rabbit detrusor. Am J Physiol Cell Physiol, 2005. 289(1): p. C12-21.

141. Speich, J.E., C. Dosier, L. Borgsmiller, K. Quintero, H.P. Koo, and P.H. Ratz, Adjustable passive length-tension curve in rabbit detrusor smooth muscle. J Appl Physiol, 2007. 102(5): p. 1746-1755.

142. Speich, J.E., K. Quintero, C. Dosier, L. Borgsmiller, H.P. Koo, and P.H. Ratz, A mechanical model for adjustable passive stiffness in rabbit detrusor. J Appl Physiol, 2006.

143. Spencer, A., Deformations of fibre-reinforced materials. Oxford science research papers. 1972, Glasgow: Oxford university press. 128.

144. Spencer, A.J.M., Continuum mechanics. 1980, New York: Longman Scientific & Technical. 183.

145. Spirka, T.A. and M.S. Damaser, Modeling physiology of the urinary tract. J Endourol, 2007. 21(3): p. 294-299.

146. Stella, J.A. and M.S. Sacks, On the biaxial mechanical properties of the layers of the aortic valve leaflet. J Biomech Eng, 2007. 129(5): p. 757-766.

147. Strumpf, R.K., J.D. Humphrey, and F.C. Yin, Biaxial mechanical properties of passive and tetanized canine diaphragm. Am J Physiol, 1993. 265(2 Pt 2): p. H469-475.

148. Sun, W., M.S. Sacks, T.L. Sellaro, W.S. Slaughter, and M.J. Scott, Biaxial mechanical response of bioprosthetic heart valve biomaterials to high in-plane shear. Journal Biomechanical Engineering, 2003. 125: p. 372-380.

149. Sverdlik, A. and Y. Lanir, Time-dependent mechanical behavior of sheep digital tendons, including the effects of preconditioning. J Biomech Eng, 2002. 124(1): p. 78-84.

150. Taber, L.A., Biomechanics of growth, remodeling, and morphogenesis. Applied Mechanics Reviews, 1995. 48: p. 487-545.

151. Taber, L.A., Nonlinear theory of elasticity. Applications in biomechanics. 2004: World Scientific Publishing Co. Pte. Ltd.

152. Toosi, K.K., J. Nagatomi, M.B. Chancellor, and M.S. Sacks, The effects of long-term spinal cord injury on mechanical properties of the rat urinary bladder. Ann Biomed Eng, 2008. 36(9): p. 1470-1480.

153. Truesdell, C. and W. Noll, The nonlinear field theories of mechanics. 3rd ed, ed. S.S. Antman. 2004, Berlin: Springer-Verlag.

154. Tsamis, A. and N. Stergiopulos, Arterial remodeling in response to hypertension using a constituent-based model. Am J Physiol Heart Circ Physiol, 2007. 293(5): p. H3130-3139.

155. Tsamis, A. and N. Stergiopulos, Arterial remodeling in response to increased blood flow using a constituent-based model. J Biomech, 2009. 42(4): p. 531-536.

156. Tsamis, A., N. Stergiopulos, and A. Rachev, A structure-based model of arterial remodeling in response to sustained hypertension. J Biomech Eng, 2009. 131(10): p. 101004.

157. Ushiki, T. and M. Murakumo, Scanning electron microscopic studies of tissue elastin components exposed by a koh-collagenase or simple koh digestion method. Arch Histol Cytol, 1991. 54(4): p. 427-436.

158. Valentin, A., L. Cardamone, S. Baek, and J.D. Humphrey, Complementary vasoactivity and matrix remodelling in arterial adaptations to altered flow and pressure. J R Soc Interface, 2009. 6(32): p. 293-306.

159. Valentin, A. and J.D. Humphrey, Evaluation of fundamental hypotheses underlying constrained mixture models of arterial growth and remodelling. Philos Transact A Math Phys Eng Sci, 2009. 367(1902): p. 3585-3606.

160. Valentin, A. and J.D. Humphrey, Modeling effects of axial extension on arterial growth and remodeling. Med Biol Eng Comput, 2009. 47(9): p. 979-987.

161. Van Mastrigt, R., Mechanical properties of (urinary bladder) smooth muscle. J Muscle Res Cell Motil, 2002. 23(1): p. 53-57.

162. Van Mastrigt, R., B.L.R.A. Coolsaet, and W.A. Van Duyl, The passive properties of the urinary bladder in the collection phase. Urologia Internationali, 1978. 33: p. 14-21.

163. Van Mastrigt, R., B.L.R.A. Coolsaet, and W.A. Van Duyl, First results of stepwise straining of the human urinary bladder and human bladder strips. Investigative Urology, 1981. 19(1): p. 58-61.

164. Vesentini, S., C.F. Fitie, F.M. Montevecchi, and A. Redaelli, Molecular assessment of the elastic properties of collagen-like homotrimer sequences. Biomech Model Mechanobiol, 2005. 3(4): p. 224-234.

165. Wagg, A. and C.H. Fry, Visco-elastic properties of isolated detrusor smooth muscle. Scand J Urol Nephrol Suppl, 1999. 201: p. 12-18.

166. Wang, Y. and M.M. Hassouna, Neuromodulation reduces c-fos gene expression in spinalized rats: A double-blind randomized study. J Urol, 2000. 163(6): p. 1966-1970.

167. Watanabe, H., K. Akiyama, T. Saito, and F. Oki, A finite deformation theory of intravesical pressure and mural stress of the urinary bladder. Journal of Experimental Medicine, 1981. 135: p. 301-307.

168. Watanabe, T., D.A. Rivas, and M.B. Chancellor, Urodynamics of spinal cord injury. Urol Clin North Am, 1996. 23(3): p. 459-473.

169. Watton, P.N., N.A. Hill, and M. Heil, A mathematical model for the growth of the abdominal aortic aneurysm. Biomech Model Mechanobiol, 2004. 3(2): p. 98-113.

170. Watton, P.N., Y. Ventikos, and G.A. Holzapfel, Modelling the growth and stabilization of cerebral aneurysms. Math Med Biol, 2009. 26(2): p. 133-164.

171. Weld, K.J. and R.R. Dmochowski, Effect of bladder management on urological complications in spinal cord injured patients. J Urol, 2000. 163(3): p. 768-772.

172. Weld, K.J., M.J. Graney, and R.R. Dmochowski, Differences in bladder compliance with time and associations of bladder management with compliance in spinal cord injured patients. J Urol, 2000. 163(4): p. 1228-1233.

173. Wells, P.B., J.L. Harris, and J.D. Humphrey, Altered mechanical behavior of epicardium under isothermal biaxial loading. J Biomech Eng, 2004. 126(4): p. 492-497.

174. Wognum, S., C.E. Lagoa, J. Nagatomi, M.S. Sacks, and Y. Vodovotz, An exploratory pathways analysis of temporal changes induced by spinal cord injury in the rat bladder wall: Insights on remodeling and inflammation. PLoS ONE, 2009. 4(6): p. e5852.

175. Wognum, S., D.E. Schmidt, and M.S. Sacks, On the mechanical role of de novo synthesized elastin in the urinary bladder wall. J Biomech Eng, 2009. 131(10): p. 101018.

176. Yang, W., T.C. Fung, K.S. Chian, and C.K. Chong, Directional, regional, and layer variations of mechanical properties of esophageal tissue and its interpretation using a structure-based constitutive model. J Biomech Eng, 2006. 128(3): p. 409-418.

177. Yoshimura, N., C.P. Smith, M.B. Chancellor, and W.C. De Groat, Pharmacologic and potential biologic interventions to restore bladder function after spinal cord injury. Curr Opin Neurol, 2000. 13(6): p. 677-681.

178. Zulliger, M.A., P. Fridez, K. Hayashi, and N. Stergiopulos, A strain energy function for arteries accounting for wall composition and structure. J Biomech, 2004. 37(7): p. 989-1000.

179. Zulliger, M.A., A. Rachev, and N. Stergiopulos, A constitutive formulation of arterial mechanics including vascular smooth muscle tone. Am J Physiol Heart Circ Physiol, 2004. 287(3): p. H1335-1343.

180. Zulliger, M.A. and N. Stergiopulos, Structural strain energy function applied to the ageing of the human aorta. J Biomech, 2007. 40(14): p. 3061-3069.